AD-766 754

MIXING INVESTIGATION OF HYDROGEN AND SUPERSONIC FLUORINE FLOWS

Stewart G. Chapin

Martin Marietta Corporation

Prepared for:

Air Force Weapons Laboratory

June 1973

DISTRIBUTED BY:

NTIS

National Technical Information Service
U. S. DEPARTMENT OF COMMERCE
5285 Port Royal Road, Springfield Va. 22151

AFWL-TR-
72-242

AD 766754

MIXING INVESTIGATION OF HYDROGEN AND SUPERSONIC FLUORINE FLOWS

Stewart G. Chapin
Martin-Marietta Corporation

TECHNICAL REPORT NO. AFWL-TR-72-242

June 1973

Reproduced by
NATIONAL TECHNICAL
INFORMATION SERVICE
US Department of Commerce
Springfield, VA. 22151

AIR FORCE WEAPONS LABORATORY
Air Force Systems Command
Kirtland Air Force Base
New Mexico

Approved for public release; distribution unlimited.

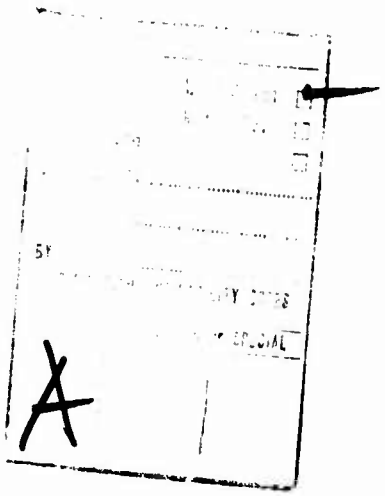

AIR FORCE WEAPONS LABORATORY
Air Force Systems Command
Kirtland Air Force Base
New Mexico 87117

When US Government drawings, specifications, or other data are used for any purpose other than a definitely related Government procurement operation, the Government thereby incurs no responsibility nor any obligation whatsoever, and the fact that the Government may have formulated, furnished, or in any way supplied the said drawings, specifications, or other data, is not to be regarded by implication or otherwise, as in any manner licensing the holder or any other person or corporation, or conveying any rights or permission to manufacture, use, or sell any patented invention that may in any way be related thereto.

DO NOT RETURN THIS COPY. RETAIN OR DESTROY.

UNCLASSIFIED

Security Classification

DOCUMENT CONTROL DATA - R & D

(Security classification of title, body of abstract and indexing annotation must be entered when the overall report is classified)

1 ORIGINATING ACTIVITY (Corporate author)	2a. REPORT SECURITY CLASSIFICATION
Martin-Marietta Corporation Denver, Colorado 80201	UNCLASSIFIED
	2b. GROUP

3 REPORT TITLE

MIXING INVESTIGATION OF HYDROGEN AND SUPERSONIC FLUORINE FLOWS

4 DESCRIPTIVE NOTES (Type of report and inclusive dates)

19 January 1972 through 1 February 1973.

5 AUTHOR(S) (First name, middle initial, last name)

Stewart G. Chapin

6. REPORT DATE	7a. TOTAL NO. OF PAGES	7b. NO. OF REFS
June 1973	176	49

8a. CONTRACT OR GRANT NO.	9a. ORIGINATOR'S REPORT NUMBER(S)
F29601-72-C-0044	
b. PROJECT NO.	AFWL-TR-72-242
1256	
c.	9b. OTHER REPORT NO(S) (Any other numbers that may be assigned this report)
Task 06	
d.	

10. DISTRIBUTION STATEMENT

Approved for public release; distribution unlimited.

11 SUPPLEMENTARY NOTES	12. SPONSORING MILITARY ACTIVITY
	AFWL (LRT) Kirtland AFB, NM 87117

13. ABSTRACT

(Distribution Limitation Statement A)

Experimental data from two shock tube/shock tunnel facilities capable of simulating the operational conditions of continuous flow chemical laser devices are presented. One facility is specifically designed for reproducing the reaction mixing region developed when hydrogen is injected through various sonic ports into a supersonic fluorine carrying stream; the other facility simulates the parallel shear layer mixing developed between a supersonic fluorine carrying stream and an adjacent supersonic hydrogen carrying stream. Established experimental techniques, including the Mach-Zehnder interferometer, rapid scanning infrared spectrometer, pitot pressure probes, and thermocouple temperature probes, have been employed to map flow conditions within the test section mixing layer. A theoretical model of the parallel shear flow turbulent mixing region is described and results from this model are compared with measured monochromatic fringe-shift profiles. Reasonably good agreement has been demonstrated between theoretical predictions and the experimental profiles for two widely different experimental situations.

Details of illustrations in this document may be better studied on microfiche.

DD FORM 1 NOV 65 1473

UNCLASSIFIED

Security Classification

14. KEY WORDS	LINK A		LINK B		LINK C	
	ROLE	WT	ROLE	WT	ROLE	WT
Mixing Reacting flow Supersonic flow Parallel mixing Injection mixing, HF laser						

MIXING INVESTIGATION OF HYDROGEN AND SUPERSONIC FLUORINE FLOWS

Stewart G. Chapin

Martin-Marietta Corporation

TECHNICAL REPORT NO. AFWL-TR-72-242

Approved for public release; distribution unlimited.

ic

FOREWORD

This report was prepared by Martin-Marietta Corporation, Denver, Colorado, under Contract F29601-72-C-0044. The research was performed under Program Element 62301D, Project 1256, Task 06, and was funded by the Advance Research Project Agency under ARPA Order 1256.

Inclusive dates of research were 19 January 1972 through 1 February 1973. The report was submitted 19 May 1973 by the Air Force Weapons Laboratory Project Officer, Dr. Leroy E. Wilson (LRT).

The Contractor's report number is MCR-73-37.

This technical report has been reviewed and is approved.

Leroy Wilson
LEROY E. WILSON
Project Officer

JOHN C. RICH
Colonel, USAF
Advanced Technology Branch

DONALD L. LAMBERSON
Colonel, USAF
Laser Division

ABSTRACT

(Distribution Limitation Statement A)

Experimental data from two shock tube/shock tunnel facilities capable of simulating the operational conditions of continuous flow chemical laser devices are presented. One facility is specifically designed for reproducing the reaction mixing region developed when hydrogen is injected through various sonic ports into a supersonic fluorine carrying stream; the other facility simulates the parallel shear layer mixing developed between a supersonic fluorine carrying stream and an adjacent supersonic hydrogen carrying stream. Established experimental techniques, including the Mach-Zehnder interferometer, rapid scanning infrared spectrometer, pitot pressure probes, and thermocouple temperature probes, have been employed to map flow conditions within the test section mixing layer. A theoretical model of the parallel shear flow turbulent mixing region is described and results from this model are compared with measured monochromatic fringe-shift profiles. Reasonably good agreement has been demonstrated between theoretical predictions and the experimental profiles for two widely different experimental situations.

CONTENTS

Section		Page
I	INTRODUCTION AND SUMMARY.	1
II	EXPERIMENTAL FACILITY DESCRIPTION	5
	1. INJECTION SHOCK TUNNEL	5
	2. PARALLEL MIXING SHOCK TUNNEL	17
	3. THEORETICAL PERFORMANCE ANALYSIS OF SHOCK TUBE/ SHOCK TUNNEL	21
	4. DIAGNOSTIC INSTRUMENTATION	31
III	EXPERIMENTAL RESULTS.	60
	1. SUMMARY OF AVERAGE DENSITY PROFILES	60
	2. SUMMARY OF RAPID-SCAN RESULTS	90
	3. SUMMARY OF PITOT PROBE RESULTS	98
	4. SUMMARY OF STATIC PRESSURES	101
	5. SUMMARY OF TEMPERATURE MEASUREMENTS	104
IV	THEORY AND ANALYSIS OF PARALLEL TURBULENT MIXING LAYERS .	107
	1. TURBULENT TRANSPORT MODELS	107
	2. ANALYTICAL TECHNIQUES	114
	3. RESULTS OF ANALYSIS OF PARALLEL TURBULENT MIXING LAYERS	129
	4. EXTENSION OF ANALYSIS TO INJECTION MIXING	142
V	DISCUSSION OF RESULTS	146
	1. EXPERIMENTAL RESULTS	146
	2. ANALYTICAL RESULTS	148
VI	CONCLUSIONS AND RECOMMENDATIONS	155
	REFERENCES	157

Preceding page blank

ILLUSTRATIONS

Figure		Page
1.	Injection Facility Schematic.	6
2.	Gas-Handling Schematic.	8
3.	Injection Test Section	9
4.	Mach 5.0 Nozzle Block Details	10
5.	Injection Test Section.	11
6.	Opened Test Section Diaphragm	12
7.	Orifice Splitter Plate Schematic	15
8.	Orifice Splitter Plate	15
9.	Slotted Splitter Plate	16
10.	Parallel Mixing Facility Schematic	18
11.	Parallel Mixing Test Section Schematic	19
12.	Parallel Mixing Test Section	20
13.	Fluorine Dissociation Fraction vs Incident Shock Mach Number	26
14.	Nozzle Exit Static Pressure vs Incident Shock Mach Number	28
15.	Nozzle Exit Static Pressure vs Incident Shock Mach Number	29
16.	Generalized Ray Diagram	32
17.	Schematic of Basic MZI Arrangement	34
18.	Schematic of MZI Installation Showing Shock Tube and Radiation Stop.	36
19.	Generalized Light Ray Path	37
20.	Refractive Index vs λ	42

		Page
21.	Experimental Setup for Refractive Index Measurements of HF and F_2	43
22.	Fringe Shift vs Pressure for Refractive Index Measurement of HF	45
23.	Rapid Scanning Spectrometer Optical Schematic	48
24.	Shock Tube with Rapid Scanning Spectrometer in Position	49
25.	E_c (λ) vs λ for the Injection Mixing Rapid Scanning Spectrometer Calibration	54
26.	E_c (z_i) vs z_i Position for the Injection Mixing Rapid Scanning Spectrometer Calibration	55
27.	Pitot Probe	57
28.	Side-Wall Static Pressure Transducer Locations	58
29.	Thermocouple Probe	59
30.	Comparison of Slotted Injection Snapshot Interferograms, λ = 4358Å	64
31.	Comparison of Orifice Injection Snapshot Interferograms, λ = 4358Å	67
32.	Interferometric Results, Runs 72072503 and 72060804	68
33.	Interferometric Results, Runs 72072101 and 72061502	69
34.	Interferometric Results, Runs 72071803 and 72061701	70
35a.	Comparison of Fringe-Shift Profiles for 150- and 50-psi Slotted H_2 Injection at 5 Torr	72
35b.	Comparison of Fringe-Shift Profiles for 150- and 50-psi Slotted H_2 Injection at 8 Torr	73
35c.	Comparison of Fringe-Shift Profiles for 150- and 50-psi Slotted H_2 Injection at 12 Torr	74
35d.	Comparison of Fringe-Shift Profiles for 150- and 50-psi Orifice H_2 Injection at 5 Torr	75

		Page
35e.	Comparison of Fringe-Shift Profiles for 150- and 50-psi Orifice H_2 Injection at 10 Torr	76
35f.	Comparison of Fringe-Shift Profiles for 150- and 50-psi Orifice H_2 Injection at 12 Torr	77
36.	Mixing Layer Width vs Injection Pressure	79
37.	Typical Fringe Shift Showing Assumed Species Distribution Used for Computing Averaged Number Densities	80
38.	Averaged Values for Number Density Distributions for Selected Injection Mixing Cases	81-82
39.	Comparison of Parallel Mixing Interferograms	85
40.	Comparison of Fringe-Shift Profiles for Three Parallel Mixing Experiments	87
41.	Comparison of Fringe-Shift Profiles for Three Parallel Mixing Experiments	88
42.	Comparison of Fringe-Shift Profiles for Three Parallel Mixing Experiments	89
43.	Run 72072101 Showing 12-mm Slit Height	91
44.	Total 2.7-μm Emission (Upper Trace) and Time Mark Indicating Duration of a Single Scan of the Spectrometer (Lower Trace)	92
45.	Rapid Scanning Infrared Spectrometer Traces	92
46.	Schematic of Nominal HF Emission Spectra.	94
47.	Specific Radiation Intensity vs Downstream Distance for Two Different Injection Pressures	95
48.	2.795-μm Radiation in Three Parallel Mixing Streams at Five Stations Downstream of Splitter Plate	97
49.	Pitot Survey Results for 150-psi H_2 Injection with Slotted Injector Plate	100
50.	Pitot Survey Results for No Injection with Slotted Injector Plate	100

		Page
51.	Schematic of Injection Mixing Nozzle Blocks Showing Location of Static Pressure Ports	101
52.	Static Side-Wall Pressure Measurements	102
53.	Average Static Pressure (Torr) 150-psi H_2 Injection M_5 = 5.4, p_1 = 8 Torr (He + F_2, 50% by vol.)	103
54.	Average Static Pressure (Torr) No Injection M_5 = 5.4, p_1 = 8 Torr (He + F_2, 50% by vol.).	105
55.	Temperature Survey with 150-psi H_2 Injection	106
56.	Experimentally Determined Mixing Parameter.	111
57.	Sketch of Mixing Layer.	113
58.	Interrelationship of Subroutines in the Mixing Analysis Computer Code	124
59.	Computed Temperature Profiles for Run 72091301, Frozen Chemistry	131
60.	Computed Fringe-Shift Profiles for Run 72091301, Frozen Chemistry	132
61.	Computed H_2 and F Species Profiles for Run 72091301, Frozen Chemistry	133
62.	Computed Temperature Profiles for Run 72091301, Non-equilibrium Chemistry	134
63.	Computed Fringe-Shift Profiles for Run 72091301, Non-equilibrium Chemistry	135
64.	Computed HF Species Profiles for Run 72091301, Non-equilibrium Chemistry	136
65.	Computed Temperature Profiles for Run 72111602, Non-equilibrium Chemistry	137
66.	Computed Fringe-Shift Profiles for Run 72111602, Non-equilibrium Chemistry	138
67.	Computed HF Species Profiles for Run 72111602, Non-equilibrium Chemistry	139

Page

68. Injection Mixing Flow Field 143

69. Plume Analysis Results. 144

70. Run 72091301: Fringe-Shift Profiles 151

71. Run 72111602: Fringe-Shift Profiles 152

72. Run 72091301: Fringe-Shift Profiles 153

73. Run 72111602: Fringe-Shift Profiles 154

Table

I Equilibrium Composition of F_2/He Mixtures 22

II Summary of Area Ratios 25

III Experimental Values of A and B for Various Species . . . 46

IV Computed Values of C_{ji} Coefficients 46

V Interferogram Summary for Slotted H_2 Injection 61

VI Interferogram Summary for Orifice H_2 Injection 62

VII Parallel Mixing Interferogram Summary (All Mixtures 50% by Volume). 84

VIII Parallel Mixing Infrared Survey Data (All Mixtures 50% by Volume). 96

IX Total Integrated Radiation from 2.6 to 3.1 μm 99

X Chemical Reaction and Rate-Constant Equations 120

XI Initial Conditions for Mixing Layer Analyses 130

SYMBOLS

Except where otherwise noted in the text, the symbols used have the meaning, value and units as given below

C	Ratio of available chemical energy to fluid kinetic energy	
C_i	Constant in expression for $\dot{y}_i$,	gm-mole/cm^3-sec
D	Dissociation energy,	ev
E_c	Output voltage from gas source,	mv
E_g	Output voltage from calibration source,	mv
G_λ	Specific radiation intensity,	w/cm^3 - μ-sr
K	Gladstone-Dale constant,	cm^3/gm
L	Geometrical path length,	cm
N_λ	Planck's blackbody function,	w/cm^2 - μ-sr
N	Exponent in conservation equations (0 for two-dimensional flow and 1 for axisymmetric flow)	
P	Pressure,	dynes/cm^2
P_c	Radiant power to detector calibration source,	w/μ
P_g	Radiant power to detector test condition,	w/μ
$Q_{e\ell}^{F}$	Electronic partition function for F	
$Q_{e\ell}^{F_2}$	Electronic partition function for F_2	
R	Universal gas constant,	erg/gm-mole-°K

$R(t)$	Residue term in approximate chemical solution method	
Re	Reynolds number	
S	Entropy	
Sc_t	Turbulent Schmidt number, $Le_t \times Pr_t$	
T	Static temperature,	°K
W	Molecular weight,	gm/gm-mole
W	Fringe width,	cm
X_j	Mole fraction of j^{th} species	
Y	Third body molar concentration,	gm-mole/cm^3
a	Exponent in correlation equation for σ	
a	Coefficient in stream function forms of the conservation equation,	$(erg/cm^2)\left(\frac{gm}{cm^3}\right)$
$a_{i\ell}$	Coefficient in solution for $\dot{y}_i$,	sec^{-1}
b	Mixing layer width,	cm
c	Constant of proportionality between b and x	
c_p	Specific heat at constant pressure,	erg/gm-°K
$\bar{e}_p$	Mixture specific heat at constant pressure,	erg/gm-°K
$d_{i\ell}$	Coefficient in truncated series solution for y_i	
h	Enthalpy,	erg/gm
h	Planck's constant	
k	Constant of proportionality in equation for ε	

k	Total number of chemical species in mixture	
k	Boltzmann's constant	
k'	Total number of reacting species in mixture	
k_f	Forward reaction rate constant	
k_b	Backward reaction rate constant	
m	Mass,	gm
n	Refractive index	
p	Pressure,	torr
t	Time,	sec
u	Velocity in x direction,	cm/sec
u'	Turbulent fluctuation velocity,	cm/sec
v	Velocity in y or ψ direction,	cm/sec
v'	Turbulent fluctuation velocity,	cm/sec
$\dot{w}$	Chemical production rate,	sec^{-1}
x,y	Coordinate directions	
y	Molar concentration,	$gm\text{-}mole/cm^3$
α	Mass fraction	
β	Dissociation fraction	
ζ	Velocity parameter	
ζ	Number moles He per mole F_2	
γ	Specific heat ratio	
δ	Boundary layer thickness,	cm

δ	Fringe shift	
ε	Turbulent eddy viscosity,	cm^2/sec
ε_v	Turbulent eddy viscosity,	gm/cm-sec
η	Similarity variable, $\sigma y/x$	
λ	Wavelength,	microns
μ	Viscosity,	cm^2/sec
ν	Stoichiometric coefficient	
ξ_λ	Monochromator and detector efficiency factor	
ρ	Density,	gm/cm^3
ρ	Number density	cm^{-3}
σ	Mixing layer growth rate parameter	
τ_{xy}	Shear stress,	$dyne/cm^2$
ψ	Stream function,	gm/cm-sec
θ_D	Characteristic dissociation temperature	
θ_r	Characteristic rotational temperature	
θ_v	Characteristic vibrational temperature	
Ω	Solid angle	

Superscripts

$(\bar{})$	Mean value
$(\,)'$	Denotes reactant in chemical reaction
$(\,)''$	Denotes product in chemical reaction
$(\dot{})$	Time rate of change

Subscripts

max	Maximum
min	Minimum
STP	Standard temperature and pressure
a	Conditions ahead of shock wave a = 1 refers to incident shock a = 2 refers to reflected shock
b	Conditions behind shock wave b = 2 refers to incident shock b = 5 refers to reflected shock
e	Mixing layer edge condition
e	Nozzle exit plane condition
i	Chemical species
j	General summation index
ℓ	General summation index
m	Finite difference mesh node index, r direction
n	Finite difference mesh node index, x direction
o	Reference conditions

SECTION I

INTRODUCTION AND SUMMARY

The use of gas-phase chemical reactions in high-speed flow systems, both as energy sources and as mechanisms for achieving population inversion, has introduced complex fluid dynamic phenomena into the technology of high-energy laser systems. The complexity arises from the coupling of gas dynamics and nonequilibrium gas-phase chemical reactions. It is now apparent that the design of satisfactory reaction/mixing regions for an HF chemical laser will require optimization of the plenum and nozzle block designs in terms of the gas dynamics and chemical kinetics.

The results of a combined theoretical and experimental investigation of the supersonic mixing of hydrogen, fluorine, and helium diluent are presented in this report. The principle objective of this effort was to demonstrate the feasibility of developing an experimentally verified analytical procedure for evaluating the mixing region, such as would exist in the optical cavity of a laser device, in terms of its potential for producing laser power. The experimental program used two separate facilities to investigate, first, two different methods for injecting hydrogen into a supersonic fluorine carrying stream, and second, mixing of two parallel supersonic fluorine and hydrogen carrying streams. Diagnostic equipment used interchangably with each of the two basic facilities included a Mach-Zehnder interferometer, rapid scanning infrared spectrometer, pitot and static pressure probes, and a thermocouple temperature probe.

The configurations that were tested in the experimental phase are:

1) Multiple-orifice injection of hydrogen between adjacent supersonic streams of partially dissociated (> 70 percent) fluorine plus helium diluent;

2) Slot (or slit) injection of hydrogen between adjacent supersonic streams of partially dissociated (> 70 percent) fluorine plus helium diluent;

3) Mixing of adjacent parallel supersonic streams, one containing partially dissociated fluorine plus diluent and the other containing hydrogen plus argon.

Using the multiple-orifice hydrogen injection facility, monochromatic snapshot interferograms of the mixing region were recorded for 15 different test conditions. The test conditions were composed of five separate injector conditions for each of three different exit static pressures in the fluorine nozzle. Infrared emission intensity was not recorded for these tests due to poor transmission of the viewing windows available during the test period. Complete static and total pressure surveys were conducted for one nozzle exit pressure and three injector conditions, using pure fluorine in the nozzle reservoir. The results of these surveys verified the uniform quality of the flow field at the nozzle exit plane.

Monochromatic snapshot interferograms were also obtained for the slot hydrogen injection scheme for 15 different test conditions. These tests comprised five different injection conditions for each of three fluorine nozzle exit static pressures. Rapid-scan infrared emission intensities were recorded through a sapphire window at 25 stations along the nozzle axis downstream of the injector. Two different injector supply pressures were considered for a constant value of the nozzle exit static pressure. These data are reported in terms of average radiating power density at 2.79 μm in the mixing region. Static and total pressure surveys were recorded for two different injector pressure conditions and a single nominal value of the nozzle exit static pressure. Using a tungsten/tungsten-26% rehenium thermocouple, a temperature survey of the mixing region was attempted. A 2-mil-dia thermocouple junction did record an average value of the temperature across the mixing region, but the slow response ($\sim$ 4 msec) of this probe produced questionable results. A 1-mil thermocouple junction was obtained late in the program and gave a better time response ($\sim$ 1 msec) than did the 2-mil wire. However, it was very fragile and failed after four shots. A shielded, vented version of this probe should work quite well and will be used in future experiments with this facility.

The data obtained from the parallel stream mixing configuration were somewhat limited in extent due to time constraints and the stronger emphasis placed on testing two hydrogen injection concepts. A total of nine monochromatic snapshot interferograms were recorded of the shear layer mixing zone. For one of these tests, helium was substituted for hydrogen to illustrate a nonreacting mixing condition. Rapid-scan infrared emission spectra were obtained at five different stations downstream of the initial point of mixing for each of three different parallel mixing conditions. Static pressure measurements corresponding to each of the nozzle exit conditions were recorded.

The major theoretical efforts in this study were directed toward predicting the profiles of those flow parameters that could be observed within the mixing layer in configuration 3 of the experimental phase. A previously developed analysis of the turbulent mixing of hydrogen/oxygen supersonic shear layers was extensively revised and improved during this effort in an attempt to accurately account for the chemical kinetic and mixing parameters unique to the hydrogen/fluorine system. This analysis and the associated computer code employ an explicit finite difference technique for solving the boundary layer type equations that describe chemically reacting turbulent mixing layers. Program options include consideration of either equilibrium or finite-rate chemical kinetics and uniform or arbitrary initial flow-property profiles. This theoretical mixing analysis technique was used to predict test section parameters corresponding to two experimental configurations for which snapshot monochromatic interferograms were recorded. Fringe-shift profiles were computed through the mixing region as the most direct means of comparison with experimental data. A nonequilibrium calculation (finite-rate chemistry) was performed for one set of experimental conditions and both nonequilibrium and frozen-flow (nonreacting chemistry) calculations were performed for a second set of experimental conditions. In both of these cases, the experimental fringe-shift data are compared with the theoretical predictions.

The mixing analysis program contains a similarity parameter, σ (constant related to the mixing layer growth rate), whose value can be estimated from previous experimental evidence. To date, only one such estimated value of σ has been used in these calculations. As a result, comparisons reported here must be considered to represent the zeroth order in the theoretical/data correlation procedure, which can be refined with additional efforts.

As a result of the studies reported here, some insight into coupling between gas dynamic processes and nonequilibrium chemistry associated with high-energy chemical lasers has been derived. Many characteristics of operational devices have been observed in these studies, under conditions that lend themselves to quantitative analysis. The capability of the two-dimensional shock tube/shock tunnel facilities to produce two-dimensional mixing layers over a range of conditions for both injection and parallel stream mixing has been demonstrated. Monochromatic snapshot interferograms graphically depict the growth of the mixing region in each of these facilities and, when reduced, result in detailed profiles of average density through the mixing layer. The rapid scanning infrared spectrometer has produced detailed emission spectra for selected portions

of the mixing region. From these spectra, the total number density of excited hydrogen-fluoride molecules within the mixing region can be deduced. Pitot probe surveys have verified the uniformity of the nozzle exit flow fields.

A significant feature of our experimental approach is that it does produce mixing layers that lend themselves to quantitative analysis. This has been demonstrated by applying a theoretical mixing analysis computer program to the test conditions corresponding to two different parallel mixing experiments. Even though a complete understanding of the many complex problems has not yet been achieved, the ability of the analysis to correctly predict important features of the experimental profiles within the mixing layer is most encouraging. Past experience with hydrogen/oxygen mixing layers indicates that, with some adjustment of the empirical parameters within the analytical program, a close correlation between measured profiles and computed profiles can be obtained. Once this goal has been reached, the program can be used to extend the results over a much wider range of flow parameters. This achievement will be a valuable asset for the design of mixing regions of large-scale continuous-flow devices.

SECTION II

EXPERIMENTAL FACILITY DESCRIPTION

The two experimental facilities used in this program are both adaptations of test equipment developed at Martin Marietta for examining the turbulent mixing of parallel supersonic flows in the presence of hydrogen/oxygen reactions as encountered in air-augmented propulsion systems. Each of these two facilities uses the shock heated gases produced at the end-wall region of a shock tube as supply reservoirs for two-dimensional nozzles. In the injection mixing facility, the nozzle is separated into two half nozzles by a splitter plate from which hydrogen can be injected into the supersonic fluorine stream by different means at the downstream end of the splitter plate. The supersonic parallel mixing shock tunnel consists of two adjacent two-dimensional nozzles supplied by gases produced within the shock tube end-wall region. The most advantageous characteristic of these configurations is that they produce well-defined two-dimensional flow fields with convenient provisions for varying flow parameters such as test section pressures, temperatures, degree of dissociation, and fuel-to-oxidizer ratios. The mixing region for each facility can be viewed through optical windows mounted in the test section region, and the two-dimensionality of the flow fields provides a convenient means for mapping the mixing regions by optical techniques such as the Mach-Zehnder interferometer and a rapid scanning spectrometer. Complete details for each of these basic facilities, the associated instrumentation, and theoretical analysis is given in the following four subsections.

1. INJECTION SHOCK TUNNEL

The principal dimensions of the injection mixing facility are given in Figure 1. The driver consists of an 8-ft-long section of circular tubing with an 8-in. internal diameter connected by a 1-ft-long transition section to provide a smooth interface between the circular driver and the square driven tube. The main diaphragm station is located at the downstream end of the transition station, and a mechanical harpoon is used to initiate the rupture of the aluminum diaphragm at the appropriate time. The driven tube consists of five sections of 5-in.^{2} aluminum tube with a total length of 37 ft, and terminates at the two-dimensional nozzle block assembly. A thin (0.010 in.) aluminum diaphragm seals off the driven section from the test section and dump tank assembly. A mild steel dump tank (20-in. outside diameter by 15-ft-long) is connected to the downstream end of the aluminum test section assembly.

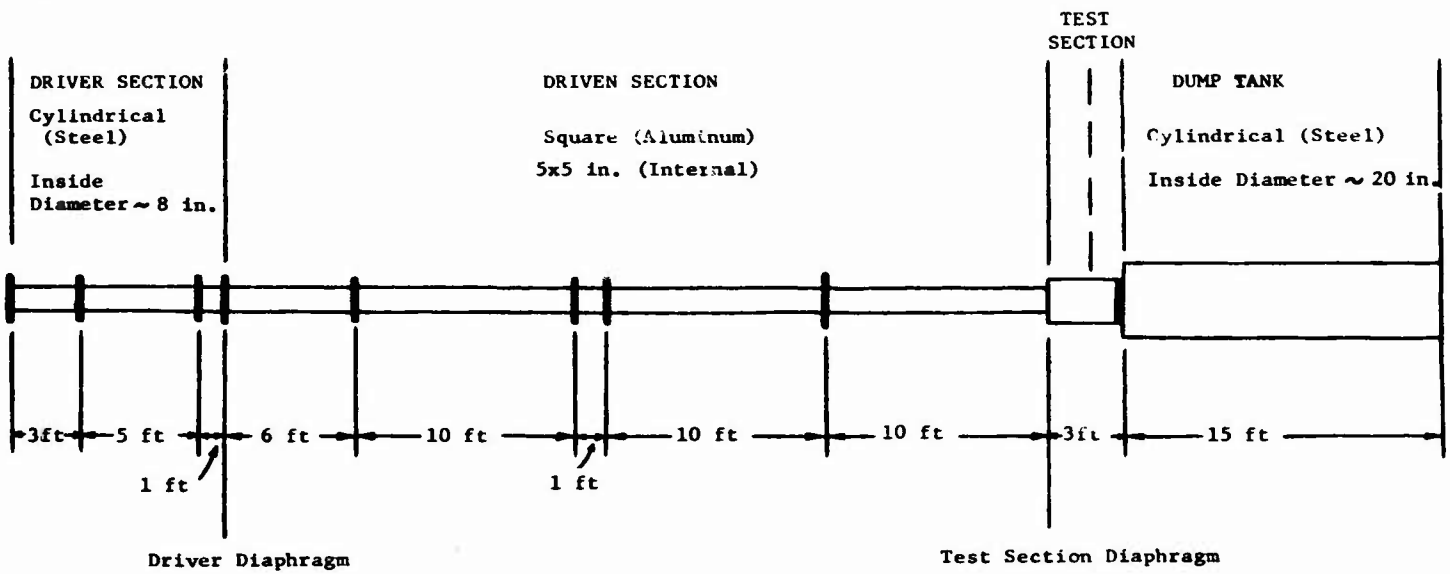

Figure 1. Injection Facility Schematic

Because of the particularly noxious and corrosive nature of the fluorine test gas, special handling and cleaning procedures were required. Both the driven shock tube sections and the nozzle assembly were throughly degreased and then exposed to pure fluorine gas at 30 psia for at least 1 hr. This well-established procedure forms an aluminum fluoride coating on the exposed aluminum surfaces by a process where the fluorine replaces oxygen in the initial aluminum oxide coating. This procedure allows the driven section to be filled with up to 50 torr of pure fluorine without a measurable decay in pressure for up to 30 minutes for a leak-tight assembly.

The fluorine handling procedure used with each of these two facilities is shown schematically in Figure 2. Bottles containing fluorine are always maintained in the laboratory at subatmospheric pressures so that, in the event of a leak, air will pass into the plumbing system rather than fluorine escaping. The shock tube dump tank assembly has a volume that is sufficiently large to ensure that the final resulting pressure at the conclusion of a run is again subatmospheric. As indicated in Figure 2, the mechanical pumps all exhaust through a common line that passes the exhaust gas through a charcoal filter before it is released to the atmosphere. The postshot operational procedure requires an immediate evacuation to at least 20 torr and a subsequent refilling to atmospheric pressure with dry nitrogen. This mixture is evacuated a second time to 10 torr and then refilled with dry nitrogen before opening the assembly for diaphragm replacement. This general cleaning and gas handling procedure has been very successful, as indicated by almost daily incident-free operation for more than 12 months.

Details of the Mach 5.0 nozzle blocks and splitter plate assembly are shown in Figures 3 and 4, and Figure 5 is a photograph of the actual assembly with one side plate removed. The field of view covered by the optical windows is shown outlined in the drawing of Figure 3, and the actual nozzle contour dimensions are given in the insert tabulation of Figure 4.

Figure 6, a photograph of the thin aluminum test section diaphragm taken after a test shot, shows that the aluminum is sheared very nicely by the sharp leading edge of the injector splitter plate and rests smoothly against the leading edges of the nozzle blocks. These diaphragms are very consistent in opening and no measurable material loss has ever been detected, with the following exceptions. On two different test occasions, the test section diaphragm was torn very badly; this could always be traced to material loss of the driver diaphragm.

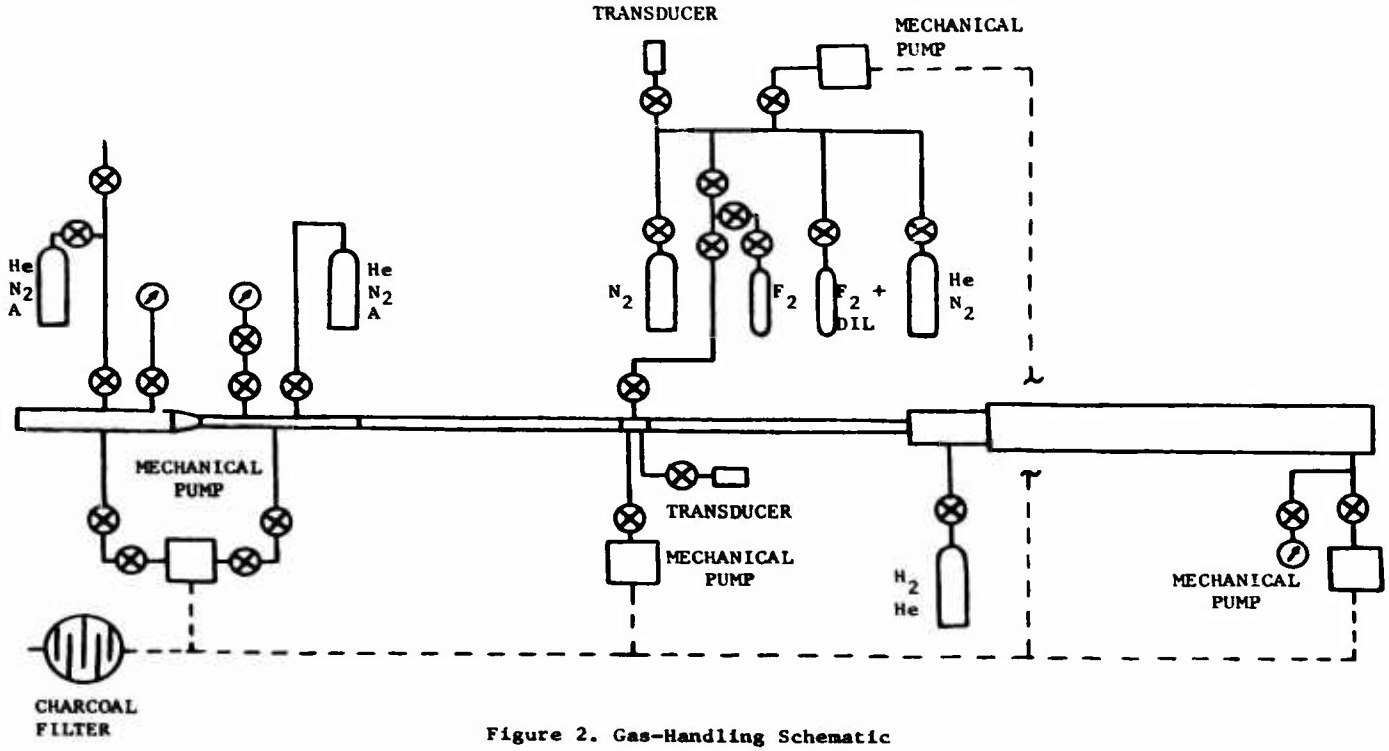

Figure 2. Gas-Handling Schematic

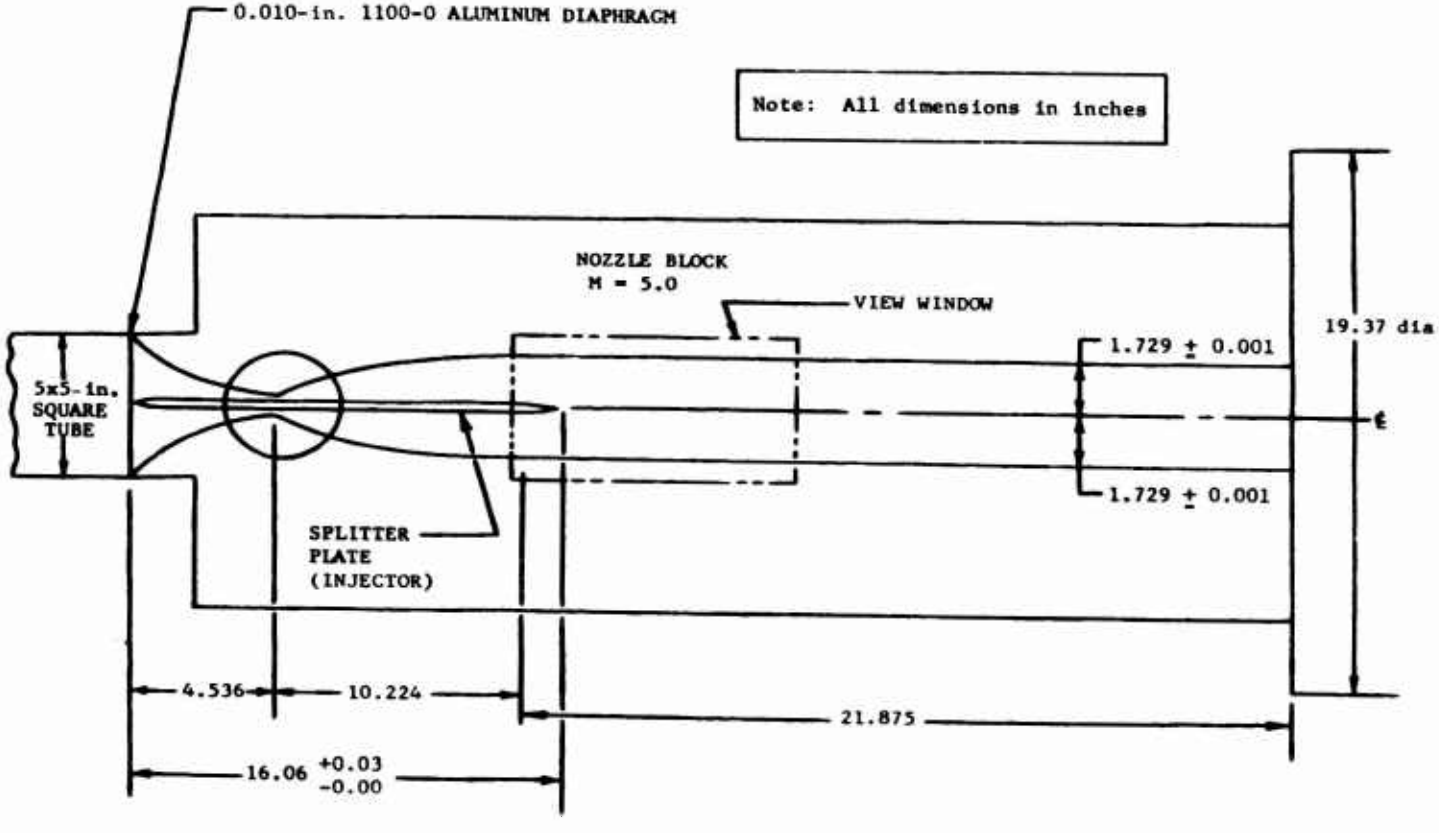

Figure 3. Injection Test Section

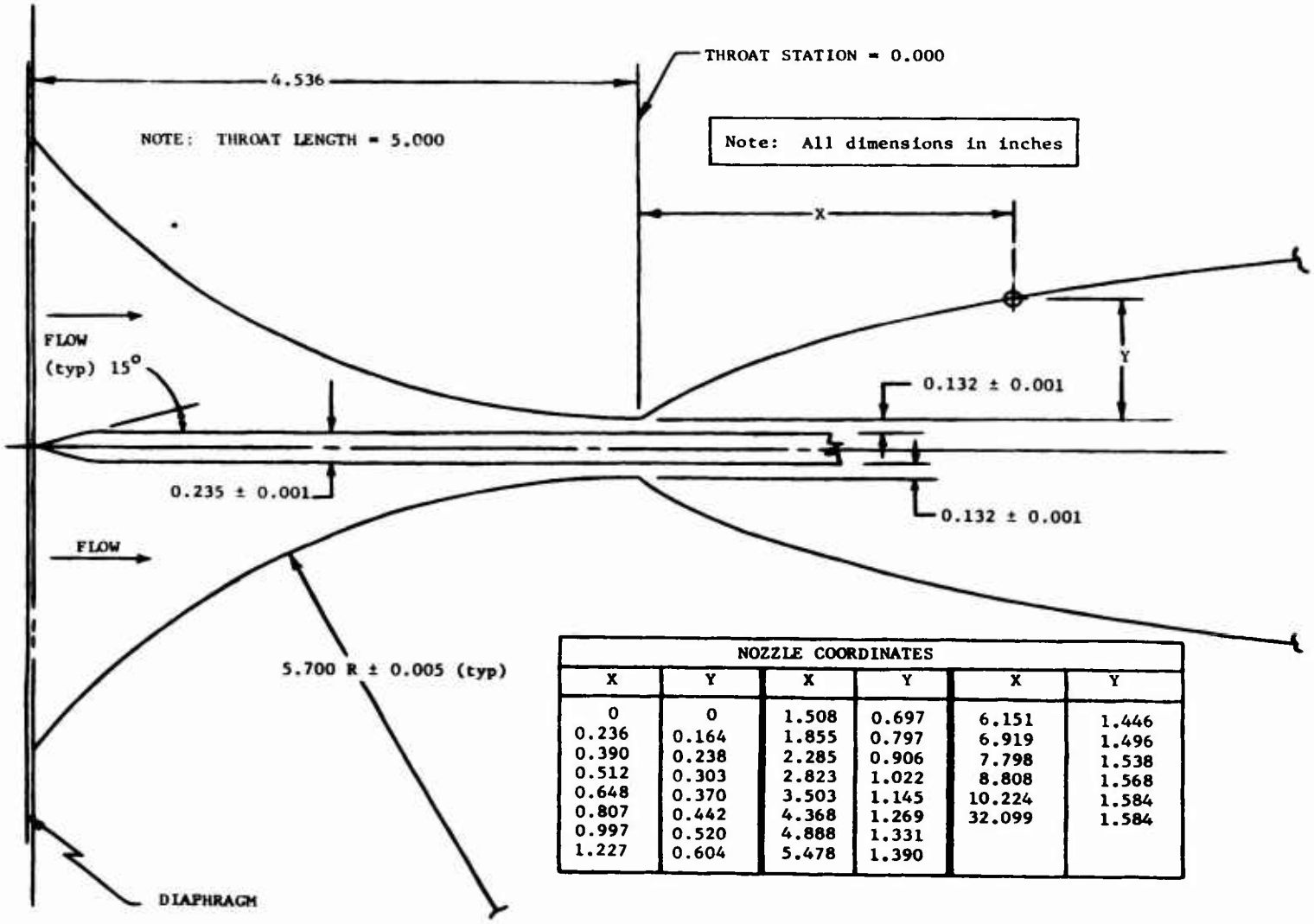

NOZZLE COORDINATES

X	Y	X	Y	X	Y
0	0	1.508	0.697	6.151	1.446
0.236	0.164	1.855	0.797	6.919	1.496
0.390	0.238	2.285	0.906	7.798	1.538
0.512	0.303	2.823	1.022	8.808	1.568
0.648	0.370	3.503	1.145	10.224	1.584
0.807	0.442	4.368	1.269	32.099	1.584
0.997	0.520	4.888	1.331		
1.227	0.604	5.478	1.390		

Figure 4. Mach 5.0 Nozzle Block Details

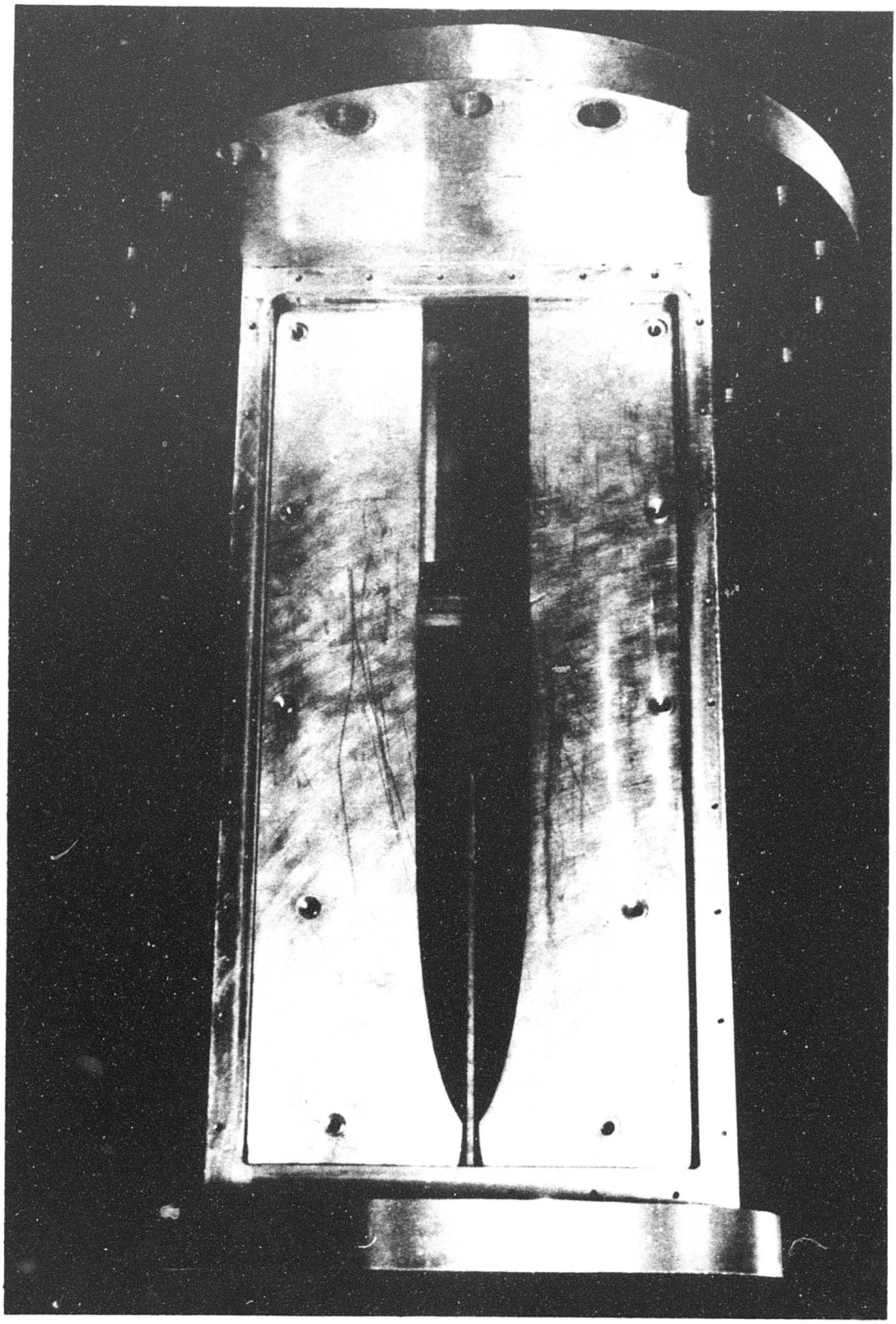

Figure 5. Injection Test Section

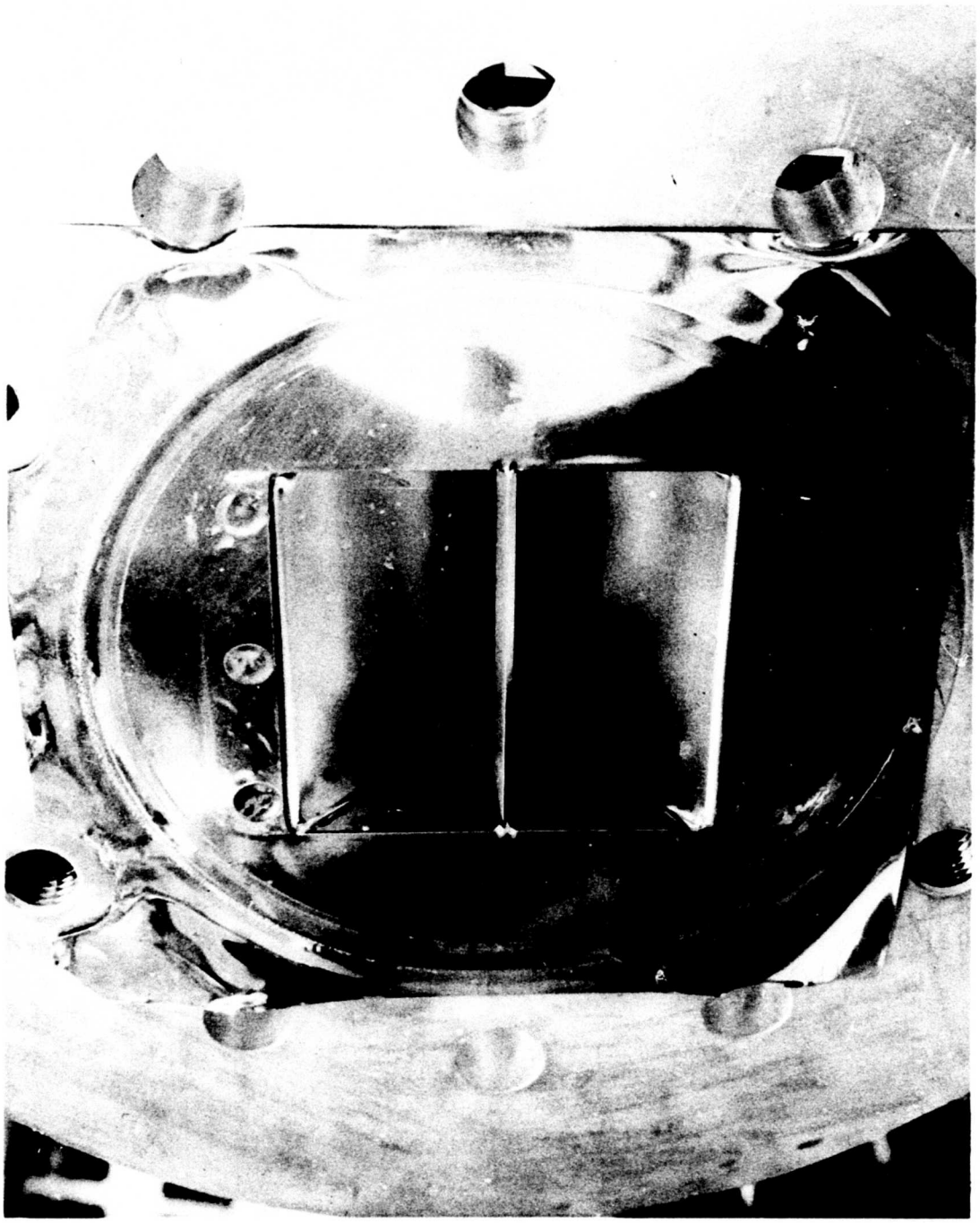

Figure 6. Opened Test Section Diaphragm

A typical test shot sequence of events consists of evacuating the three separate facility chambers as indicated in Figure 1 using mechanical vacuum pumps. The shock tube driven section and the dump tank plus test section are evacuated to a pressure level of at least 10 microns, while the driver section is evacuated to a pressure of at least 10 torr. The desired test gas (pure fluorine or a 50% by volume mixture of fluorine and helium) is loaded into the driven tube and the initial load pressure is measured with one of three available types of stainless steel diaphragm pressure transducers. The most sensitive transducers (Statham PA731TC's, 0 to 2 psia range) are used to measure the lower initial load pressure between 3 and 25 torr, and two less sensitive transducers (Viatran 105's with No. 603 signal conditioner, 0 to 5 and 0 to 15 psia ranges) are used for higher initial load pressures. These gages are fluorine compatible, at least at these low pressure levels, and they are checked frequently against a Wallace Tiernan absolute pressure dial gage. This procedure assures an accuracy in the initial fill pressures of at least ±1%.

Immediately after filling the test section, the dump tank pump valve is shut off, and the high-pressure driver gas is loaded into the driver section to the desired level. The driver pressure is measured with a Heise pressure gage of appropriate range. Once the required pressure level is obtained, the mechanical harpoon is released, breaking the driver diaphragm. Immediately after the shot, the driven section mechanical pump valve is opened, and the residual gas is pumped through the charcoal filter. As described earlier, the final pressure in the entire facility is always maintained at or below atmospheric pressure to minimize the fluorine hazard. This entire procedure requires less than 2 minutes from start of test gas fill to actual test shot. The leak rate in the driven tube is less than 1 micron/minute, thus ensuring a high degree of purity in the test gas sample.

It is well known (Ref. 1) that conditions in the quiescent gas behind the reflected shock can be accurately computed, given the initial test gas conditions (composition and pressure) and incident shock wave velocity. Three stations (12 in. apart) are provided for measuring the initial shock velocity, and the last station is located 3 in. from the test section diaphragm station. Shock wave arrival at each of these stations is detected by one of two types of pressure transducers that were used in this study, and the output is recorded on both a dual-beam oscilloscope and a paralleled Beckman Time Interval Meter. The pressure transducers used for detecting shock arrival were either the Piezotronics PCB113A21 gage with a model 480A power supply or a Kistler type 603A gage with a model 504 charge amplifier. Two separate time

intervals were recorded with the three pickup stations used. Hence, shock velocity attenuation could be measured if, in fact, it did exist. In all of this work, time intervals accurate to within ±1 μsec were obtained, and, within this accuracy, the shock velocity was constant over the span for which it was measured. The last shock velocity station (located 3 in. from the end wall) could also be used as a check on the theoretically predicted equilibrium pressure behind the reflected shock. Thin-film heat transfer gages were also used as shock arrival detectors in the early phase of this program, but were never completely satisfactory because the fluorine attacked and destroyed the sensitive elements, usually after six to eight test shots.

Initial test gas mixtures containing 50% (by volume) fluorine plus helium were used in most of these test conditions, and these mixtures were prepared and allowed to stand for at least 2 hr before their use to ensure complete mixing. Some of the first test gas mixtures used in this study were prepared by simply separately adding each test gas to the driven tube section. The resulting shock velocities could never be predicted for mixtures prepared in this way, and it was concluded that improper mixing was responsible for this situation. The final procedure where the gases were premixed proved much more satisfactory, and the resulting measured shock velocities were in excellent agreement with predicted values.

As previously described, hydrogen (helium in some cases) was injected into the supersonic fluorine carrying streams from ports located at the downstream end of the splitter plate. Two different splitter plates, one containing 18 orifices (0.020 in. in diameter) and the other containing a series of slots (0.0028 in. wide and covering 90% of the available exit length) were used in this study. A detailed sketch of the orifice injector splitter plate is shown in Figure 7, and Figure 8 is a photograph of this splitter plate looking upstream toward the nozzle throat. Figure 9 is a sketch and photograph of the slotted hydrogen injector splitter plate with the trailing edge tilted to expose the interior construction. The injectant gas flow through each of these splitter plates is activated by a microswitch on the harpoon mechanism shaft that breaks the driver diaphragm. Adjusting this switch position permits the gas flow to the injector to be timed so that the injection flow starts approximately 1 msec before start of fluorine nozzle flow. Pressure on the injection line was varied from 50 to 150 psi under no-flow conditions.

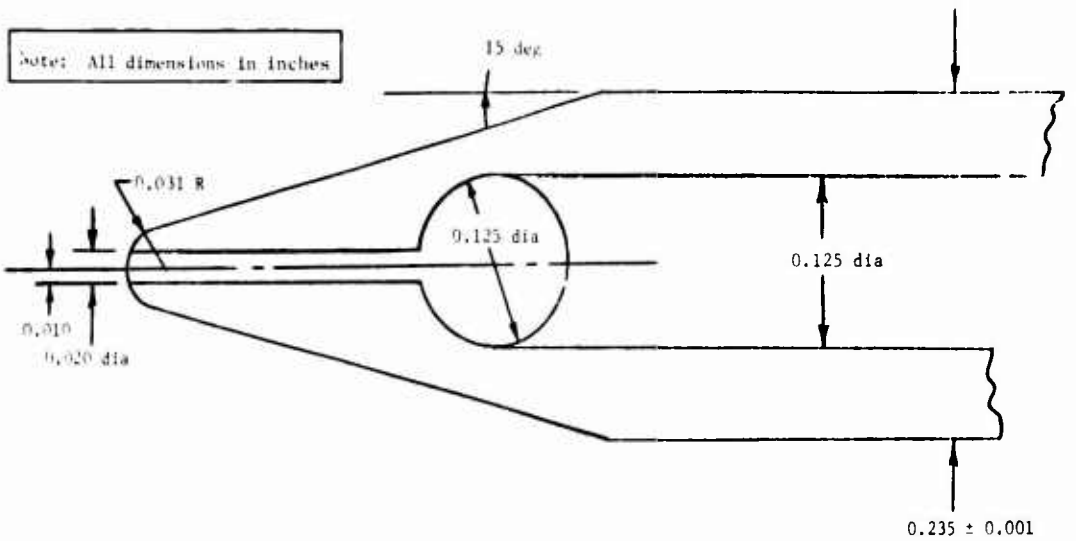

Figure 7. Orifice Splitter Plate Schematic

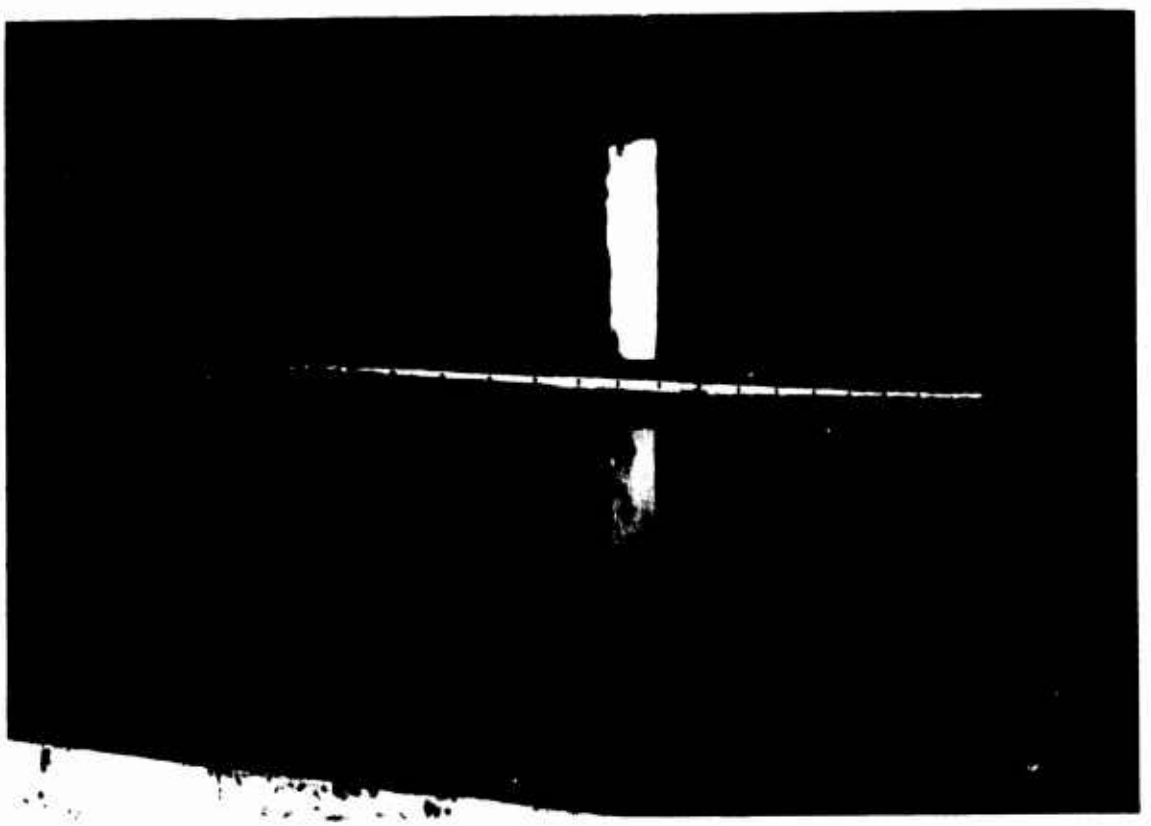

Figure 8. Orifice Splitter Plate

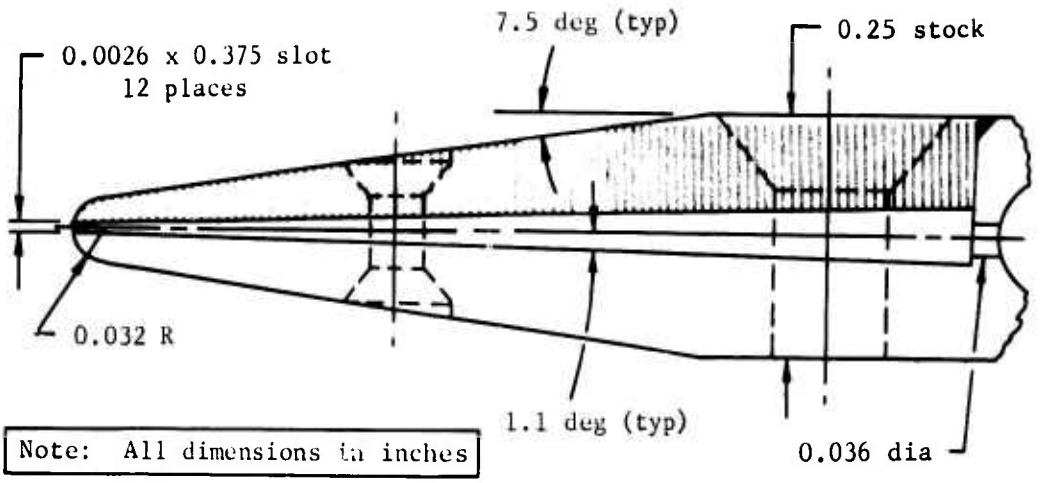

a. Schematic

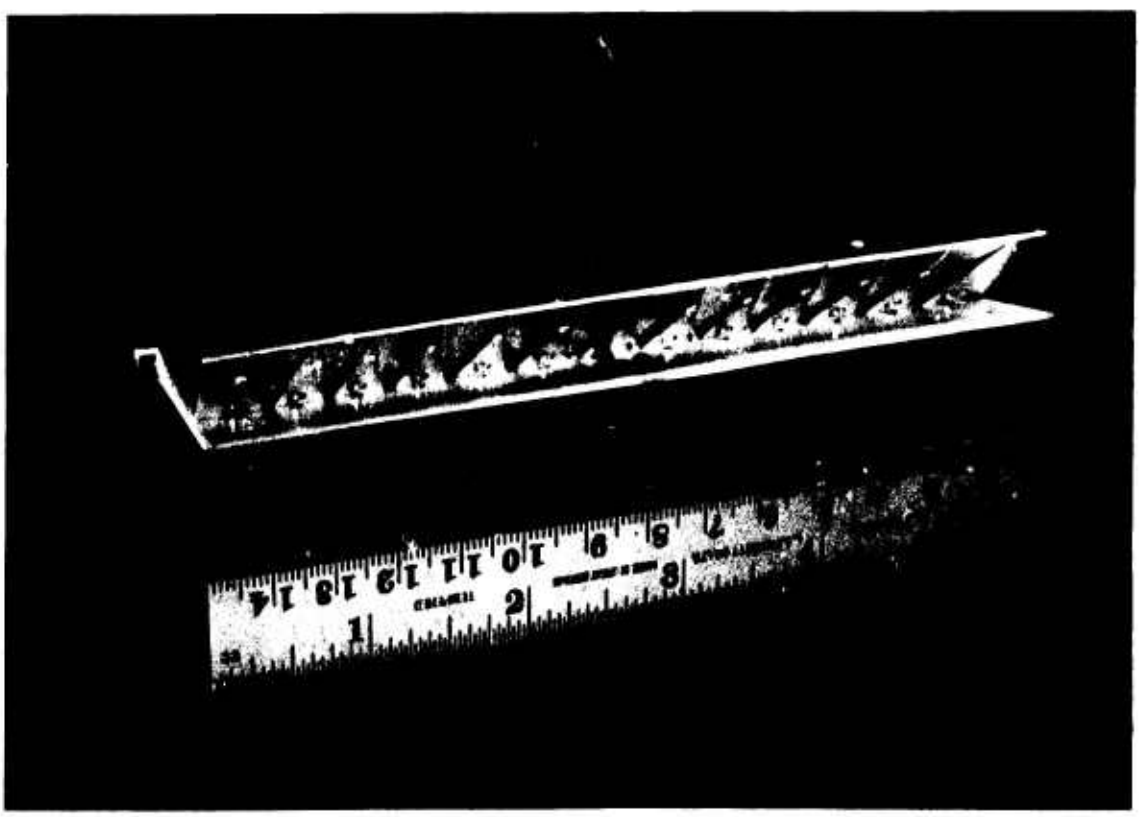

b. Photograph

Figure 9. Slotted Splitter Plate

2. PARALLEL MIXING SHOCK TUNNEL

This facility is very similar to the basic injection shock tube/shock tunnel facility except that part of the driven tube is divided into two parallel chambers. The high-pressure, high-temperature gas produced behind the reflected shock wave in each chamber is then expanded through two-dimensional supersonic nozzles, and the resulting parallel supersonic streams are then allowed to mix. The mixing zone can be observed through a pair of optical quality quartz windows. The principal dimensions of this facility are shown in Figure 10, where the driver and dump tank chambers are identical with those described for the injection mixing facility.

As shown in Figure 10, the split tube assembly consists of two sections that total 16 ft long. The square (not divided) 10-ft-long buffer chamber is used as a conventional shock tube section, and the initial shock wave generated in this section simply passes through the thin Teflon diaphragm (0.002 in.) at Station A almost undisurbed. This shock wave then simultaneously initiates two separate shock waves in the divided tube section. Argon has been used in the buffer section of this facility both for convenience and because a heavy monatomic gas provides a higher degree of stability for the driver and driven gas interface (Ref. 1).

Figure 11 is a schematic of the two full nozzles used for these tests. Each of these nozzles is designed for an ideal gas Mach number of 4.5, and the contours are different because of the different value of γ (specific heat ratio c_p/c_v) for the two different gases. A sketch of the field of view provided by the optical window is shown superimposed on this figure. A photograph of the assembled nozzle blocks and test section is shown in Figure 12, with one side of the test section removed.

The gas handling procedure, shock arrival stations, and instrumentation for this facility are identical with those described for the injection mixing facility. Shock arrival stations are located in both chambers used as supply reservoirs for the nozzles because the initial load conditions and shock Mach numbers will generally be different on each side of the divided chamber.

The divided driven sections are constructed of aluminum by cutting the 5x5-in.^{2} tube along its full length and then inserting a 1/4 in. aluminum plate between the two. A continuous weld is used to seal this divider plate, and great care is taken to ensure that no leaks exist between tubes.

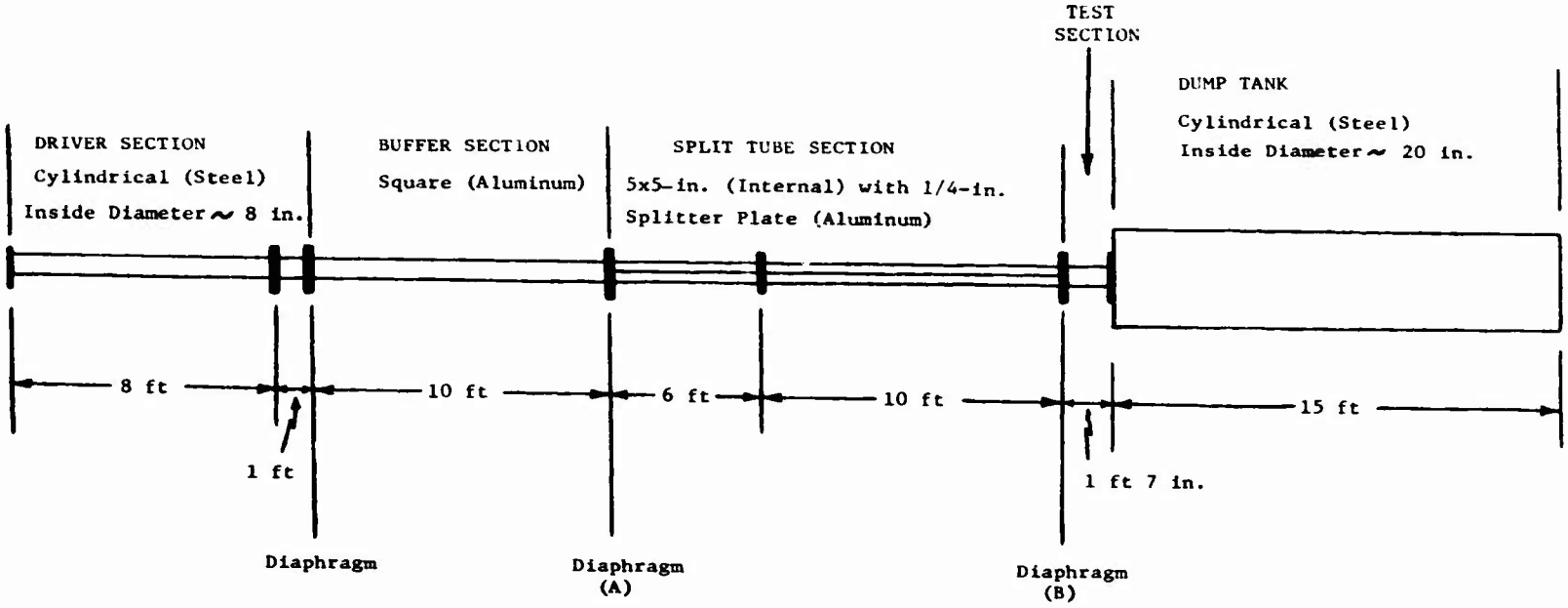

Figure 10. Parallel Mixing Facility Schematic

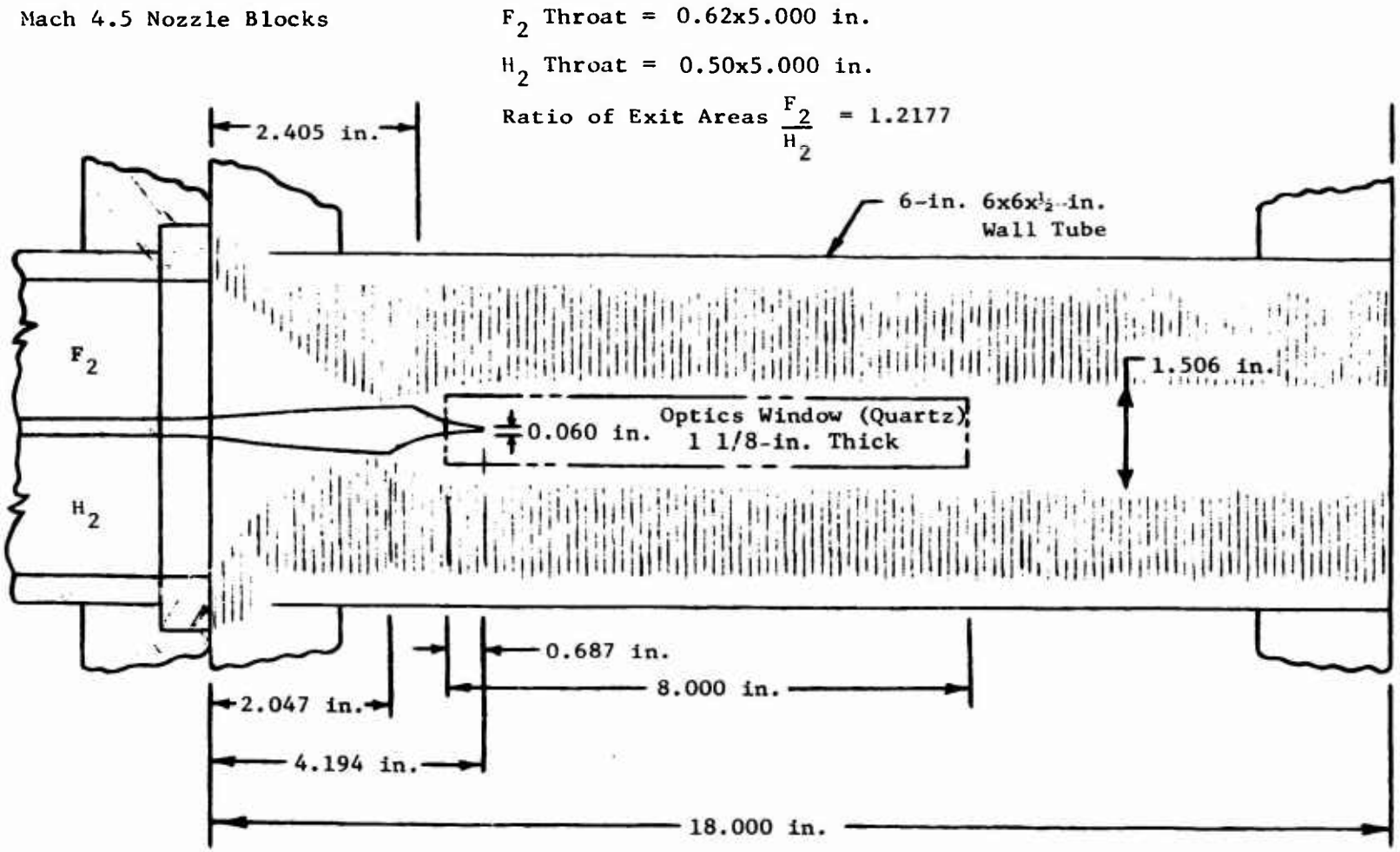

Figure 11. Parallel Mixing Test Section Schematic

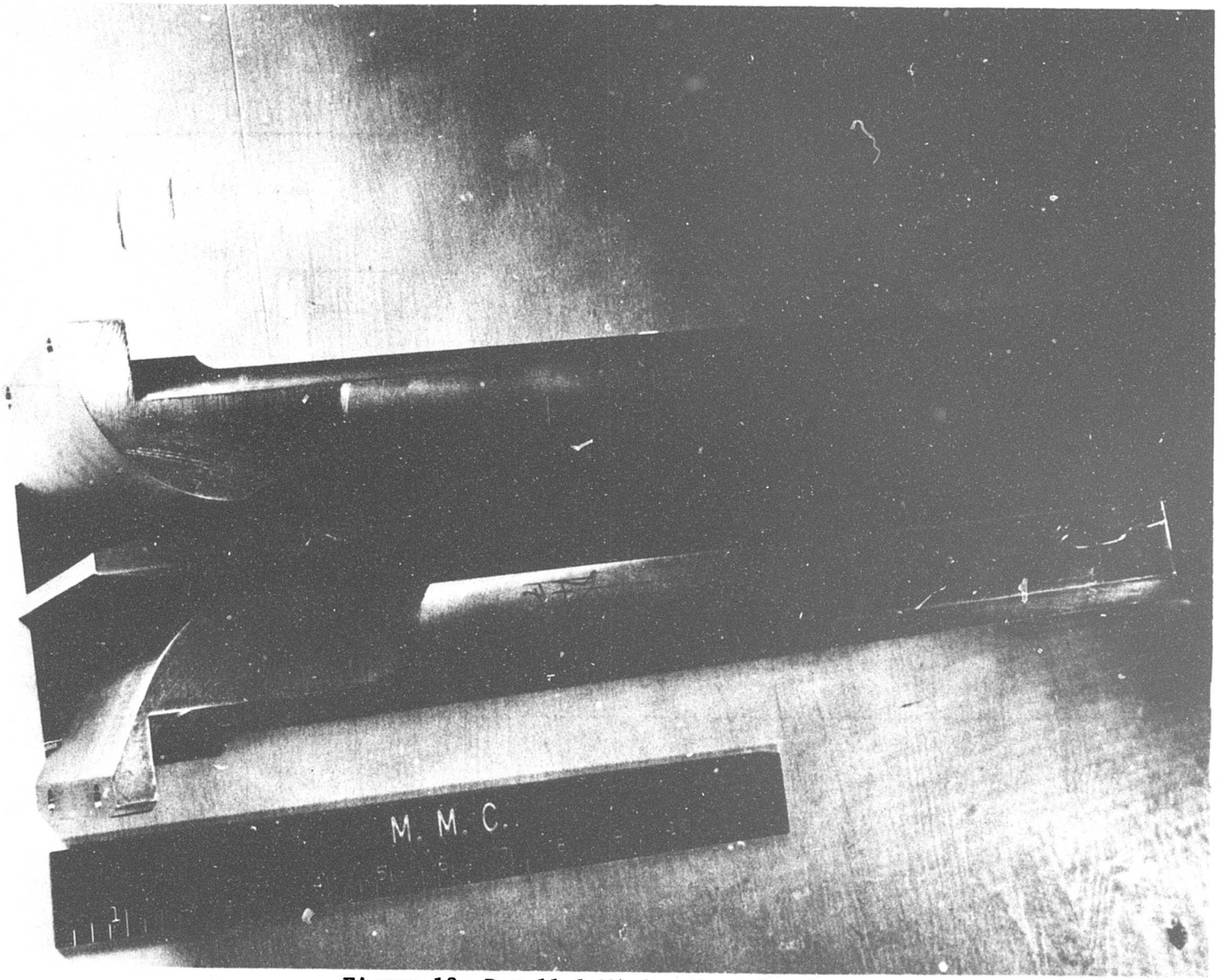

Figure 12. Parallel Mixing Test Section

3. THEORETICAL PERFORMANCE ANALYSIS OF SHOCK TUBE/SHOCK TUNNEL

The basic shock tube performance analysis in both the incident and reflected shock regions was based on treatment of the shock heated gases as equilibrium mixtures (Ref. 2). The nozzle expansion processes were computed assuming an equilibrium sudden-freeze model (Ref. 3) to predict the exit plane thermodynamic conditions. A summary description of the analytical procedures and typical results are presented in this subsection.

To be assured that the degree of ionization can be neglected for typical conditions behind the reflected shock, an equilibrium composition calculation for a mixture of fluorine molecules and atoms was performed. The results of this calculation, assuming a 2000°K gas temperature and using data from JANAF tables (Ref. 4), indicated that the degree of ionization is much less than 0.1%. Therefore, no charged particle species need be considered in the analysis.

Furthermore, it was assumed that for the frozen expansion case considered here, all thermodynamic states of the F_2 and F could be treated by ideal gas theory. Thus, for the equilibrium reaction

$$F_2 \rightleftharpoons 2F \tag{1}$$

the equilibrium constant, K_p, is given by

$$K_p = \frac{X_F^2}{X_{F_2}} P \tag{2}$$

where X_F is the mole fraction of fluorine atoms, X_{F_2} is the mole fraction of fluorine molecules, and P is the total pressure, in atmospheres, of the mixture. The equilibrium constant as a function of temperature for Equation (1) is obtained from reference 4.

For the mixture we can write

$$X_F + X_{F_2} = 1 \tag{3}$$

Substituting Equation (3) into Equation (2) and solving for X_F yields

$$X_F = \frac{-\left(K_p/P\right) + \sqrt{\left(K_p/P\right)^2 + 4\left(K_p/P\right)}}{2} \tag{4}$$

The positive root is always selected because $0 \leq X_F \leq 1$. This calculation proceeds in a straightforward manner once temperature and pressure are specified. The helium atoms of the initial gas mixture will always be in the ground state, and there will be no ionization of helium at this temperature level. For an initial ideal gas mixture containing one mole of F_2 and β moles of helium, the moles of helium can be expressed as

$$\beta = \frac{X_{He}}{1 - X_{He}} \tag{5}$$

where X_{He} is the mole fraction of helium in the initial fluorine/helium mixture. The material balance for the equilibrium calculation given by Equation (1) may be determined as follows:

Basis: 1 mole of F_2 gas (initially undissociated)

β = moles of He/mole of F_2

α = moles of F_2 dissociated

Table I summarizes the expressions for the resultant composition of the initial mixture, as well as the final equilibrium mixture.

Table I EQUILIBRIUM COMPOSITION OF F_2/He MIXTURES

Component	No. of Moles		Mole Fraction
	Initial	Equilibrium	
He	β	β	$X_{He} = \frac{\beta}{1 + \alpha + \beta}$
F_2	1	$1 - \alpha$	$X_{F_2} = \frac{1 - \alpha}{1 + \alpha + \beta}$
F	0	2α	$X_F = \frac{2\alpha}{1 + \alpha + \beta}$

Thus, the equilibrium constant for the fluorine dissociation reaction is given by

$$K_p = \frac{X_F^2}{X_{F_2}} P = \frac{(2\alpha)^2}{(1 + \alpha + \beta)(1 - \alpha)} P \tag{6}$$

This expression leads to the quadratic equation,

$$\left(4 + \frac{K_p}{P}\right) \alpha^2 + \frac{\beta K_p}{P} \alpha - \frac{K_p}{P} (1 + \beta) = 0 \tag{7}$$

The value of α is, again, obtained from the positive-root solution,

$$\alpha = \frac{-\frac{\beta K_p}{P} + \sqrt{\left(\frac{\beta K_p}{P}\right)^2 + 4\left(4 + \frac{K_p}{P}\right)\left(\frac{K_p}{P}\right)(1 + \beta)}}{2\left(4 + \frac{K_p}{P}\right)} \tag{8}$$

Note that when $\beta = 0$, Equation (6) reduces to the result obtained for a pure fluorine gas. The mole fraction of each component in the mixture is obtained by substituting α from Equation (8) for each value of K_p, which is determined by the temperature, the pressure, and the initial composition, into the appropriate expressions from Table I. Application of this analysis over the temperature range (300 to 2000°K) and pressure range (2 to 5 atmospheres) appropriate to the experimental study demonstrates that the important chemical species in the gas models are F_2, F, and He for both the reflected shock region of the injection shock tube and the fluorine side of the parallel mixing shock tube.

Perhaps the most significant result of these considerations is that the flow fields in the injection shock tube and the parallel mixing shock tube can be treated by ideal dissociating gas theory in the reflected shock region before the nozzle expansion. This means that the equilibrium thermochemical state of the mixtures in the reflected shock region can be determined by solving the well-known shock crossing relations (Ref. 1) for conservation of mass, momentum, and energy, along with satisfaction of the law of mass action for an ideal dissociating gas and the appropriate thermal and caloric equations of state. These equations were solved numerically for a range of initial driven tube conditions and shock strengths encompassing the desired experimental test conditions to give quantitative information about the thermochemical state of the reflected shock region. The general forms of the equations that were solved for the postshock thermochemical state of the gas are

Conservation of mass

$$\rho_a u_a = \rho_b u_b \tag{9}$$

Conservation of momentum

$$\rho_a u_a^2 + P_a = \rho_b u_b^2 + P_b \tag{10}$$

Conservation of energy

$$h_a + \tfrac{1}{2}u_a^2 = h_b + \tfrac{1}{2}u_b^2 \tag{11}$$

Thermal equation of state

$$P = (1 + \alpha)\,\rho RT \tag{12}$$

Caloric equation of state

$$T_b = \left(h_b - \alpha_b D\right) \left[\left(4 + \alpha_b\right) R\right] \tag{13}$$

From the law of mass action (Ref. 2), the dissociation fraction, α, is given by

$$\frac{\alpha_b^2}{1 - \alpha_b} = \frac{\rho_D}{\rho_b} e^{\frac{-\theta_D}{T_b}} \tag{14}$$

where θ_D is the characteristic dissociation temperature for the diatomic species (in this case F_2) and the constant ρ_D is given by (Ref. 5)

$$\rho_D = \left[m\left(\frac{\pi mk}{h^2}\right)^{3/2} \theta_r \sqrt{T} \left(1 - e^{\frac{-\theta_v}{T}}\right) \frac{\left(Q_{e\ell}^F\right)^2}{\left(Q_{e\ell}^{F_2}\right)} \right] \tag{15}$$

where

m = mass of the atomic species

θ_r = characteristic rotational temperature

θ_v = characteristic vibrational temperature

$Q_{e\ell}$ = electronic partition function

k = Boltzmann's constant

h = Planck's constant

The subscripts, a and b, denote the equilibrium states ahead of and behind the shock wave, respectively. For the incident shock, the values of a and b are 1 and 2, respectively, and for the reflected shock a and b are 2 and 5, respectively.

A computer program was developed to solve these equations iteratively for both the incident shock and the reflected shock regions. The results of these solutions were used to model the nozzle expansions and the thermochemical state of the expanded helium/fluorine mixtures. Figure 13 shows the fluorine dissociation level in the reflected shock region for different initial driven tube pressures as a function of initial shock Mach number. From these results, it is clear that the dissociation level is higher for lower initial pressure at any given value of initial shock Mach number. Table II summarizes the nozzle dimensions used in this study.

Table II SUMMARY OF AREA RATIOS

Nozzle	Throat Dimension, in.	Exit Dimensions, in.	A/A*
Injection Facility	0.264 high by 0.500 wide	3.439 high by 0.500 wide	13.10
Parallel Mixing Facility	H_2 nozzle 0.050 high by 5.00 wide	H_2 nozzle 0.794 high by 5.00 wide	15.88
	F_2 nozzle 0.062 high by 5.00 wide	F_2 nozzle 0.652 high by 5.00 wide	10.51

Note: "A" denotes the area of the nozzle exit plane and "A*" denotes the area of the nozzle throat.

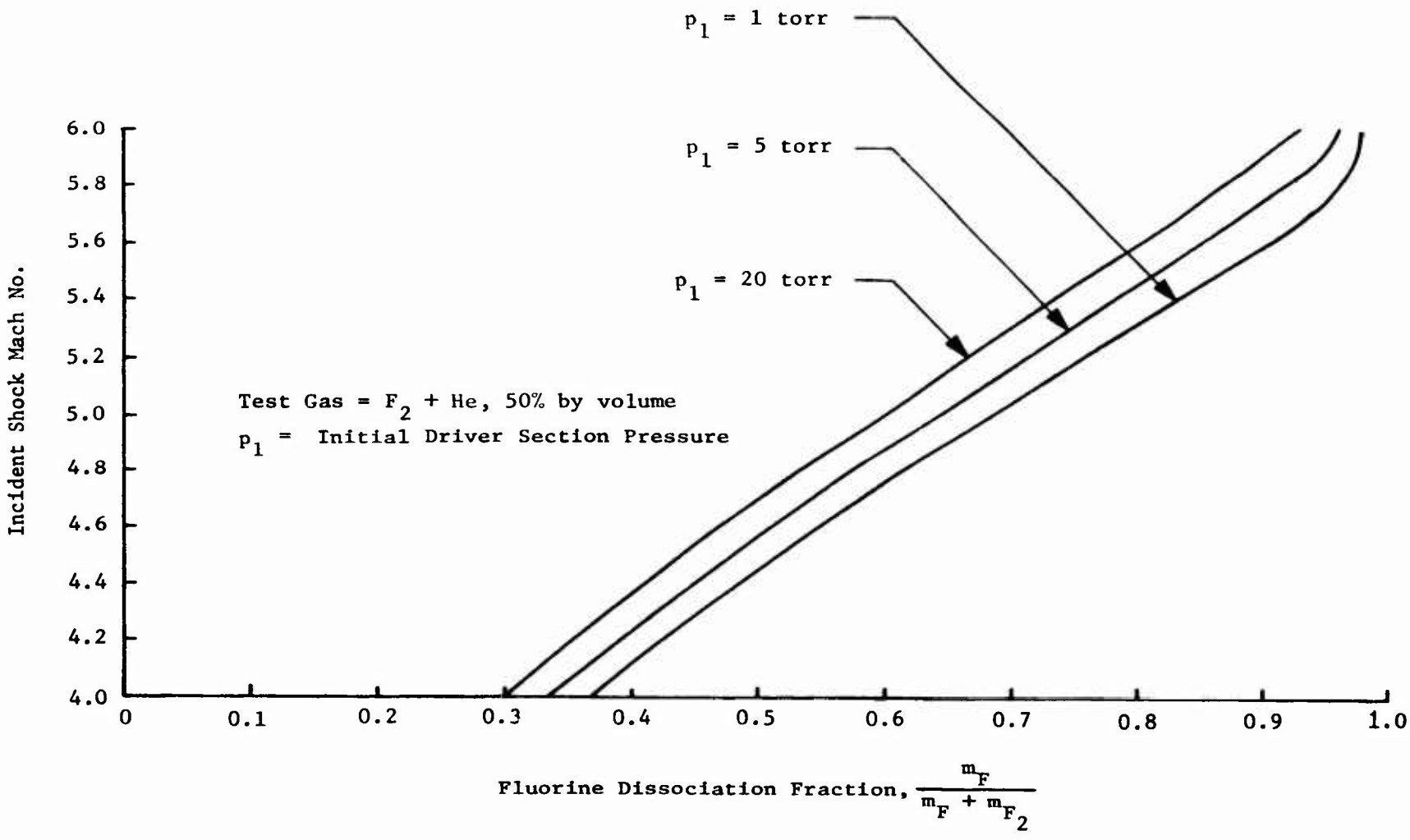

Figure 13. Fluorine Dissociation Fraction vs Incident Shock Mach Number

Figure 14 shows the computed nozzle exit pressures as a function of initial driven tube conditions and shock strength for a nozzle with $A/A^* = 13.1$. Again, for a fixed initial shock Mach number, the nozzle exit pressure increases with p_1. The results given in Figure 14 are for the injection mixing nozzle and a 50% by volume test gas mixture of He and F_2. Figure 15 shows typical nozzle exit static pressures for the parallel mixing hydrogen nozzle ($A/A^* = 15.88$). A complete set of these data and several cross plots were used to design the run conditions for this study.

The nozzle expansion processes were modeled using a similar set of conservation equations and thermodynamic state equations as used for the reflected shock analysis, together with suitable modifications for the boundary layer formation along the nozzle walls. The procedure discussed here was applied to the performance analysis of both the injection shock tube nozzles and the parallel mixing shock tube nozzles whose designs and geometries have already been discussed. In both cases, the reflected shock region represents a stagnation reservoir and the real-gas expansion processes were carried out to determine the thermochemical changes at the nozzle exit planes. The conservation of mass equation for a converging/diverging nozzle with adiabatic inviscid flow is used, along with conservation of momentum and energy and the thermal and caloric equations of state. Again, the equations were solved by iteration to give exit plane values of the flow velocity and the thermodynamic properties of the gas mixtures, as a function of the nozzle area expansion ratio.

The governing equations for the nozzle flow field are:

Conservation of mass

$$\rho u A = C_1 = \text{constant} \tag{16}$$

Conservation of energy

$$h + \tfrac{1}{2} u^2 = C_2 = \text{constant} \tag{17}$$

Conservation of momentum

$$u \frac{du}{dx} + \frac{1}{\rho} \frac{dP}{dx} = 0 \tag{18}$$

Thermal equation of state

$$P = (1 + \alpha) \rho R T \tag{19}$$

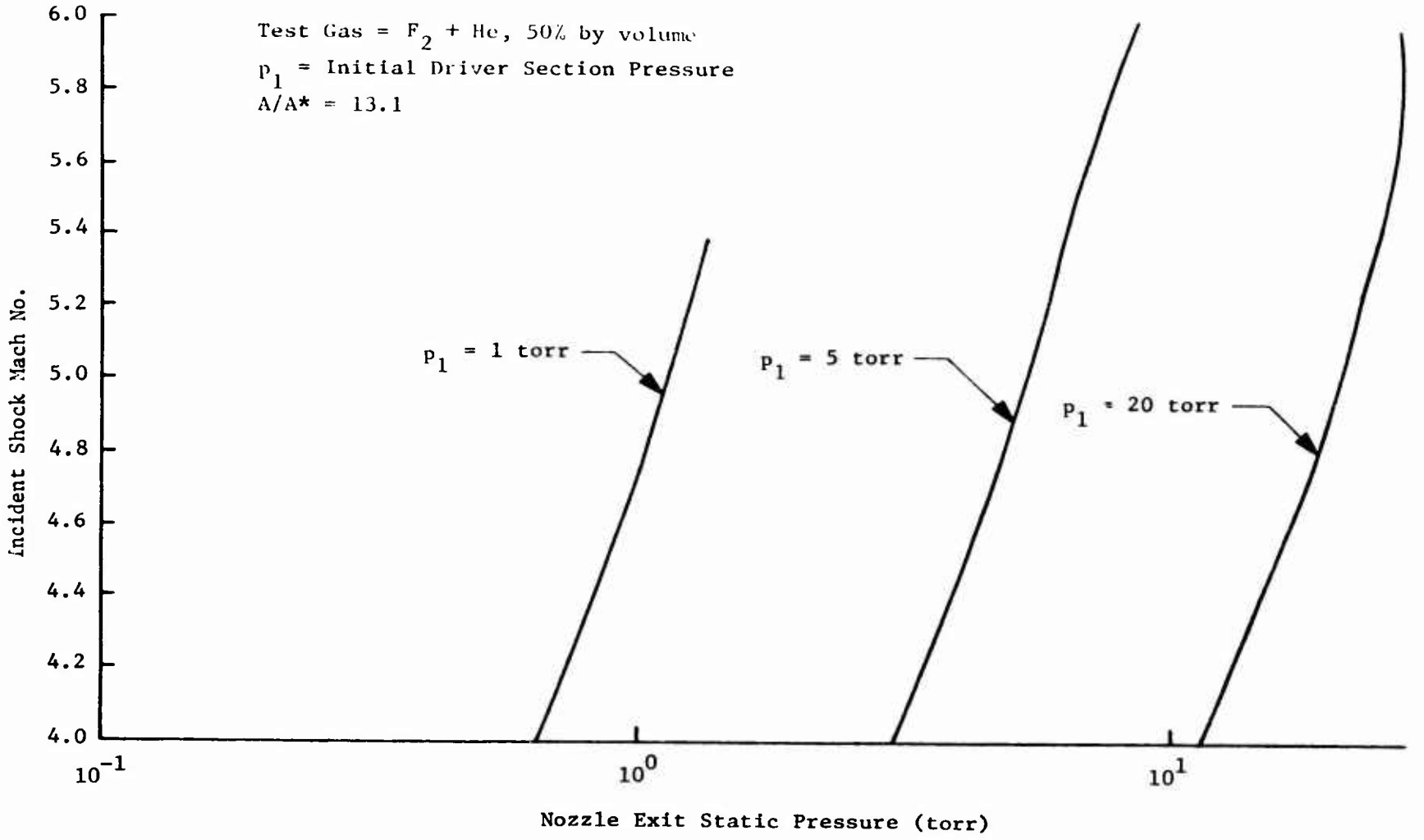

Figure 14. Nozzle Exit Static Pressure vs Incident Shock Mach Number

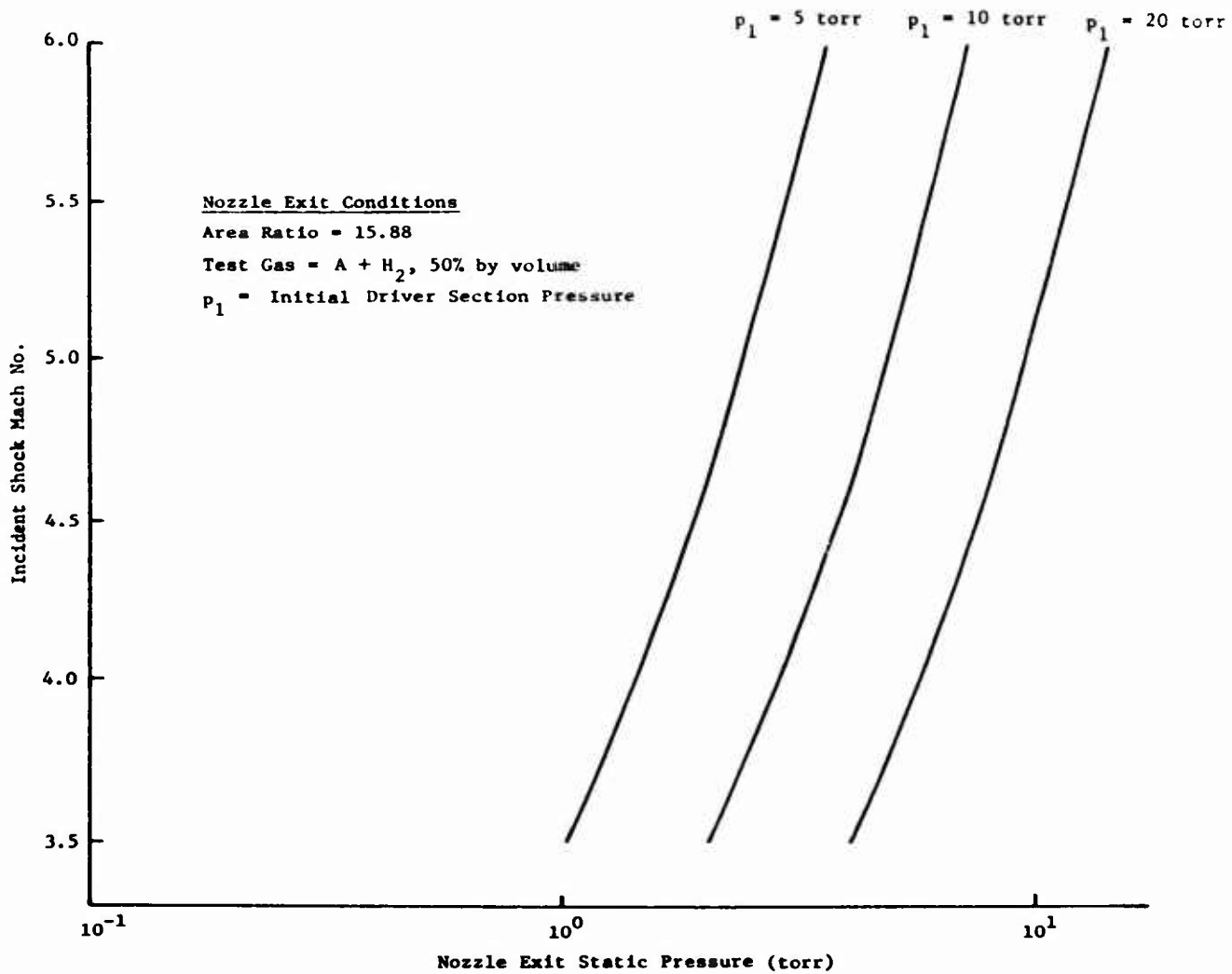

Figure 15. Nozzle Exit Static Pressure vs Incident Shock Mach Number

Caloric equation of state

$$h = (4 + \alpha)\, T + \alpha D \tag{20}$$

The law of mass action is given by:

$$\frac{\alpha}{1 - \alpha} = \frac{D}{\rho} e^{-\frac{\theta_D}{T}} \tag{21}$$

where α is taken as constant at the value computed for reflected shock conditions. This system of equations was solved by iteration to give thermodynamic conditions at the nozzle exit planes.

In all cases, the experimentally measured static pressures at the nozzle exits are higher than the theoretically predicted exit plane pressures. This discrepancy was not discovered until late in the experimental program and, hence, could not be corrected in time to rerun the series of interferometric tests. Two possible causes are being investigated to explain this difference. First, nozzle boundary layers are being reexamined theoretically in more detail to determine if they are really sufficiently large to change the effective nozzle area ratio. Second, reflected shock/boundary layer interactions unique to reactive diatomic gases that appear to result in higher reflected shock pressures are being examined.

The initial boundary layer thickness estimates at the nozzle exit planes were based on conventional simplified techniques (Ref. 6) that use the local flow-field Reynolds number and the length of the nozzle wall as the characteristic dimension, X. The exit plane Reynolds number can be expressed as:

$$Re = \frac{\rho_e u_e X}{\mu_e} \tag{22}$$

where the subscript e denotes properties evaluated at the nozzle exit plane. The laminar boundary layer thickness is then given by

$$\delta = 5\sqrt{\frac{\mu X}{\rho u}} \tag{23}$$

which can be rewritten as

$$\delta = 5\sqrt{\frac{X^2}{Re}} \tag{24}$$

These equations give typical boundary layer thicknesses of 0.05 in. for the parallel mixing hydrogen carrying nozzle and 0.03 in. for the fluorine carrying nozzle. Based on these numbers, it was originally concluded that boundary layers would not alter the effective nozzle area ratio in a significant manner. It is possible that a turbulent boundary layer is, in fact, more nearly correct for the flow condition here. The criterion for determining the nature of the wall boundary layer is the relative magnitude of the momentum thickness Reynolds number Re_θ. That is, if Re_θ (based on freestream conditions) is less than 500, the boundary layer can be assumed laminar, while values greater than 500 indicate the presence of a turbulent boundary layer. These calculations and consideration of increased reflected shock pressures are in progress.

4. DIAGNOSTIC INSTRUMENTATION

Three basically different experimental techniques were employed in this program to measure the variations in flow-field properties within the mixing region downstream of the nozzle exit. The three different techniques include a Mach-Zehnder interferometer (MZI) designed to map the mixing layer, a rapid scanning spectrometer to map the infrared emission intensity within the mixing layer, and a series of probe measurements tailored to mapping the temperature and static and pitot pressures at the nozzle exit region and in the mixing layers. The actual instrumentation and the basic techniques are interchangable for both the injection mixing and the parallel shear flow experiments with only minor variations. The remainder of this subsection will be devoted to a detailed discussion of these diagnostic techniques and the generalized data reduction procedure that has been used in this study.

a. Mach-Zehnder Interferometer - All optical examinations of compressible fluid flows are based on the fundamental premise that variations in density across the transluminated medium give rise to variations in the absolute local index of refraction that, in turn, affect the traversing light rays. Appropriate optical equipment is then used to translate the resulting effect into variations of intensity of illumination on a screen or photographic plate. The basic physical laws used in interpreting these effects are Fermat's law of stationary transit time and Snell's law of refraction at surfaces of discontinuity of refractive index, $n(x,y,z)$.

The principal feature of all of the well-known optical systems can best be described in the following manner. Consider a disturbance in a flow field that is illuminated by a parallel beam of light that can be observed on a screen (Fig. 16).

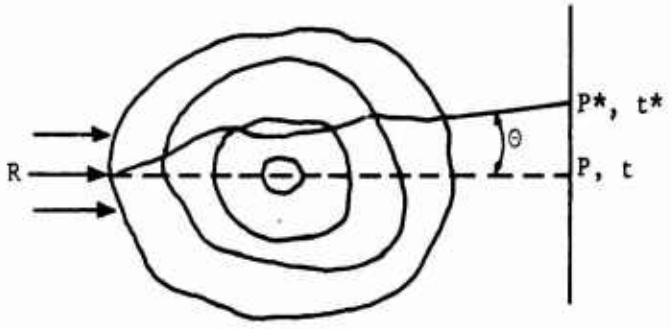

Figure 16. Generalized Ray Diagram

Consider next what happens to a single ray, like R, as it transverses the disturbance. In the absence of any disturbance, the ray would arrive at the point P on the screen at a time t. However, the presence of the disturbance alters the path of the ray R, and it actually arrives at the screen at point P* at time t* and from a direction characterized by θ.

The insertion of appropriate optical equipment into the existing light path gives a record of either the phase lag (t*- t), the deflection (θ), the displacement (P*- P), or, in general, some combination of all three of these quantities at the position of the screen. The phase lag determination is the physical basis for interferometry, while measuring the deflection angle forms the basis of schlieren methods and the displacement is measured by the familiar shadowgraph technique. The theory of each of these systems gives a unique correspondence between the intensity of illumination at the screen and n (x,y,z). Once n (x,y,z) is known, an analysis based on electromagnetic theory gives the gas intensity in terms of n and a constant, K (Gladstone-Dale). This relationship is

$$n-1 = K \tag{25}$$

where K is a function of the molecular weight and the polarizability per atomic particle. In general, the polarizability is a function of wavelength but this dependency is very weak and can usually be ignored.

In optical systems where either the deflection (θ) or the phase lag ($t^* - t$) is to be measured, the displacement ($P^* - P$) must be eliminated. To accomplish this, an objective or field lens is used to focus a particular plane of the test section on the observation screen.

As mentioned, the basic quantity measured in interferometry is the phase lag associated with a reference beam passing through an undisturbed gas as compared to its traversing a disturbance under investigation. To understand how the interference technique works, consider a Mach-Zehnder interferometer (MZI) shown in Figure 17 where one assumes that all of the optical components are perfect. First, note that the division of amplitude at the beam splitter produces two coherent waves. Now if the traversal time for the two waves to reach the second beam splitter via two different paths is exactly the same, the two waves will reconstruct the original wave front. Otherwise, we may expect to obtain some interference phenomena that will be evidenced by a pattern of fringes. The possibility of this interference occurring can be explained in any of three ways: the four optical plates may not be exactly parallel to each other; the linear distances along the two paths may not be identical; and a change in refractivity due to a disturbance in the test section may change the phase velocity of the test beam relative to the reference beam.

The ray diagram shown in Figure 17 could have been drawn for the case where two distinct sets of fringes are visible (broken lines). Generally this "lost" set of fringes is not used, as the quality (a result of imperfect beam splitters) is not as good as that of the fringes formed by the primary beam. As will be discussed in Section III, Martin Marietta used the secondary fringe pattern to observe the total integrated radiation intensity from the mixing region.

If one enclosed the entire instrument with a box and viewed the exit beam only, there would be no way to describe what optical elements were inside the box. Doing this, one could actually see two apparent sources and the light rays intersecting at some plane within the enclosure. This plane then is the location at which the fringes appear to be formed but, of course, there can actually be no interference until the two beams are reunited at the last beam splitter. This is the old idea of forming a real image (at the film plane) of a virtual object (the apparent intersection of the test and reference beams). The main utility of the MZI is the wide range of choice one has in locating the plane of intersection (i.e., the focal plane within the test section) and adjusting the

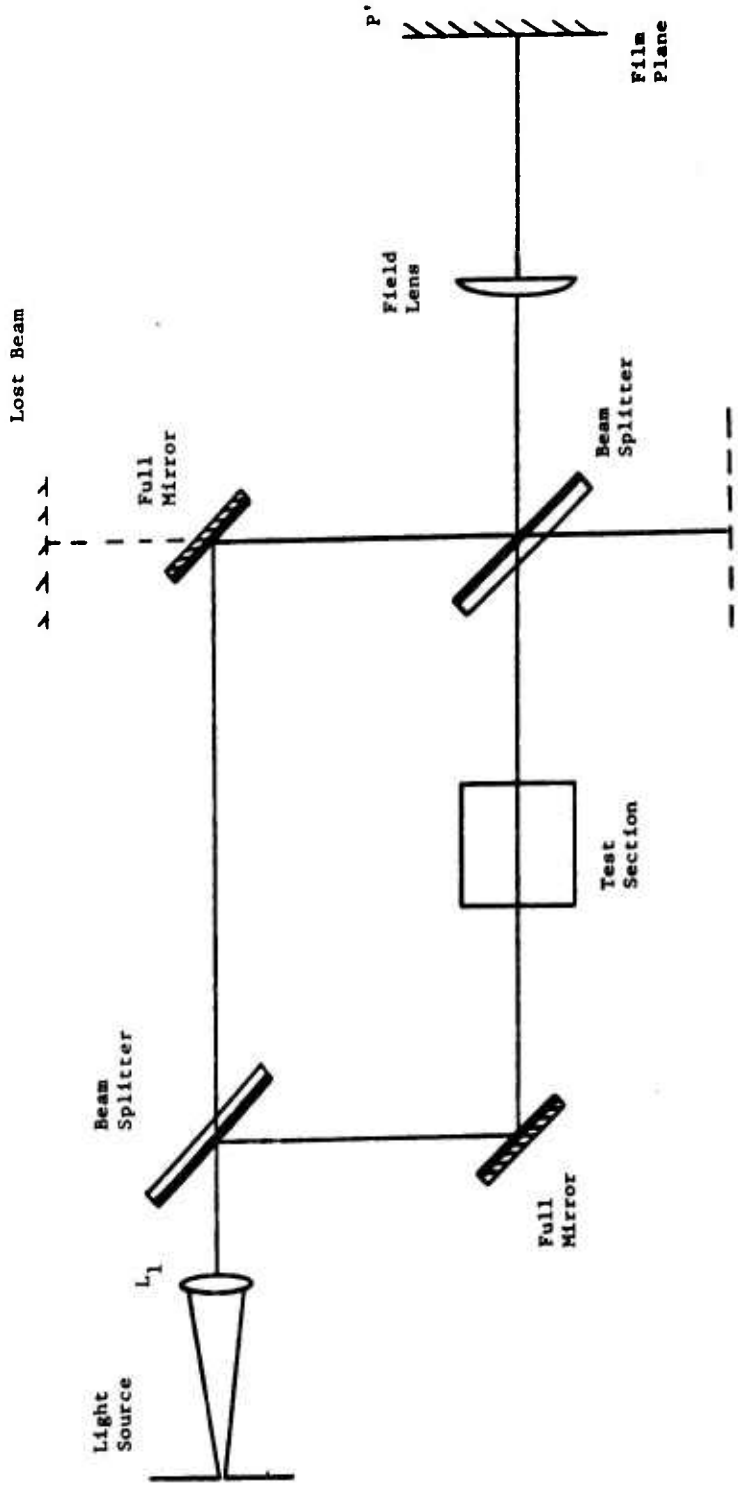

Figure 17. Schematic of Basic MZI Arrangement

width and orientation of the fringes. The fringe width, W, from linear theory is related to the apparent angle of intersection, φ, of the two beams by

$$W = \frac{\lambda}{\varphi} \tag{26}$$

where λ is the wavelength of the light source. Adjustment of either of the beam splitters allows control over both the final fringe width and fringe orientation.

The actual construction of the MZI used in this study is by now considered as conventional and, hence, will not be discussed in great detail. There are a number of excellent descriptions in the literature of the problems of design, construction, and alignment adjustments of this type of interferometer (Ref. 7 thru 9). Figure 18 is an isometric sketch of the associated test hardware and the MZI mounted with its plane of centers perpendicular to the axis of the shock tube. The lower beam passes through two windows mounted at the nozzle exit region of the test section, and the upper beam passes through a matched pair of windows in the compensating beam. Both the test section windows and the compensating windows are made of optically flat ($\lambda/10$) schlieren quality quartz with faces parallel to within 0.0005 in. Figure 18 also shows the concept of a radiation stop that is employed on the camera side of the MZI. The diffuse burst of radiation from the mixing layer is sufficiently intense to overexpose the interferogram recording film unless some effective radiation stop is employed. As illustrated in Figure 18, the field lens is some distance from the test section, and the collimated beam from the light source is completely transmitted through the pin hole located at the focal point of the lens while the diffuse radiation from the mixing layer is blocked at the focal plane of the field lens. This technique has been used in this study and the resulting interferograms are not influenced by the radiation resulting from either the mixing region or the driver gases arriving at the end of the uniform test flow.

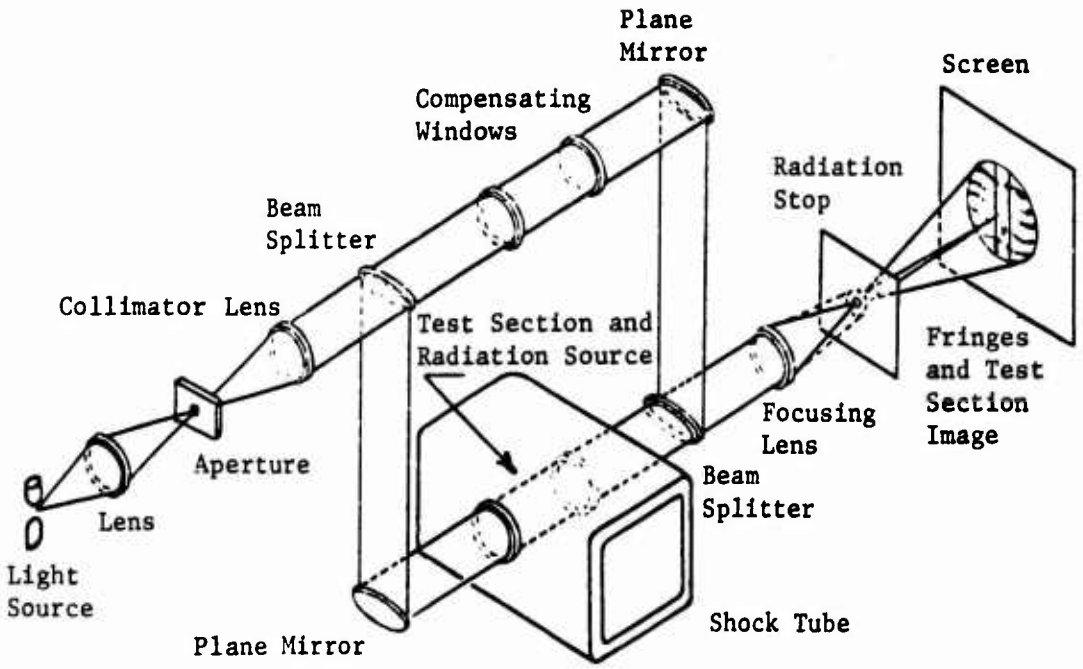

Figure 18. Schematic of MZI Installation Showing Shock Tube and Radiation Stop

As previously mentioned, a great many practical details such as alignment, light source size, imperfections in the optical components, and proper choice of fringe width and orientation must be considered in obtaining high-quality interferograms. Without intending to underestimate the importance of these practical aspects, which are generally a matter of experience and practice, a generalized discussion of the evaluation of an interferogram is presented.

The concept fundamental to the interferometric determination of the density distribution in gas flows is that if a change in the test section density by an amount $\Delta\rho$ occurs, then the resulting phase change produces a fringe shift, δ (nondimensional number), given by

$$\delta = \frac{[(n-1)]\,L}{\lambda} = \frac{K\,\Delta\rho}{\lambda}\,L \qquad (27)$$

where K is the Gladstone-Dale constant (~0.22 cm^3/gm for air) and L is the geometrical path length over which the change occurs. Knowing K, L, and δ enables one to calculate $\Delta\rho$ from a measurement of δ. The above equation is written for a change in optical path (or density) which is the same for all light rays and, hence, results in a uniform translation without distortion of the entire fringe pattern. In a more realistic case, we must assume that the test section density is a function of the spatial coordinates. Thus, in a two-dimensional flow field, the optical path of the light rays will depend on the particular (x,y) coordinates at which the Z traversal is made (see Fig. 19).

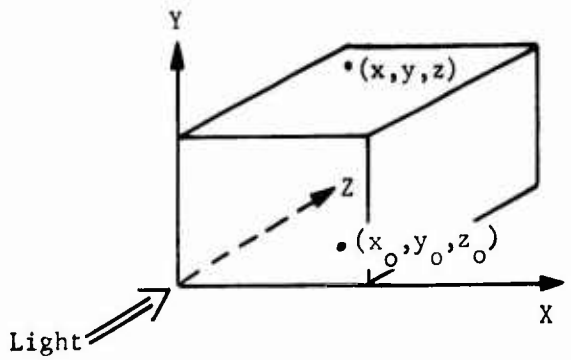

Figure 19. Generalized Light Ray Path

The optical path is defined by the following integral equation over the path, s

$$\Psi_{\text{optical path}} = \int_0^L n\,(x,y,z)\,ds \tag{28}$$

where ds is an element of distance along the actual path a light ray travels. Consider now a situation where the refractive index is uniform in the reference leg and a function of (x,y,z) in the test section. Then, if there is some portion of the flow field in the test section that is known to be uniform (say x_o,y_o,z_o), the fringe shift between the nonuniform portion of the field and the uniform (reference position in this example) part is given by:

$$\delta\,(x,y) = \frac{1}{\lambda} \int_0^L \left[n\,(x,y,z) - n\,(x_o,y_o,z_o) \right] ds \tag{29}$$

The important point to notice here is that the reference beam need not actually be in a leg of the instrument that is exterior to the test section. In fact, for the example situation described above, one does not require a "no-flow" interferogram in addition to the flow interferogram. That is, the change in density is measured relative to some portion of the flow field where the density is already known and the fringe shift of interest is shown on a single flow-field interferogram. In this study, a no-flow interferogram was used in conjunction with the flow interferogram to establish the overall density in the undisturbed nozzle exit region before mixing.

Returning now to the generalized integral equation for $\delta(x,y)$, if the path deviation of the actual light ray from a straight line is not large, one can approximate ds (actual path segment) by dz (ideal path segment). Doing this, and using the relationship between n and ρ, the generalized expression for fringe shift becomes

$$\delta(x,y) = \frac{K}{\lambda}\left[\int_0^L \rho(x,y,z)\,dz - \int_0^L \rho\left(x_o,y_o,z_o\right)\,dz_o\right] \tag{30}$$

Further simplification of this result is possible if one assumes that the flow-field variables are two-dimensional and, as such, depend only on (x,y). In this case, the basic evaluation equation becomes

$$\frac{\lambda}{KL}\,\delta(x,y) = \rho(x,y) - \rho_o \tag{31}$$

One useful scheme for gaining confidence in the assumption that the deviation of a light ray is small (i.e., ds ≈ dz) is to very carefully focus on a grid network (most often etched on the exit window of the test section) and photograph it under flow and no-flow conditions. If one cannot detect a distortion of this grid work under actual flow conditions, then the assumption of approximating ds by dz is for all practical purposes a valid one. In this same regard, when the interferometer is used for examining regions, such as boundary layers, where there are large density gradients, it is necessary to consider the possibility of an error in the measured fringe shift that occurs as a result of refraction of the light rays. That is, the gradient in density will cause a light ray to bend in the direction of increasing density and, hence, follow a curved path through the test section rather than

the straight path that is assumed in the above theoretical discussion. This phenomenon can result in two main effects: First, each ray in the strong gradient region will travel over a longer optical path; second, along this path, the refractive index (and, hence, density) is constantly changing. Several authors have addressed this problem, including Howes and Buchele (Ref. 10) and Bunting and DeVoto (Ref. 11). The main conclusion drawn by each of these authors is that the fringes should be focused at the 2/3 span of the test section rather than center span to minimize the refractive error. This study always used the 2/3 span location for focusing the fringes even though the gradients here are not nearly as large as those in, for example, a thermal boundary layer.

The above discussion has been a rather generalized treatment of the basic principles of interferometry. A more specialized treatment starting from these general results is presented in the following paragraphs. This division of discussion is necessary because several bench experiments were required in this study to generate refractive index variations for F_2 and HF, which had not previously been reported in the literature. Thus, the details of measuring refractive indices of gases and the application of interferometric techniques to multicomponent gases will now be discussed starting with the results of the above generalized discussion.

As shown above, the absolute fringe shift, δ, for monochromatic illumination at wavelength, λ, for a two-dimensional flow field is given as

$$\delta = \frac{(n-n_o)\ L}{\lambda} \tag{32}$$

where n is the refractive index for the test case under consideration, n_o is the refractive index for some initially known conditions, and L is the physical pathlength of the test cell. The reference conditions for measuring the refractive indices of HF and F_2 are an initially evacuated test cell where n_o can be taken as unity. Hence, using this criterion as a basis, the expression for δ can be written as

$$\delta = \frac{(n-1)\ L}{\lambda} \tag{33}$$

Recalling now the relationships between refractive index and density, for the present situation using an initially evacuated test cell as reference, the absolute fringe shift can be written as

$$\delta = \frac{(n-1)\ L}{\lambda} = \frac{K\rho L}{\lambda} \tag{34}$$

Because all of the refractive index data to be used in this study are referenced to standard conditions of temperature and pressure, the above relationship can be written as

$$\delta = \frac{\left(n_{STP}-1\right)}{\rho_{STP}}\ \frac{L\rho}{\lambda} \tag{35}$$

where the ratio

$$\frac{(n-1)}{\left(n_{STP}-1\right)} = \frac{K\rho}{K\rho_{STP}} \tag{36}$$

has been used along with the fact that K remains only a slightly varying function of λ.

Now the refractive index of any given chemical species i can be expressed in terms of the usual two-term Cauchy formula

$$(n-1)_i = A_i \left(1 + \frac{B_i}{\lambda^2}\right) \tag{37}$$

where A_i and B_j are uniquely determined for each of the chemical species involved. These constants have been experimentally determined for [illegible] and HF, and these data will be presented later in this section.

Continuing now with the above expression for the fringe shift of a single component gas, one can write

$$\delta(\lambda_j) = C_j \tag{38}$$

where

$$C_j = \frac{\left(n_{STP}-1\right)}{\rho_{STP}}\ \frac{L}{\lambda_j}$$

and λ_j denotes the different wavelengths at which interferograms were recorded.

If the test section contains several chemical species, then their respective concentrations at any given point in the flow field can be deduced from interferograms by noting that the total composite fringe shift, $\delta\left(\lambda_j\right)$, at a point is just the superposition of the fringe shifts, $\delta_i\left(\lambda_j\right)$, due to each of the chemical species i. Here one should note that a different wavelength interferogram is required for each different chemical species to be determined. Expanding the above single species equation using self-explanatory notation gives

$$\delta\left(\lambda_j\right) = \sum_i \delta_i\left(\lambda_j\right) \tag{39}$$

or

$$\delta\left(\lambda_1\right) = C_{1HF}\,\rho_{HF} + C_{1F_2}\,\rho_{F_2} + C_{1H_2}\,\rho_{H_2} \tag{40}$$

$$\delta\left(\lambda_2\right) = C_{2HF}\,\rho_{HF} + C_{2F_2}\,\rho_{F_2} + C_{2H_2}\,\rho_{H_2} \tag{41}$$

$$\delta\left(\lambda_3\right) = C_{3HF}\,\rho_{HF} + C_{3F_2}\,\rho_{F_2} + C_{3H_2}\,\rho_{H_2} \tag{42}$$

where

$$C_{ji} = \frac{\left(n_{STP} - 1\right)_i}{\lambda_j}\,\frac{L}{\rho_{STP}}$$

which are the three simultaneous equations that can be solved for ρ_{HF}, ρ_{F_2}, and ρ_{H_2} once the C_{ji} coefficients are known, and the $\delta\left(\lambda_j\right)$'s are measured.

Before proceeding further with this discussion, the results of bench experiments conducted on a separate IRAD task (Ref. 12) to obtain the A and B coefficients in the Cauchy representation of the refractive index of F_2 and HF will be discussed.

The refractive indices of argon, fluorine, and hydrogen fluoride have been measured directly and, along with values quoted by Allen (Ref. 13), are plotted in Figure 20. The method used here is based on the fringe shift observed with an MZI as a small test cell is slowly filled with the gas to be observed. Figure 21 shows a diagrammatic sketch of the test setup.

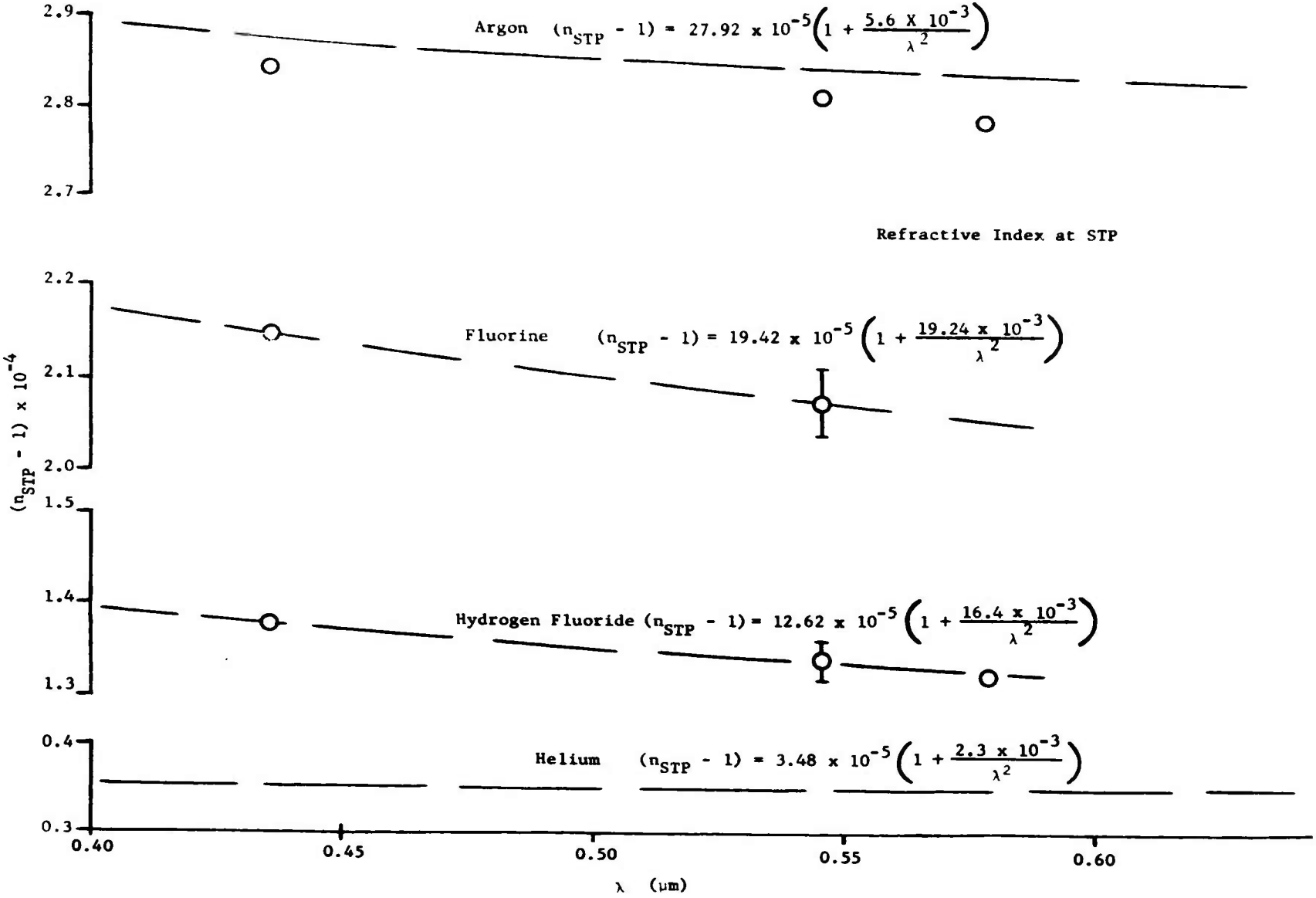

Figure 20. Refractive Index vs λ

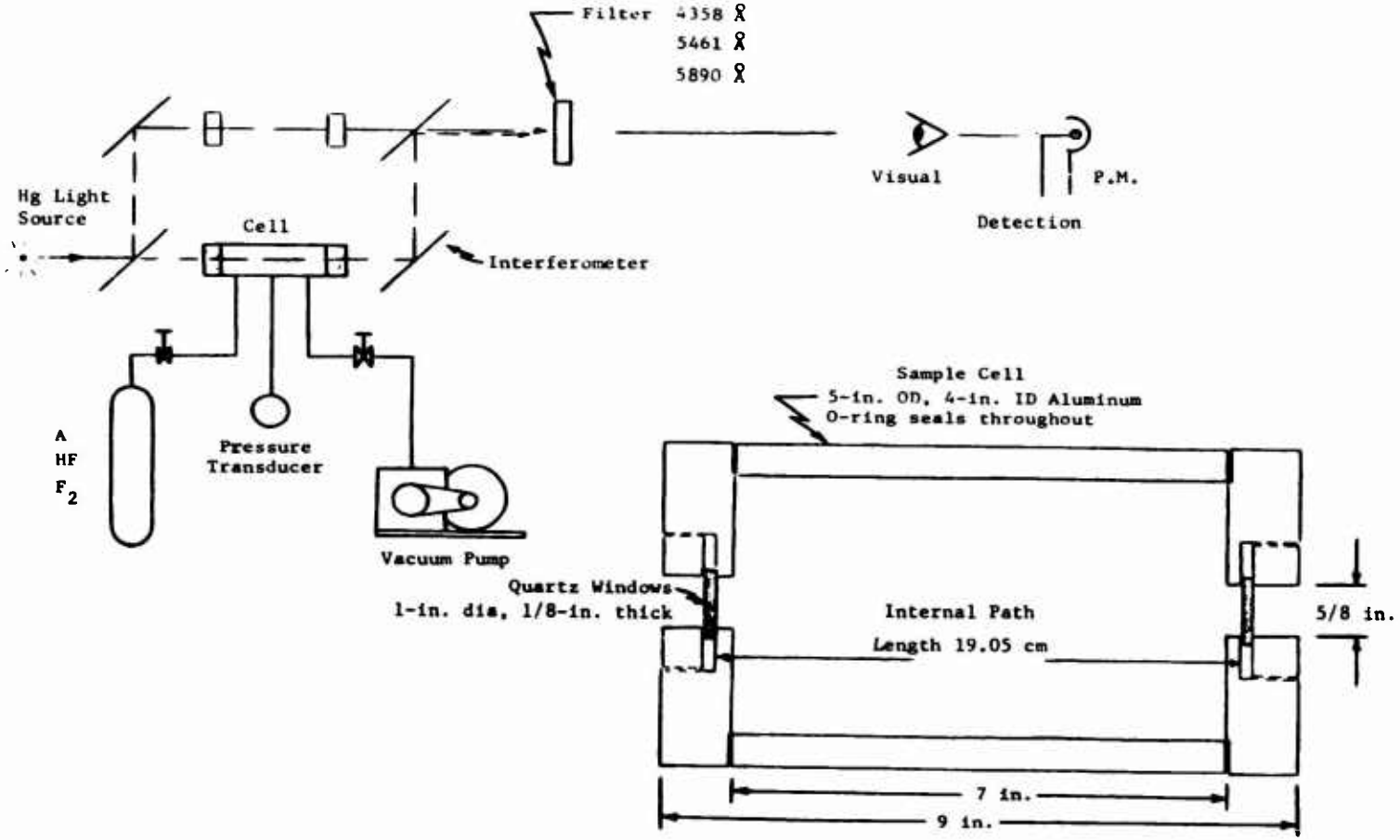

Figure 21. Experimental Setup for Refractive Index Measurements of HF and F_2

As has been shown in this section, the fringe shift, δ, observed as the chamber pressure is changed from a value where density is denoted by ρ_1 to a final pressure with density corresponding to ρ_2, can be expressed as

$$\delta = \frac{n_{STP}-1}{\rho_{STP}} (\rho_2 - \rho_1) \frac{L}{\lambda} \tag{43}$$

For the bench condition established for this purpose, ρ_1 is identically zero, so the observed fringe shift will be given by

$$\delta = \frac{n_{STP}-1}{\rho_{STP}} \rho_2 \frac{L}{\lambda} \tag{44}$$

or expressed in terms of experimental observables (assuming a perfect gas)

$$n_{STP}-1 = \frac{\delta}{\rho_2} T_2 \frac{P_{STP}}{T_{STP}} \frac{\lambda}{L} \tag{45}$$

The technique employed here was to measure δ as the test cell pressure was varied very slowly. Increasing the test cell pressure rapidly resulted in a nonisothermal expansion of the gas and thus a changing temperature. In the experiments with HF as a test gas, it was necessary to monitor the test cell temperature in addition to the pressure because the windows in the cell were destroyed if the pressure was allowed to rise sufficiently slowly to maintain an isothermal expansion. Fringe-shift data for each of the three test gases considered (A, F_2, HF) were recorded as a function of temperature and pressure at three separate wavelengths. Data points for pressure and fringe shift were plotted for each different wavelength (see Fig. 22), and the experimental value of $n_{STP}-1$ was determined from the measured slope using Equation 45. Because of the uncertainty in both pressure and temperature, an error bar as shown in Figure 20 was assigned to each of these values. Doing this for each of the three different observed wavelengths allows one to produce plots of $(n_{STP}-1)$ vs λ such as those shown in Figure 20. This variation of n-1 with λ is then used to produce the A and B constants in the Cauchy formula, Equation 37, with the results as shown in Table III.

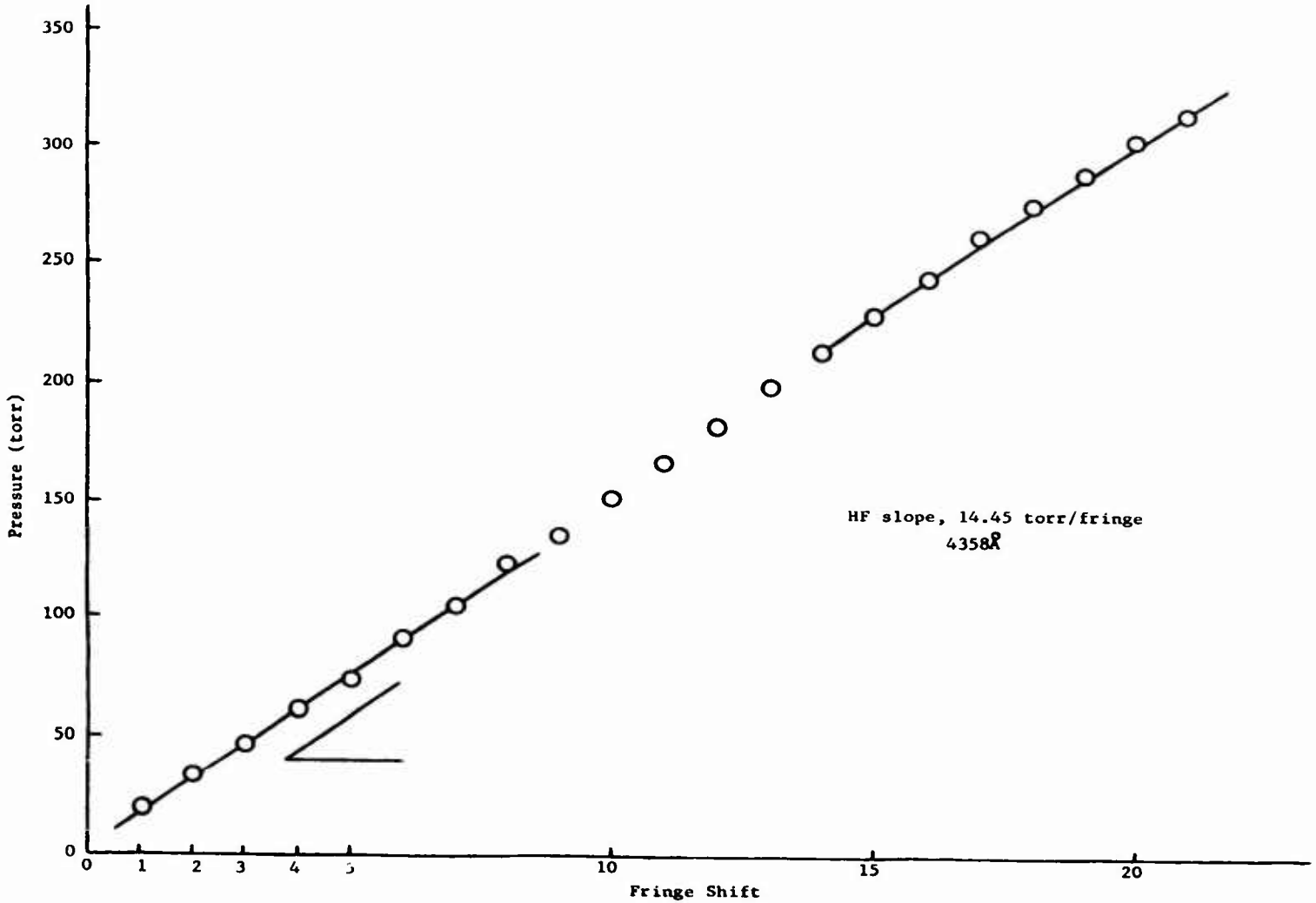

Figure 22. Fringe Shift vs Pressure for Refractive Index Measurement of HF

Table III

EXPERIMENTAL VALUES OF A AND B FOR VARIOUS SPECIES

Species	A	B, μm^2
HF	12.62×10^{-5}	16.40×10^{-3}
F_2	19.42×10^{-5}	19.24×10^{-3}
A	27.92×10^{-5}	5.60×10^{-3}
H_2	13.58×10^{-5}	7.52×10^{-3}

Returning now to the set of three simultaneous equations for solving for ρ_{F_2}, ρ_{HF} and ρ_{H_2}, one can use the results of Table III to compute the C_{ji} coefficients in these equations. Using the values from Table III, the actual test section span of 5 in., and Loschmidts number for ρ_{STP}, the C_{ji} coefficients corresponding to the three wavelengths used for recording the interferometric results were computed and are given in Table IV.

Table IV

COMPUTED VALUES OF C_{ji} COEFFICIENTS

j	λ, Å	C_{jHF}, cm^3	C_{jF_2}, cm^3	C_{jH_2}, cm^3
1	4358	1.487×10^{-18}	2.319×10^{-18}	1.531×10^{-18}
2	4880	1.306×10^{-18}	2.033×10^{-18}	1.357×10^{-18}
3	6100	1.021×10^{-18}	1.583×10^{-18}	1.073×10^{-18}

By inserting each of these nine C_{ji} coefficients into the previously developed set of simultaneous equations, one can, in principle, obtain absolute number densities through the mixing layer by measuring corresponding fringe shifts at three different wavelengths. As it turns out, this ambitious task is not possible because the solution set to these equations is extremely sensitive to the precision to which the resulting fringe shifts can be measured. There are two different ways of seeing that this is indeed the case in the present situation. First, one can consider each of the elements, C_{ji}, in a row of the matrix as being a component of a three-dimensional vector. Doing this, normalizing the vectors,

and taking the dot product of each vector with the others results in dot products extremely close to unity. This means that the vectors are almost colinear and, hence, finding a solution set involves finding the difference between very small vectors that consist of the closure vector between any two pairs. Another way of looking at this overall problem is to note that the three plots of n_{STP}-1 vs λ are very nearly parallel, even though displaced in absolute value. After a careful analysis of the values involved, it turns out that one needs to know the absolute fringe shifts for each of the different wavelengths to better than 0.001 fringe. This type of precision is beyond the present capability and, hence, the three wavelength solutions originally planned for determining absolute number densities are not possible. These number densities are obtained by another technique involving certain additional assumptions that will be explained in Section III.

The scheme used to reduce the interferometric data involved a Scherr Tumico optical comparator. This comparator has a very fine X-Y translational table and an enlarging viewer with crosshairs. A negative of the interferogram is placed on the translational table, and the enlarged fringes plus crosshairs are viewed on a screen. An X-Y scan is performed on both the flow and no-flow negatives with corresponding fringe maxima and minima recorded. These raw data are then reduced in terms of absolute fringe shift (i.e., fringe movement between no-flow and flow negatives divided by original fringe spacing) at preselected downstream stations measured from the edge of the splitter plate. Results of these efforts and a summary of the data obtained will be presented in Section III.

b. Rapid Scanning Spectrometer - An OCLI Model 501 rapid scanning spectrometer was used to monitor the absolute emission intensity between 1.7 and 4.7 μm within the mixing zone of both the H_2 injection and the parallel shear flow experiments. Figure 23 is a schematic representation of the optical system. Figure 24 is a photograph of the spectrometer located at the shock tube test section. Translation supports mounted to the basic instrument cover provide a means for varying the focal point location to any given station within the mixing layer.

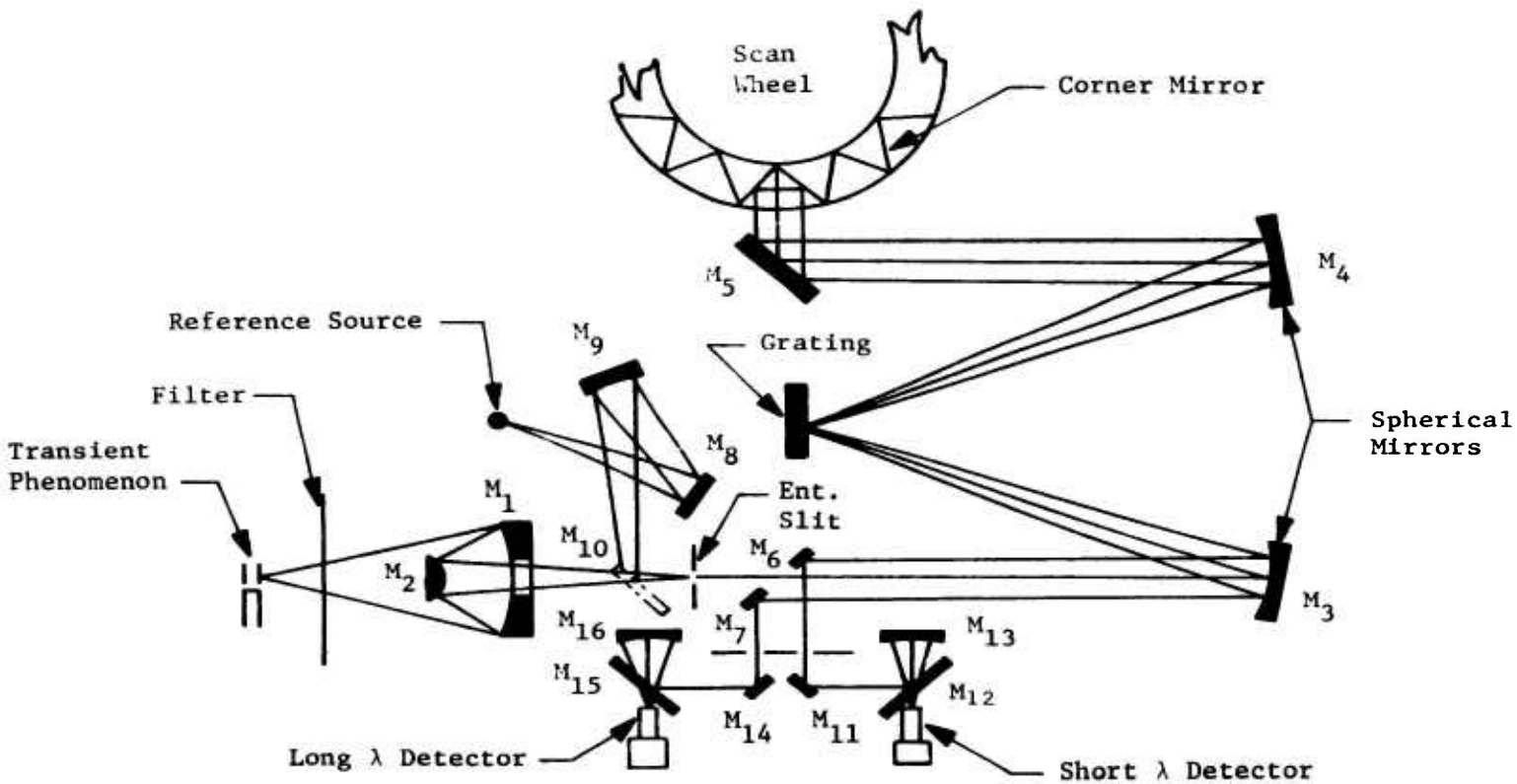

Figure 23. Rapid Scanning Spectrometer Optical Schematic

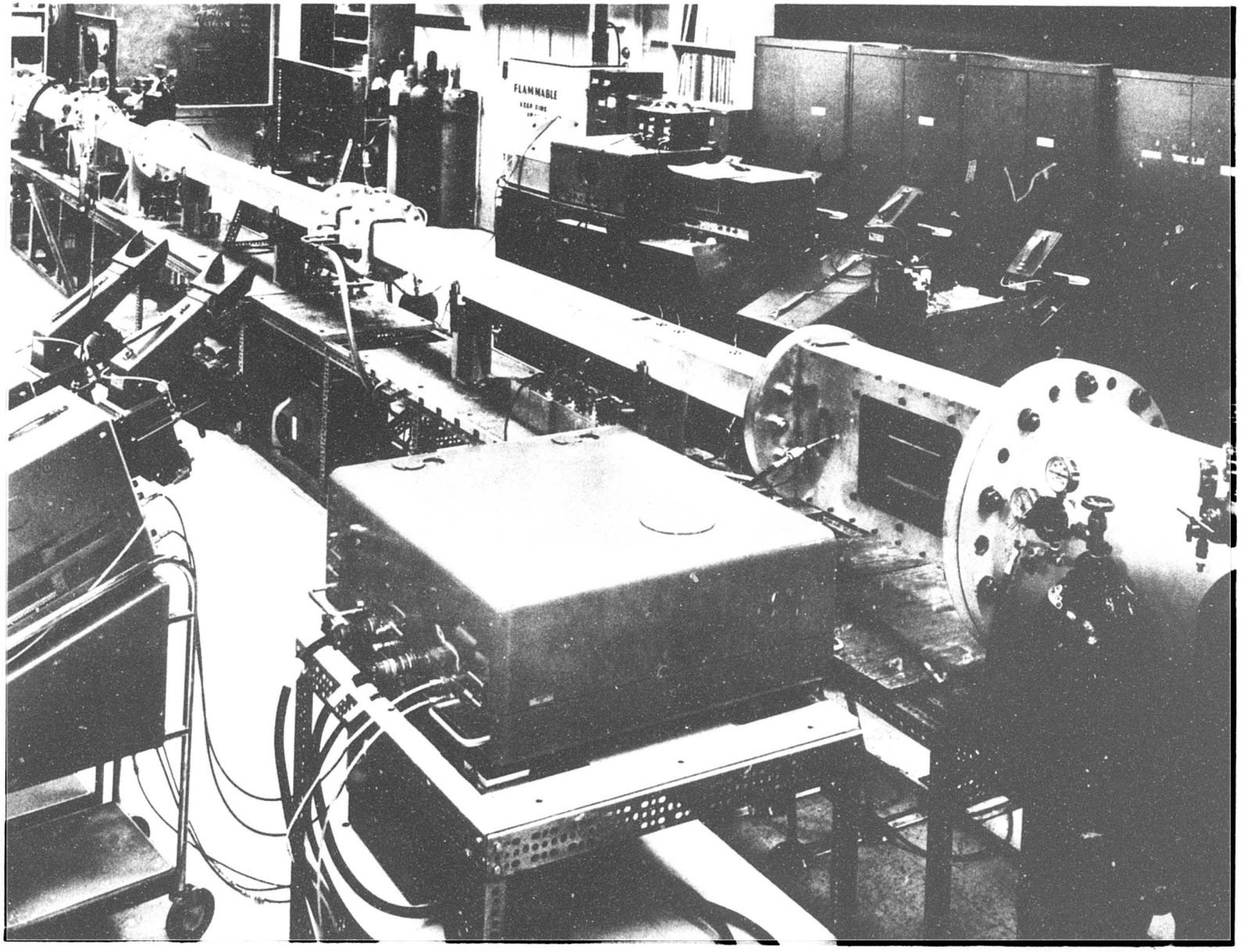

Figure 24. Shock Tube with Rapid Scanning Spectrometer in Position

The Model 501 collects radiation from any given zone of the reaction layer through a variable focus Cassegrainian optical system. This radiation then passes through a double pass grating monochromator optical system onto a double-exit slit and detector configuration. A scan wheel equipped with corner mirrors causes the second pass radiation to sweep in wavelength across the fixed exit slits. The shorter wavelength half of the spectrum is scanned across one exit slit at the same time that the longer wavelength portion is scanned across the other exit slit. The availability of two exit slits allows coverage over a broader spectral region with higher resolution and provides a wavelength overlap useful in checking system accuracy. The spectral region to be scanned is determined by the gratings, filters, and detectors used. The detectors used in this study are indium arsenide (InAs) and indium antimonide (InSb) cooled to LN_2 temperature. The signal resulting from the detected radiation is displayed on two separate oscilloscopes and recorded photographically. The Model 501 has a built-in secondary standard of radiation that can be used, when fully calibrated, to convert observed radiation signals to units of absolute radiance. This instrument is capable of a full spectral scan between 1.7 and 4.7 μm in 1 msec, with a repetition time of 1.25 msec.

The data reduction procedure used here for deducing the specific gas intensity from measured spectrometer signals is similar to that outlined by Menard and Thomas (Ref. 14). The portion of their analysis that follows serves as an introduction to the specific details of the present calibration.

Assuming an optically thin gas and an isotropic radiation source, the radiant power (w/μm) to the detector, at a specific wavelength λ, is given as

$$P_g = \tau_\lambda G_\lambda \iiint d\Omega \, dA dz \tag{46}$$

and the power from the standard calibration source is given as

$$P_c = \tau_\lambda N_\lambda \iint d\Omega \, dA \tag{47}$$

where τ_λ is a combined parameter containing all transmission losses, monochromator efficiency, and detector sensitivity, G_λ is the specific radiation intensity (w/cm^3 -μm -sr) of the gas, Ω is the solid angle where A is the cross-sectional area of the field of

view rays as defined by the entrance optics, and z is the coordinate along the optical path. N_λ, the intensity (w/cm^2 -μm -sr) of the blackbody calibration source, is given in terms of the absolute temperature of the cavity by Planck's radiation law,

$$N_\lambda = \frac{C_1}{\lambda^5}\left[\frac{1}{e^{C_2/\lambda T}-1}\right] \tag{48}$$

C_1 and C_2 are the first and second radiation constants given by Stair, Johnston, and Halbach (Ref. 15) as

$$C_1 = 1.19088 \times 10^{-12}\ w\text{-}cm^2/sr$$

$$C_2 = 1.4380\ cm\text{-}°K$$

Over the linear response range of the photo detectors, the output voltage, E, is proportional to the input power, P. Therefore, by taking the ratio of Equations (46) and (47), the specific intensity emitted by the gas at wavelength λ is given as

$$G_\lambda = KN_\lambda \frac{E_g}{E_c} \tag{49}$$

where K, the view factor coefficient, is defined by

$$K = \frac{\iint d\Omega\ dA}{\iiint d\Omega\ dA\,dz} \tag{50}$$

An analytical solution of Equation (50) would be very difficult for the particular geometry used in this experiment, so an alternative method is employed to determine K experimentally. Integration of Equation (47) over the path length, L (shock tube width), yields

$$\int_0^L P_c\,dx = \xi_\lambda N_\lambda \iiint d\Omega\ dA\,dz \tag{51}$$

Combining Equation (51) and Equation (46), once again assuming linear detector response, G_λ is given as

$$G_\lambda = N_\lambda \frac{E_g}{\int_0^L E_c\,dz} \tag{52}$$

The integral $\int_0^L E_c(z)\,dz$ is obtained experimentally by moving the calibration source along the optical path from 0 to L and integrating a plot of resulting outputs.

Equating Equation (52) and Equation (49), the constant, K, is given by

$$K = \frac{E_c(z)}{\int_0^L E_c(z)\,dz} \tag{53}$$

Although E_c is a function of λ and z, K is only a function of z as can be seen from Equation (50). To determine K for any convenient location such as z_i, the $\int_0^L E_c(z)\,dz$ need be measured only once at any desired wavelength, λ_o. Thus, at z_i,

$$K(z_i) = \frac{E_c(\lambda_o, z_i)}{\int_0^L E_c(\lambda_o, z)\,dz} \tag{54}$$

After K has been determined as above, G_λ can be computed from Equation (49) once $E_c(z_i)$ is known as a function of λ. The measurements of $E_c(z_i)$ vs λ are obtained by placing the calibration source at z_i and measuring the wavelength dependence of the output signal. The only restriction on z_i is that it be within the optical path. For convenience, the centerline of the shock tube where the entrance slit of the spectrometer is focused is always used. Note, at this point, that the interferograms were taken at the 2/3 span of the test section rather than the centerline span solely to minimize refractive errors.

Wavelength calibration of the spectrometer was accomplished by using a series of calibrated narrow-band infrared filters. These filters were inserted between the calibrated blackbody and the entrance optics of the spectrometer. A total of 10 separate filters were used, and a resulting average dispersion of 0.223 μm/cm was determined.

The absolute intensity calibration was accomplished using a bench setup with a calibrated blackbody cavity located at the simulated shock tube centerline. The centerline position can be located quite carefully by backlighting the entrance slit of the spectrometer with a strong diffuse light source and then placing the exit of the blackbody cavity at the image of the entrance slit. The entrance optics are adjusted to give a one-to-one magnification of the entrance slit as viewed from the shock tube centerline.

As a precaution against possible damage in shipment, the linearity of the slit opening was checked before the calibration tests. This check was accomplished by measuring the spectrometer output, at a fixed wavelength, for various physical slit widths. Because the output intensity varies as the square of the slit width, a plot of slit width vs square root of intensity should define a straight line passing through the origin. Any deviation from this straight line represents an irregularity in the slit opening. Failure to pass through the origin represents an error in the zero setting of the slit width dial. This check was performed, and the straight line defined by the data points passed through the origin of the plot well within experimental error limitations.

The blackbody source used for this calibration was operated at a temperature of 1000 ± 2°C. Before each calibration run, the cavity was allowed 90 minutes to stablize, and all tests were accomplished without interruption. Data points for the curves of E_c (·) vs · were taken with z_i corresponding to the centerline location and a 0.500 mm slit width. Results from this calibration test for the injection mixing (employing a 2-in.-diameter sapphire viewing window) are shown in Figure 25 where one can notice the atmospheric H_2O and CO_2 absorption bands between 2.65 and 2.90 μm. Figure 26 shows the resulting calibration curve of $E_c(z_i)$ vs z_i at a fixed wavelength (= 3.06 μm) when the calibration souce is moved along the z_i coordinate. Integrating the area under this curve provides the necessary input to evaluate the viewfactor constant, K, which for this case turns out to be 0.111 cm^{-1}.

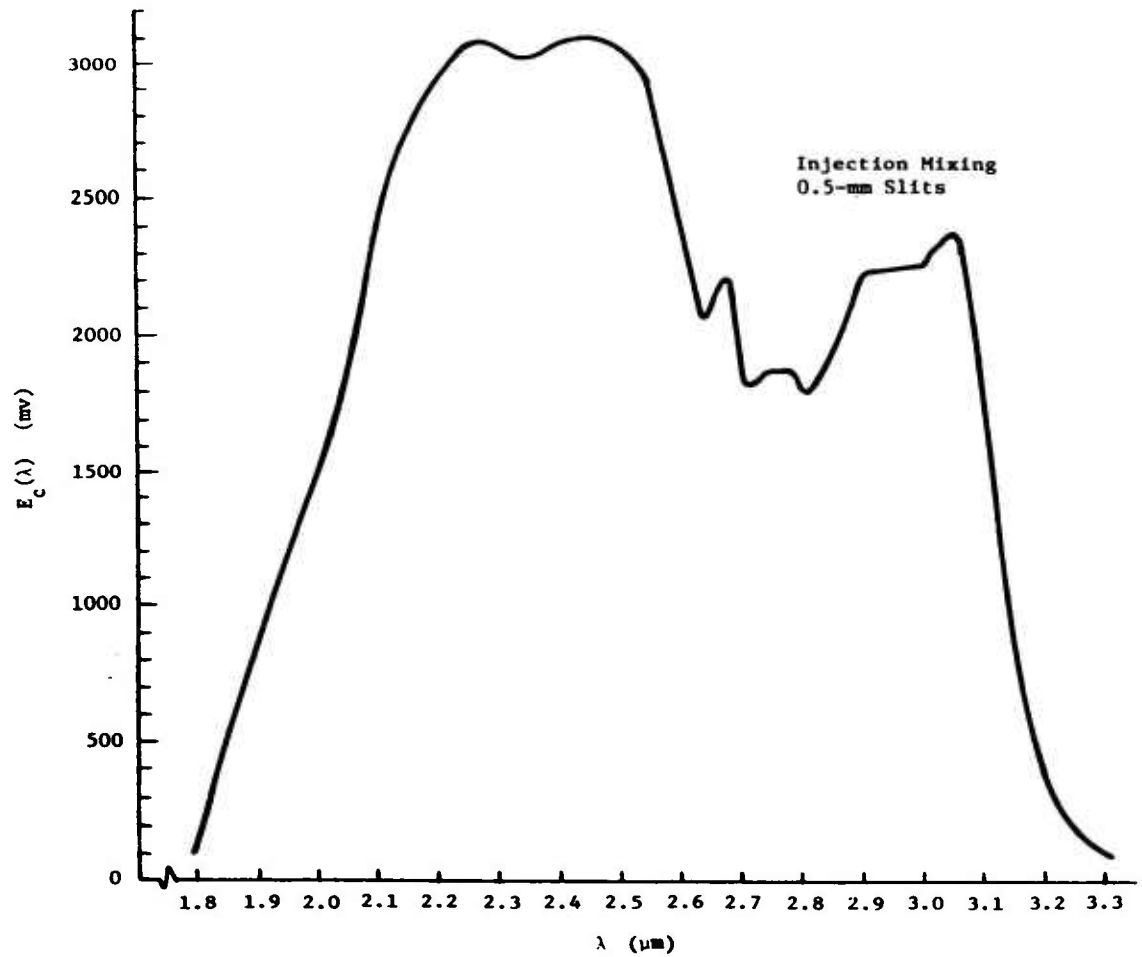

Figure 25. $E_c(\lambda)$ vs λ for the Injection-Mixing Rapid Scanning Spectrometer Calibration

$$\text{Area} = 16.75 \text{ in.}^2 = 103 \text{ cm}^2$$

$$1 \text{ cm}^2 = 200 \text{ mv-cm}$$

$$\int_o^L E_c\left(\lambda_o, z_i\right) dz = \frac{108 \text{ cm}^2}{1 \text{ cm}^2} 200 \text{ mv-cm}$$

$$= 21{,}600 \text{ mv-cm}$$

$$K = \frac{E_c\left(\lambda_o, z_i\right)}{\int_o^L E_c\left(\lambda_o, z_i\right) dz} = \frac{2{,}380 \text{ mv}}{21{,}600 \text{ mv-cm}}$$

$$K = 0.1105 \text{ cm}^{-1}$$

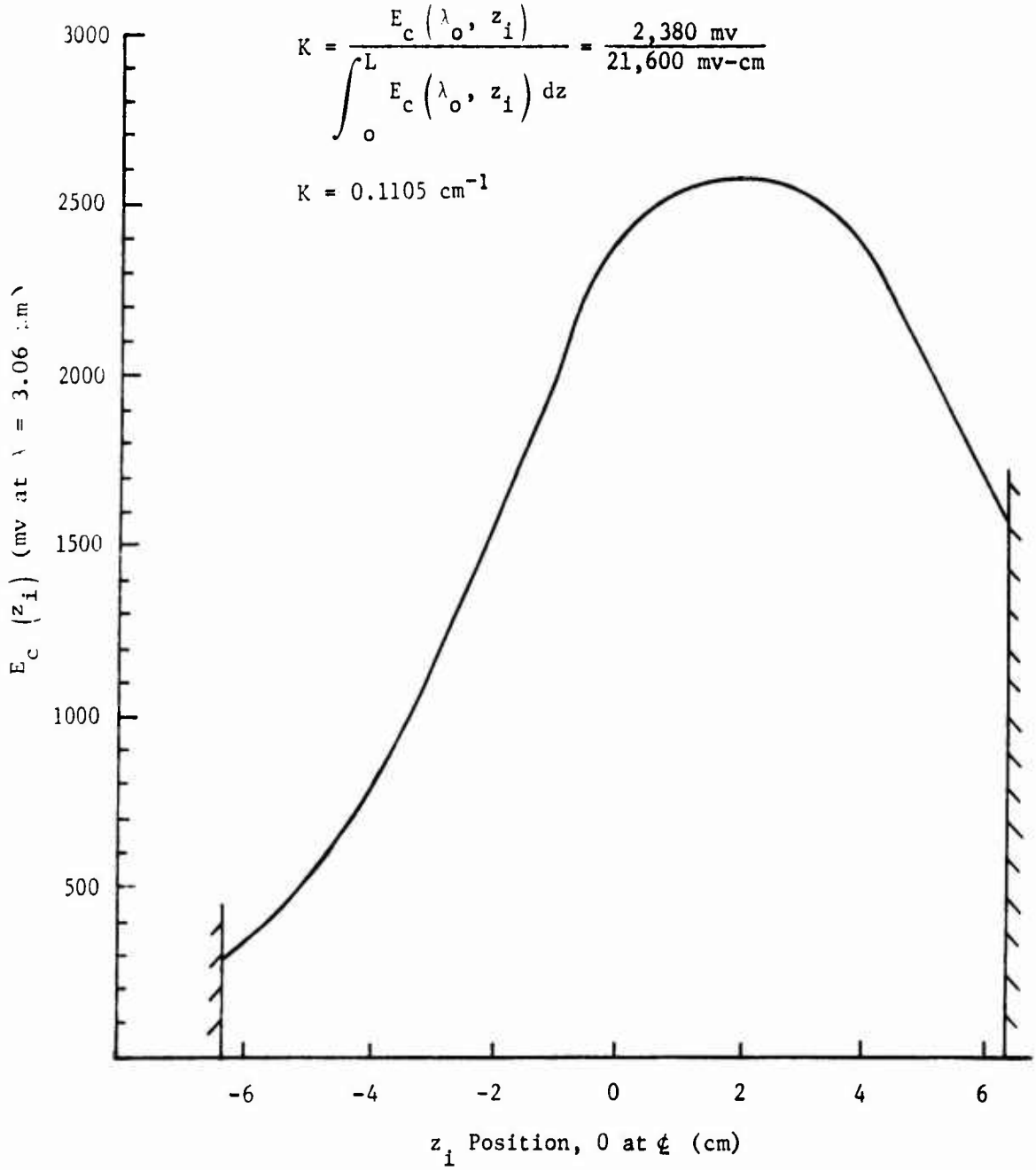

Figure 26. $E_c(z_i)$ vs z_i Position for the Injection-Mixing Rapid Scanning Spectrometer Calibration

c. Pitot Probe - A sketch and a photograph of the actual pitot probe rake is shown in Figure 27. Two pitot tubes were employed for each run, and the rake position could be located in any of seven different basic positions shown in Figure 27. At each different basic position, the probes could be located in any of 13 different vertical positions. Kulite strain-gage type pressure transducers were used in these probes, and each transducer was calibrated in place before starting any given survey. Typical calibration constants for these transducers are 0.15 mv/torr. The natural damped ringing frequency of the tube geometry and mounting cavity was computed on the basis of the Helmholtz resonator formulation and a useful recording frequency of 1.22 kc was indicated. The pitot probe data were all recorded using a 1 kc RC filter network, and the data were reduced using the Rayleigh pitot-tube formulation given by Shapiro (Ref. 16).

d. Static Pressure Probes - Figure 28 is a photograph of the side-wall mounting plate with the static pressure locations indicated. Quartz crystal PCB Model 113-821 transducers were mounted in each of the positions indicated in the photograph. A complete series of static pressures was recorded by successively repeating the run conditions. As will be discussed in Section III, this side-wall static pressure is used in conjunction with the pitot probe pressure to predict the Mach number in the exit region and the mixing layer from experimental results.

e. Temperature Probe - Figure 29 is a photograph of the 1 mil tungsten/tungsten-26% rhenium thermocouple wire. This probe was mounted in the same holder that was used for the pitot probe survey and it could be moved over a wide range of locations, both in the nozzle exit region and the mixing layer. Results from each of these three types of probes and further discussion will be presented in Section III, when the actual data are given.

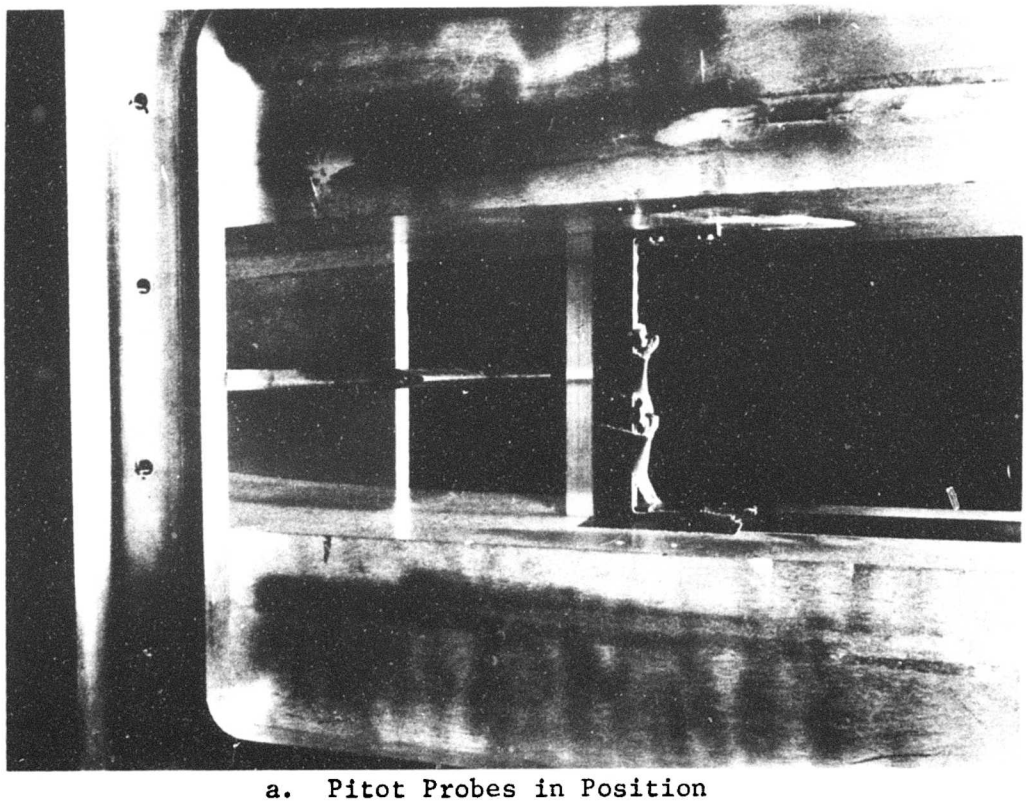

a. Pitot Probes in Position

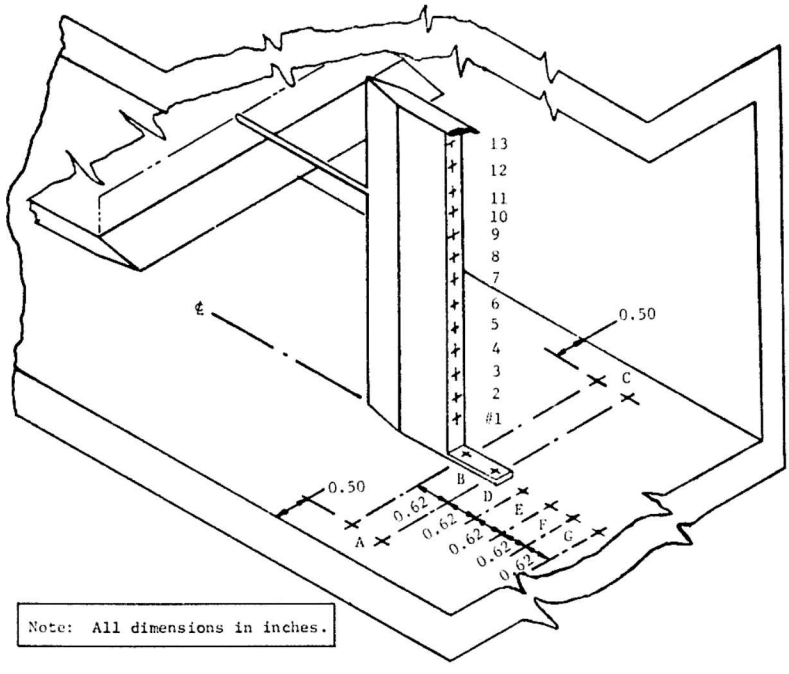

b. Pitot Probe Rake

Figure 27. Pitot Probe

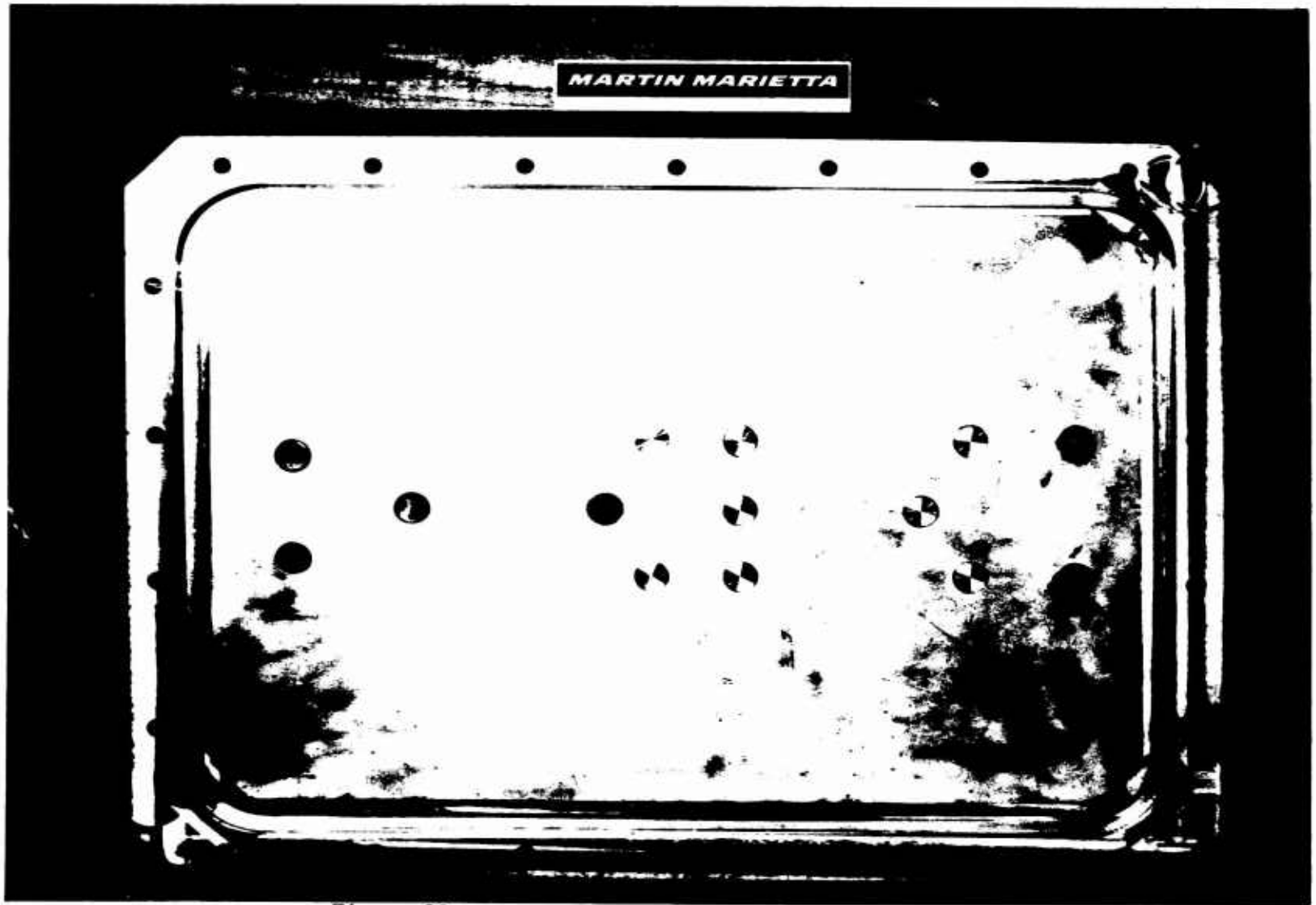

Figure 28. Side-Wall Static Pressure Transducer Locations

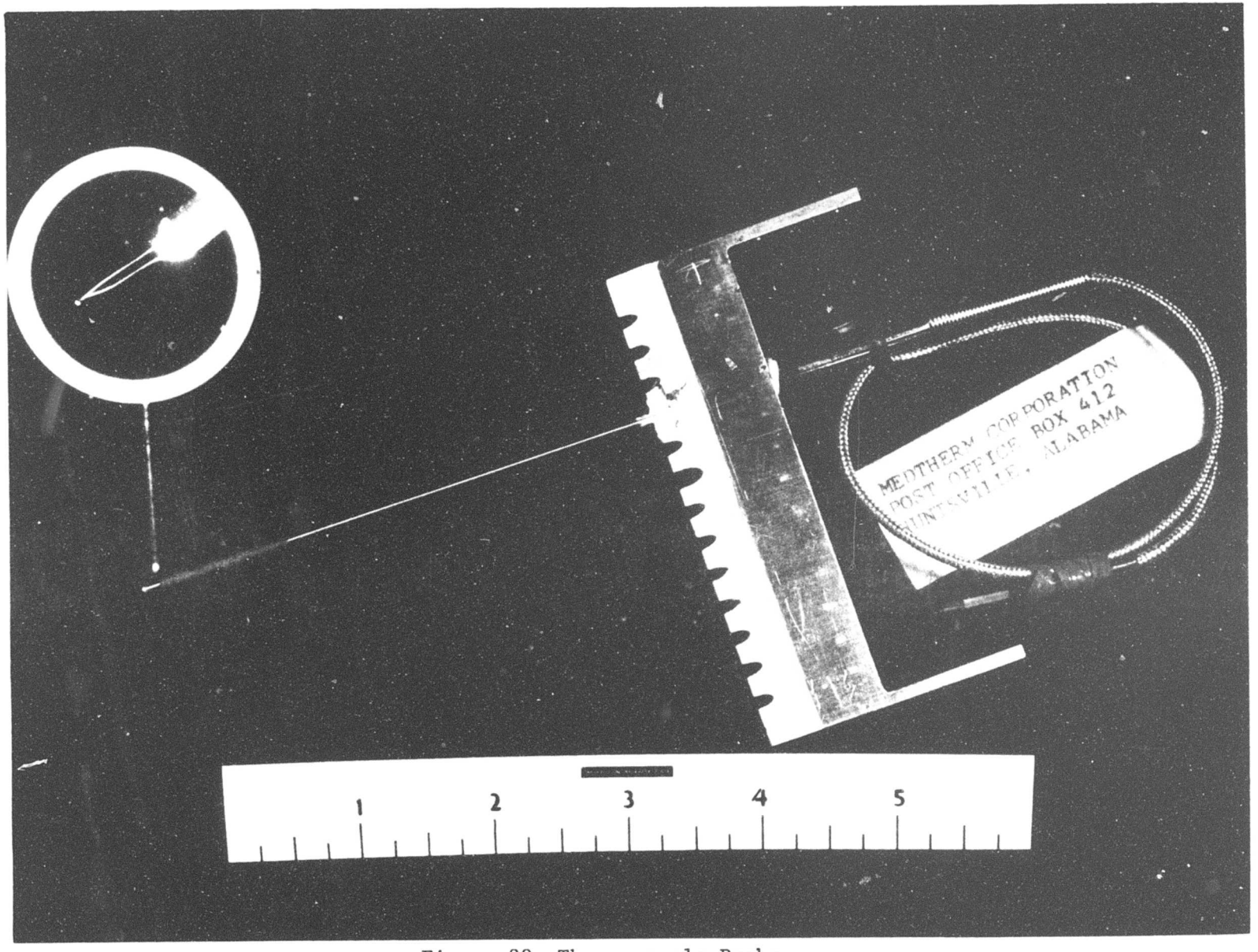

Figure 29. Thermocouple Probe

SECTION III

EXPERIMENTAL RESULTS

As described in Section II, two basically different experimental methods were used to investigate the flow-field parameters within the mixing layer during the time interval that the overall $H_2 + F_2 + M$ reaction was taking place. The experimental data from these different techniques will now be presented by proceeding first with a summary and selected details of the H_2 injection results, followed by a summary and selected details of the parallel shear flow mixing experiments.

1. SUMMARY OF AVERAGE DENSITY PROFILES

a. Injection Mixing - A series of experiments was conducted in the injection shock tunnel facility, where the basic supersonic fluorine carrying stream was unchanged and the hydrogen injection splitter plate was varied to determine its influence on the overall extent of the mixing layer. As described in Section II, two splitter plates were used as nozzle dividers. One of these contained a series of sonic orifices for injecting hydrogen into the freestream. The other was constructed with a series of two-dimensional slots from which the hydrogen was injected into the fluorine stream.

Table V is a summary of the slotted hydrogen injection mixing experiments and Table VI is a summary of the orifice hydrogen injection mixing experiments. Each of these tables contains the coded run number (year, month, day, shot), initial test gas mixture, initial test gas loading pressure (p_1), incident shock Mach number (M_s), injectant gas type, injectant gas pressure (p_{inj}), test section static pressure (p_e), degree of F_2 dissociation (α_{F_2}), and freestream exit-plane Reynolds number (Re/x). These experiments were designed to produce nominal test section static pressures of 5, 10, and 20 torr while maintaining a dissociation level of 70% for the fluorine behind the reflected shock. As indicated in Tables V and VI, five different injection conditions were run for each set of nominal conditions. That is, the manifold pressures feeding the different hydrogen injection ports were varied from 50 to 150 psi to distinguish this type of influence on the mixing layer, and a 150 psi helium injection case was run to distinguish the influence of a no-reaction case compared to the reaction case.

Table V

INTERFEROGRAM SUMMARY FOR SLOTTED H_2 INJECTION

Run No.	Test Gas Mixture by Volume	p_1 torr	M_s	Injectant	p_{inj} psi	p_e, torr	α_{F_2}, %	Re/x cm^{-1}
72071802	50%He/50%F_2	12	5.58	None	-	15.0	82.0	
72071803	50%He/50%F_2	12	5.58	H_2	150	15.0	82.0	
72071901	50%He/50%F_2	12	5.54	H_2	100	15.0	80.0	
72071902	50%He/50%F_2	12	5.54	H_2	50	15.0	80.0	1.786×10^4
72071903	50%He/50%F_2	12	5.58	None	-	15.0	82.0	
72071904	50%He/50%F_2	12	5.58	H_2	150	15.0	82.0	
72072101	50%He/50%F_2	8	5.34	H_2	150	9.8	75.5	
72072104	50%He/50%F_2	8	5.30	H_2	100	9.6	75.0	
72072106	50%He/50%F_2	8	5.30	H_2	50	9.6	75.0	1.233×10^4
72072401	50%He/50%F_2	8	5.34	None	-	9.8	75.5	
72072402	50%He/50%F_2	8	5.34	He	150	9.8	75.5	
72072503	50%He/50%F_2	4	5.30	H_2	150	4.99	76.0	
72072504	50%He/50%F_2	4	5.34	H_2	100	5.05	77.0	0.6449×10^4
72072701	50%He/50%F_2	4	5.30	H_2	50	4.99	76.0	
72072601	50%He/50%F_2	4	5.30	He	150	4.99	76.0	
72072603	50%He/50%F_2	4	5.42	None	-	5.20	80.0	

Table VI

INTERFEROGRAM SUMMARY FOR ORIFICE H_2 INJECTION

Run No.	Test Gas Mixture by Volume	p_1 torr	M_s	Injectant	p_{inj} psi	p_e, torr	α_{F_2}, %	Re/x cm^{-1}
72071701	50%He/50%F_2	12	5.54	H_2	150	15.0	80.0	
72071702	50%He/50%F_2	12	5.58	None	-	15.0	81.0	
72071703	50%He/50%F_2	12	5.54	H_2	100	15.0	80.0	1.829×10^4
72071704	50%He/50%F_2	12	5.54	H_2	50	15.0	80.0	
72071801	50%He/50%F_2	12	5.54	He	150	15.0	80.0	
72052503	F_2	3	7.18	H_2	100			
72061502	50%He/50%F_2	10	5.08	H_2	150	10.8	65.0	
72061503	50%He/50%F_2	10	5.35	H_2	100	12.2	74.5	
72061504	50%He/50%F_2	10	5.39	H_2	50	12.5	76.0	1.381×10^4
72061602	50%He/50%F_2	10	4.95	None	-	10.0	61.0	
72061603	50%He/50%F_2	10	5.11	He	150	11.0	66.0	
72060804	50%He/50%F_2	5	5.19	H_2	150	5.8	71.0	
72060901	50%He/50%F_2	5	5.08	H_2	100	5.5	68.0	
72061301	50%He/50%F_2	5	5.27	H_2	50	6.0	74.0	7.749×10^3
72061302	50%He/50%F_2	5	5.27	None	-	6.0	74.0	
72061303	50%He/50%F_2	5	5.05	He	150	5.4	66.0	

Injection pressures quoted here were the values measured at the solenoid valve inlet located approximately 3 in. from the outside wall of the test section under no-flow conditions. The feed line supplying both the orifice injection ports and slotted injection ports has a cross-sectional area more than twice that of the total injection area. This area ratio should be sufficient to ensure a minimum pressure drop (not over 5%) between the large bottle supply source and the small chamber orifice feed manifold.

Several test cases indicated in Tables V and VI are for runs with no injection to allow comparisons of the mixing regions with and without the disturbances that are necessarily generated by the injection process.

Figure 30 shows six monochromatic interferograms that were recorded at 4358 Å for the slotted hydrogen injection mixing case. The run code number is indicated on each figure to allow a more detailed identification of the shot conditions by referring to Table V. Initial driver and driven tube load pressures for each of these separate runs were held constant to within experimental uncertainties. As Table V indicates, incident shock Mach numbers for a given series all agree to with $\pm$ 0.04; hence, resulting test section conditions can be assumed to be identical for all practical purposes. The first four interferograms shown in Figure 30 correspond to the various different injection pressures, including the 150-psi helium injection.

Figure 30e shows an interferogram of the flow field with no injection, and Figure 30f is the corresponding zero field interferogram taken immediately before running the test. As can be noted in Figure 30e, the no-injection flow interferogram shows almost no fringe distortion except just downstream in the wake region of the splitter plate. Even in this wake region, the fringe distortion is extremely small (<0.1 fringe). Notice that the term "fringe distortion" has been used here because there is in fact an actual overall uniform fringe shift between the no-flow field (Figure 30f, test section evacuated) and the flow field. Under these test conditions, fringe shift at the nozzle exit location and at all undisturbed regions of the flow field is approximately 2.5 fringes, as will be shown when the final reduced results are presented. This kind of qualitative result would indicate that any overall fringe distortion (as appears in the first interferograms of Figure 30) would necessarily result from the injection process and/or the chemical reaction.

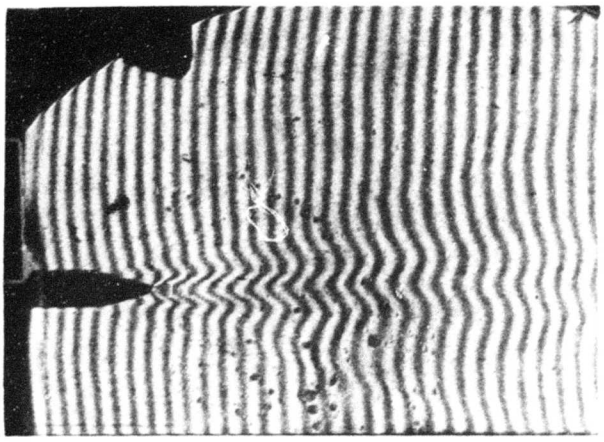

a) 72061502 150-psi H_2 Injection

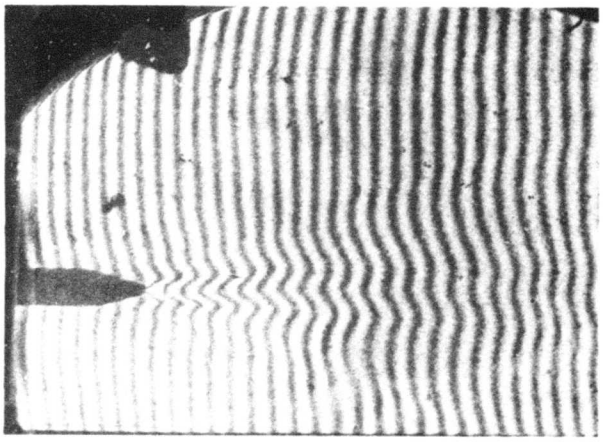

b) 72061503 100-psi H_2 Injection

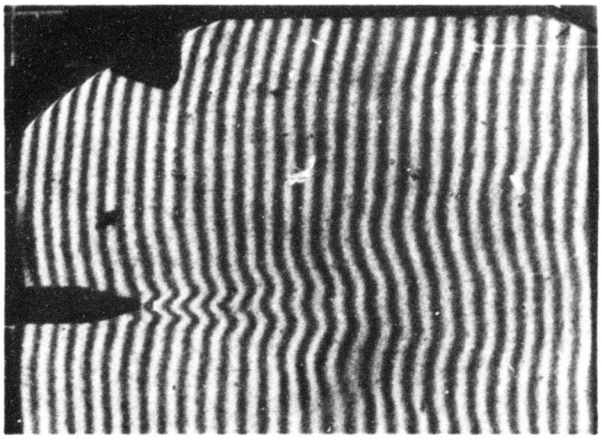

c) 72061504 50-psi H_2 Injection

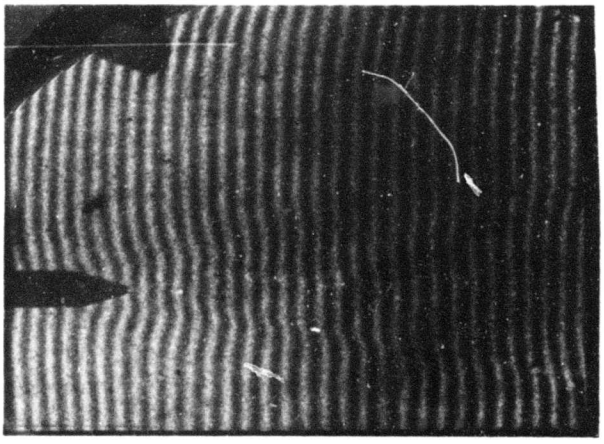

d) 72061603 150-psi He Injection

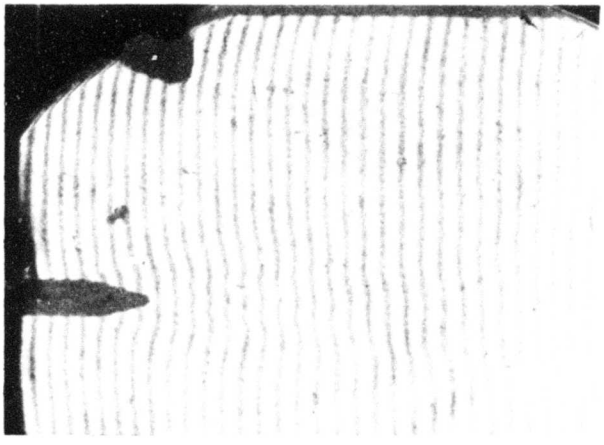

e) 72061602 No Injection

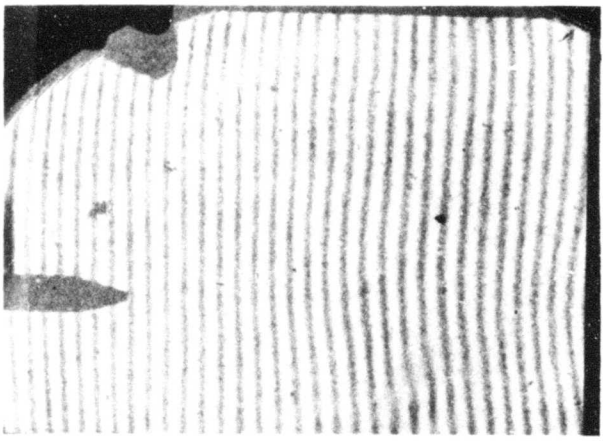

f) 72061602 No Flow

Figure 31. Comparison of Orifice Injection Snapshot Interferograms, $\lambda = 4358$ Å

Consider now the interferogram of Figure 30d, where 150-psi helium is used as an injectant. Here, it is well known that the helium will not react with the fluorine in the supersonic freestream; hence, this record visually displays the net result of the flow-field characteristics when a simple nonreacting injection process occurs. Notice in this record that, just downstream of the injection location, a very small fringe distortion (Fringes bending toward the splitter plate indicate an increase in density.) does occur, but overall this effect is small and is very limited in the direction normal to the plane of the injection points. This type of record also provides direct experimental evidence that at least no strong shock-wave-type disturbances result from the basic gas dynamic injection process.

Moving now to the first three interferograms in Figure 30, where the results for the different H_2 injection feed pressures are presented, a casual glance at these records would lead one to conclude that the overall plume boundary downstream of the 50-psi H_2 injection case is greater in extent than is the plume for the 150-psi H_2 injection case. In fact, a careful examination of these records will show this to be true. Here we are identifying the apparent plume boundaries with the rather sharp fringe shift that is quite visible in Figure 30a. This same type of boundary can be identified in each of these interferograms, but the close fringe spacing makes it a little more difficult to visualize. In general, one must look at the final reduced fringe-shift data to see this effect. In each of the records, a fringe disturbance that bends a given fringe toward the splitter plate indicates an overall increase in the number density relative to the undisturbed fringe condition that exists in the freestream region. Again, it is quite apparent from these records that a larger fringe shift occurs within the mixing region for the 150-psi H_2 injection case than occurs for either the 100- or the 50-psi injection case. It is also apparent from these two cases that the extent of the apparent reaction region is continued further downstream for the 150-psi H_2 injection case than is true for either of the other two injection pressures. Detailed fringe-shift profiles, mixing layer growth, and density profiles will be presented for the slotted injection test cases following a brief discussion of the orifice H_2 injection interferograms.

We proceed next with the interferometric results for the orifice H_2 injection splitter plate. The total area of the series of sonic orifices is less than that available in the slotted injection case by a factor of two; hence, the comparison must be considered

with this fact in mind. Using the same general approach to the discussion here as was followed for the slotted injection case, Figure 31 shows six interferograms with varying hydrogen injection pressure, helium injection, and no-injection conditions. Here again, more complete details for the run conditions are given in Table VI with identification made through the run code numbers. As was the case for the slotted injection scheme, the no-injection interferogram of Figure 31e indicates that only a very small fringe disturbance is visible in the wake region of the orifice. Here again, the uniform fringe shift between the flow and no-flow interferograms is approximately 2.5 fringes. Considering next the 150-psi helium injection interferogram shown in Figure 31d, it is clear that no large disturbances are visible as a result of the gas dynamic simulation of the injection process without chemical reactions. In all these interferograms, a uniform fringe shift or a fringe distortion that causes a fringe to bend toward the splitter plate indicates an increase in density.

The first three interferograms of Figure 31 show the results of varying hydrogen injection pressure from 150 to 50 psi. Here again, as was the case for the slotted injection scheme, the most noticeable effect that can be observed from a casual inspection is the increased downstream extent of the mixing region characteristic of the higher injection pressure. In the three cases shown here, growth of the mixing region does not appear to be strongly influenced by changing injection pressures, and the plume boundaries appear to be slightly larger for the higher hydrogen injection pressure. Before presenting the actual reduced interferograms for these two different hydrogen injection techniques, it should be pointed out that a Mach disc is almost always visible in these interferograms just downstream of the hydrogen injection location. This effect is especially visible in Figures 30a, 31a, and 31c.

As the previous discussion indicates, a simple visual observation of the snapshot interferograms does yield valuable qualitative information about the two different injection techniques. However, to extract the maximum amount of information, a detailed examination of the reduced interferograms is obviously required.

Discussion and comparison of selected results from the two different injection cases will now be presented. Figures 32, 33, and 34 show the reduced interferometric results for six of the 150-psi hydrogen injection cases. Each figure contains fringe-shift profiles as a function of test section coordinates (x,y)

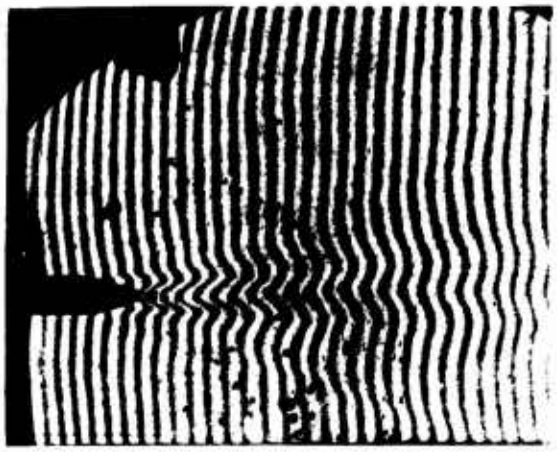

a) 72061502 150-psi H_2 Injection

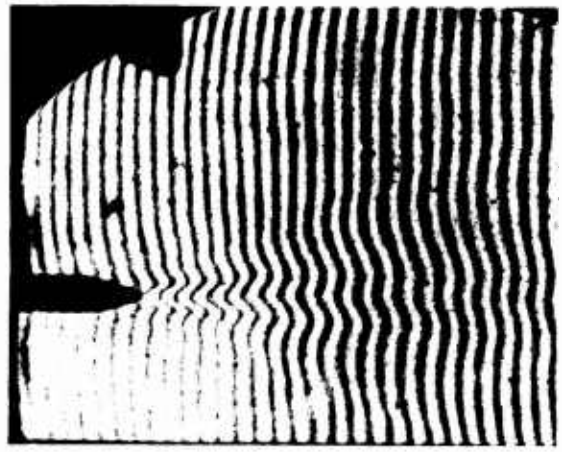

b) 72061503 100-psi H_2 Injection

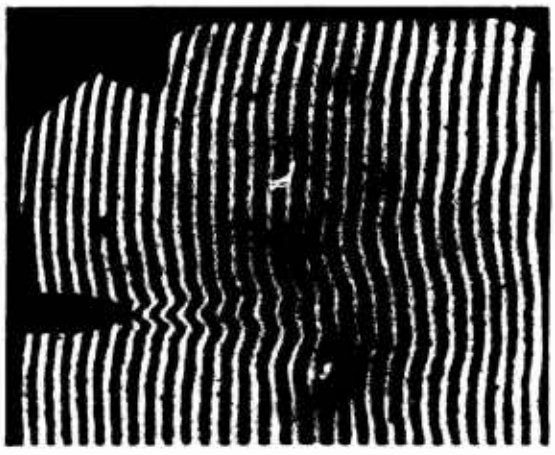

c) 72061504 50-psi H_2 Injection

d) 72061603 150-psi He Injection

e) 72061602 No Injection

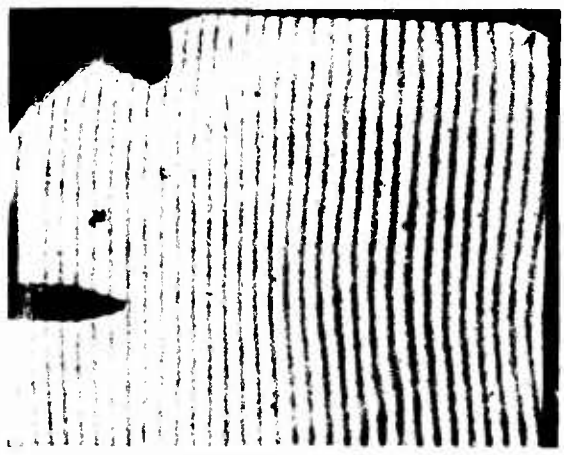

f) 72061602 No Flow

Figure 31. Comparison of Orifice Injection Snapshot Interferograms, λ = 4358 Å

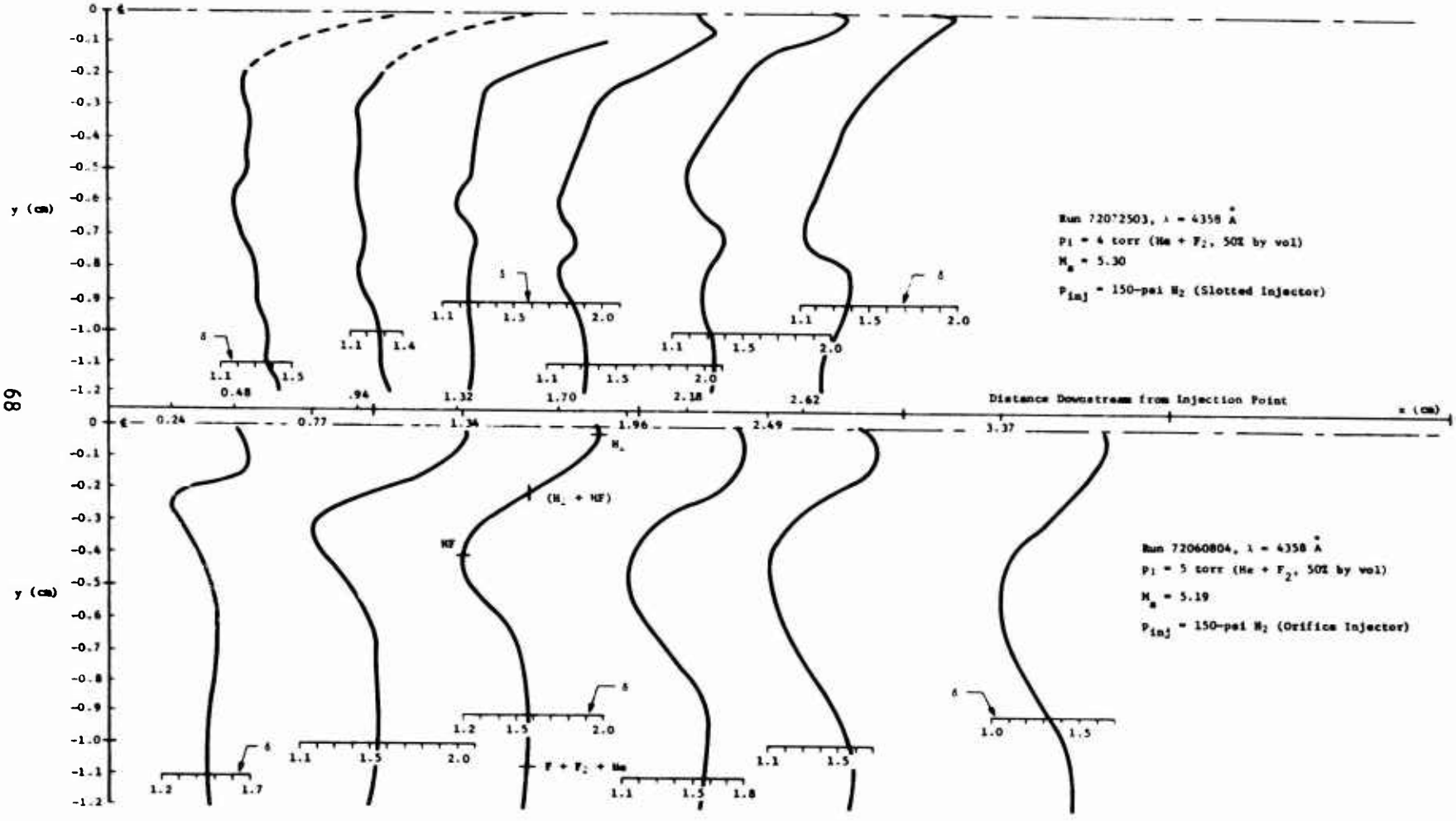

Figure 32. Interferometric Results, Runs 72072503 and 72060804

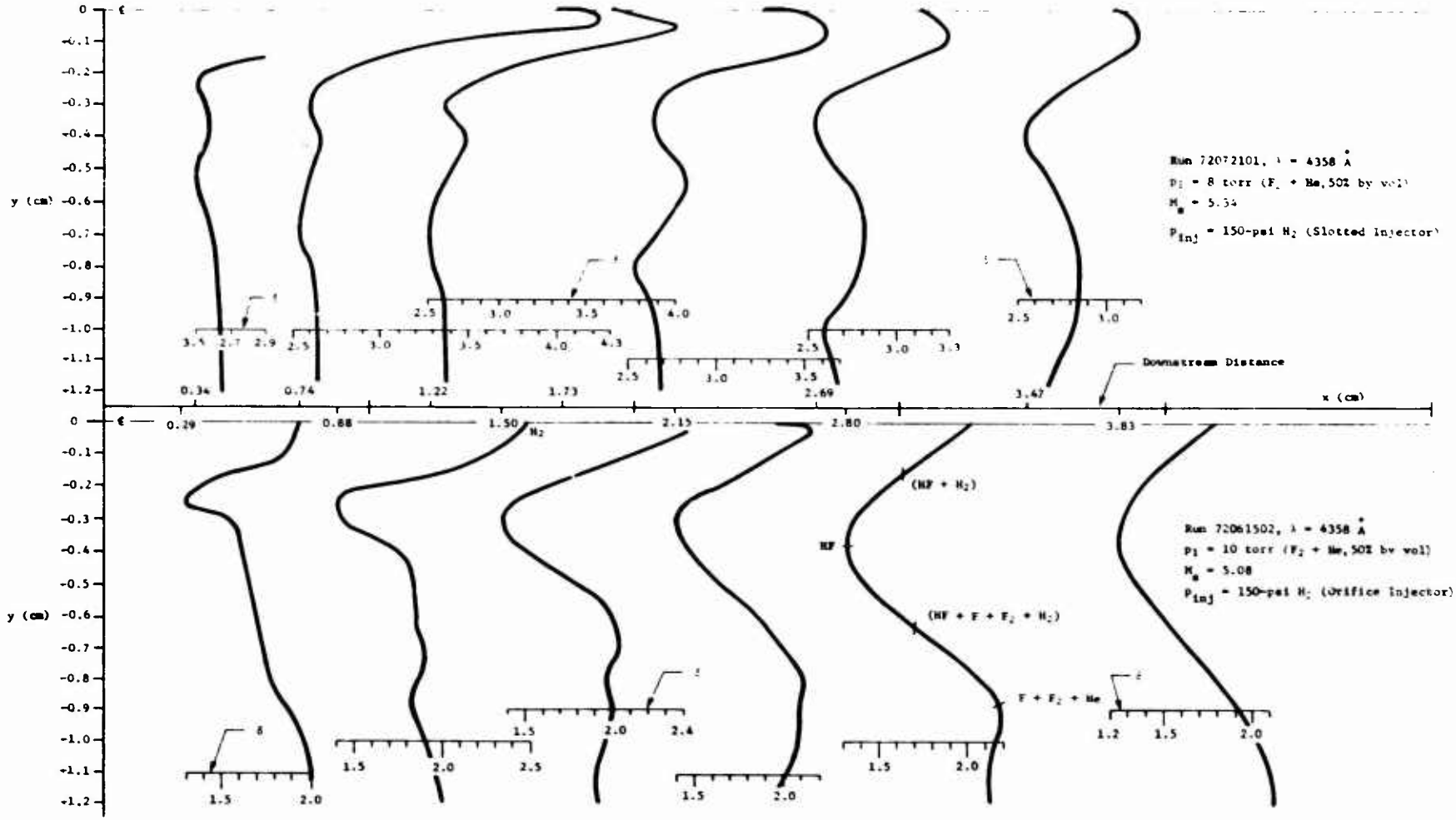

Figure 33. Interferometer Results, Runs 72072101 and 72061502

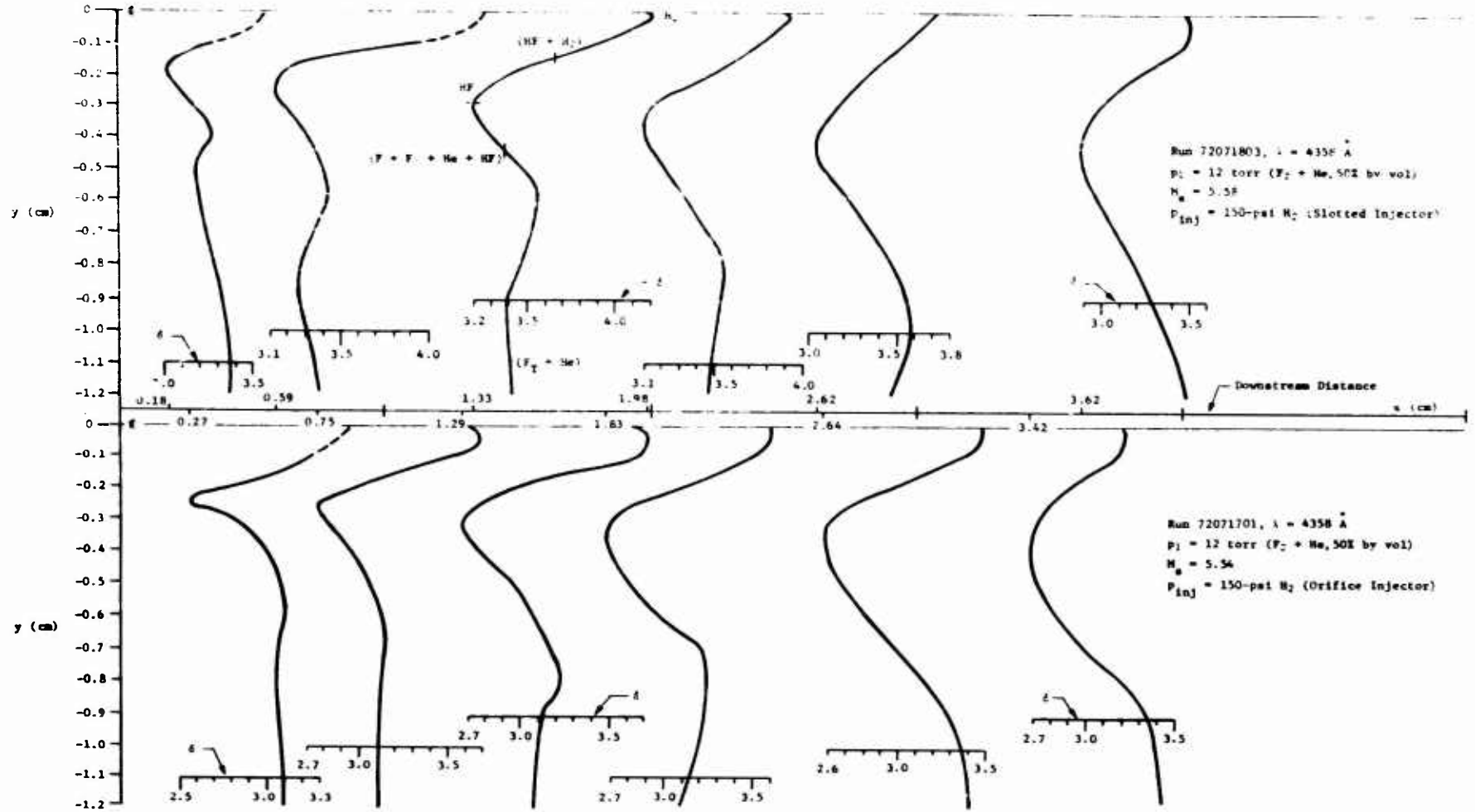

Figure 34. Interferometer Results, Runs 72071803 and 72071701

for identical test section conditions using the orifice and slotted H_2 injector splitter plates. Again the reader is reminded that the maximum value of fringe shift (δ) corresponds to the maximum total density level. The results presented in Figure 33 were taken from the interferograms that were presented and discussed in connection with Figures 30a and 31a. The first point to note here is that the fringe-shift profiles are presented for only one half of the mixing region, as the injection mixing experiments are symmetrical about the plane of the injection ports. The nominal designed test section static pressures in Figures 32, 33, and 34 are 5, 10, and 15 torr, respectively, and, as indicated in each of these figures, the maximum fringe shift occurs along the centerline. This indicates that the peak density always occurs along a plane containing the injection ports. The reduction in fringe shift along this centerline plane moving downstream from the splitter plate indicates that the peak density is gradually decaying as the diffusive mixing increases. Another important feature apparent in Figures 32, 33, and 34 is the increase in total fringe shift in the undisturbed region, indicative of the increase in test section static pressure. This effect is expected because the absolute fringe shift is a measure of the density change and each of these fringe shifts is referenced to an initially evacuated test chamber. Before proceeding with a discussion of these results in terms of number density profiles, we will next present comparison fringe-shift results for the 50-psi hydrogen injection and the 150-psi hydrogen injection experiments.

Figure 35 shows the fringe-shift profiles from 12 of the experimental runs given in Tables V and VI. Each of the a through f segments of Figure 35 contains comparable fringe-shift profiles showing the difference between 150- and 50-psi hydrogen injection for a given set of test section conditions. Figures 34a, b, and c are results for the slotted injection splitter plate for nominal test section static pressures of 5, 10, and 15 torr, respectively, while the c, d, and e segments of Figure 35 are results for the orifice injector splitter plate at 5, 10, and 15 torr, respectively. The most obvious feature in this comparison is that the downstream influence of the 50-psi hydrogen injection is decreased as compared with the 150-psi injection. That is, the fringe distortion decreases faster for the lower injection pressure and for the 5-torr static pressure cases (Figures 35a and d); the measurable effect of the 50-psi injection does not extend beyond 1.8 cm downstream of the injection point, while, for the 150-psi case, this effect can still be measured up to 3.5 cm downstream of the injection point. The other noticeable effect here is that the overall widths of the mixing regions for the orifice injection cases are generally

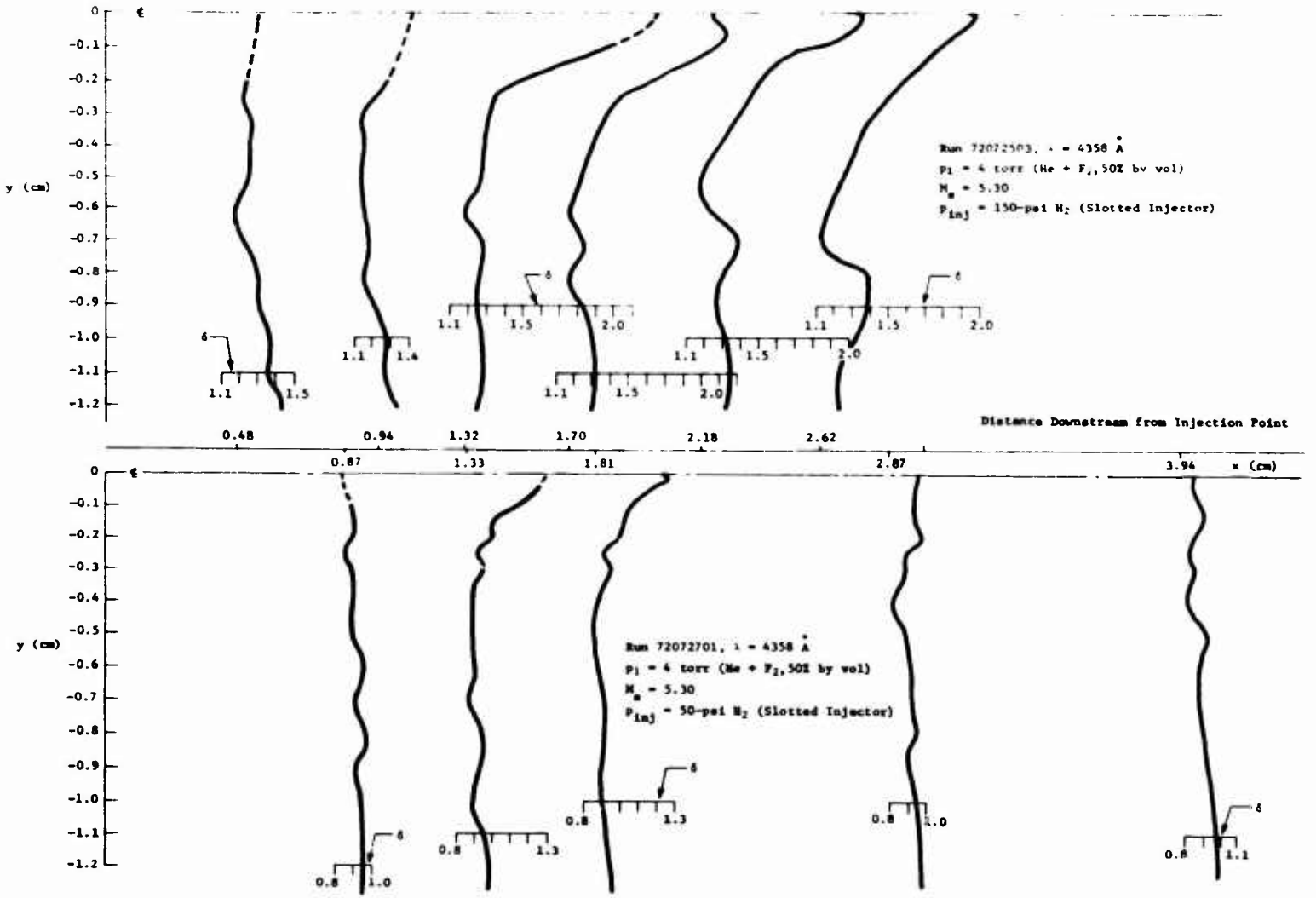

Figure 35a. Comparison of Fringe-Shift Profiles for 150- and 50-psi Slotted H_2 Injection at 5 Torr

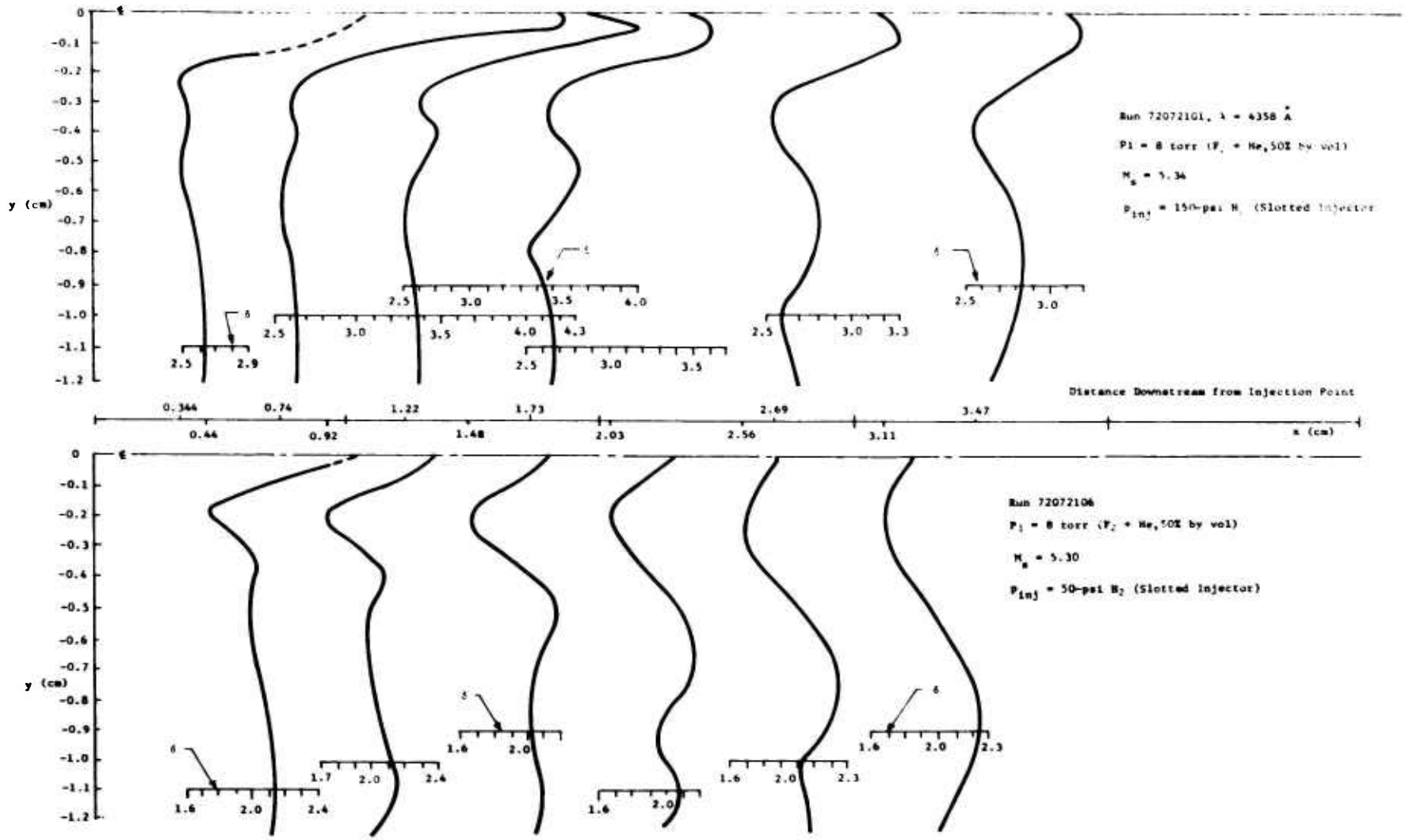

Figure 35b. Comparison of Fringe-Shift Profiles for 150- and 50-psi Slotted H_2 Injection at 8 Torr

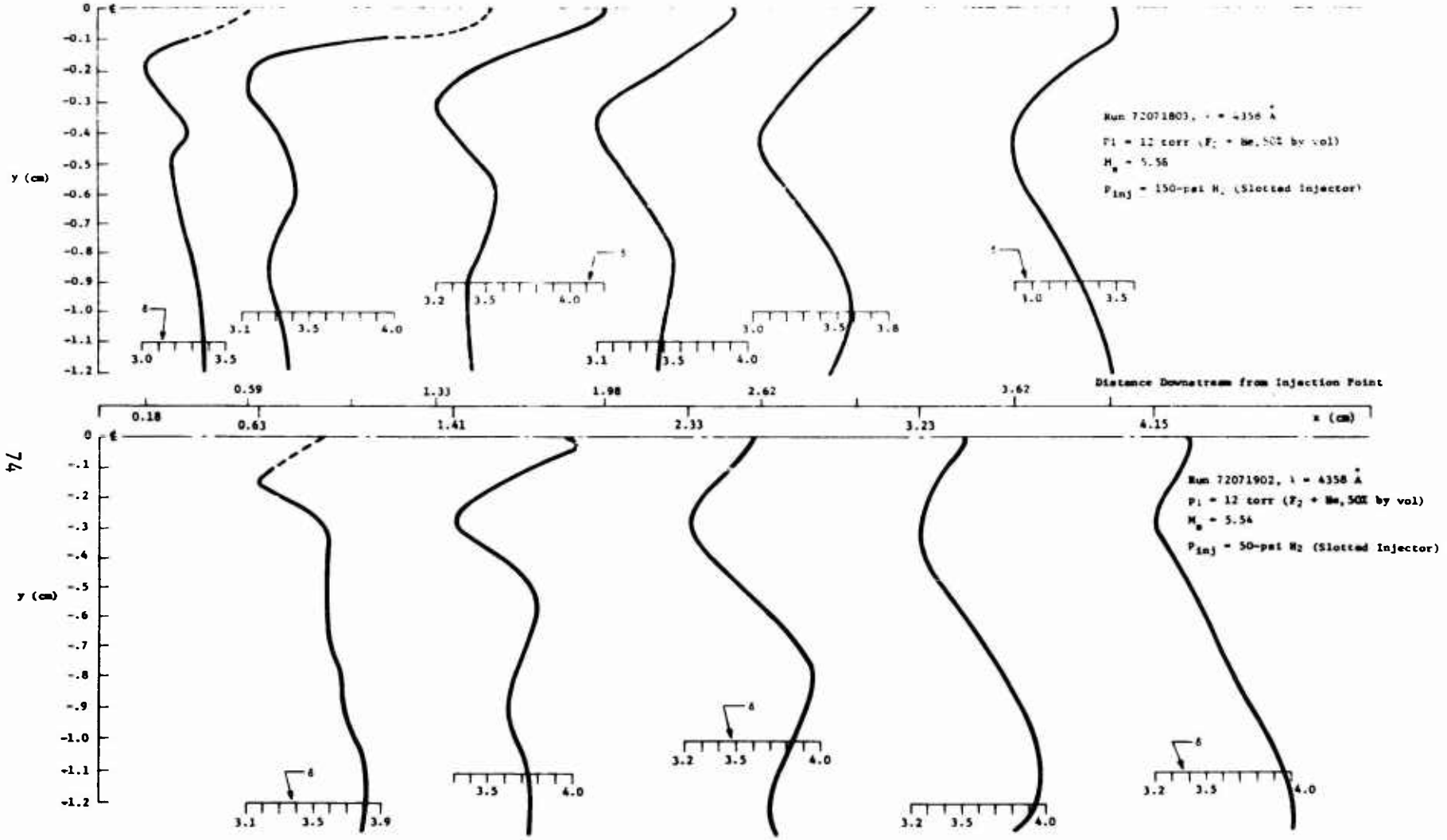

Figure 35c. Comparison of Fringe-Shift Profiles for 150- and 50-psi Slotted H_2 Injection at 12 Torr

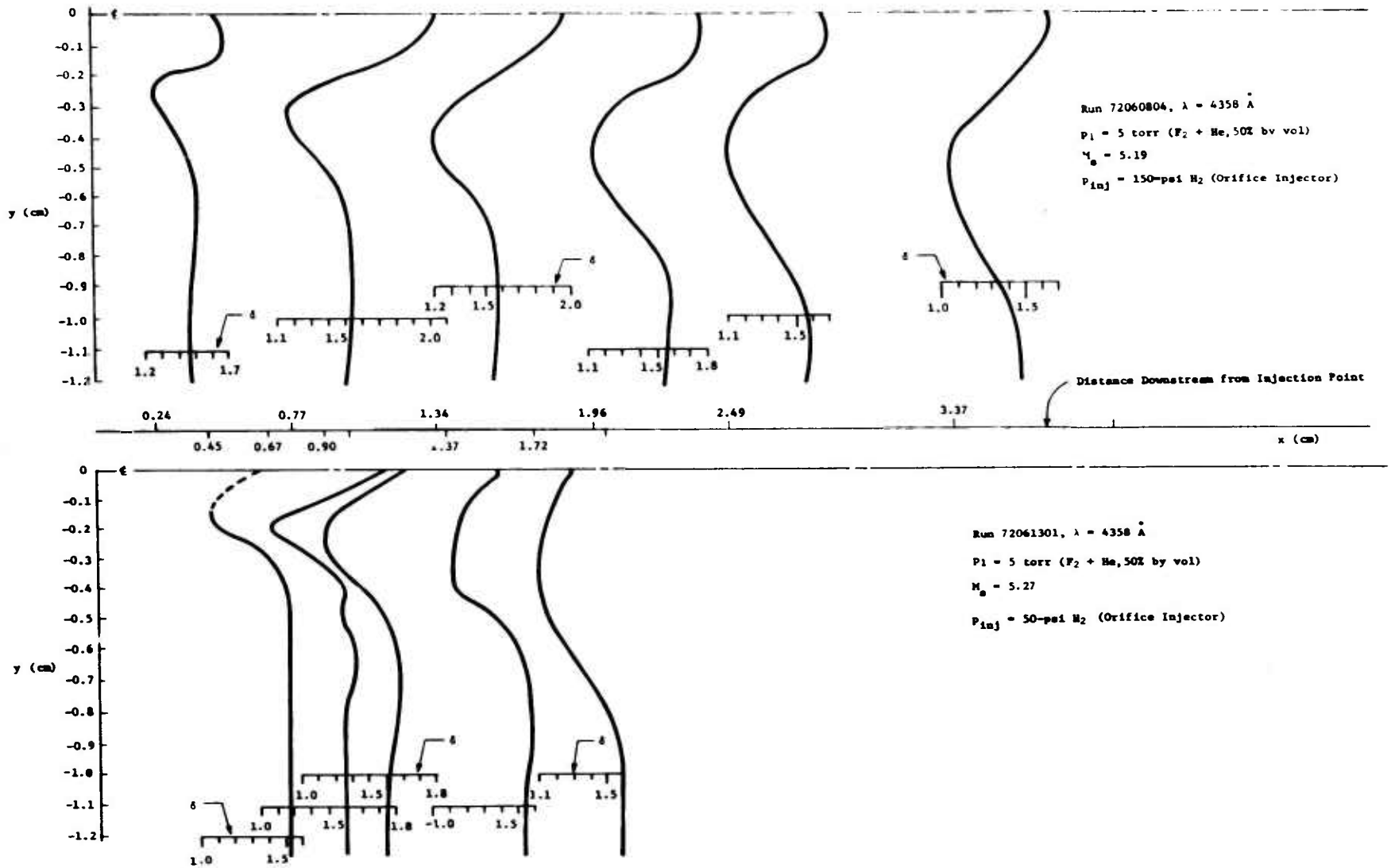

Figure 35d. Comparison of Fringe-Shift Profiles for 150- and 50-psi Orifice H_2 Injection at 5 Torr

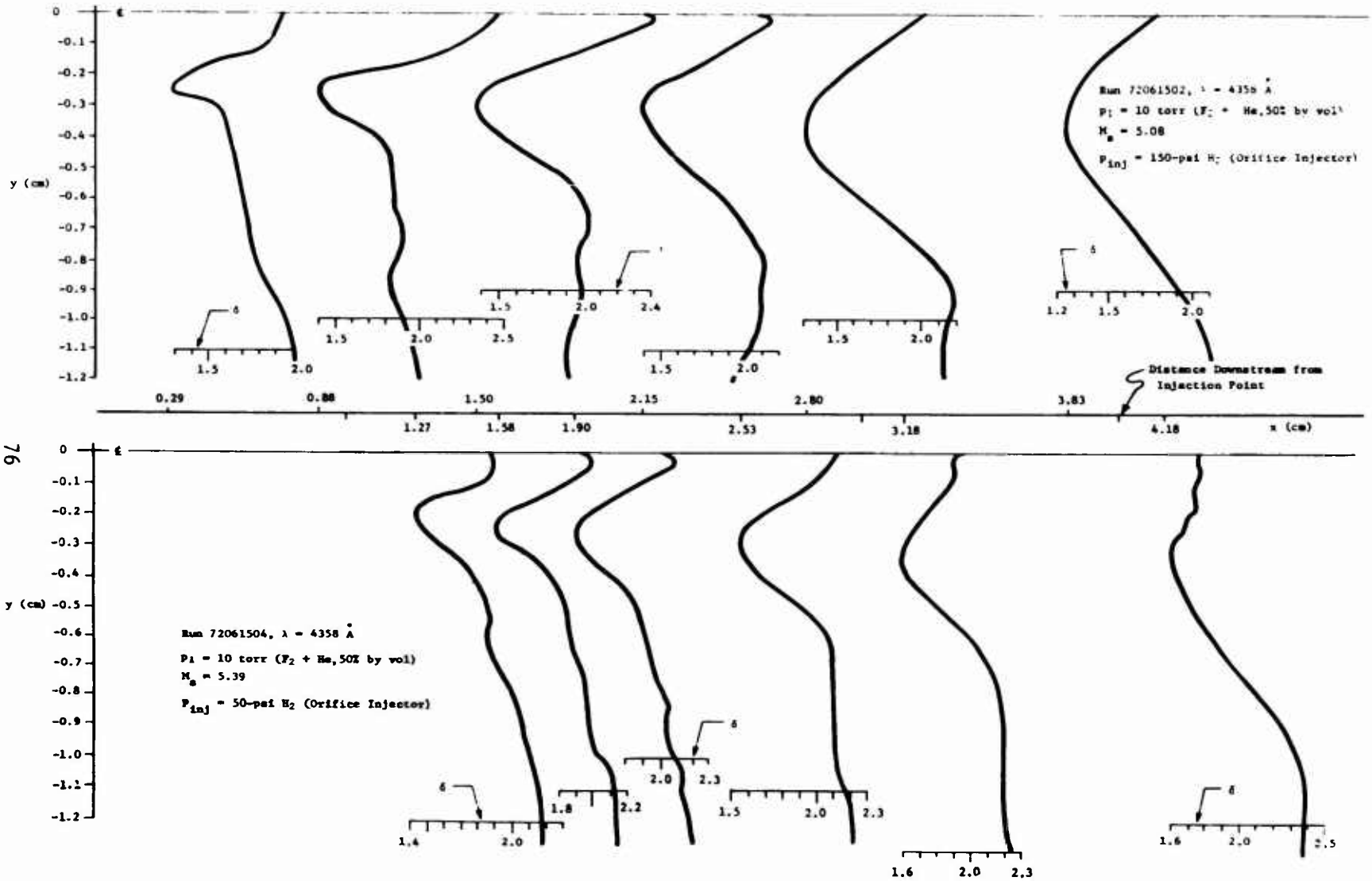

Figure 35e. Comparison of Fringe-Shift Profiles for 150- and 50-psi Orifice H_2 Injection at 10 Torr

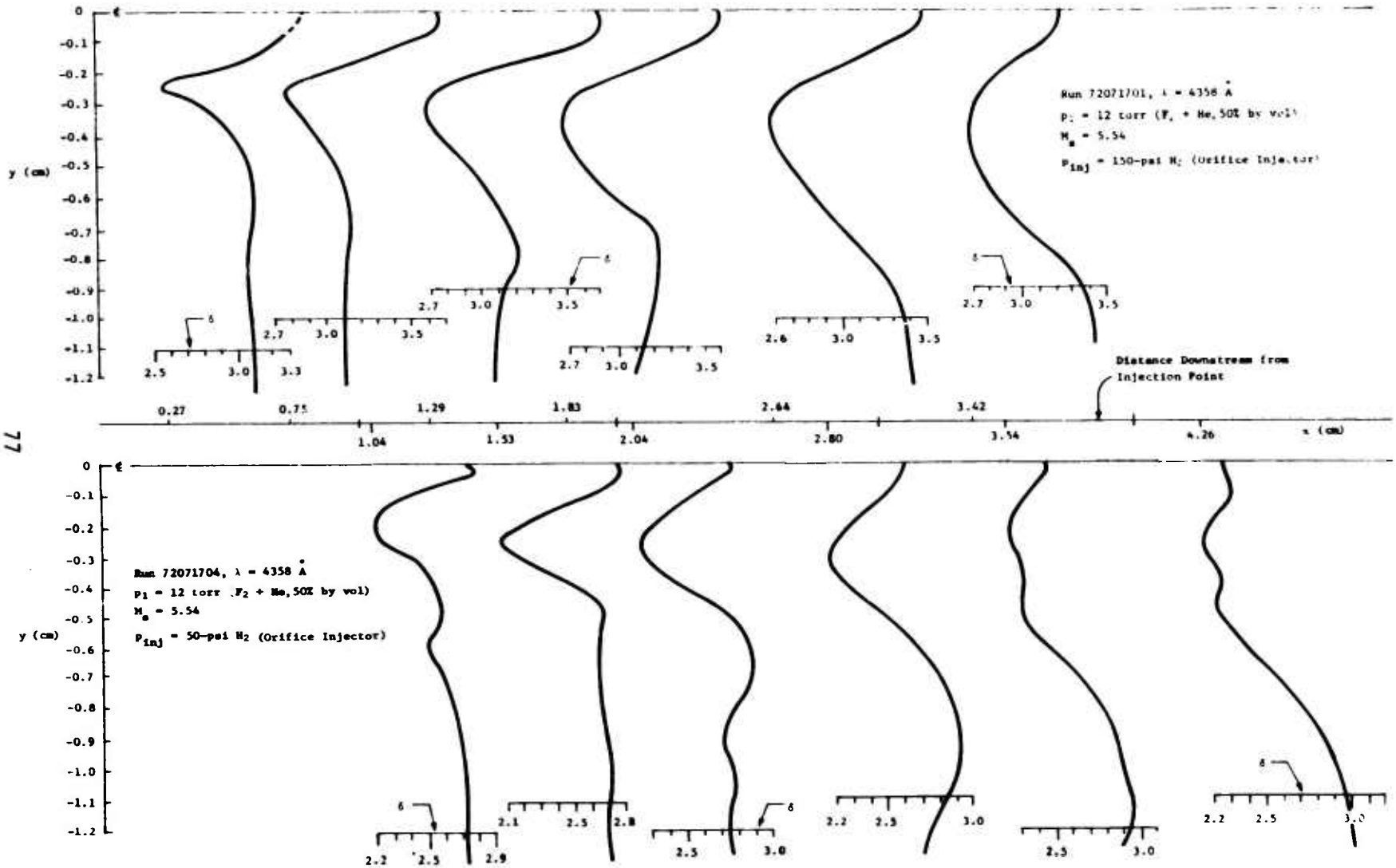

Figure 35f. Comparison of Fringe-Shift Profiles for 150- and 50-psi Orifice H_2 Injection at 12 Torr

slightly greater than the widths for the slotted injection cases. This effect is to be expected because the pluming of a two-dimensional sonic slot is less than that for a three-dimensional sonic orifice.

A quantitative measure of the reaction zone thickness can be obtained from the interferometric results by measuring the distance between fringe-shift minima at a fixed distance downstream from the point of hydrogen injection. Figure 36 shows the results obtained from the twelve interferograms recorded at three different injection pressures for the 10- and 15-torr nominal test section pressures with both the slotted and orifice injector schemes. As indicated in the inserted sketch, the thickness "d" is measured 1.5 cm downstream of the point of injection. As these results indicate, the mixing layer thickness increases with increased test section static pressure, and, for the orifice injection case, the mixing layer increases with increasing injection pressure. The mixing layer width for the slotted injection case increases only slightly with increasing injection pressure for the 15-torr test section pressure and shows an opposite trend for the 10-torr test section pressure.

Averaged density profiles have been computed at three different downstream stations for four of the hydrogen injection mixing cases. Two slotted and two orifice injection runs with 50- and 150-psi injection, respectively, were chosen as representative for this comparison. As explained in Section II, it was impossible to compute species number densities with the multiple wavelength technique; hence, to accomplish this objective, it was necessary to make certain assumptions in this procedure. Figure 37 shows a typical fringe-shift profile and an indication of the assumptions that were made in this data reduction procedure. That is, it was assumed that the fringe shift along the centerline plane was due to hydrogen molecules; the minimum fringe shift within the mixing layer was due solely to hydrogen-fluoride molecules; the fringe shift within the nozzle exit region (external to the mixing layer) was due to the combined contribution of fluorine atoms, fluorine molecules, and helium; and the fringe shift at intermediate points was due to an averaged value of the constituents. The averaged number density profiles presented for the four runs in Figure 38 were computed using the theoretical development of Section II and the curves are smoothed values computed with the assumptions listed above.

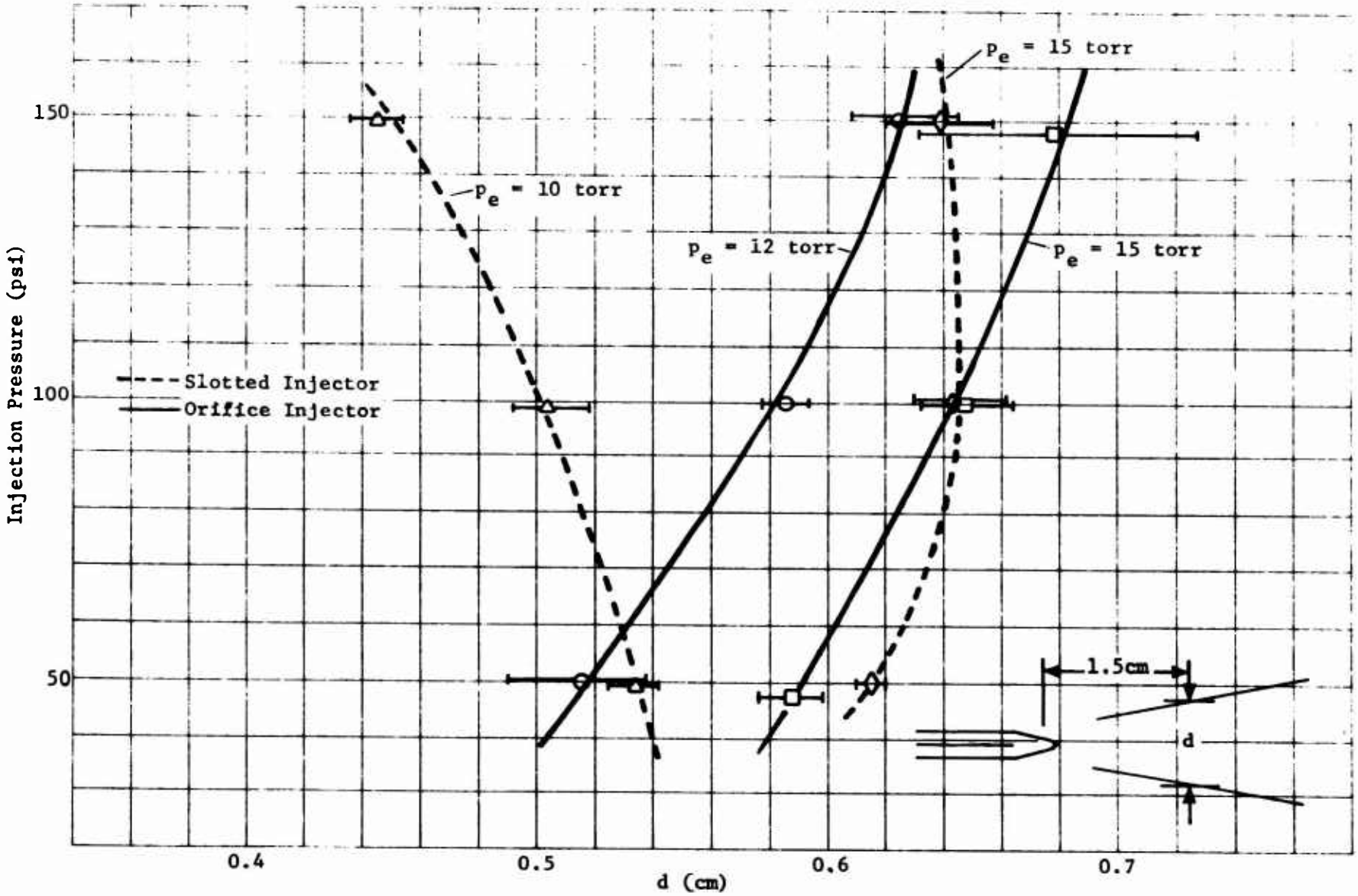

Figure 36 Mixing Layer Width vs Injection Pressure

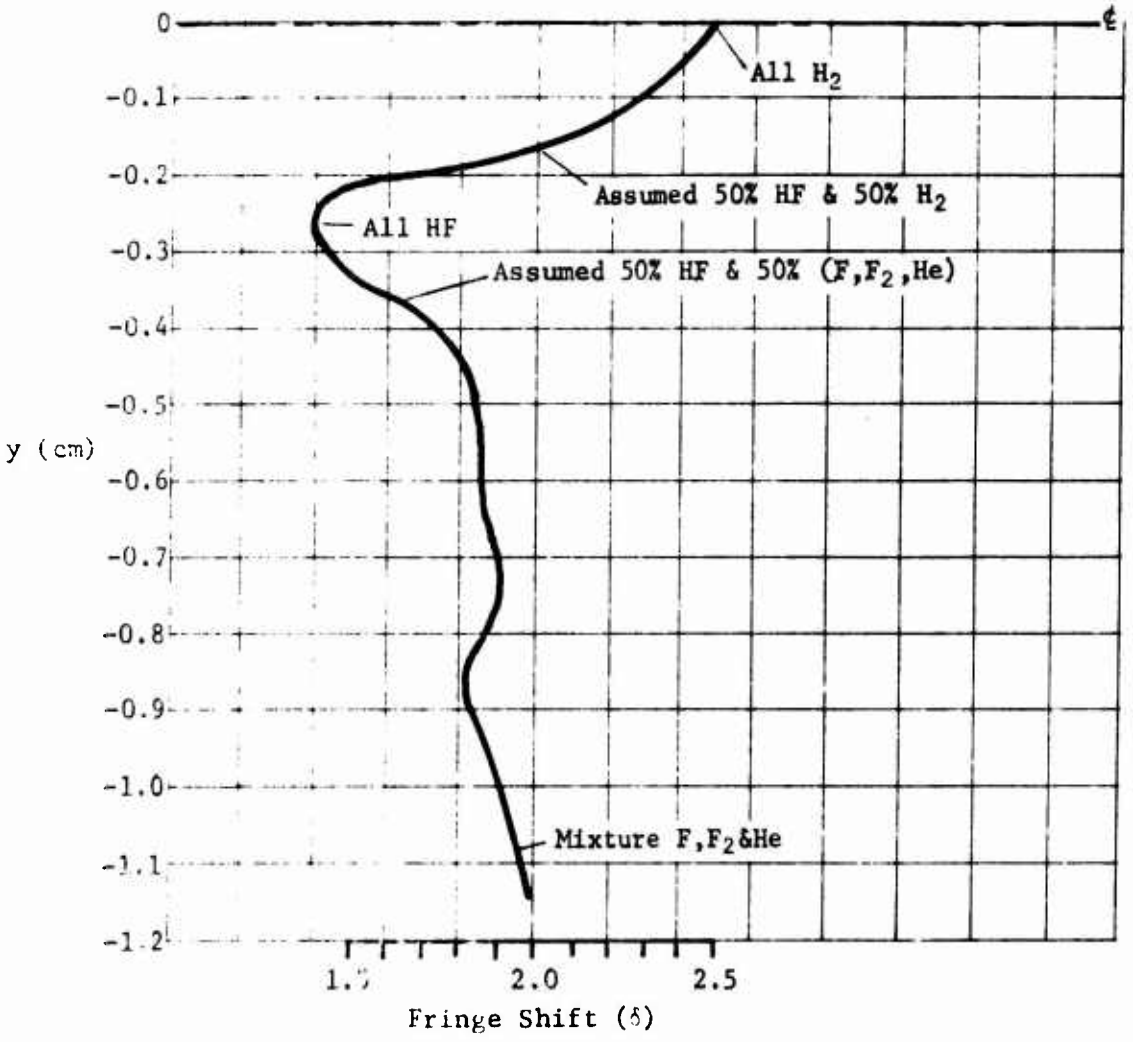

Figure 37 Typical Fringe Shift Showing Assumed Species Distribution Used for Computing Averaged Number Densities

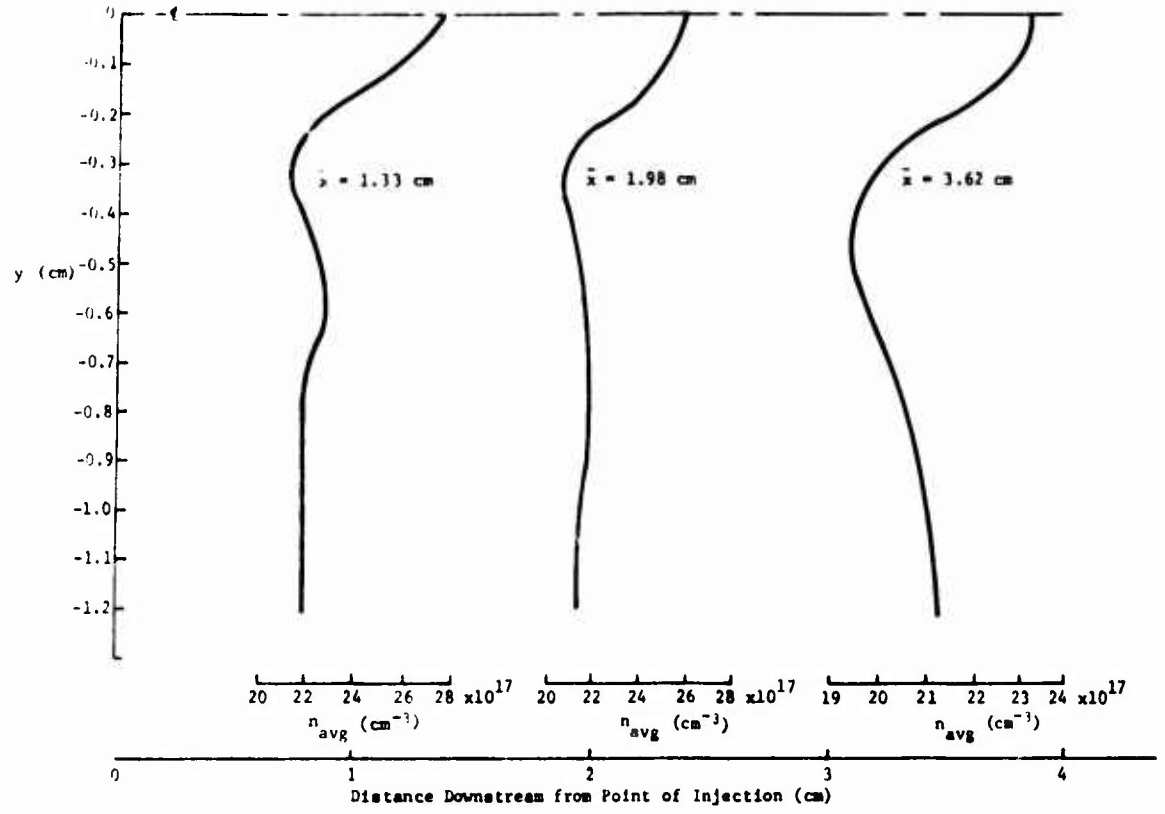

a. 150-psi Slotted H_2 Injection

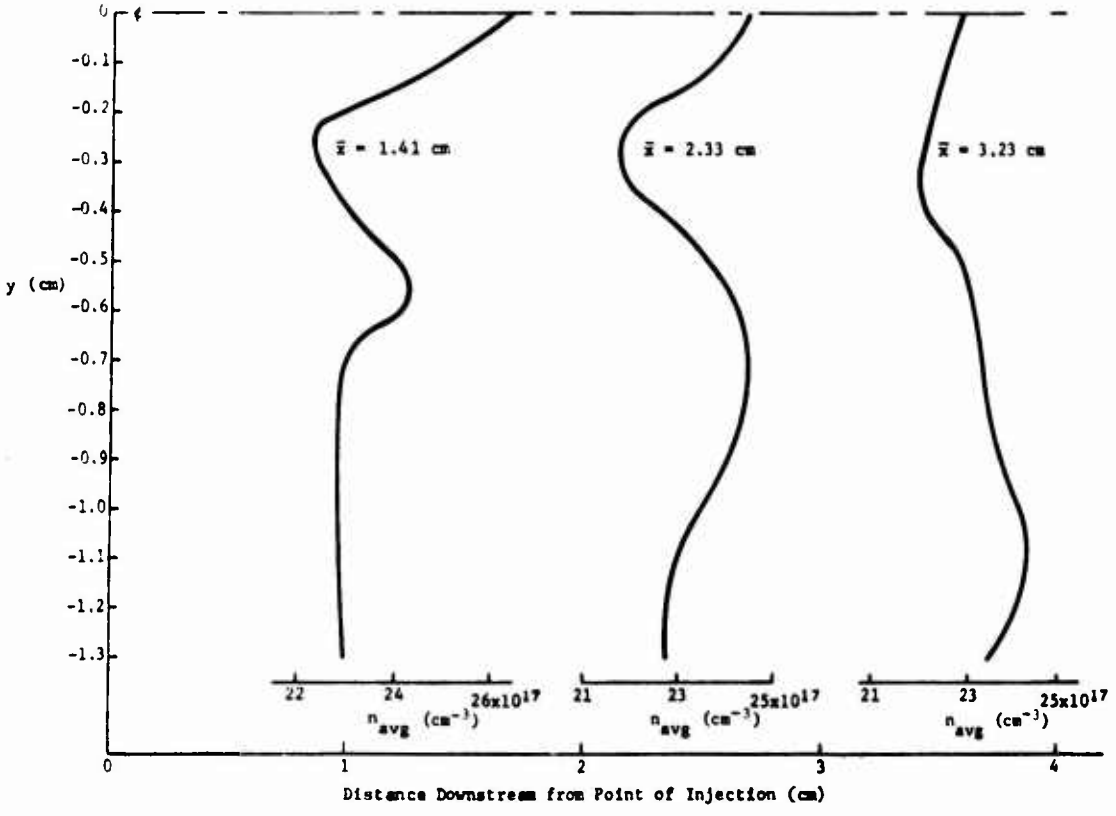

b. 50-psi Slotted H_2 Injection

Figure 38. Averaged Values for Number Density Distributions for Selected Injection Mixing Cases

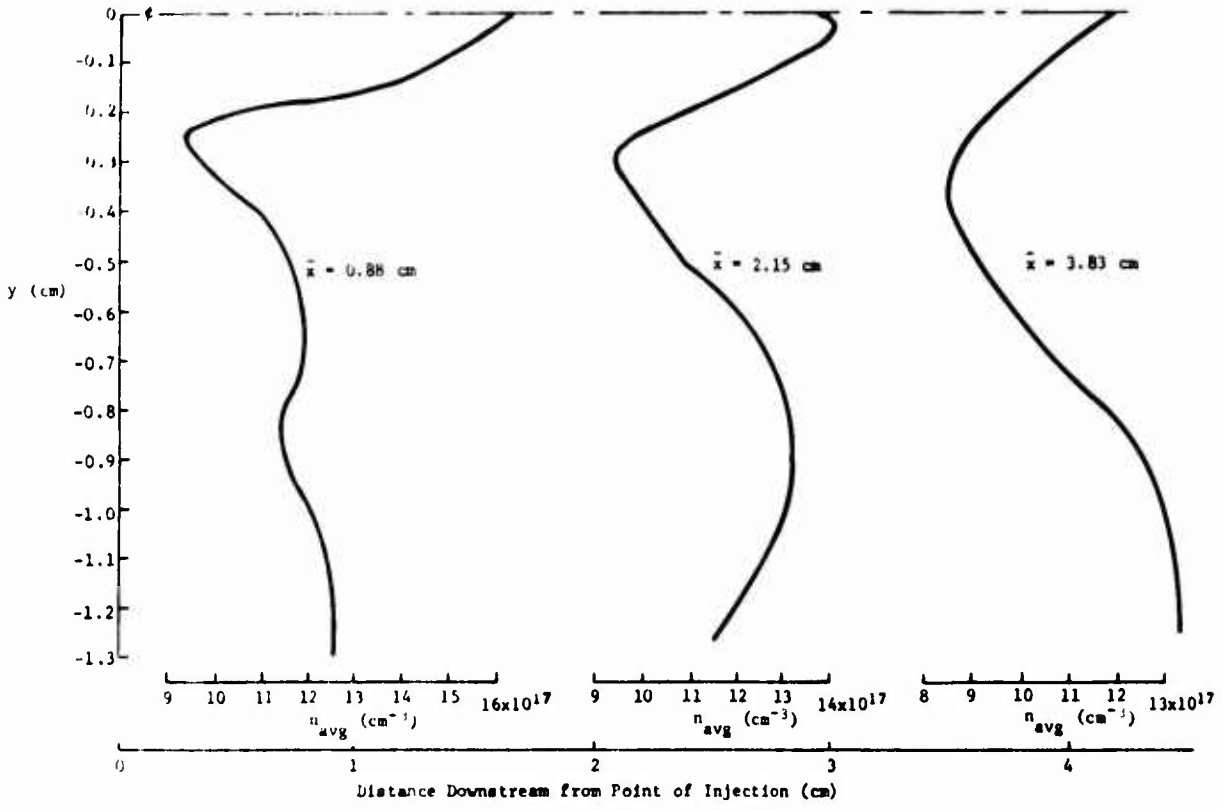

c. 150-psi Orifice H_2 Injection

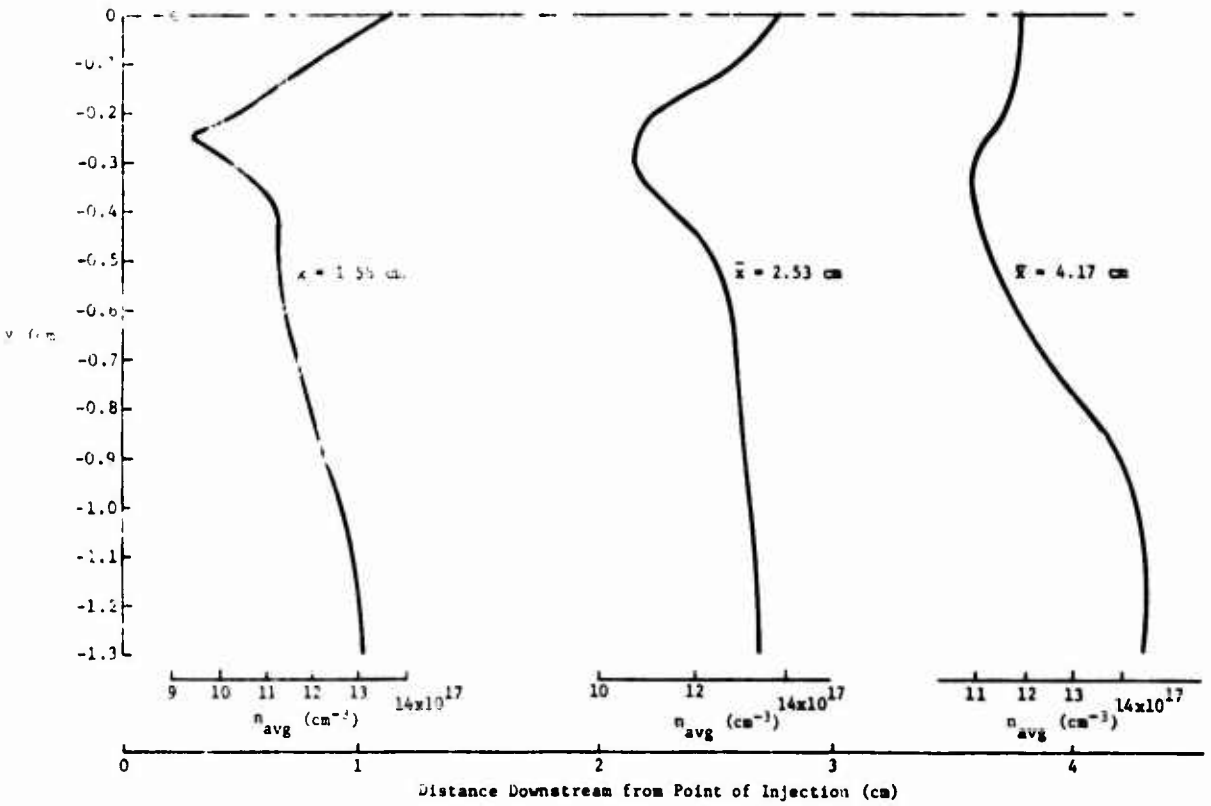

d. 50-psi Orifice H_2 Injection

Figure 38. Averaged Values for Number Density Distributions for Selected Injection Mixing Cases (concl)

As the profiles of Figure 38 indicate, the hydrogen number density moving downstream along the plane of injection decreases, thus indicating an increase in the diffusive mixing of the hydrogen. A comparison between the slotted hydrogen injection and the orifice hydrogen injection also shows the higher number densities along the centerline for the slotted injection scheme. This is an indication of the fact that the mass flow through the slotted injector was greater (by a factor of 2) than that through the orifice injector. The HF number densities (minimum values in each of these profiles) are almost identical for each of the different injection pressures, but differ again by roughly a factor of two between the slotted and the orifice cases. The fact that the HF number densities for the different injection pressures are almost identical is also shown in the infrared emission results that will be presented later.

b. Parallel Mixing - To examine the resulting chemically reacting mixing region, the buffer-driven, split shock tube/shock tunnel facility described in Section II was used to generate two adjacent parallel supersonic streams. The data to be presented in this discussion were all taken in that facility under a variety of conditions designed to increase understanding of the influence of the exothermic chemical reaction on the diffusive mixing regions under conditions closely simulating the large continuous-flow HF chemical laser devices. Table VII is a complete listing of the interferometric records obtained in this effort. Specific experimental results presented later in this discussion can be identified in more detail by referring to the run code numbers, which are shown with the results in Table VII.

Three interferograms for the parallel mixing cases are shown in Figure 39. These particular records were chosen because they represent extreme flow-field variations between the hydrogen carrying stream and the fluorine carrying stream. Figure 39a shows a case in which the experimentally measured nozzle exit static pressures are very nearly matched. Note that the design nozzle exit static pressures and the measured nozzle exit pressures are in considerable disagreement. This point has been discussed in Section II. In this record, a fringe bending away from the nozzle wall end indicates a decrease in average density compared to the undisturbed freestream density. The record of Figure 39a clearly indicates that the average density just downstream of the splitter plate is much less than the density in both of the nozzle exits. Proceeding further downstream in the mixing layer, this density profile tends to smooth out, and a very weak pressure adjustment wave is clearly visible on the F_2 + He nozzle side.

Table VII

PARALLEL MIXING INTERFEROGRAM SUMMARY (ALL MIXTURES 50% BY VOLUME)

Run No.	p_1	p_1	M_s	M_s	Calculated Results										Experimental		Calculated	
	H_2+A	F_2+He	H_2+A	F_2+He	p_e	p_e	α_{F_2}	T_e	T_e	V_e	V_e	P_5	P_5	ΔV,	p_e	p_e	Re_e	Re_e
					H_2+A,	F_2+He,	F_2+He,	H_2+A,	F_2+He,	H_2+A,	F_2+He,	H_2+A,	F_2+He,		H_2+A,	F_2+He,	H_2+A	F_2+He
	torr	torr			torr	torr	%	°K	°K	fps	fps	atm	atm	fps	torr	torr		
72091301	20	20	4.25	4.48	6.56	19.44	51	450.9	264	8436	6716	3.19	5.42	1720	48.10	46.47	116	146
72110901	20	10	4.38	5.01	7.04	14.63	72	476	250	8669	7119	3.42	4.01	1550	48.1	41.0	116	125
72110902	17.5	6	4.57	5.42	6.60	10.13	89	516	242	9022	7545	3.26	3.21	1477	48.1	40.0	107	85
72110903	20	6	4.46	5.42	7.351	10.13	89	495	242	8792	7545	3.64	3.21	1247	48.9	34.0	116	85
72111401	10	5	4.10	4.68	8.62	6.45	63	420	241	8136	6660	1.46	1.60	1476			140	88
72111402	8	3	4.38	5.08	8.24	5.70	77	475	235	8661	7053	1.36	1.31	1608			125	82
72111403	10	3	4.20	5.01	9.24	5.68	75	440	230	8333	38	1.54	1.23	1345			139	83
	H_2	F_2+He	H_2	F_2+He	H_2	F_2+He	F_2+He	H_2	F_2+He	H_2	F_2+He	H_2	F_2+He		H_2	F_2+He	H_2	F_2+He
72111602	85	20	2.08	4.32	5.32	19.65	46	159	264	13920	6530	1.90	4.54	7390			107	148
	He+A	F_2+He	He+A	F_2+He	He+A	F_2+He	F_2+He	He+A	F_2+He	He+A	F_2+He	He+A	F_2+He		He+A	F_2+He	He+A	F_2+He
72111303	16.5	6	4.68	5.46	3.56	10.5	91	367	243	2618	7677	2.92	2.86	5059			53	102

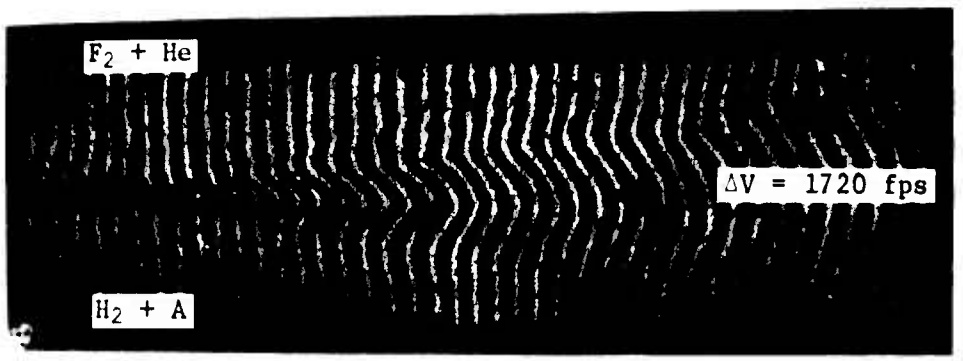

a) Run 72091301

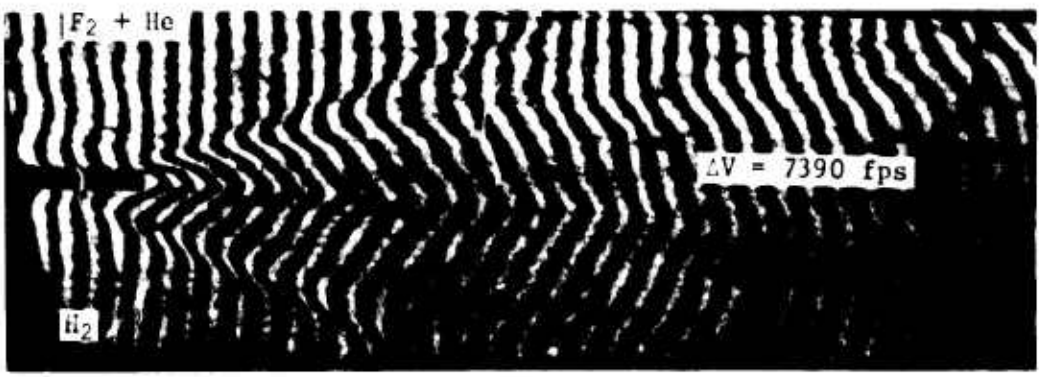

b) Run 72111602

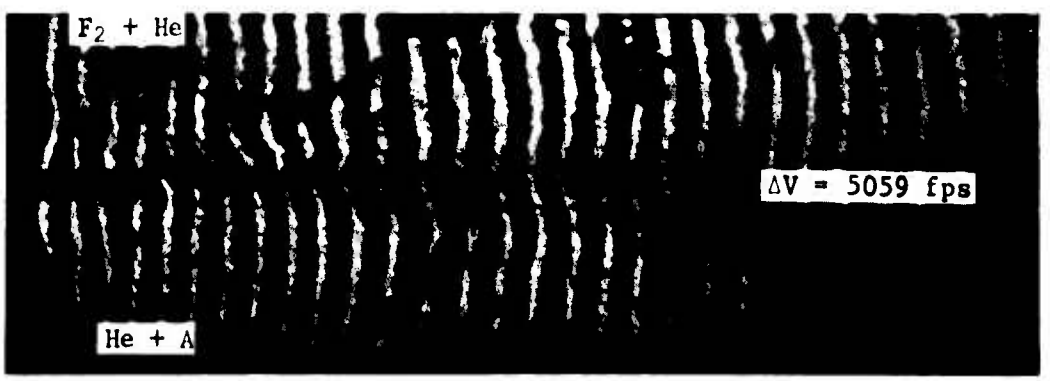

c) Run 72111303

Figure 39. Comparison of Parallel Mixing Interferograms

Figure 39c is a run with conditions close to those of the run presented in Figure 39a, except that the hydrogen has been replaced by helium. This interferogram is then a representation of the mixing region without the chemical reaction effects. It is quite clear from a comparison of these two cases that the chemical reaction does indeed markedly modify the mixing region both in extent and overall density profiles.

Figure 39b shows the results for a mixing layer in which pure hydrogen is used as a supply for one of the nozzles. In this record, the pressure adjustment waves are very clear, and it would appear that much more combustion is now occurring. These general remarks will be extended and explained in more detail in Section V, where the detailed results of the parallel mixing interferometric data are compared with the theoretical results of the mixing code to be described in Section IV.

The data from these interferograms were reduced in the same manner as described for the injection mixing, except that, in this situation, there will never be a plane of symmetry, and thus the entire record must be reduced. This data reduction has been accomplished for all shots listed in Table VII and the fringe-shift profiles for six of the cases are presented in Figures 40, 41, and 42.

The reduced interferometric results presented in Figure 40 correspond to the three interferograms in Figure 39. These results are plotted with a common downstream axis and individual fringe-shift profiles at various distances downstream from the common nozzle end wall. Additional details of the flow-field conditions can be obtained by referring to Table VII and the run code number.

The fringe distortion for run 72091301 occurs primarily in the wake region downstream of the common nozzle end wall. Moving downstream to approximately 3 cm, this distortion has almost completely disappeared. We tentatively identify this result as indicating that no appreciable reaction has occurred in this case. The fringe-shift profiles for run 72111602, where a large ΔV between the two streams and pure hydrogen are used, do indicate that a strong reaction has occurred, as shown by the large fringe distortion in the center region.

The fringe-shift profiles for six additional parallel mixing experiments are shown in Figures 41 and 42. The most important aspect of the results for these six cases is that there is only limited apparent reaction occurring. This conclusion is based on a

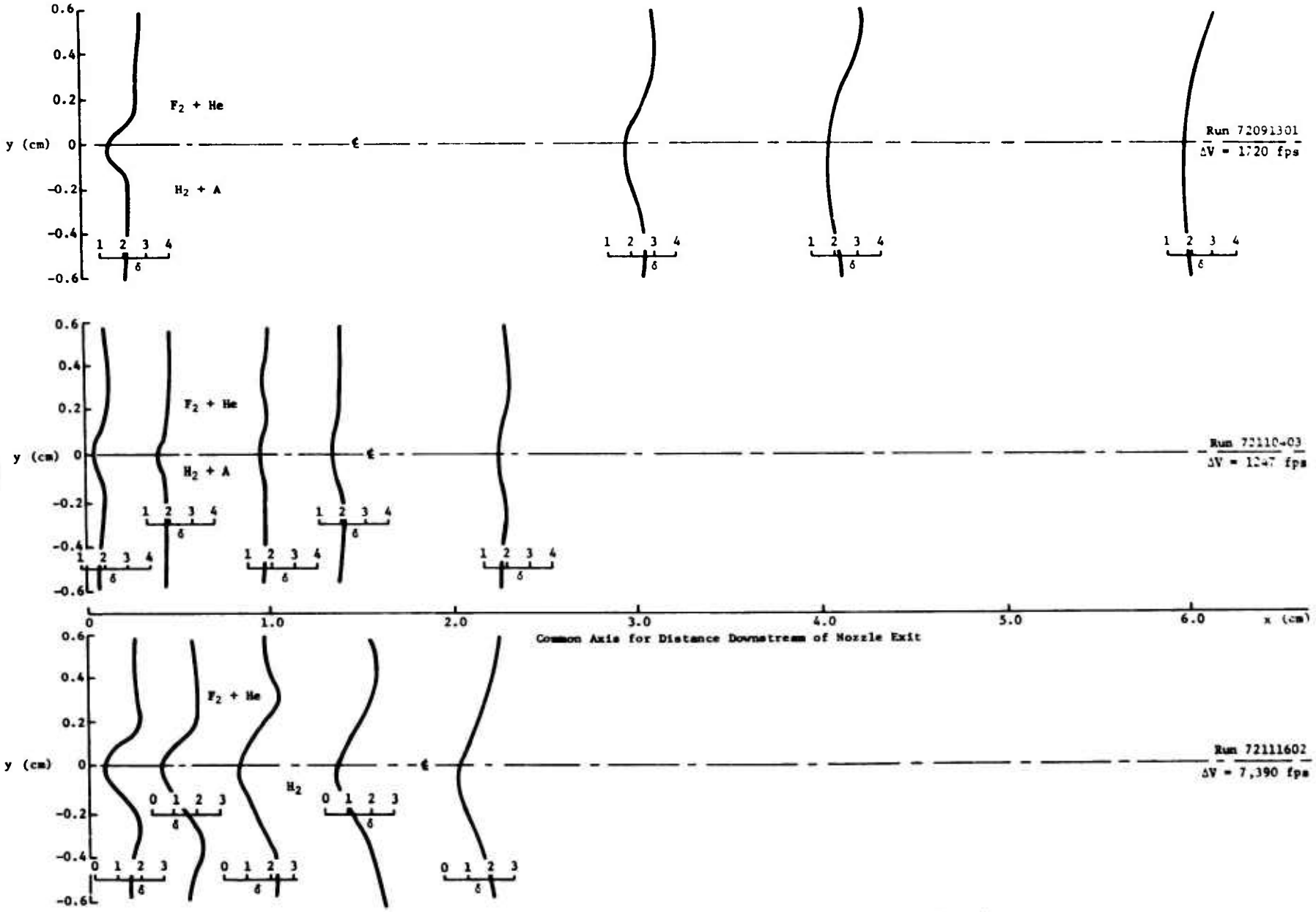

Figure 40. Comparison of Fringe-Shift Profiles for Three Parallel Mixing Experiments

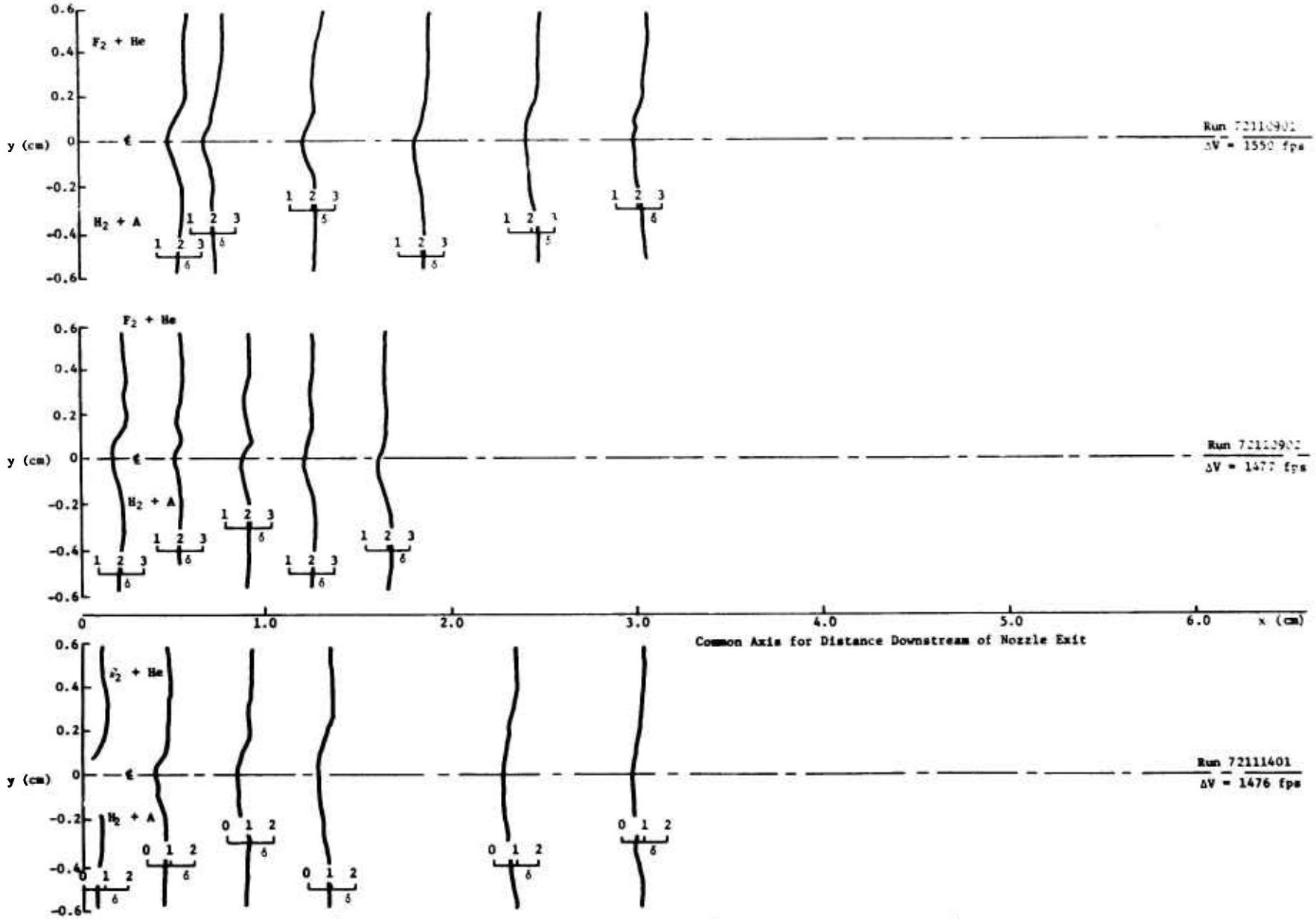

Figure 41. Comparison of Fringe-Shift Profiles for Three Parallel Mixing Experiments

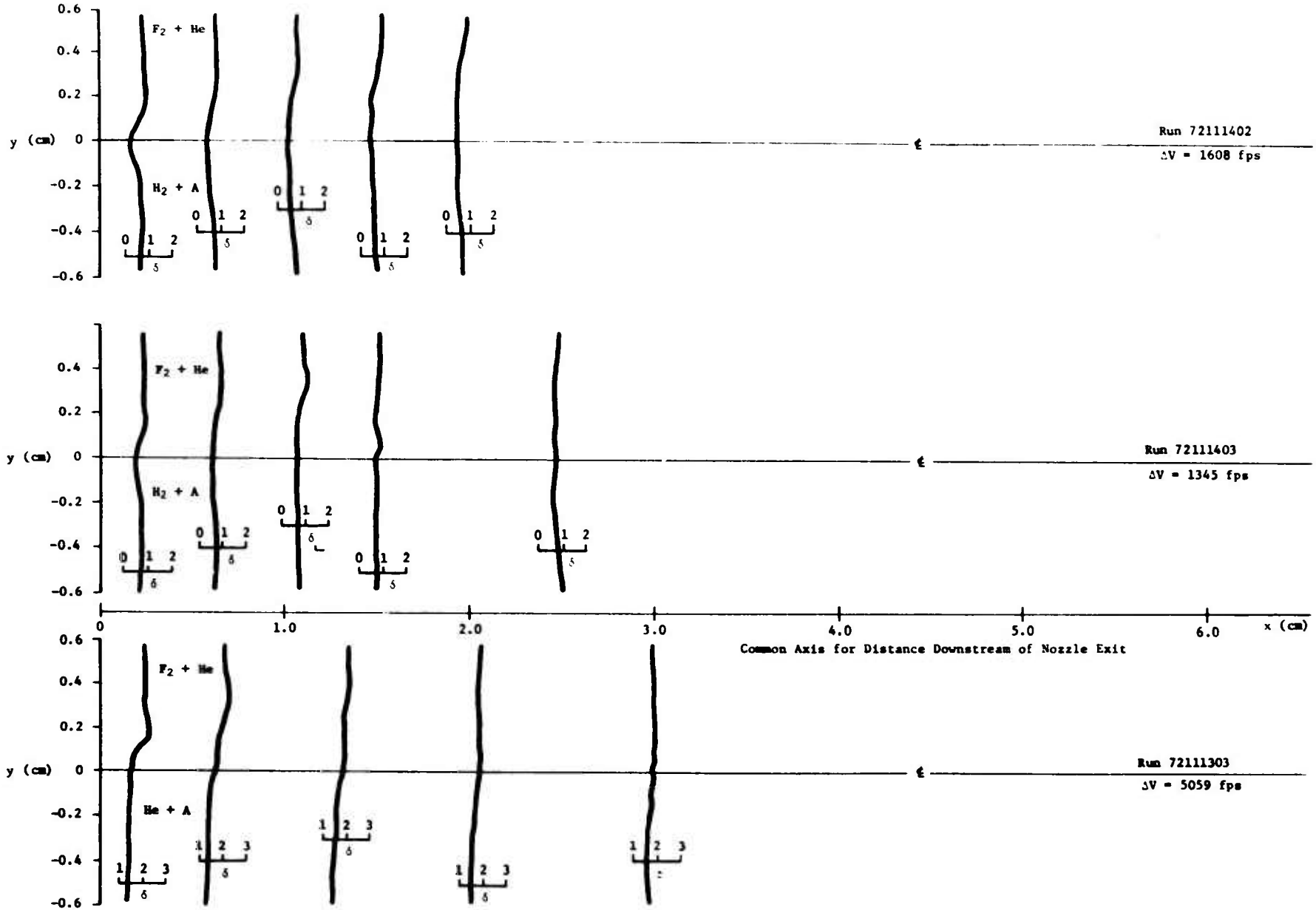

Figure 42. Comparison of Fringe-Shift Profiles for Three Parallel Mixing Experiments

comparison of the first five cases with the results for the case (run 72111303) where helium replaces hydrogen in the initial test gas mixture. That is, all the results in Figure 41 and 42 are essentially identical and, since one of these cases is clearly a nonreacting case, it would appear that only limited reaction could be occurring in either of the other experiments. Additional comments and comparisons of the parallel mixing experimental results with theoretical prediction will be presented in Section V.

2. SUMMARY OF RAPID-SCAN RESULTS

A rapid scanning infrared spectrometer was used in both the injection and parallel mixing facilities to monitor the radiation emission from excited HF molecules created in the mixing layer. The 12-mm-long spectrometer entrance slit was focused at the centerline span of the test section with a magnification factor of unity. Slit widths of 0.5 and 1 mm were used in various experiments. To eliminate the absorption characteristic of quartz, a sapphire window was used for a viewing port with the spectrometer. The quartz test section windows used for the interferograms could not be used here because they contain water that absorbs radiation in the spectral region of interest.

In the injection mixing facility, a series of separate experiments, holding test section flow conditions essentially constant, were performed as the spectrometer was translated in a downstream direction moving away from the hydrogen injection ports. Figure 43 is an interferogram of the test conditions (run 72072101) for which an extensive series of infrared emission scans was recorded. The 12-mm field of view is shown superimposed over the mixing region. The slotted injector splitter plate was used in this series and 25 stations, varying from 0.318 cm to 7.62 cm downstream of the splitter plate edge, were observed.

The exact starting time for any given spectral scan could not be controlled in this experiment to within 1.25 msec due to the completely random starting signals derived from the incident shock wave. That is, the spectral scans can only be initiated when the corner-mirror rotating wheel is properly positioned, and this occurs every 1.25 msec. To ensure that a region of uniform flow was observed by the rapid scanning spectrometer, a separate time-resolved observation of the radiation emission was recorded using an indium antimonide detector in conjunction with a 2.7-μm narrow-bandpass filter. This detector was on the opposite side of the shock tunnel test section, facing the entrance slit of the spectrometer, with a view angle covering the entire mixing region. An oscilloscope

record of this 2.7-μm radiation is shown in the top trace of Figure 44, along with a time mark (lower trace) from the rapid scanning spectrometer that allows one to identify the particular scan recorded during the initial phase of the mixing. Each of the four time marks represents a scan from the spectrometer, with the left time mark corresponding to the lower trace in the radiation record of Figure 45. The marker placed on the second trace from the bottom of Figure 45 corresponds to the intensity versus wavelength record that is consistent with the most uniform flow time, as indicated in Figure 44. This particular infrared scan is considered in the data reduction.

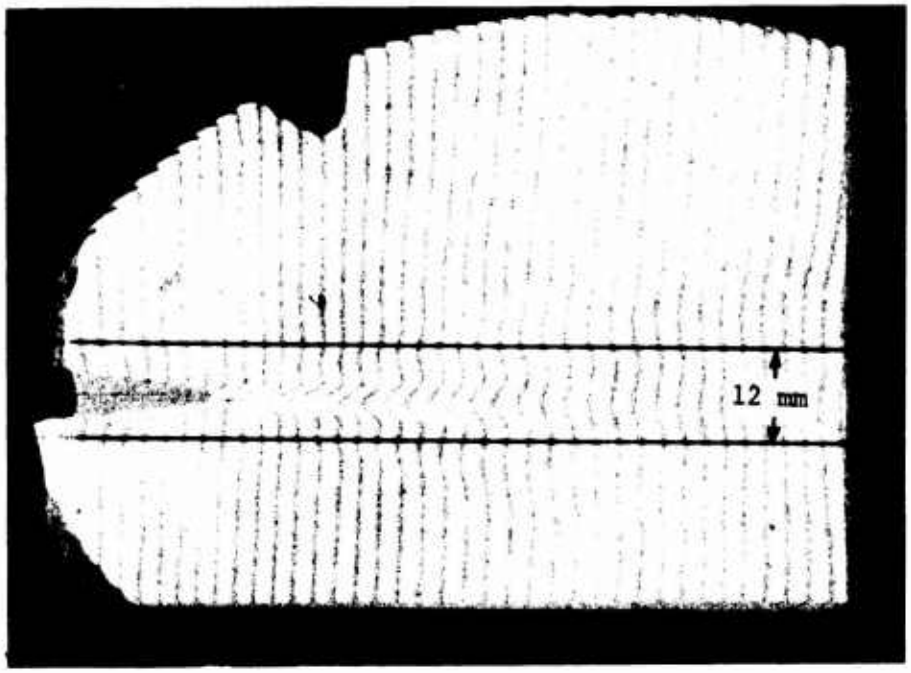

Figure 43. Run 72072101 Showing 12-mm Slit Height

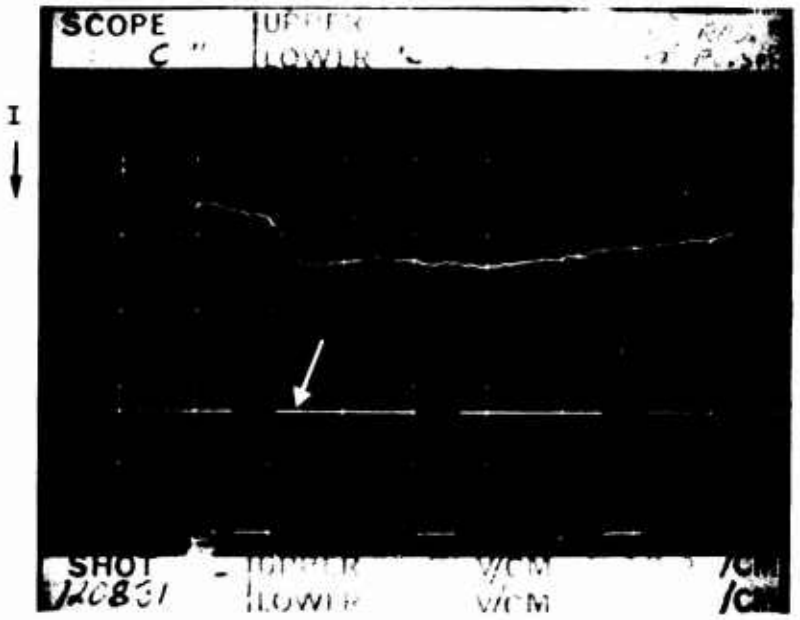

Figure 44. Total 2.7-μm Emission (Upper Trace) and Time Mark Indicating Duration of a Single Scan of the Spectrometer (Lower Trace)

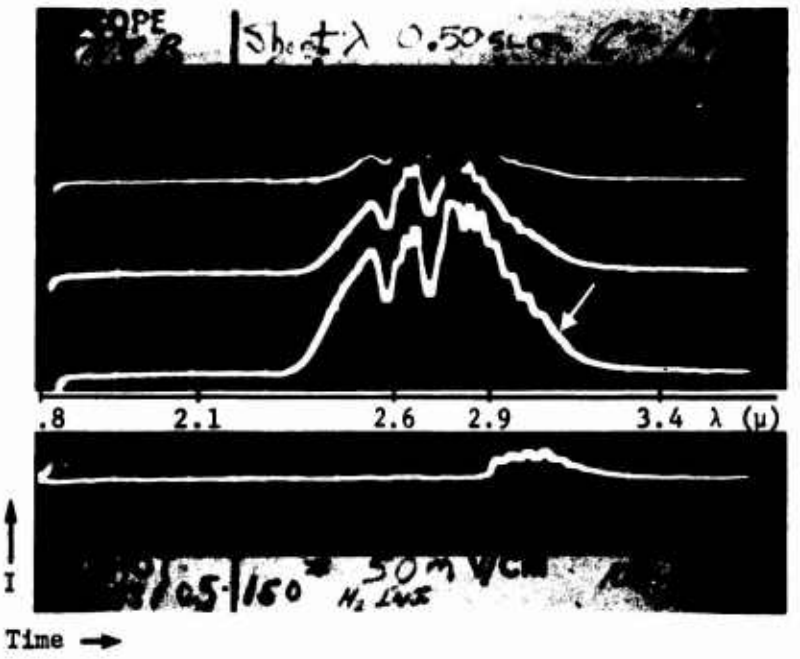

Figure 45. Rapid Scanning Infrared Spectrometer Traces

The radiation observed in Figure 45 is emitted chiefly from transitions in the 1-0 and 2-1 vibrational bands. The radiation from 2.5 to 3.1 μm consists of the overlapping P-branches of the two bands. The region below 2.6 μm consists of radiation from the partial overlap of the R-branches of the respective bands. Figure 46 is a schematic representation of an intensity-versus-wavelength plot of hydrogen fluoride for temperatures at which higher rotational states are populated. This would correspond to plume conditions where combustion takes place. The spectrometer thus measures a composite of the radiation from several bands. There undoubtedly is some radiation contributed by the 3-2 band; however, the third vibrational level is not likely to be highly populated for present test conditions.

As a standard or figure of merit, the specific radiation intensity, G_λ, at 2.795 μm has been used as a means for comparing the experimental infrared emission results corresponding to 50- and 150-psi hydrogen injection pressures for the slotted splitter plate. This particular frequency was selected because it corresponds to one of the major lasing transitions in the 2-1 band of HF. The two curves, shown on separate plots in Figure 47, represent a least-squares fit of the measured values of G_λ (evaluated at 2.795 μm) as a function of distance downstream from the splitter plate. It is evident from Figure 47 that a variation of injector pressure by a factor of three has virtually no effect on the radiation at corresponding downstream positions. A number of no-injection test runs were interspersed with these runs at various downstream locations, and in all cases there was no indication whatsoever of any radiation between 1.7 and 4.7 μm. This type of check was necessary because in some of our earlier results we did see very unusual radiation bands that were later traced to oil contamination in the hydrogen injection lines. It should also be pointed out that a concentrated effort was made to determine if any radiation could be observed at the higher wavelengths. These efforts did not indicate the presence of radiation beyond the 3.1-μm level under any conditions.

The remainder of this section will be devoted to a general discussion of the infrared emission radiation measured with the parallel mixing facility. The general experimental technique used with the parallel mixing facility was identical to that for the injection mixing facility except that the downstream survey was not as extensive due to the limited extent of the sapphire viewing window. Table VIII summarizes the experimental conditions that were used for the parallel mixing infrared spectral

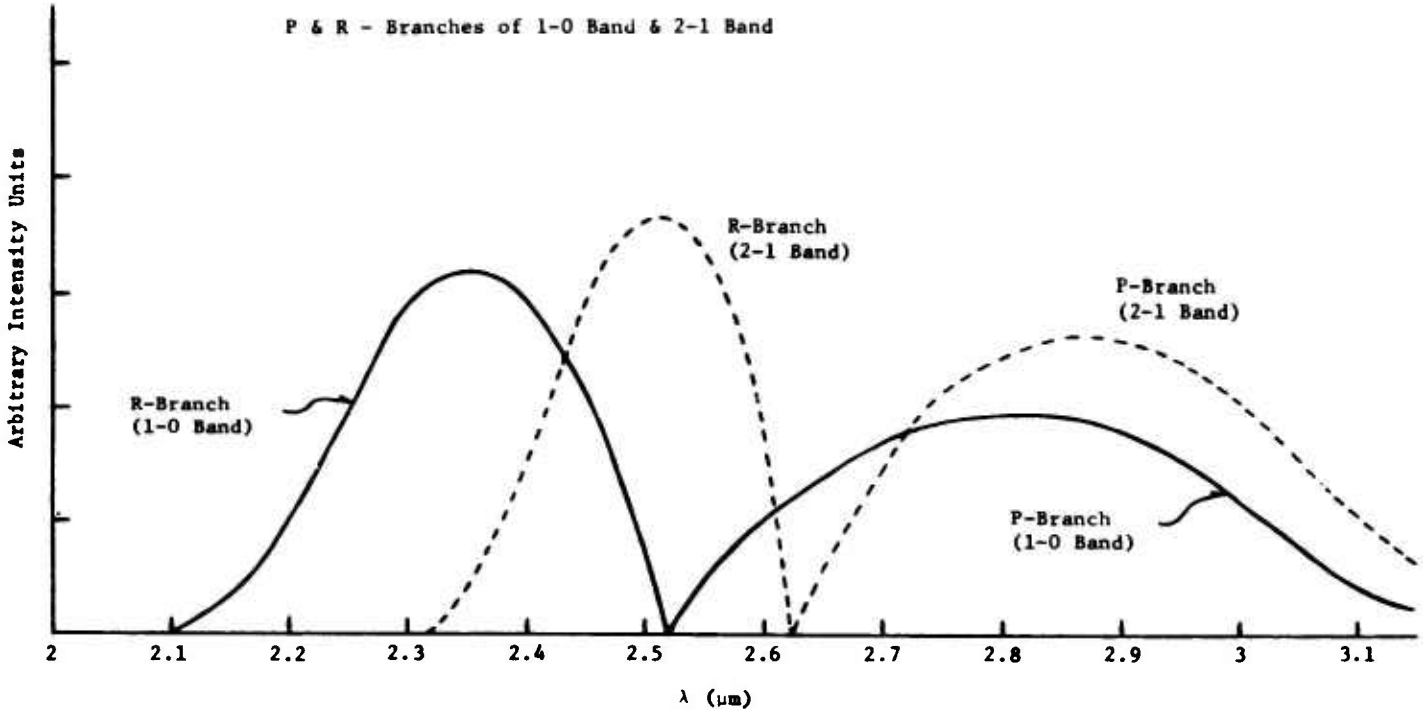

Figure 46. Schematic of Nominal HF Emission Spectra

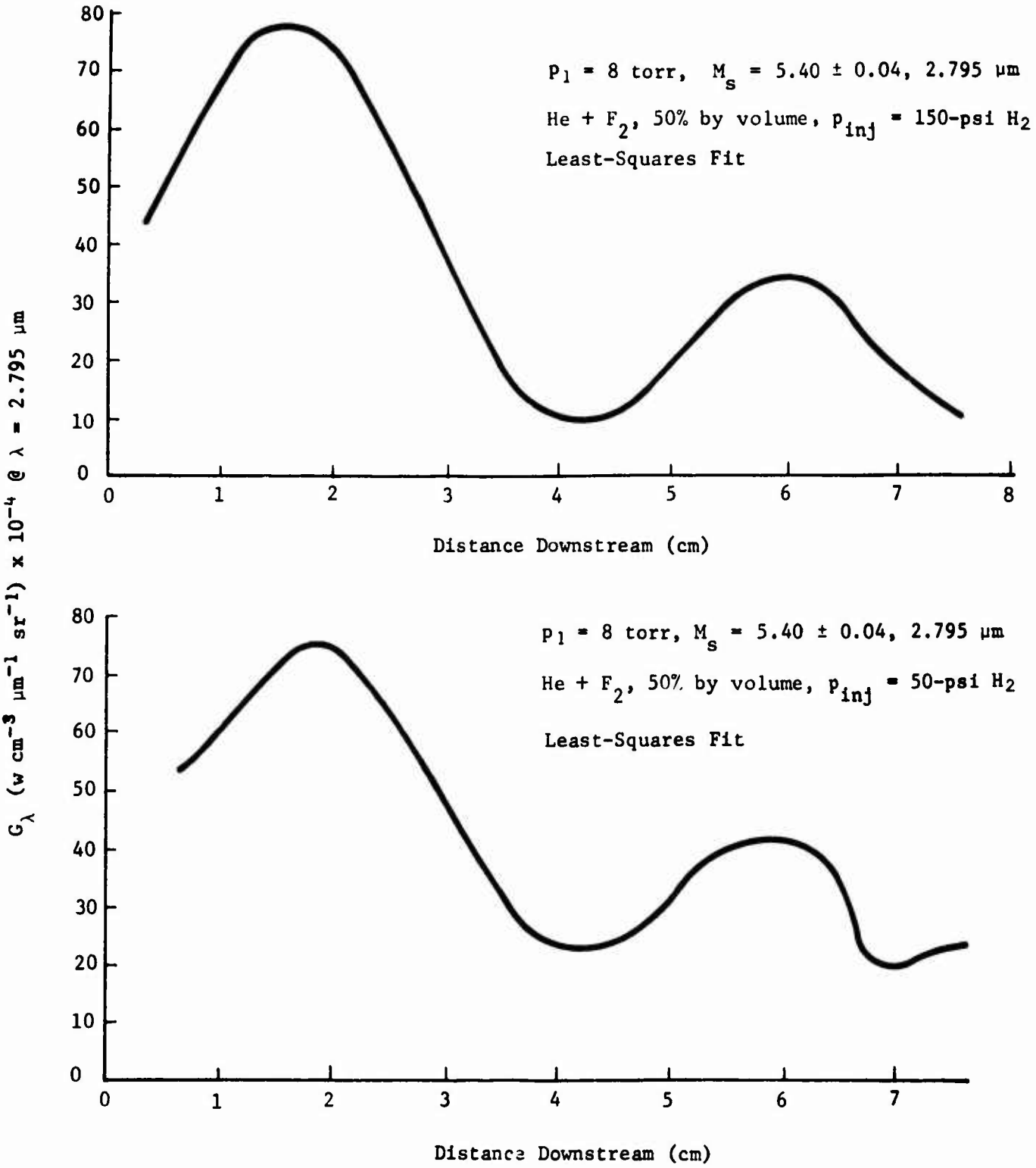

Figure 47. Specific Radiation Intensity vs Downstream Distance for Two Different Injection Pressures

Table VIII
PARALLEL MIXING INFRARED SURVEY DATA
(ALL MIXTURES 50% BY VOLUME)

Run No.	Matching Interferogram	p_1 lower H_2 + A, torr	p_1 upper He + F_2, torr	M_s H_2 + A	M_s He + F_2	Focus*, in.
72101101		20	6	4.46	5.34	7/32
72101102		20	6	4.43	5.26	5/32
72101201	72110903	20	6	4.38	5.22	3/32
72101202		20	6	4.40	5.34	9/32
72101701		20	6	4.27	5.22	11/32
72102001		17.5	6	4.51	5.34	11/32
72102301		17.5	6	4.38	5.44	9/32
72102401	72110902	17.5	6	4.49	5.34	7/32
72102402		17.5	6	4.49	5.38	5/32
72102403		17.5	6	4.46	5.34	3/32
72102601		20	10	4.48	4.97	3/32
72102602		20	10	4.35	4.94	5/32
72102701	72110901	20	10	4.35	5.04	7/32
72103001		20	10	4.35	5.00	9/32
72103002		20	10	4.25	4.94	11/32

*Focus distance measured downstream from termination point of the two adjacent nozzles.

surveys. This table contains identification data for 15 separate runs recorded for three different basic sets of test conditions. Three matching interferogram test conditions have been reproduced in this effort, and the run identification number for the corresponding interferogram is listed with each of the series of five infrared spectral emission runs. Here again, the same figure of merit (i.e., G_λ at 2.795 μm) is used as a means for comparing the infrared emission as a function of downstream location. Measured values of G_λ at five different downstream locations are shown in Figure 48. Emission data for each of the three different basic sets of test conditions are shown on separate axes, and the matching interferogram run numbers are also identified. It would appear from this limited survey that conditions corresponding to interferogram 72110901 produced the best reacting mixture about 1 cm

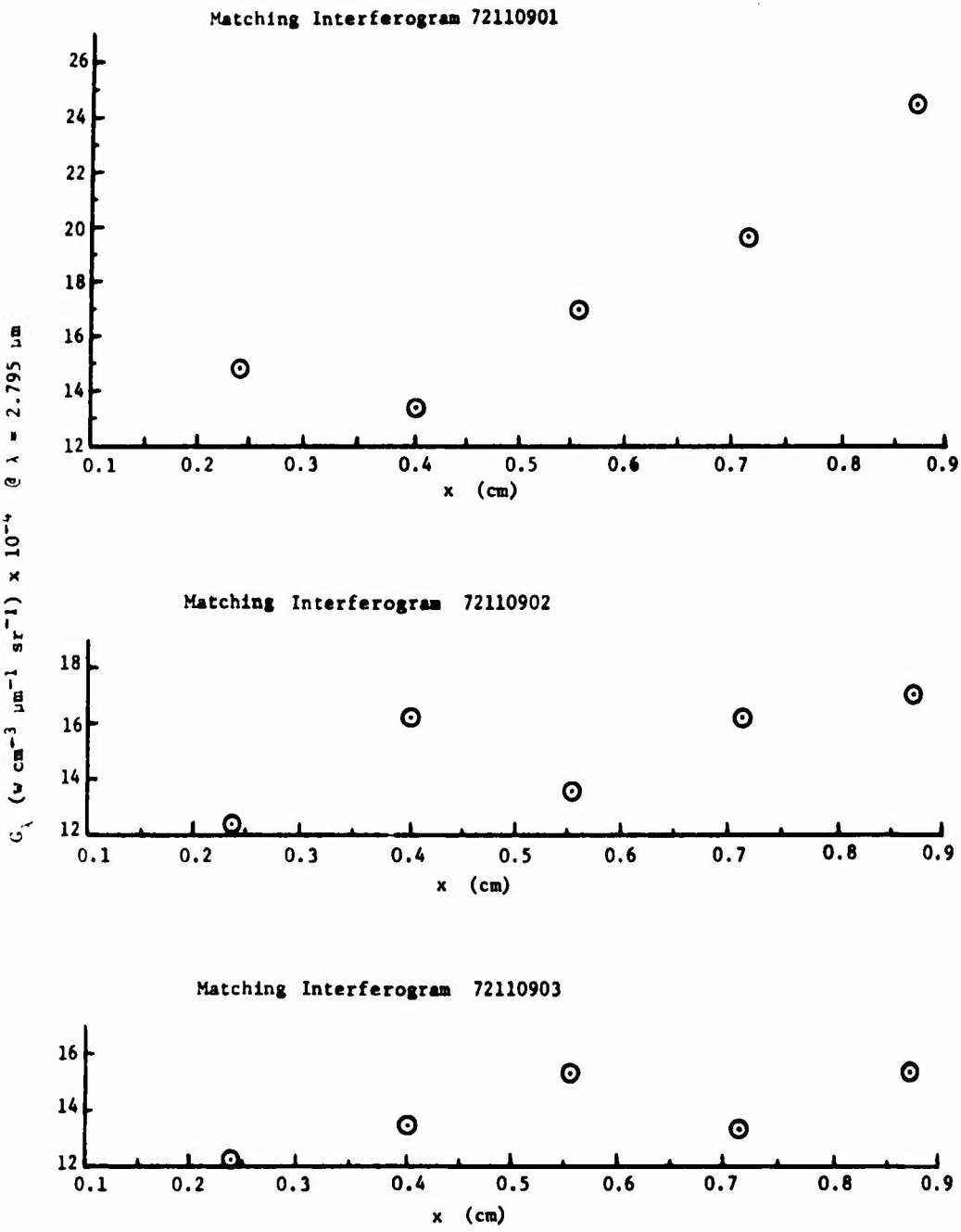

Figure 48. 2.795-μm Radiation in Three Parallel Mixing Streams at Five Stations Downstream of Splitter Plate

downstream of the splitter plate. The other two experimental conditions produced considerably less radiation and thus less reacting mixture at all positions. It should also be noted that no radiation was ever observed in the parallel mixing experiments for wavelengths greater than 3.1 μm.

To gain some idea of the combustion efficiency in the mixing layer, the total integrated radiation intensity from 2.6 to 3.1 μm was evaluated for each of the runs listed in Table VIII. The radiation power density in watts per cubic centimeter was obtained by evaluating the area within the experimentally obtained curve of G_λ vs λ for λ values between 2.6 and 3.1 μm. Table IX summarizes total radiation output determined in this manner for each of the parallel mixing experiments. The number of radiative transitions per second from the upper to the lower state can also be evaluated by assuming that the average energy per transition is that associated with the 2.795-μm line. This line represents a transition with an energy increment of 7.1066×10^{-20} joules. Dividing the power density obtained experimentally by this energy value then gives the number of transitions in emission occurring in a cubic centimeter of radiating HF gas per second. Self-absorption was not taken into account because the gas is assumed to be optically thin. The last column of Table IX lists the averaged number of radiative transitions obtained from the measured radiation emission levels.

3. SUMMARY OF PITOT PROBE RESULTS

A discrete-point pitot probe survey of the nozzle exit and mixing layer region was obtained using the rake assembly and pitot probe geometry described in Section II. Two pitot tubes were employed with every run, and the basic rake position was moved into each of seven different locations. At each separate basic position, the probes were located in 13 different stations. This type of survey was conducted for the slotted injection splitter plate under conditions essentially identical to those used for the interferogram of run 72072101. A corresponding case was also run under conditions with no injection. The data that were taken with the pitot tubes in a fixed position (with the base being moved across the width of the test section) indicated that the flow field was indeed uniform to within the accuracy of these measurements.

Figures 49 and 50 show the actual data points and a smoothed curve connecting them for the 150-psi hydrogen injection case and the zero-injection case for this extensive series of runs in which the basic conditions remained unchanged. As indicated in Figure 49 for the 150-psi hydrogen injection case, the minimum pitot pressure is observed along the centerline plane of injection and then increases to a peak value within the mixing layer before decaying to a freestream value out near the nozzle walls. This same type of basic variation in pitot pressure can be observed for the no-injection case, but the variations are much smaller. The average value of the pitot pressure near the wall in each different rake position is approximately 16 psi. Table V gives more complete details of the reference conditions (i.e., run number 72072101) for which this survey was recorded. As will be discussed later, an extensive static pressure survey for these same test section conditions was conducted and an average test section static pressure of 30 torr has been measured. Using these two values with the classical Rayleigh pitot tube formula and the theoretical value of γ for the reflected shock region, one obtains an exit Mach number of 4.5 for this nozzle. The actual design Mach number for this nozzle was 5, so this type of agreement is considered to be good.

Table IX
TOTAL INTEGRATED RADIATION FROM 2.6 TO 3.1 μm

Run No.	Interferogram	Power w/cm^3	Transitions/cm^3 sec
72102601		64.5×10^{-4}	9.06×10^{16}
72102602		55.5×10^{-4}	7.80×10^{16}
72102701	72110901	79.5×10^{-4}	11.18×10^{16}
72103001		85.6×10^{-4}	12.03×10^{16}
72103002		122.2×10^{-4}	17.20×10^{16}
72102001		69.3×10^{-4}	9.75×10^{16}
72102301		75.0×10^{-4}	10.53×10^{16}
72102401	72110902	57.6×10^{-4}	8.10×10^{16}
72102402		86.8×10^{-4}	12.05×10^{16}
72102403		63.0×10^{-4}	8.85×10^{16}
72101101		65.5×10^{-4}	9.20×10^{16}
72101102		56.9×10^{-4}	8.00×10^{16}
72101201	72110903	54.0×10^{-4}	7.60×10^{16}
72101202		57.4×10^{-4}	8.06×10^{16}
72101701		73.8×10^{-4}	10.38×10^{16}

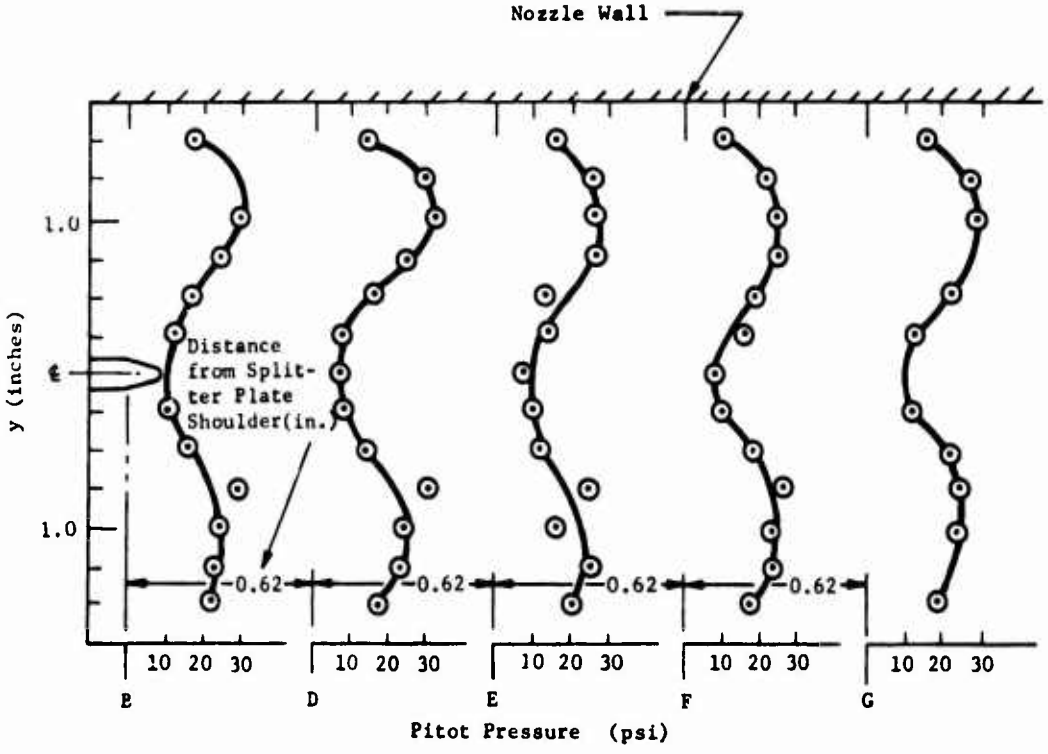

Figure 49. Pitot Survey Results for 150-psi H_2 Injection with Slotted Injector Plate [M_s = 5.4, p_1 = 8 torr (He + F_2, 50% by volume)]

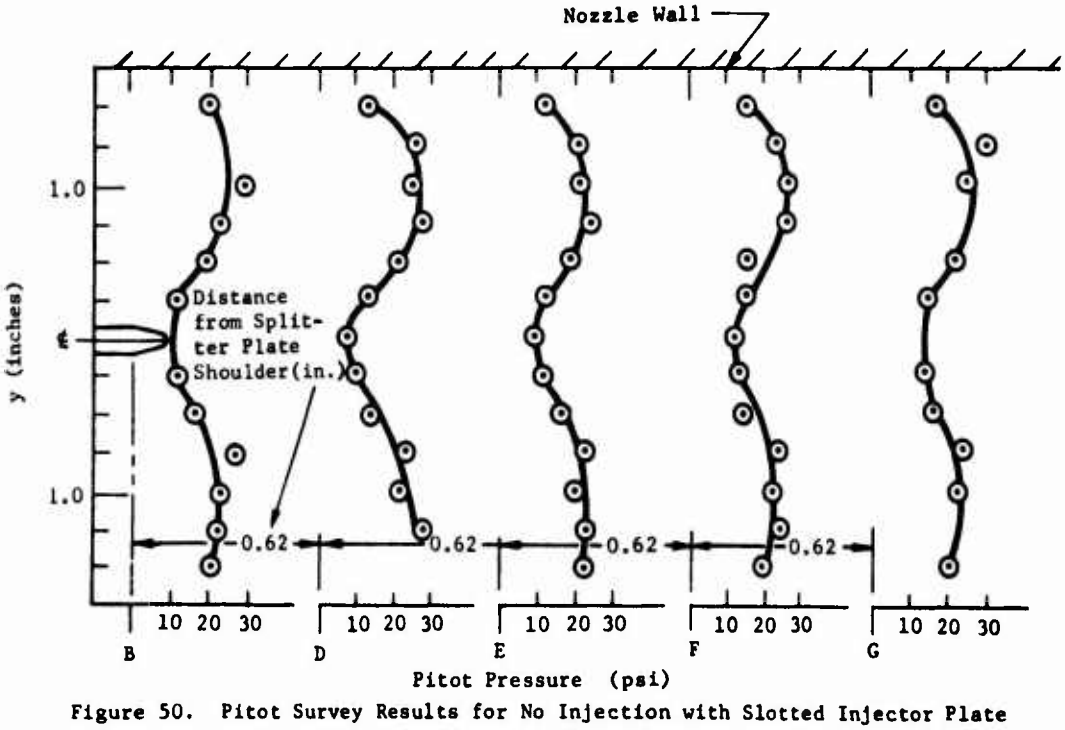

Figure 50. Pitot Survey Results for No Injection with Slotted Injector Plate [M_s = 5.4, p_1 = 8 torr (He + F_2, 50% by volume)]

4. SUMMARY OF STATIC PRESSURES

A complete series of side-wall static pressure measurements has been recorded for one basic set of test conditions in the injection mixing facility where the nozzle exit conditions and hydrogen injection pressures corresponding to interferometric data run 72072101 were reproduced. This complete static pressure survey was provided for this particular set of conditions because they also correspond to the conditions for which the extensive IR scans and pitot probe surveys were obtained. That is, we have chosen a single set of run conditions (viz, 72072101) and then proceeded with the most extensive possible surveys with each of the basic experimental techniques. Static pressures have also been recorded at only one station in the nozzle exit region for each of the other basic sets of run conditions in both the injection mixing facility and the parallel shear flow facility.

Figure 51 is a sketch of the injection mixing nozzle blocks showing the relative positions of the static pressure ports at which the full static pressure survey was recorded. Ten separate stations, as shown, were used to obtain these data. The results of a no-injection and a 150-psi H_2 injection are shown in Figures 52 and 53. Each of these figures shows the average value of at least three different runs for all positions recorded. At the time of this particular survey, we were using pressure transducers that had been in service for a long time and the noise level for these gages was poor. New transducers were installed after these data were obtained, and they provide a much better signal-to-noise ratio.

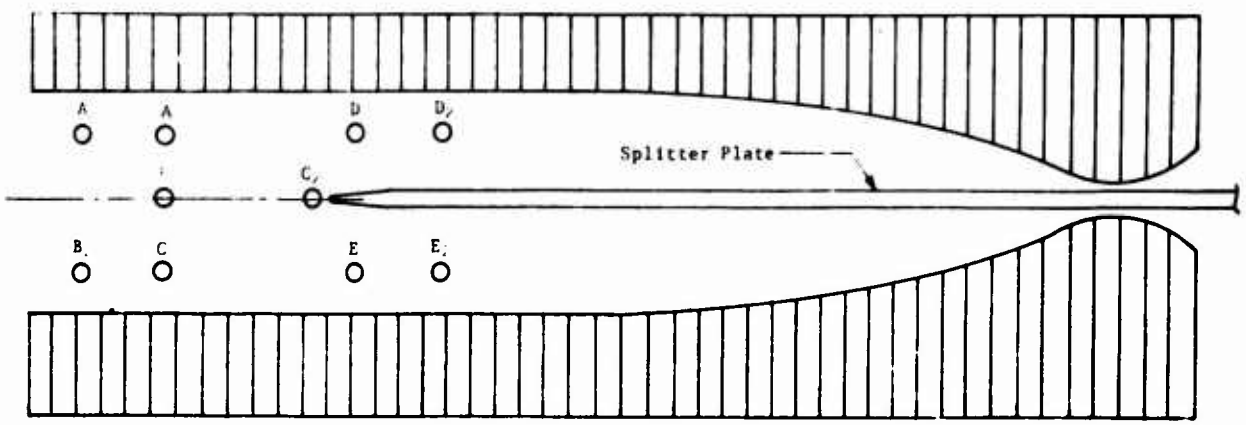

Figure 51. Schematic of Injection Mixing Nozzle Blocks Showing Location of Static Pressure Ports

Figure 52 is a typical scope record obtained with these new gages where two transducer locations on either side of the injector plate are displayed in the two separate traces. These records indicate that the static pressures at stations D and E for the injection nozzle exits are indeed quite uniform.

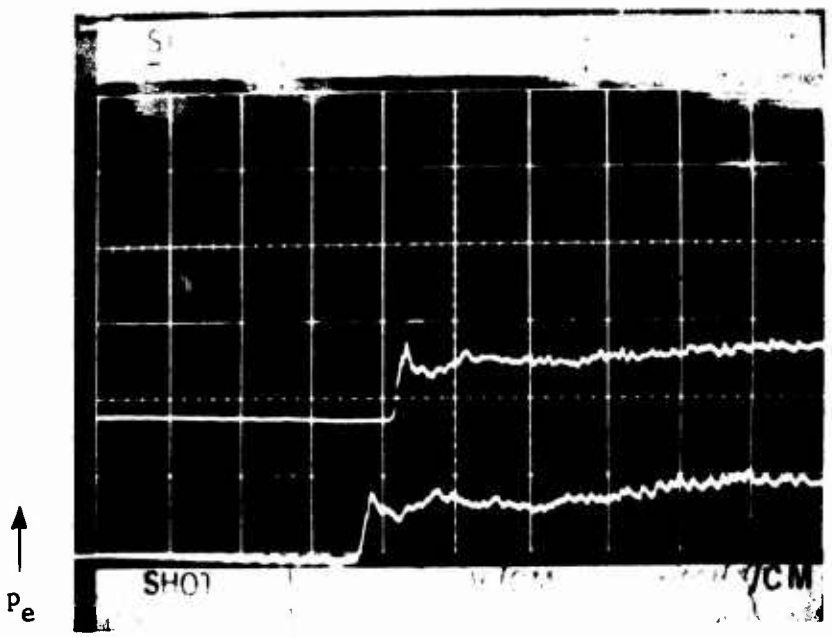

Figure 52. Static Side-Wall Pressure Measurements

Figure 53 shows the results obtained from a series of test runs for the initial 8-torr pressure of a 50% by volume mixture of He + F_2 with no injection and with an average initial shock Mach number of 5.4. As the values shown here indicate, the average test section static pressure is approximately 30 torr at all stations except C_2, which is located just downstream of the splitter plate. As indicated and discussed in Section II, the nominal test section pressure computed for these run conditions is actually 10 torr; hence, the measured value is some three times higher than we had anticipated. The specific reasons for this disagreement are discussed in Section II.

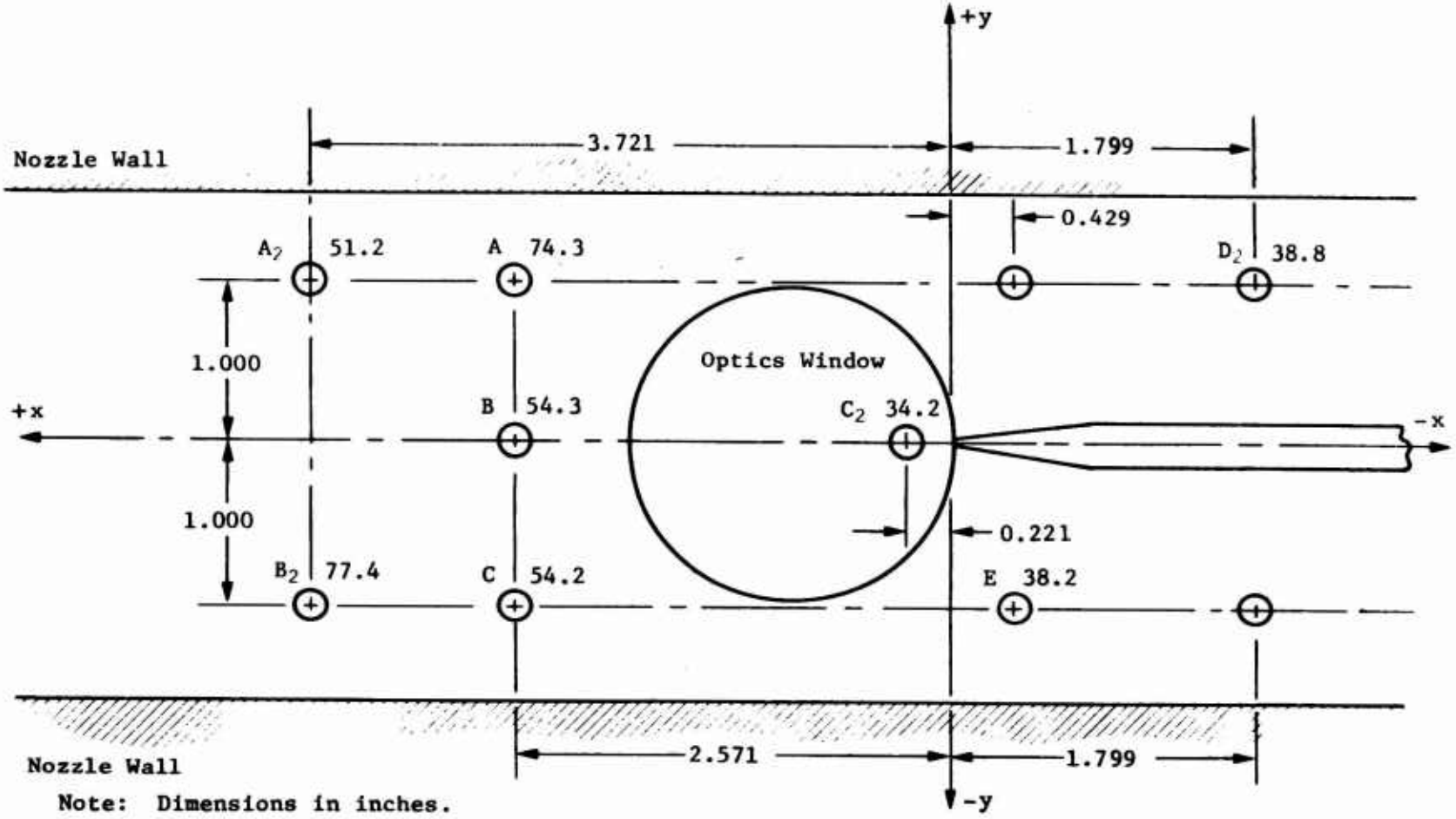

Note: Dimensions in inches.

Figure 53. Average Static Pressure (torr), 150-psi H_2 Injection, M_s = 5.4, p_1 = 8 torr ($He + F_2$, 50% by vol)

Figure 54 shows the measured static pressure values for these same run conditions with a 150-psi hydrogen injection case. As the values indicate, the static pressure downstream of the nozzle exit is increased by factor of 1.8 over the zero-injection case. Values presented for this case are averaged results of two different repeated runs, and, here again, the noise level was not as good as we can now expect to obtain with the new gages. Values for the static pressure measurements obtained with parallel mixing configurations are given in Table VII, along with the summary conditions for the interferometric data.

5. SUMMARY OF TEMPERATURE MEASUREMENTS

Two custom-made tungsten/tungsten-rhenium thermocouple probes, described in Section II, were obtained with the intent of conducting a complete total temperature survey of the mixing region. Due to delayed delivery and the extremely long rise time (~4 msec) of the 2-mil-diameter probe, only a limited number of data points were obtained. The test conditions for this survey were identical to those for the interferometric data run 72072101, and a hydrogen injection pressure of 150-psi was used. The results of this survey presented in Figure 55 are certainly questionable in terms of the final absolute value because the probe was not shielded and no attempt was made to account for radiation. These results do indicate a very symmetrical temperature profile over the mixing region, with the peak measured temperature occurring at a station 1 in. above the centerline plane.

Four different runs with the 1-mil-diameter probe have been obtained, and, as anticipated, the rise time for this configuration is approximately 2 msec, which is well within usable limits. This particular probe survived four runs before being destroyed, and because we have just identified a new source for replacement junctions at less than $10 per junction, we feel that a very accurate temperature survey can now be obtained with small additional effort to provide an effective shield.

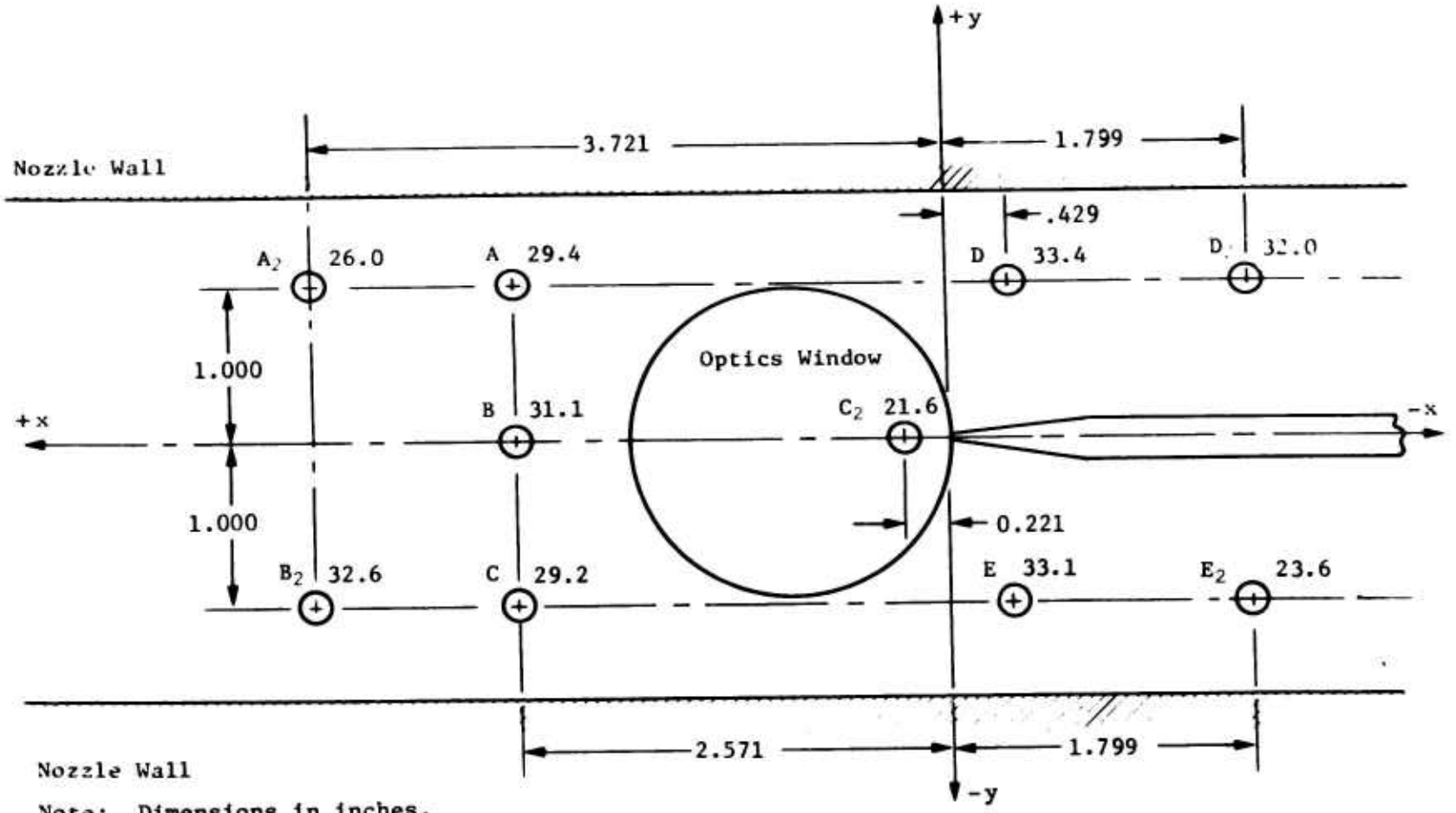

Figure 54. Average Static Pressure (torr), No Injection, M_s = 5.4, p_1 = 8 torr (He + F_2, 50% by vol)

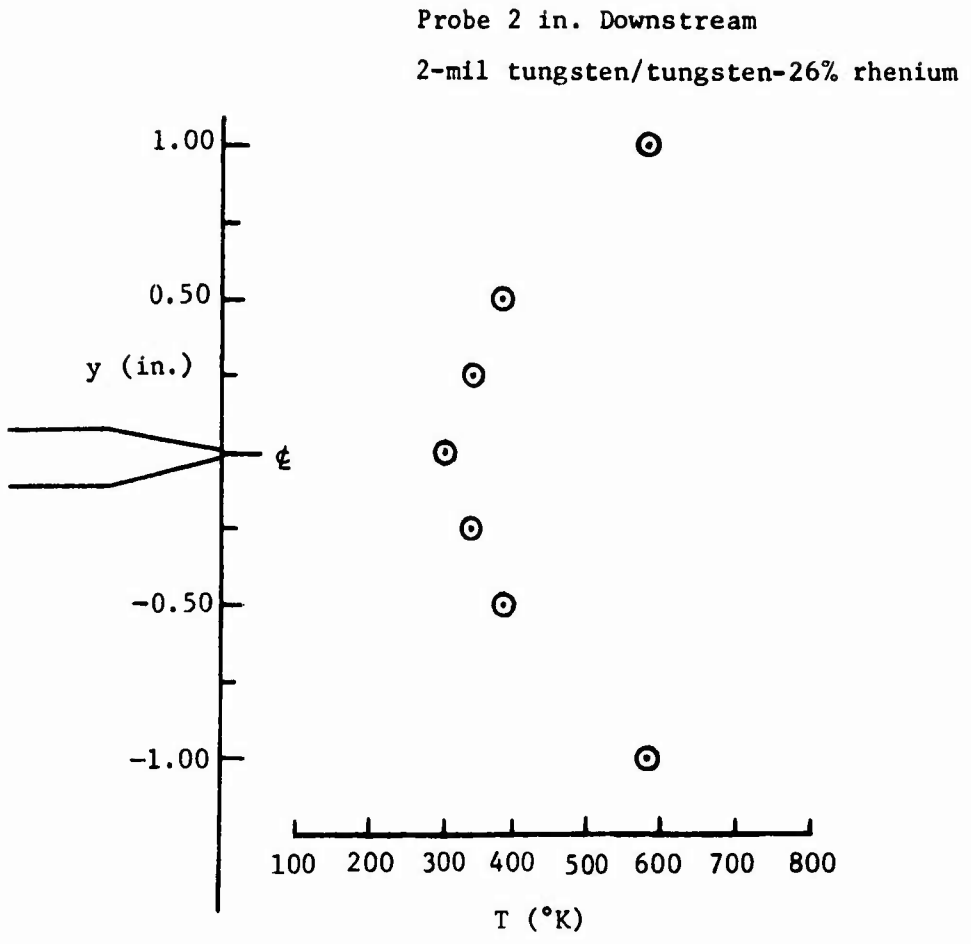

Figure 55. Temperature Survey with 150-psi Slotted H_2 Injection

SECTION IV

THEORY AND ANALYSIS OF PARALLEL TURBULENT MIXING LAYERS

1. TURBULENT TRANSPORT MODELS

Historically, turbulence in compressible flow has been analyzed by employing extensions of concepts and methods obtained from experience with turbulence in incompressible flow. Advances in the understanding of turbulence in supersonic flows have stemmed almost entirely from the pioneering work of Kovasznay (Ref. 17) and Morkovin (Ref. 18) in the development of the hot wire anemometer technique as a reliable method for quantitative observation of compressible turbulence.

Interpretation of experimental results, such as those obtained by Morkovin (Ref. 19), Kovasznay (Ref. 20), Kistler (Ref. 21), and Demetriades (Ref. 22), has established that in nonreacting compressible turbulent flow, the basic mechanisms for turbulent transport are essentially the same as those for incompressible turbulent flow, as long as the fluctuation velocities are subsonic. Such results lead to the conclusion that density fluctuations and pressure fluctuations in nonreacting compressible turbulent mixing layers do not contribute significantly to the turbulent transport, and compressibility is felt only through the temperature and compression effects on the mean density.

On the other hand, it has been demonstrated by Glass (Ref. 23) that intense sound impingement can drastically change the characteristics of turbulent jets. Sanderson and Steel (Ref. 24) have shown that exothermic reactions may induce a dramatic increase in turbulent mixing layer growth rate. Experimental observations of combustion in turbulent boundary layers by Wooldridge and Muzzy (Ref. 25) show a similar effect, in contradiction to earlier results by Kulgein (Ref. 26).

Engineering analyses of reacting compressible turbulent mixing have traditionally employed phenomenological models of turbulent transport properties adapted from nonreacting incompressible experience, without attempt to account for a direct influence of exothermic energy on the transport processes. An extensive review and comparison of such transport models as employed in nonreacting turbulent flows has been published by Harsha (Ref. 27).

Such phenomenological models of turbulent transport may be termed "eddy viscosity" models, in that they attempt to relate the turbulent shear stress to local flow conditions in a manner that is analogous to the dependence of laminar viscosity on local flow conditions. It is well known that the mechanics of the generation of turbulence or change in the character of turbulence cannot be defined uniquely by mean local flow conditions alone. Nonetheless, such approaches have exhibited much success in predicting the gross behavior of mixing flows, particularly when sufficient experimental data exist to permit empirical correlations of the transport models.

Over the past 20 years or so many workers have attempted to construct models of turbulent flow based on closure of the system of equations of turbulent motion at a higher order than that treated by the phenomenological eddy viscosity approach. Recently, such approaches have yielded excellent results in the prediction of compressible turbulent boundary layer phenomena. The work of Donaldson (Ref. 28), for example, has proved particularly fruitful. He closes the system of equations by mathematically modeling the appropriate terms in the equations for the second order correlations of fluctuating quantities so that the terms possess the correct tensor qualities but are tractable to computation. However, such methods are not sufficiently well in hand to permit their application to the general problem of mixing with chemical reactions.

Consequently, in the development of a practical analytical method for the routine engineering prediction of turbulent mixing flow with chemical reactions, one has little choice but to employ one of the phenomenological or eddy viscosity models. Our approach is to select a reasonable eddy viscosity model and to experimentally determine the adjustable parameters of that model over a range of conditions that are pertinent to the hydrogen-fluoride chemical laser. This approach is a continuation of work that began some years ago with the supersonic mixing of hydrogen and oxygen (see Ref. 24, 29 thru 37). We have selected Prandtl's third eddy viscosity model [see for instance Hinze (Ref. 38)]. For compressible flow we find that, with the boundary layer approximation, the gradient of the turbulent shear stress may be written

$$\frac{\partial \tau_{xy}}{\partial y} = -\frac{\partial}{\partial y}\left(\bar{\rho}\,\overline{u'v'}\right)$$

$$= -\frac{\partial}{\partial y}\left(\bar{\varepsilon}\,\frac{\partial \bar{u}}{\partial y}\right)^{*} \tag{55}$$

where, from Prandtl's model

$$\varepsilon = k\,b\left(\bar{u}_{max} - \bar{u}_{min}\right) \tag{56}$$

Here, b is the mixing layer width and k is a constant. This formulation yields excellent theoretical results for two-dimensional, two-stream mixing layers and co-axial stream mixing layers [see Harsha (Ref. 27)].

The available experimental results for two-stream mixing layers with chemical reactions indicate that, in terms of gross features, such layers exhibit similarity. In that case, the two-dimensional equations of motion may be written in terms of a single independent variable, $\eta = \sigma\, y/x$, where σ is a "universal" length scale or mixing layer growth rate. At the mixing layer boundary

$$\eta_b = \frac{\sigma b}{x} = \text{constant} \tag{57}$$

and

$$b = \frac{\eta_b\, x}{\sigma} = cx \tag{58}$$

The eddy viscosity model then may be written as

$$\varepsilon = \frac{x}{4\sigma^2}\left(\bar{u}_{max} + \bar{u}_{min}\right) \tag{59}$$

$$\sigma^2 = \left[4kc\,\frac{\bar{u}_{max} - \bar{u}_{min}}{\bar{u}_{max} + \bar{u}_{min}}\right]^{-1} \tag{60}$$

---

*Note that in laminar flow, $\tau_{xy} = \rho\mu\,\frac{\partial u}{\partial y}$.

It may be shown that this formulation is a "natural" definition for the eddy viscosity with either incompressible or compressible mixing layers, as long as the similarity assumption is valid.

The eddy viscosity is employed in a numerical mixing analysis program to predict contours of the dependent variables across the mixing layers. This procedure is discussed in detail in Subsection 2 of this section. The parameter, σ, is adjusted until the predicted and observed contours are in reasonable agreement. The dependent variable most easily observed for two-dimensional, supersonic, reacting mixing layers has been the index of refraction for the gas mixture.

The study attempted to find reasonable correlations for the value of σ thus determined in terms of some easily computed parameter. In the case of co-axial compressible mixing, the momentum deficit across the layer, or ρu ratio, is an important parameter. Clearly other factors, such as exit Reynolds number, also must be involved [see for instance Harsha (Ref. 27)]. Such correlation with the parallel stream data has not been found.

The amount of compressible stream data available is not large; however, there is a considerable amount of low-speed parallel stream data in the literature with a variation of the ratio of densities between the streams as large as 15. Such data for σ correlate reasonably well with a velocity parameter defined as

$$\beta = \frac{u_{max} - u_{min}}{u_{max} + u_{min}} \tag{61}$$

particularly for values of β greater than 0.3. The wide scatter of σ values for values of β less than 0.3 indicates that as the stream velocity difference decreases, the boundary layers on the stream separating surface become dominant in controlling the mixing.

The values of σ obtained in previous work, both with and without combustion, are shown in Figure 56 as a function of β, together with low-speed data by other laboratories. Recent results by other laboratories are plotted for compressible reacting flows. The values of σ derived from this latter data are not as reliable as those obtained in Martin Marietta's previous work, because only limited information was available on the specific experimental conditions and results from these laboratories.

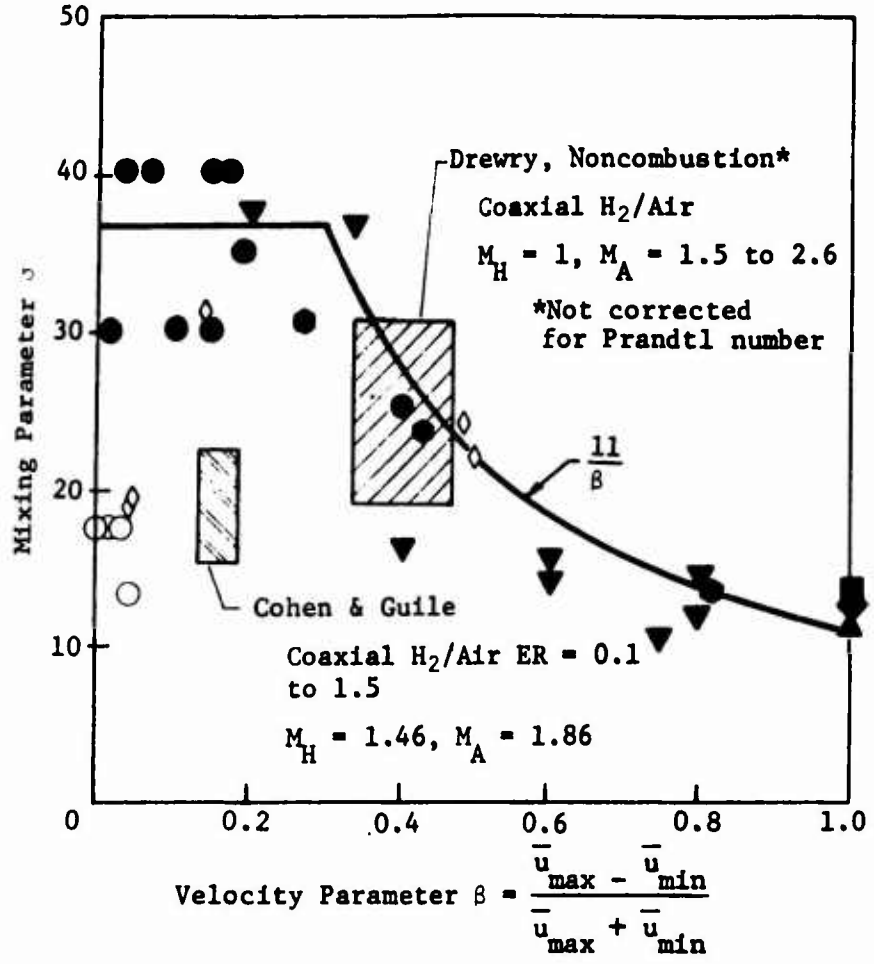

Legend:

Noncombustion Results

- ▼ Baker & Wienstein
- ■ Albertson
- ◆ Liepmann & Laufer
- ▲ Maydew & Reed
- ● Yakovlovsky (all incompressible)
- ● MMC-R-70-48638-003 (compressible, no combustion)

Combustion Results

- ○ MMC-R-70-48638-003
- ◇ Shackleford (TRW)* Private Communication 8/8/72

H_2/F - Supersonic

Figure 56. Experimentally Determined Mixing Parameter

The value of σ that best fitted a similar profile to the available data was determined. Although the points show severe scatter, there is strong evidence that at low values of the velocity parameter ($\beta \leq 0.3$), the mixing layer growth rate is strongly affected by exothermic reactions. In such cases, a σ value near 20 is used rather than the noncombustion value that is nearer 40. The large scatter of noncombustion results for low values of β is felt to be a result of initial boundary layer dominance.

Note the Drewry (Ref. 39) and Shackleford (Ref. 40) data are related to the observations of a local species mass fraction or number density, for which the transport coefficient is the eddy diffusivity or conductivity. The ratio of eddy viscosity to eddy conductivity is the turbulent Prandtl number, Pr_t. Observed values of the turbulent Prandtl number range from about 0.6 to about 1. The Drewry and Shackleford data shown on Figure 56 have not been corrected for turbulent Prandtl number, which is equivalent to setting it to one. If the value of Pr_t is taken as different from unity, the values of σ will increase by the factor $1/\sqrt{Pr_t}$.

Martin Marietta's previous work (Ref. 24) did not numerically produce realistic index of refraction contours without accounting for the boundary layers produced on the stream separating surface (see Fig. 57). Note that most of Martin Marietta's previous data were obtained for values of the velocity parameter, β, less than 0.3, which implies a boundary layer influenced mixing layer. The past work simply employed initial dependent variable contours that were consistent with observed boundary layer thicknesses. However, this procedure does not account for the transition from boundary layer controlled mixing to fully formed mixing layer flow.

In future work, Martin Marietta plans to account for this transition in the following way. Transition to turbulent mixing is assumed if the momentum thickness Reynolds number exceeds 150 at the initiation of a free shear layer [see Dryden (Ref 41) or Landau and Lifshitz (Ref. 42)]. The velocity defect employed in the transport properties, however, is taken initially as that across the boundary layer profile. As the mixing progresses, the velocity minimum resulting from the nozzle wall gradually increases. Once this defect becomes equal to the velocity difference across the mixing layer, the usual velocity difference is employed.

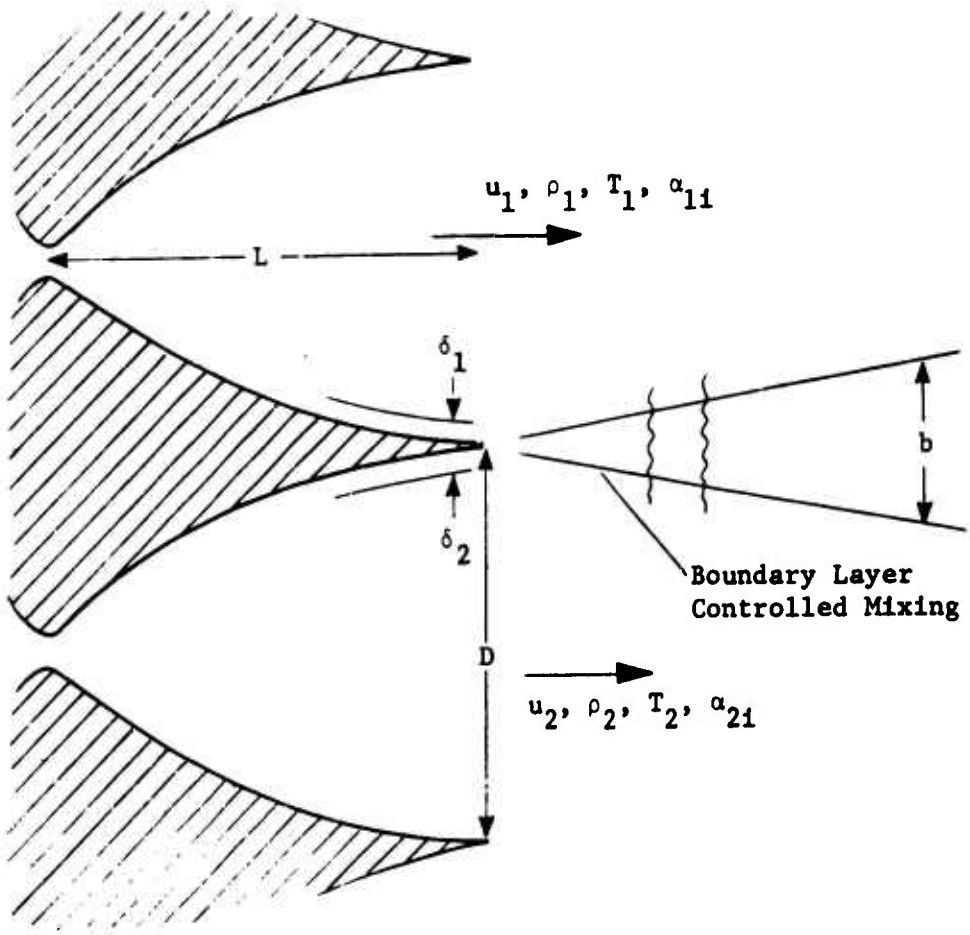

Figure 57. Sketch of Mixing Layer

The correlation given in Figure 56 appears to serve adequately for nonreacting flows, but the data on reacting flows are insufficient to allow a curve to be drawn for that category of mixing layers. As was stated earlier, the data indicate a strong effect of combustion energy release under conditions where this energy is significant in relation to the flow kinetic energy. In view of this fact, it seems reasonable to expect that any complete correlation must include a parameter to express the relative magnitudes of these two energy sources, as well as a parameter to measure the upstream boundary layer effects. Martin Marietta has been able to correlate the MMC and TRW combustion data (Ref. 36 and 40) for β less than 0.3 with the following equation:

$$\sigma = \frac{1.35\ (Re/5)^a}{1 + 0.002\ [(1 + C \cdot Re^a)\ (1 - 4\beta)]^{1.35}} \qquad (62)$$

where C = ratio of available chemical energy to the fluid kinetic energy,

Re = maximum nozzle exit Reynolds number,

a = 1/2 for laminar boundary layers and 1/5 for turbulent boundary layers,

β = velocity parameter.

The correlation is incomplete, however, because it does not readily extend to nonreacting mixing layers (C = 0) as it should. More reacting mixing layer data will be required to develop a complete correlation.

2. ANALYTICAL TECHNIQUES

The finite difference, finite chemical rate analysis employed in this work is an adaptation of one developed by Edelman and Fortune (Ref. 43). This analysis and its associated computer code were originally written for the mixing and burning of an RP-1/lox system. Modifications that were made involve addition of an equilibrium chemistry option for hydrogen/fluorine combustion, alteration of the existing nonequilibrium chemistry subroutines to reflect the hydrogen/fluorine composition of interest, and incorporation of certain features to facilitate consideration of boundary layers that form on surfaces upstream of the mixing region. Further discussion of the mixing analysis will be divided

into three parts: (1) formulation of the governing equations in finite difference form, (2) the nonequilibrium chemistry computation scheme, and (3) the computer program that employs (1) and (2) to achieve the desired solution.

a. Finite Difference Analysis of the Flow Field - Certain basic assumptions, important to the analysis described here, are:

1) Flow geometry is restricted to two-stream, parallel mixing, either axisymmetric or two-dimensional;

2) The flow field is fully turbulent; molecular transport mechanisms are assumed negligible in comparison to their turbulent counterparts;

3) Turbulent Prandtl and Lewis numbers are constant;

4) Turbulent transport may be expressed in terms of an eddy viscosity/mixing length concept;

5) The perfect gas equation of state is adopted for both individual species and mixtures;

6) The boundary layer form of the Navier-Stokes equations is assumed applicable, pressure gradient across the mixing region is assumed to be negligible;

7) Transfer of mass by thermal or pressure diffusion is neglected.

By applying these simplifying restrictions, the governing differential conservation equations for the mixing region become:

Mass:

$$\frac{\partial}{\partial x}\left(\rho u y^N\right) + \frac{\partial}{\partial y}\left(\rho v y^N\right) = 0 \tag{63}$$

Momentum:

$$\rho u \frac{\partial u}{\partial x} + \rho v \frac{\partial u}{\partial y} = -\frac{\partial P}{\partial x} + \frac{1}{y^N}\frac{\partial}{\partial y}\left(\varepsilon_v y^N \frac{\partial u}{\partial y}\right) \tag{64}$$

$$\frac{\partial P}{\partial y} = 0$$

Energy:

$$\bar{c}_p \rho u \frac{\partial T}{\partial x} + \bar{c}_p \rho v \frac{\partial T}{\partial y} = u \frac{\partial P}{\partial x} + \varepsilon_v \left(\frac{\partial u}{\partial y}\right)^2 \tag{65}$$

$$- \rho \sum_{i=1}^{k} h_i \dot{w}_i + \frac{1}{y^N} \frac{\partial}{\partial y} \left(\frac{\bar{}}{c}_p \frac{\varepsilon_v}{Pr_t} y^N \frac{\partial T}{\partial y} \right) + \frac{\varepsilon_v}{Sc_t} \frac{\partial T}{\partial y} \sum_{i=1}^{k} c_{p_i} \frac{\partial \alpha_i}{\partial y}$$

Species:

$$\rho u \frac{\partial \alpha_i}{\partial x} + \rho v \frac{\partial \alpha_i}{\partial y} = \frac{1}{y^N} \frac{\partial}{\partial y} \left(\frac{\varepsilon_v}{Sc_t} y^N \frac{\partial \alpha_i}{\partial y} \right) + \rho \dot{w}_i \tag{66}$$

where N = 0 for two-dimensional geometry and N = 1 for axisymmetric geometry. The appropriate initial and boundary conditions are:

$$x = 0 \qquad u = u(y),\ \alpha_i = \alpha_i(y),\ T = T(y)$$

$$y = 0 \qquad \frac{\partial u}{\partial y} = \frac{\partial T}{\partial y} = \frac{\partial \alpha_i}{\partial y} = 0$$

$$y \to \infty \qquad u = u_e,\ \alpha_i = \alpha_{i_e},\ T = T_e \tag{67}$$

With the inclusion of the equation of state, these equations represent a complete set, with the exception of the chemical production terms that are calculated separately.

Solution of these equations in the physical (x,y) plane may be undertaken directly. However, for purposes of this finite difference solution, it is convenient to employ a stream function transformation to the (x,ψ) plane, ψ being the stream function defined by

$$\psi^N \frac{\partial \psi}{\partial y} = \rho u y^N$$

$$\psi^N \frac{\partial \psi}{\partial x} = - \rho v y^N \tag{68}$$

This transformation satisfies the mass conservation equation identically and is straightforward in application. Note that under this transformation

$$\left(\frac{\partial}{\partial y}\right)_x = \frac{\rho u y^N}{\psi^N}\left(\frac{\partial}{\partial \psi}\right)_x$$

$$\left(\frac{\partial}{\partial x}\right)_y = \left(\frac{\partial}{\partial x}\right)_\psi - \frac{\rho v y^N}{\psi^N}\left(\frac{\partial}{\partial \psi}\right)_x \tag{69}$$

Substitution of the stream function into the momentum, energy, and species conservation equations yields:

Momentum:

$$\frac{\partial u}{\partial x} = \frac{1}{\rho u}\frac{\partial P}{\partial x} + \frac{1}{\psi^N}\frac{\partial}{\partial \psi}\left(a\,\frac{\partial u}{\partial \psi}\right) \tag{70}$$

Energy:

$$\bar{c}_p\,\frac{\partial T}{\partial x} = \frac{1}{\rho}\frac{\partial P}{\partial x} + \frac{1}{\psi^N}\frac{\partial}{\partial \psi}\left(\frac{\bar{c}_p}{Pr_t}\,a\,\frac{\partial T}{\partial \psi}\right) - \frac{1}{u}\sum_{i=1}^{k} h_i \dot{w}_i$$

$$+ \frac{a}{\psi^N}\left[\left(\frac{\partial u}{\partial \psi}\right)^2 + \frac{1}{Sc_t}\frac{\partial T}{\partial \psi}\sum_{i=1}^{k} c_{p_i}\frac{\partial \alpha_i}{\partial \psi}\right] \tag{71}$$

Species:

$$\frac{\partial \alpha_i}{\partial x} = \frac{1}{\psi^N}\frac{\partial}{\partial \psi}\left(\frac{a}{Sc_t}\frac{\partial \alpha_i}{\partial \psi}\right) + \frac{\dot{w}_i}{u} \tag{72}$$

where

$$a \equiv \frac{\varepsilon_v \rho\, u\, y^{2N}}{\psi^N} \tag{73}$$

A finite difference scheme is employed to formulate these parabolic differential equations in a form suitable for a numerical initial/boundary value marching solution. The finite difference mesh is composed of streamlines spaced at a specified $\Delta\psi$ interval and normal surfaces spaced at varying intervals, Δx, as determined by a stability criterion. This stability criterion arises from the choice of an explicit difference scheme which allows solution in each streamwise step without need for iteration. Forward differences are employed for x derivatives and central differences for ψ derivatives. For a dummy dependent variable F, these derivative forms are

$$\left(\frac{\partial F}{\partial x}\right)_{n,m} = \frac{F_{n+1,m} - F_{n,m}}{\Delta x}$$

$$\left(\frac{\partial F}{\partial \psi}\right)_{n,m} = \frac{F_{n,m+1} - F_{n,m-1}}{2\Delta\psi}$$

$$\left[\frac{\partial}{\partial \psi}\left(a\,\frac{\partial F}{\partial \psi}\right)\right]_{n,m} = \frac{a_{n,m+\frac{1}{2}}\left(F_{n,m+1} - F_{n,m}\right) - a_{n,m-\frac{1}{2}}\left(F_{n,m} - F_{n,m-1}\right)}{\Delta\psi^2} \qquad (74)$$

where

$$a_{n,m\pm\frac{1}{2}} = \frac{a_{n,m} + a_{n,m\pm1}}{2} \qquad (75)$$

and the mesh is as follows

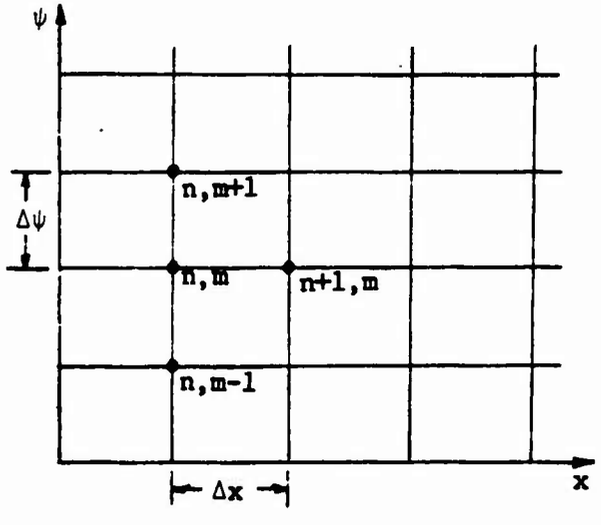

The explicit form of differencing has the disadvantage of relating Δx to $\Delta\psi$. This may lead to long solution times when the total streamwise distance to be traversed is much larger than a characteristic dimension in the cross stream (ψ or y) direction, e.g., a boundary layer thickness.

The final finite difference equations for $u_{n+1,m}$, $T_{n+1,m}$, and $\alpha_{i_{n+1,m}}$ are lengthy and will not be derived here. However, they are easily obtained by direct application of the above derivative forms to the governing equations. It is important to note, however, that these equations are uncoupled and present no difficulties for machine solution once the chemical species production rates have been obtained. This phase of the analysis will be discussed next.

b. Nonequilibrium Chemistry Analysis - Finite rate analysis is the most realistic, but also the most difficult of the various chemical analysis options. One must provide a model for the chemical processes that can be used repeatedly in the finite difference procedure without causing computer run times to become prohibitive. To achieve this, the numerous reactions that form the actual (and often undefined) chemical chains must be replaced by a limited set of important controlling reactions and appropriate reaction rate constants. Such approximations meet with success or failure depending on how well the controlling reactions are selected and how well their rate constants are known.

For analysis of the present hydrogen/fluorine system, the species selected for consideration are H, H_2, F, F_2, and HF. Provision is also made for the presence of nonreacting species He and A acting as diluents. The reactions selected as representative of the important chemical processes and their respective rate constants are shown in Table X. These reactions were selected from those given by Cohen (Ref. 44), with the production of excited HF specifically neglected.

The solution procedure adopted for our analysis follows that used by Edelman and Fortune (Ref. 43), which derives in turn from the work of Moretti (Ref. 45), and DeGroat and Abbett (Ref. 46). An outline of the major steps in this procedure will be given here, with further details available from References 45 and 46.

Table X

CHEMICAL REACTION AND RATE-CONSTANT EQUATIONS

Reaction	Rate Constant
$F_2 + M \rightleftharpoons 2F + M$	$k_f = 5 \times 10^{13} \cdot 10^{-7740/T}$
$H_2 + M \rightleftharpoons 2H + M$	$k_b = 10^{18} \cdot T^{-1}$
$HF + M \rightleftharpoons H + F + M$	$k_f = 1.2 \times 10^{18} \cdot T^{-1} \cdot 10^{-32180/T}$
$F + H_2 \rightleftharpoons HF + H$	$k_f = 2.69 \times 10^{13} \cdot 10^{-350/T}$
$H + F_2 \rightleftharpoons HF + F$	$k_f = 4.8 \times 10^{12} \cdot 10^{-525/T}$

The following thermodynamic relations for gaseous mixtures are assumed:

State:

$$P = \rho R T \sum_{i=1}^{k} \frac{\alpha_i}{W_i} \tag{76}$$

Enthalpy;

$$h = \sum_{i=1}^{k} \alpha_i h_i \tag{77}$$

Specific Heat:

$$\bar{c}_p = \sum_{i=1}^{k} \alpha_i \, c_{p_i} \tag{78}$$

As a matter of convenience for the subsequent development, a definition is presented of a molar concentration of species i

$$y_i = \frac{\rho \alpha_i}{W_i} \tag{79}$$

and a third-body concentration

$$Y = \sum_{i=1}^{k} y_i \tag{80}$$

where the summation includes all species present in the gaseous mixture.

The various chemical reactions of Table X can be written in the general form

$$\sum_{i=1}^{k} v_i' M_i \rightleftharpoons \sum_{i=1}^{k} v_i'' M_i \tag{81}$$

where the v_i' are the stoichiometric coefficients of the reactants, the v_i'' represent the corresponding coefficients for the reaction products, and the M_i represent the various chemical species. The v_i' and v_i'' are either integers or zero, the latter indicating that a species does not occur as a reactant or product. At any instant, the time rate of change of the concentration of species i in reaction j is given by

$$\dot{y}_{ij} = \left(v_i'' - v_i'\right) \left[k_f \prod_{\ell} y_{\ell}^{v_{\ell}'} - k_b \prod_{\ell} y_{\ell}^{v_{\ell}''} \right] \tag{82}$$

Summing over all reactions produces the total rate of change of concentration of species i:

$$\dot{y}_i = \sum_{j} \dot{y}_{ij} \tag{83}$$

The next step in the Moretti procedure is to linearize the equations for $\dot{y}_i$. The following assumptions are made:

1) The reaction rate coefficients k_{fj} and k_{bj} are constant throughout a step (i.e., the change in temperature throughout a step is not so large as to affect their values);

2) The sum of concentrations of all species, Y, is constant;

3) Terms involving the product of species concentrations, $y_m y_n$, can be replaced by the approximation

$$y_m y_n \approx -y_m^o y_n^o + y_m^o y_n + y_m y_n^o \tag{84}$$

where the superscript o denotes values at the beginning of a step.

Substitution of the expression from assumption 3) results in the following set of linear, nonhomogeneous, first order differential equations:

$$\dot{y}_i = \sum_{\ell=1}^{k'} a_{i\ell}\, y_\ell + C_i \tag{85}$$

where k' is the number of chemically active species.

Moretti solves these linear equations by obtaining the eigenvalues of the matrix $a_{i\ell}$. This procedure becomes unwieldy for chemical systems involving many species. DeGroat and Abbett have developed an alternative technique based on the assumption of a truncated power series solution of the form

$$y_i = \sum_{\ell=0}^{2} d_{i\ell}\, t^\ell \tag{86}$$

Substitution of this solution into the general differential equation yields residue terms:

$$R_i(t) = \sum_{\ell=1}^{2} \left[\ell d_{i\ell}\, t^{\ell-1} - \sum_{j=1}^{k'} a_{ij}\, d_{j\ell}\, t^{\ell} \right] - \sum_{j=1}^{k'} a_{ij}\, d_{jo} - C_i \qquad (87)$$

This set of equations contains two unknowns, d_{i1} and d_{i2}, for each species i. Two conditions are needed to solve for these unknowns. These may be obtained by specifying that

$$\int_{o}^{\frac{\Delta t}{2}} R_i(t)\, dt = 0$$

and

$$\int_{\frac{\Delta t}{2}}^{\Delta t} R_i(t)\, dt = 0 \qquad (88)$$

Evaluation of these integrals, employing the expression for $R_i(t)$, leads to a system of linear, nonhomogeneous, algebraic equations (10 unknowns in 10 equations). These algebraic equations are then solved for the $d_{i\ell}$ by triangularizing the coefficient matrix. The $d_{i\ell}$ being known, an explicit solution is given for the molar concentration of each species at the end of the time interval considered.

c. Computer Program - The computer program developed for analyzing hydrogen/fluorine mixing layers can be divided into three parts. The first of these involves the main program and several subroutines used for performing various initialization tasks (see Fig. 58). The other two parts are designed to compute various flow properties and solve the finite difference equations and are driven by subroutines ØNE and TWØ, respectively. The finite difference solution procedure is composed of two parts, corresponding to the gas dynamic and chemical analyses previously described. The necessary operations are designed to take place in sequence, and the procedure marches downstream in small steps as the flow solution in the mixing region is determined.

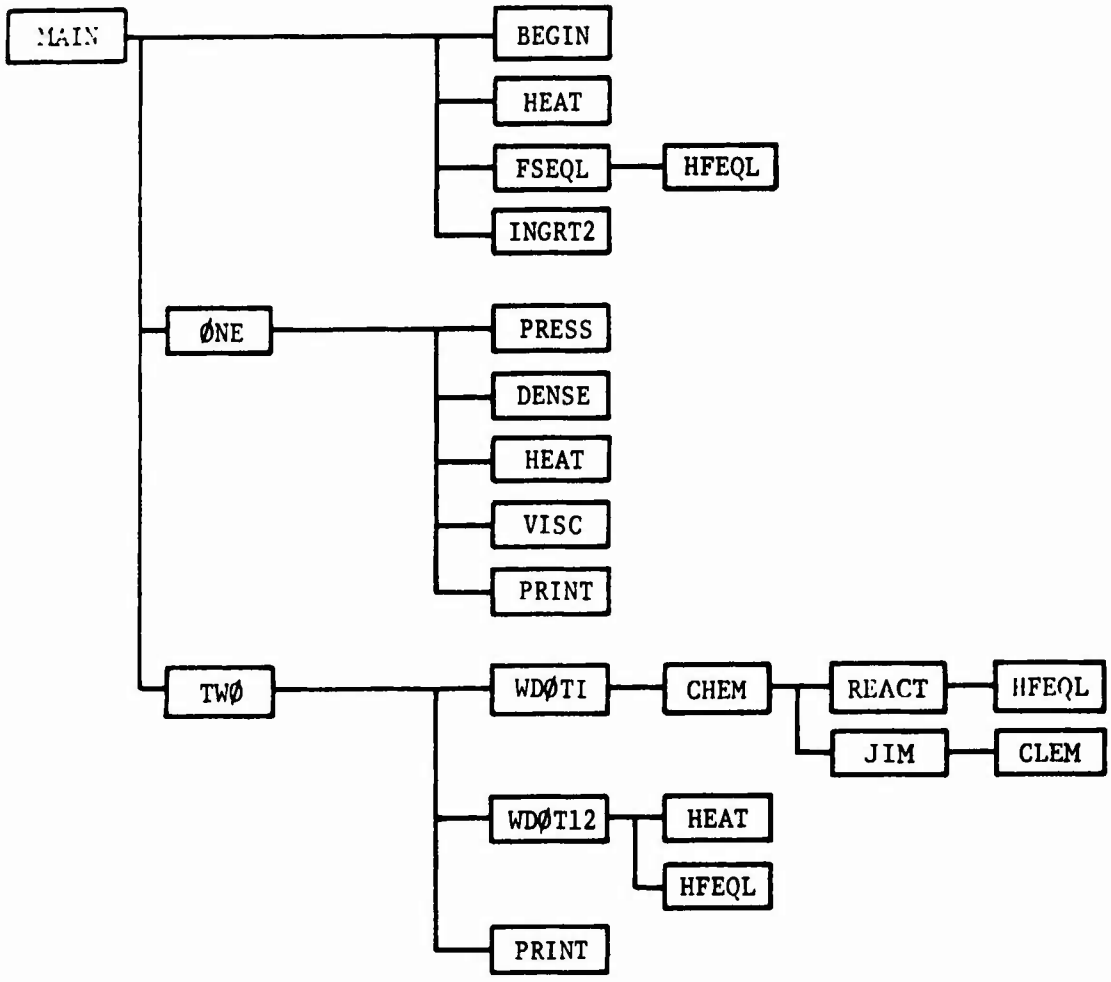

Figure 58. Interrelationship of Subroutines in the Mixing Analysis Computer Code

For convenience, the computer code is divided into several subroutines. These subroutines and their interrelationship are shown in Figure 58. The function of each subroutine is described in the paragraphs that follow.

(1) Main Program - This is the driver for the entire program. The input data are read into the computer through this routine and supplied to the various subroutines by means of CØMMØN statements and parameters in the CALL statements. In addition to various quantities used for program control, the required input data include the turbulent Lewis and Prandtl numbers, the turbulent mixing parameter, static pressure, and initial profiles of velocity, temperature, and species mass fractions. This program also writes the input data and, in the case of a power profile boundary layer, computes the initial velocity and temperature profiles. After completion of these initialization tasks, the main program acts as the driver by calling subroutines ØNE and TWØ alternately until the designated end of the problem is reached or until an error occurs. In either case, control is returned to the beginning of the program so as to run a following case if data for another problem are provided.

(2) Subroutine BEGIN - This subroutine supplies information of a basic thermodynamic nature. Specifically, it provides:

1) Molecular weights;

2) Coefficients for calculating the specific heat at constant pressure of each chemical species;

3) Coefficients for calculating the enthalpy of each species.

The coefficients for specific heat and enthalpy result from curve fits of these properties as functions of temperature and were derived from JANAF data (Ref. 47). Presently, one set of coefficients is used from 200 to 1000°K and a second set from 1000 to 3000°K.

(3) Subroutine CHEM - CHEM is the main chemistry subroutine and acts as a driver for this phase of the solution. The chemistry analysis is set up numerically so there may be several steps of the chemistry solution in the time interval corresponding to a single fluid dynamic step. CHEM controls the chemistry time step and calls the other chemistry subroutines, REACT and JIM, as many times as

needed to reach the position (or time) dictated b·· the fluid dynamic step. It also uses the species mass fractions at the end of each step to compute the enthalpy of the gaseous mixture and its temperature.

(4) Subroutine CLEM - The program solves a set of linear, nonhomogeneous, algebraic equations. The coefficient matrix and the constant term column matrix are grouped into a single matrix, which is then triangularized by reducing all the elements on one side of the diagonal to zero. At the end, one of the unknowns can be obtained directly and the others are then calculated by substitution.

(5) Subroutine DENSE - The mixture molecular weight is computed from the species mass fractions and the density is obtained from the perfect gas equation of state.

(6) Subroutine FSEQL - To solve the mixing layer problem using the equilibrium chemistry option, it is necessary to begin with equilibrium mixtures in the two freestreams. Subroutine FSEQL is called by MAIN as part of the initialization process to compute the required equilibrium mass fractions (from subroutine HFEQL) and temperature on each side of the dividing surface.

(7) Subroutine HEAT - This subroutine uses the coefficients provided in subroutine BEGIN to calculate the constant pressure specific heats and enthalpies of each species. Also obtained are the mixture specific heat and enthalpy, as defined by the mixture rules previously stated.

(8) Subroutine HFEQL - HFEQL is a special purpose routine designed to compute the species composition of an equilibrium mixture of H, F, H_2, F_2, and HF. Temperature and density of the mixture are assumed known for this solution. Portions of HFEQL are also used by FSEQL in its determination of freestream composition and by REACT to obtain equilibrium constants.

(9) Subroutine INGRT2 - The boundary layer input option is based on prescribing the behavior of the velocity and temperature profiles (presently these are simple power law profiles) over a distance specified by the boundary layer thickness. Since the initial profiles must be provided in the stream function plane, this subroutine is used to perform the transformation from boundary layer profiles in the y coordinate system to profiles in the ψ

coordinate system. A quadratic interpolation scheme is employed to obtain an evenly spaced ψ mesh from the unevenly spaced mesh resulting from this transformation.

(10) Subroutine JIM - The expressions to be solved for the unknown d_{i1} and d_{i2} coefficients form a system of 10 linear, nonhomogeneous, algebraic relations in 10 unknowns. The coefficients of these 10 unknowns, as well as the constant terms in the equations, are computed in this subroutine. The program then calls subroutine CLEM to solve the resulting matrix and uses the results to calculate the post-reaction mass fractions.

(11) Subroutine ØNE - This program calls subroutines PRESS, DENSE, and HEAT to calculate the pressure, density, specific heat, and enthalpy. It then calculates the values of the physical transverse coordinate, y, from the values of the stream function, ψ. The viscosity is obtained by calling subroutine VISC. The program keeps track of the number of axial stations and checks to see if the desired total distance downstream has been reached. If this distance has been covered, subroutine PRINT is called to write the final results.

(12) Subroutine PRESS - The input data provided in the main program contain pressure regions and a pressure polynomial for each region. These data are used by this program to compute the pressure and axial pressure gradient for a given value of the x coordinate.

(13) Subroutine PRINT - The purpose of this subroutine is to write the results obtained for values of various flow-field variables. It is called periodically from subroutine TWØ, as controlled by a printing interval specified by input, and from subroutine ØNE when the final step is completed. Variables whose values are printed include the y and ψ coordinates, temperature, enthalpy, density, velocity, fringe shift, Mach number, and species mass fractions on each streamline in the mixing region.

(14) Subroutine REACT - This subroutine calculates the forward and backward reaction rate constants for a given temperature. Subroutine HFEQL is called to provide the equilibrium constants needed for this calculation. Using the reaction rate constants, the coefficients of a_{ij} and the constants C_i of the previously developed differential equations for $\dot{y}_i$ are computed for use by subroutine JIM.

(15) Subroutine TWØ - The first step involved in this subroutine is the establishment of an axial step size that satisfies the numerical stability requirements of the chosen explicit finite difference scheme. The program has options for frozen, equilibrium, or finite-rate chemistry. In the case of frozen flow, the boundary layer equations can be solved without evaluating the species production terms. Equilibrium and finite rate problems call subroutines WDØTI2 and WDØTI, respectively, to obtain the updated information regarding chemical species concentrations at the end of a given interval. Once this is done, the program is ready to solve the mixing layer equations. The program tests for errors, with particular regard for negative species concentrations. If an error condition is detected, the problem will ultimately be terminated after printing the results. Otherwise, the program sets up tests to determine whether there is any need for increasing the width of the mixing zone. These tests check the velocity, temperature, and species mass fraction profiles for zero slope at the upper and lower edges. Because these profiles approach free-stream values asymptotically, a small finite value rather than absolute zero is used as a minimum slope requirement. The program automatically adds streamlines as needed as it marches downstream. To control the total number of streamlines being carried in the mesh, there is a provision for doubling the mesh size by discarding every other streamline. The permissible maximum number of streamlines is controlled by an input variable.

(16) Subroutine VISC - This subroutine computes the turbulent eddy viscosity according to the model previously discussed. Options for other viscosity models can be incorporated in this subprogram or another specialized version can readily be substituted.

(17) Subroutine WDØTI - The initial operations carried out in this program involve tests to see if subroutine TWØ has either doubled the mesh size or added streamlines to the mixing zone since the last chemistry calculation. If one of these procedures has occurred, appropriate adjustments are made to several parameters affecting the chemistry computations. The program then computes the diffusion time step ($\Delta x/u$) on each streamline and calls subroutine CHEM to calculate the new temperature and species mass fractions at the end of this time step.

(18) Subroutine WDØTI2 - This program performs an iterative determination of the equilibrium temperature, density, and species composition at the end of each fluid dynamic mixing step. The values of these properties resulting from the mixing process are determined in subroutine TWØ, and are modified here to reflect a new equilibrium state. Subroutine HFEQL is called to compute mass fractions for given temperature and density. Because the final temperature depends on enthalpy (and, thereby, on species mass fractions) and the final density depends on the temperature and mixture molecular weight, an iterative process is required to produce a solution for all of these variables.

3. RESULTS OF ANALYSIS OF PARALLEL TURBULENT MIXING LAYERS

Three cases were investigated using the mixing analysis program. The data for these cases represent two types of experimental runs in the parallel mixing facility. In one run a 50% mixture of fluorine and helium (by volume) was used for one stream, while a 50% mixture of hydrogen and argon formed the other stream. For the other run the argon was eliminated on the hydrogen side. Both of these situations were investigated analytically using finite-rate chemistry, and the former run was also computed using the frozen chemistry program option. Initial free-stream conditions used for these calculations are provided in Table XI. In all cases, the wall temperature of the splitter plate was assumed to be 295°K and the boundary layers were computed using 1/7 as the power for the power law profiles. The mixing parameter, σ, was taken as 20 for the reacting flows and 37 for the frozen case.

a. Chemically Frozen Flow with Argon - Consider first the results shown in Figures 59 thru 61 for the chemically frozen flow with argon present (Run 72091301). Frozen chemistry does not represent a realistic situation for hydrogen/fluorine mixing flows. However, it is useful to illustrate the results of mixing occurring without chemical reaction before proceeding to the reacting case. Note that the ordinate scale of these figures is greatly expanded relative to that used in Figures 62 thru 67.

Table XI

INITIAL CONDITIONS FOR MIXING LAYER ANALYSES

Run No.	Species Mass Fraction	P, dynes/cm^2	u, cm/sec	T, °K	δ_{BL}, cm
72091301	F 0.4162 F_2 0.4886 He 0.0952	6.306×10^4	2.050×10^5	264	0.0825
	H_2 0.0478 Ar 0.9522	6.306×10^4	2.570×10^5	450	0.1375
72111602	F 0.417 F_2 0.488 He 0.095	4.099×10^4	1.990×10^5	264	0.0765
	H_2 1.000	4.099×10^4	4.24×10^5	159	0.1275

Four temperature profiles are shown in Figure 59 to illustrate the development. The initial profile indicates the effect of a wall that is cold relative to one stream and hot relative to the other. As the flows mix, turbulent viscous heating occurs, causing the temperature to rise in the regions of maximum shear. Large gradients in the velocity profile due to boundary layers cause highest local shear levels in profiles closest to the splitter plate. The temperature profile at 0.502 cm shows residual effects of the zero velocity gradient (and consequent zero shear) at the minimum of the velocity profile. As mixing continues, the velocity gradients decrease in magnitude and shear becomes less important. At the profile position 4.466 cm downstream, the temperature peak has decreased to about 300°K as the mixing process dominates.

Figure 60 shows profiles of fringe shift computed as discussed in Section II. These profiles reflect the local density variation, as well as the species concentrations. In the constant pressure situation that holds here, the maximum in the initial profile is related to the wall temperature, which is colder than freestream on the hydrogen side. As mixing proceeds, the density decreases as the temperature increases. This causes the maximum in the fringe-shift profile to disappear and a minimum is formed in its place. Note that the depth of this minimum is somewhat smaller at the 4.466 cm position than at the preceding station. Apparently, the mixing process is now removing thermal energy from the central portion of the mixing layer at a faster rate than it is being generated. This phenomenon can also be observed in the temperature distributions of Figure 59.

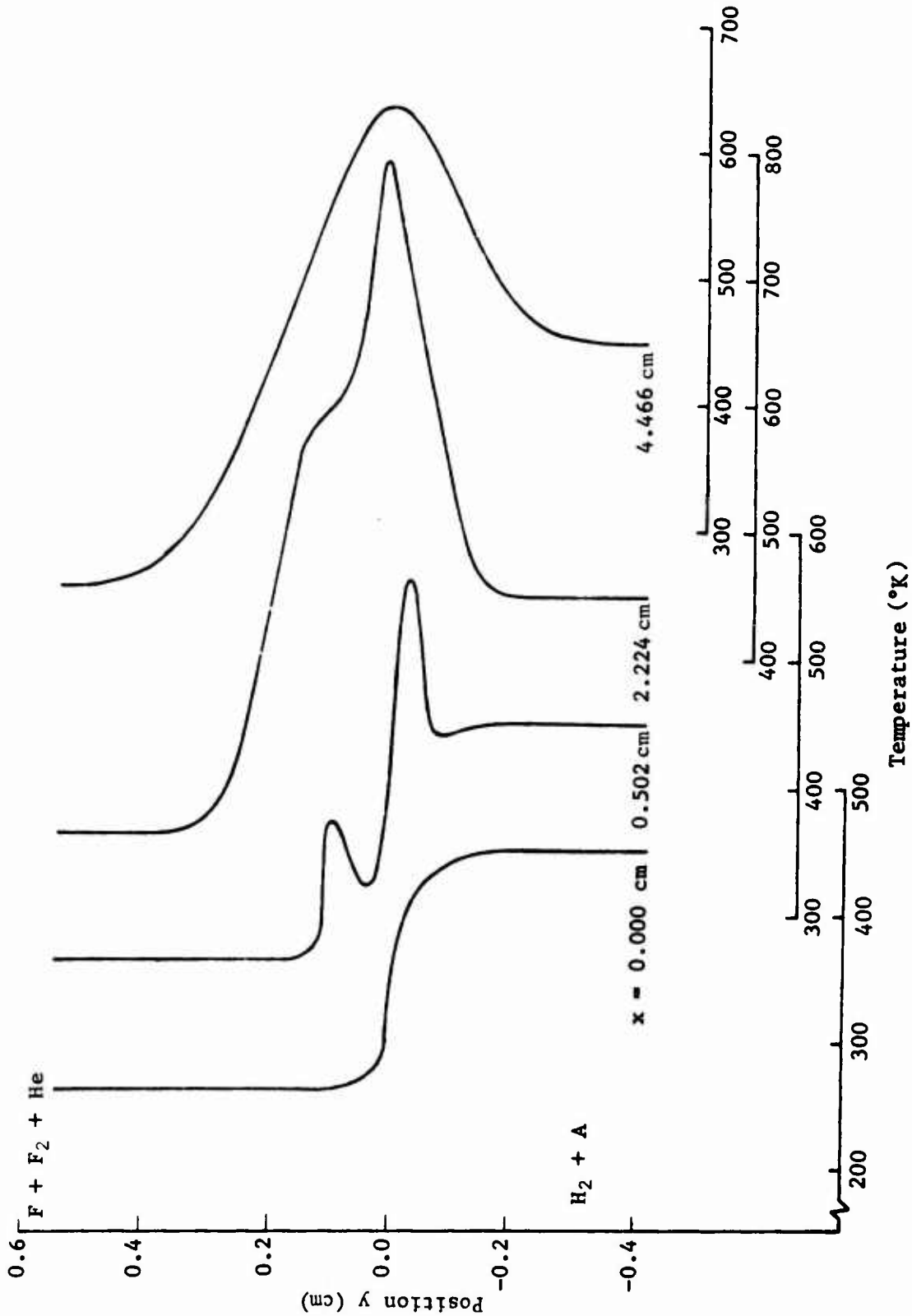

Figure 59. Computed Temperature Profiles for Run 72091301, Frozen Chemistry

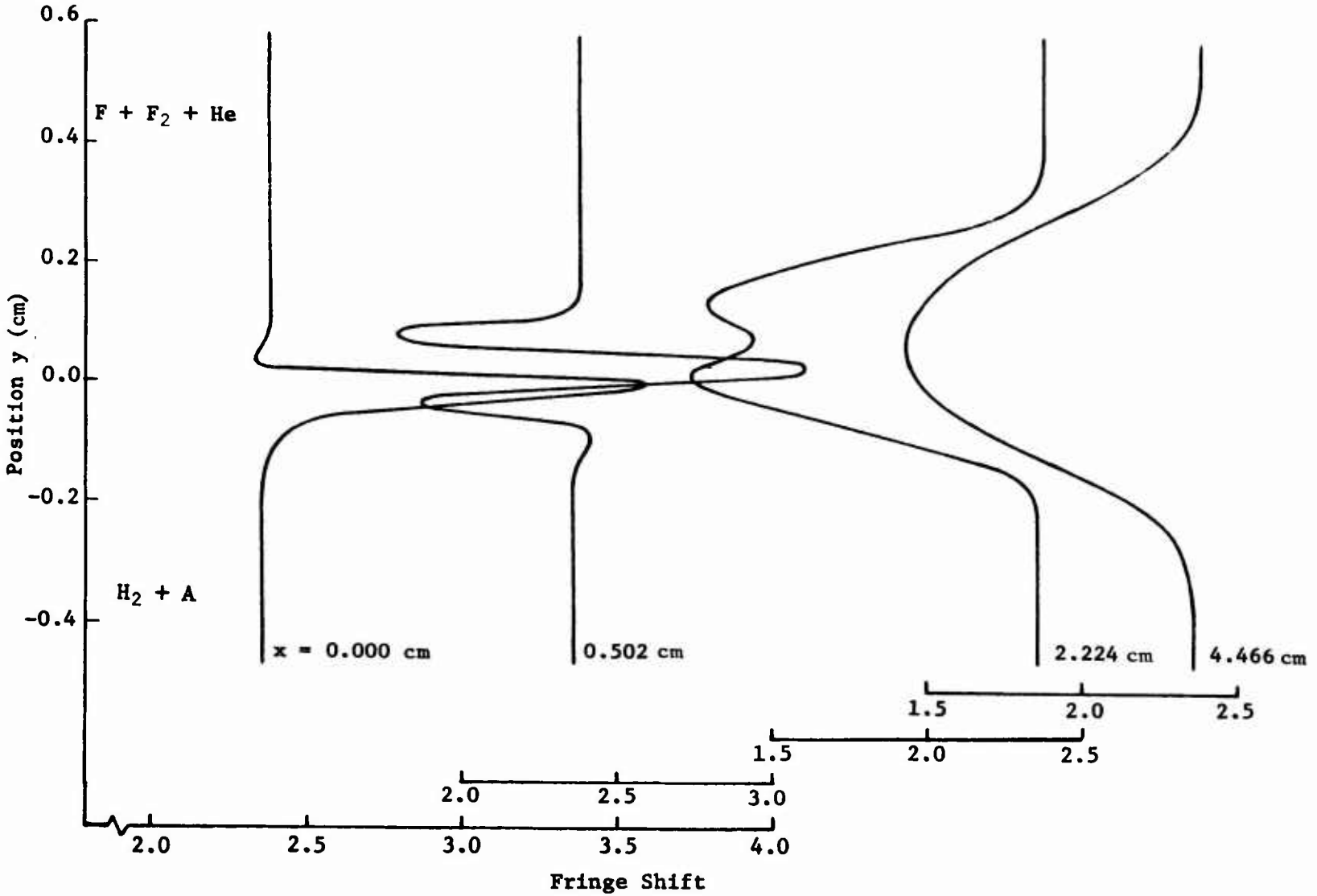

Figure 60. Computed Fringe-Shift Profiles for Run 72091301, Frozen Chemistry

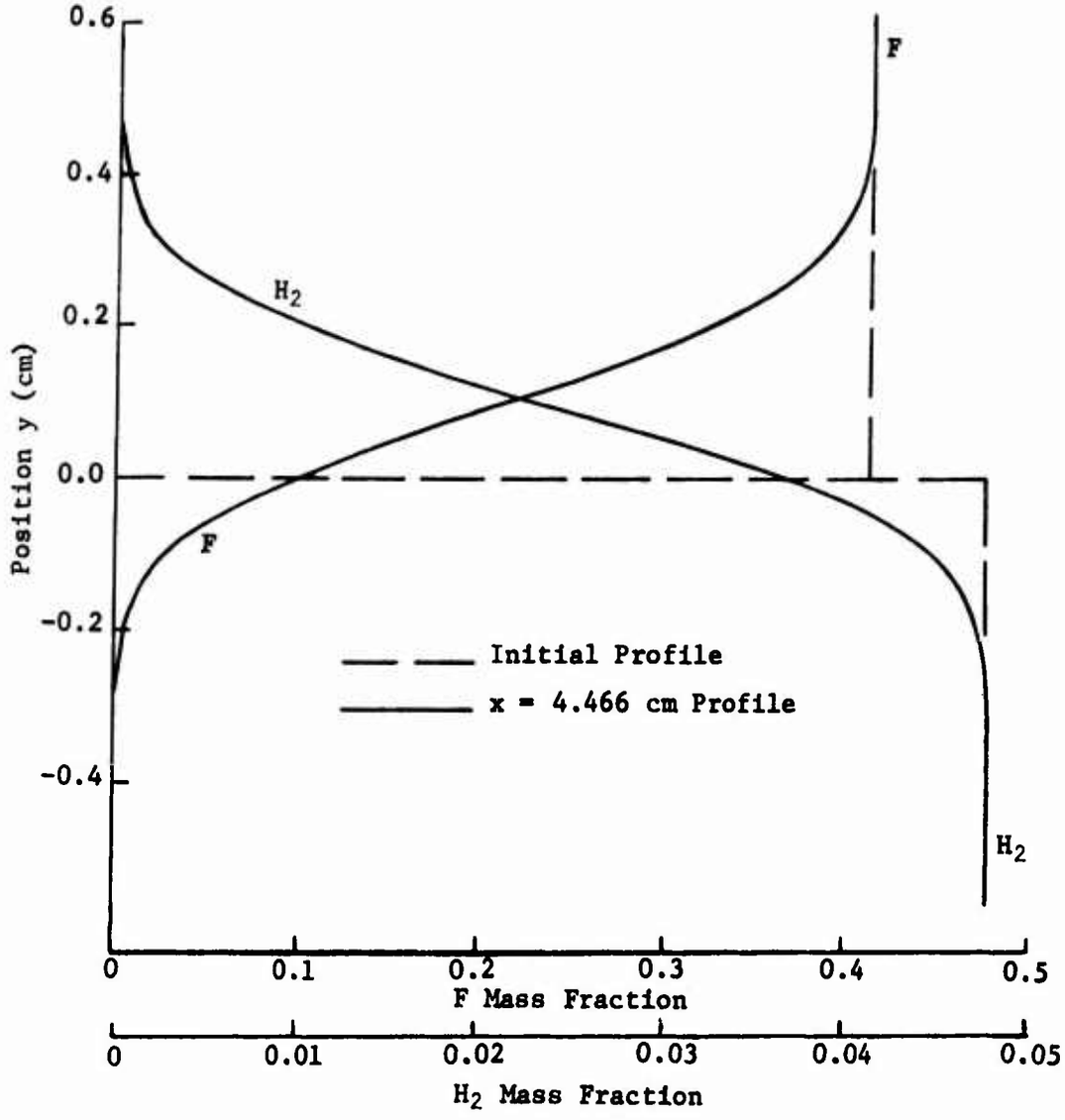

Figure 61. Computed H_2 and F Species Profiles for Run 72091301, Frozen Chemistry

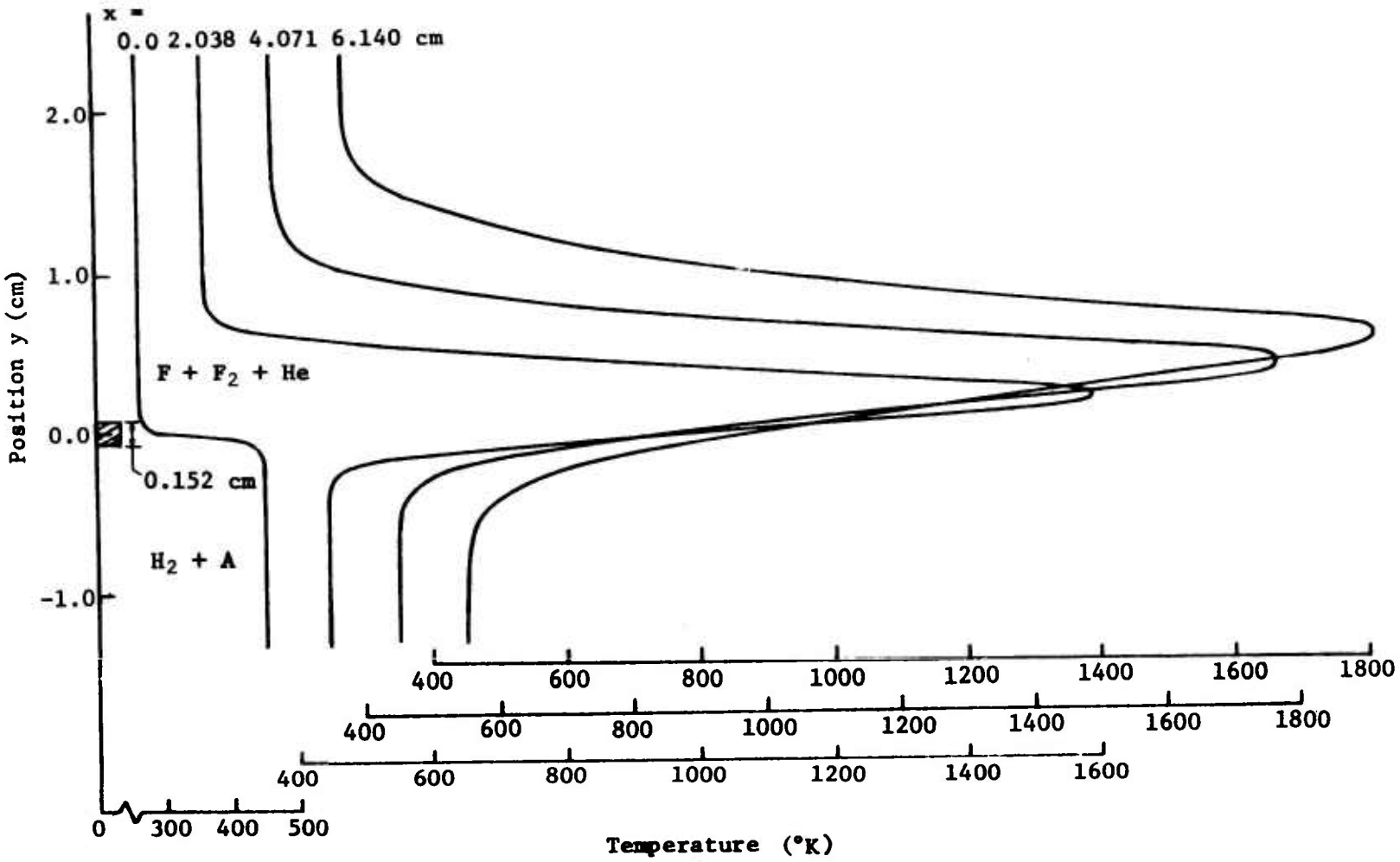

Figure 62. Computed Temperature Profiles for Run 72091301, Nonequilibrium Chemistry

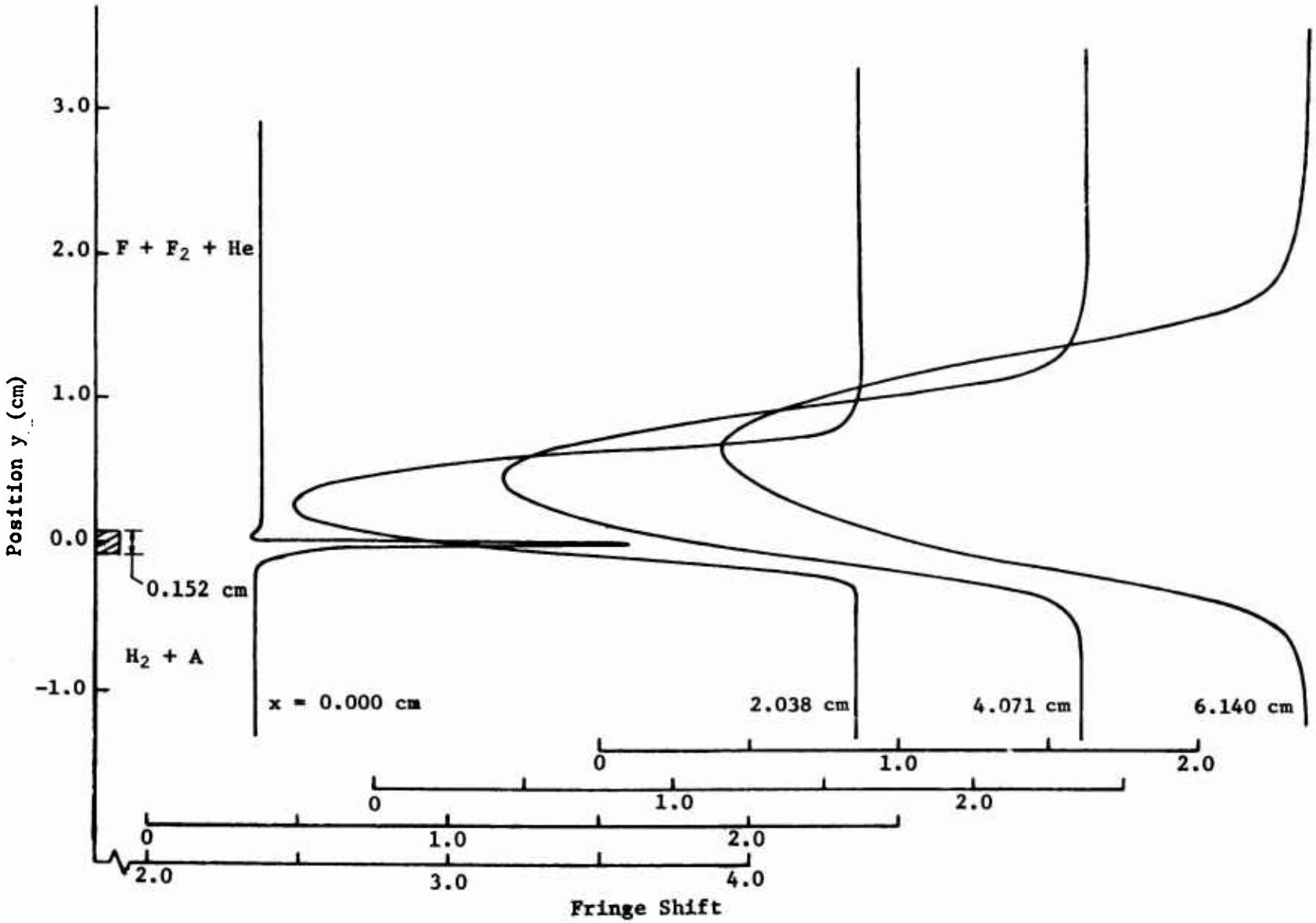

Figure 63. Computed Fringe-Shift Profiles for Run 72091301, Nonequilibrium Chemistry

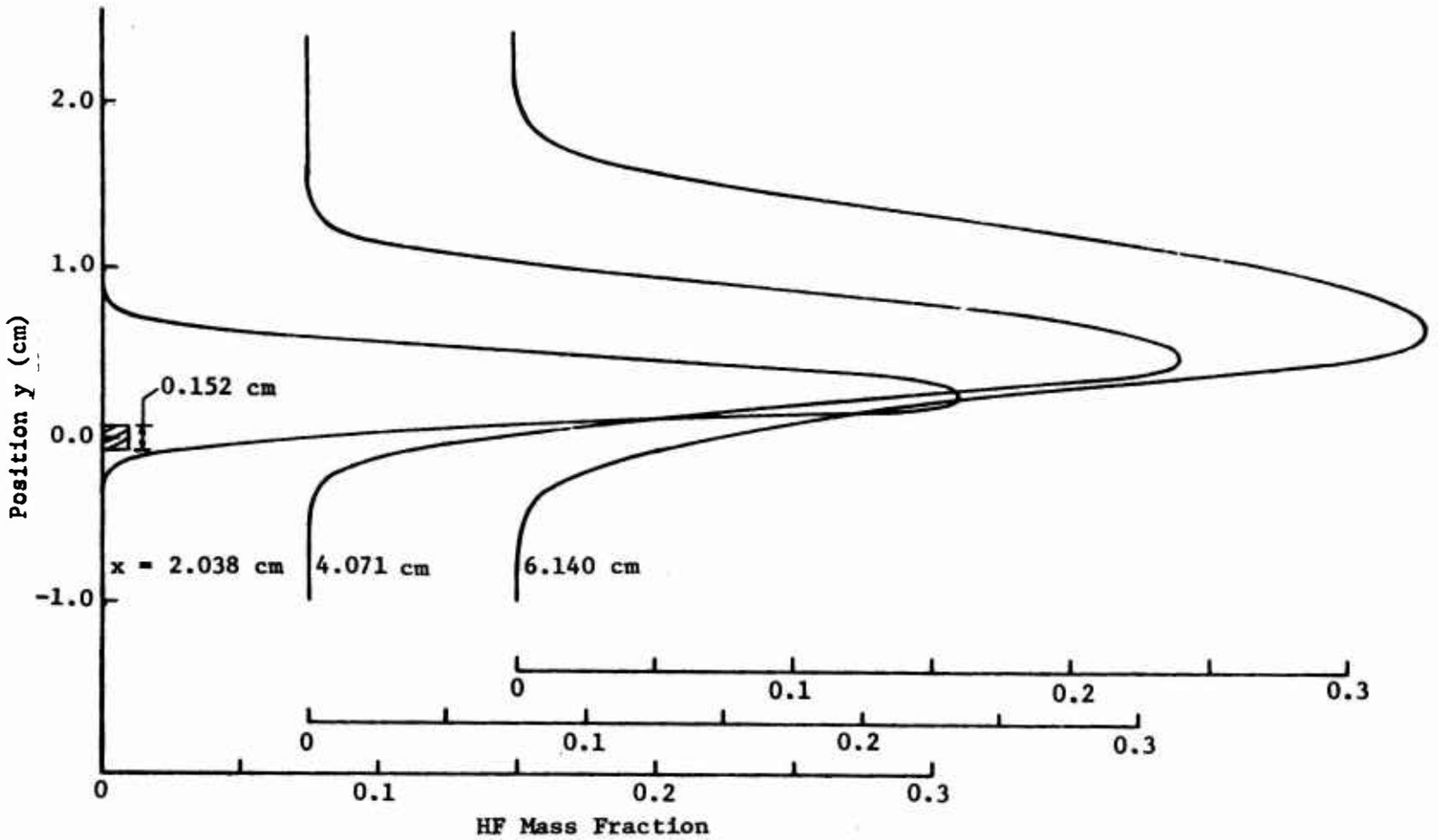

Figure 64. Computed HF Species Profiles for Run 72091301, Nonequilibrium Chemistry

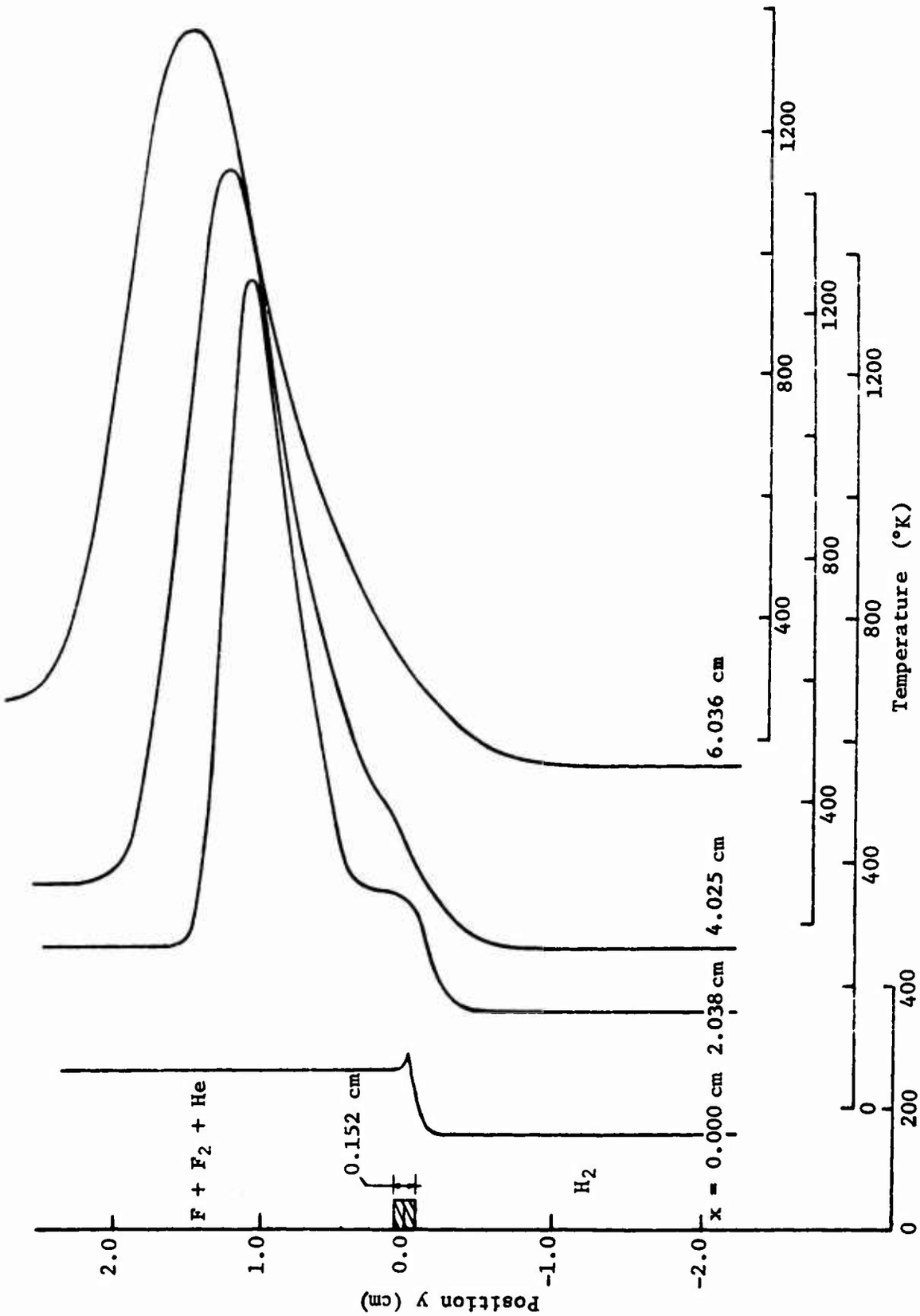

Figure 65. Computed Temperature Profiles for Run 72111602, Nonequilibrium Chemistry

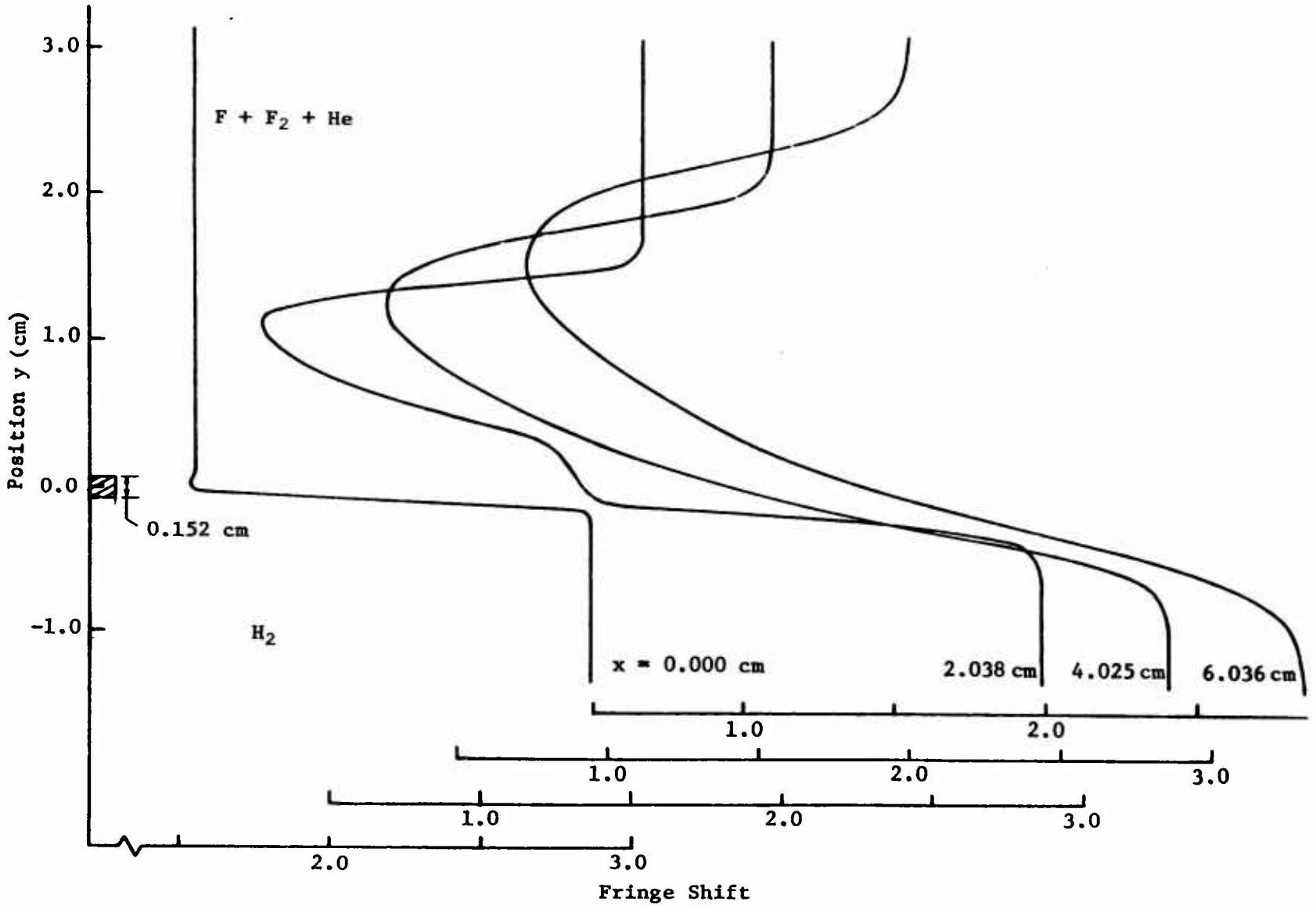

Figure 66. Computed Fringe-Shift Profiles for Run 72111602, Nonequilibrium Chemistry

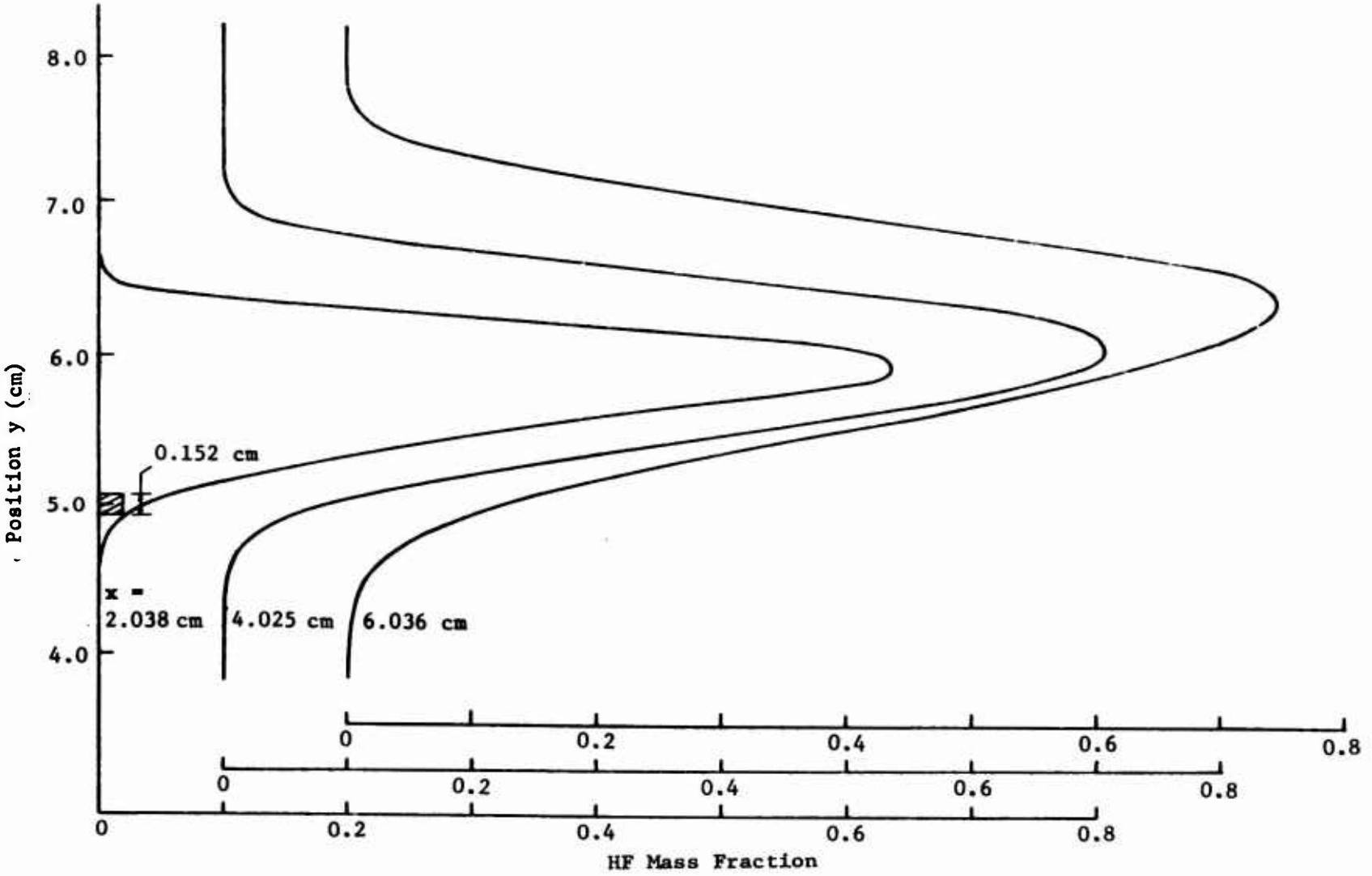

Figure 67. Computed HF Species Profiles for Run 72111602, Nonequilibrium Chemistry

Figure 61 presents the mass fraction profiles for the F and H_2 species at the initial station and 4.466 cm downstream. These profiles are typical of the shape attained when no chemical reactions are allowed and show a smooth transition from freestream values on one side of the mixing zone to zero on the opposite side.

b. Reacting Flow with Argon - The second computation is represented by Figures 62 thru 64. The initial data are the same (Run 72091301) as the preceding case, but finite-rate chemical reactions are now considered in the analysis. The processes that occur with frozen chemistry still take place in this situation, but the temperature profiles of Figure 62 illustrate that they are greatly overshadowed by the results of combustion energy release. This energy release is confined to a relatively narrow region of the flow. The mixing region at the 6.140 cm station has a total width of about 3 cm, with only about 1 cm showing significant temperature rise. This result is influenced by the chosen eddy viscosity model and the value of the associated mixing parameter, σ. Smaller values of this parameter would cause higher mixing rates and somewhat faster spreading of the reaction zone. Our experience and the data from Figure 56 indicate that the value $\sigma = 20$ is appropriate for reacting flows in the present velocity range. However, until substantiation is obtained through satisfactory correlation with experimental data, this must be considered as an assumption for analysis of the hydrogen/fluorine mixing process.

The fringe-shift distributions of Figure 63 react primarily to the density and show the expected development of a deep minimum in the high-temperature region. Because the temperature rise between the stations at 2.038 and 6.140 cm is not large, no great change is found in the value of the minimum in this region. The initial profile is identical to that seen in the frozen-chemistry case, although plotted on a different scale than in Figure 60.

Figure 64 shows how the combustion process contributes to the potential for lasing activity, as measured by the fraction of the flow that forms hydrogen fluoride. Because no HF exists until mixing commences, no initial profile is required here. As would be expected from the associated temperature distributions, the region of high HF mass fraction is fairly narrow and the peak value increases slightly as the flow moves downstream. A comparison of mixing layer growth between this case and the preceding frozen-chemistry case shows that the influence of combustion is dominant. Chemical processes control the turbulence level and fluid mechanical effects, e.g., velocity differences are secondary.

As a result, the HF species mass fraction can be considered as a primary measure of the mixing region width, while the growth as indicated by fluid mechanical properties is constrained to follow the trend established by the chemistry. This produces nearly identical mixing layer widths, independent of the property chosen as an indicator.

c. Reacting Flow without Argon - Figure 65 illustrates the streamwise development of the temperature distribution for the case in which pure hydrogen forms one stream. The density in this stream is approximately 1/5 of the density of the corresponding flow with argon. Additionally, the wall is now "hot" with respect to both freestream temperatures. Note that the peak of the temperature profile moves more rapidly toward the fluorine side of the flow than was the case in Figure 62. Abramovich (Ref. 48) has shown that a mixing layer spreads preferentially into the lower velocity stream when both flows have the same density. In the present cases (both Run 72091301 and Run 72111602) the density on the fluorine side is higher than on the hydrogen side, but the same trend with velocity is observed. However, comparison of Figures 59 and 62 (which differ only in terms of combustion effects) indicates that preferential spreading into the fluorine stream occurs more rapidly with combustion than with the chemically frozen flow. It appears, therefore, that other parameters in addition to velocity are important in determining asymetrical growth of the mixing region. Understanding of the pertinent mechanisms will require further study.

Figures 66 and 67 show the profiles of fringe shift and HF mass fraction for the pure hydrogen case. The main features of these distributions are reflections of corresponding features in the temperature profiles discussed in the preceding paragraph. Of course, the hydrogen-fluoride mass fraction is much larger than it was when argon was present as a diluent. Note also that the mixing layer at any station is substantially wider now than was the case previously. This is largely due to the higher velocity of the pure hydrogen stream.

4. EXTENSION OF ANALYSIS TO INJECTION MIXING

The flow conditions in the immediate region of injection are quite complex. Figure 68 depicts some of the features that can be expected to exist. Because the splitter plate height is large in comparison to the injector slot height, a low-velocity circulation flow will be present in the base region of the plate. As indicated, the circulation will consist of two cells which mix gases from the plume and external flow, with the possibility of burning at low velocities. It is downstream of this region that the two supersonic streams impinge on one another and supersonic turbulent mixing occurs. The flow deflections associated with the impingement of the two streams introduce a shock in the external flow, along with a new shock in the plume flow. The new shock reinforces the boundary shock that already exists in the plume flow.

An analysis of the flow situation depicted in Figure 68 has been performed. Plume flow fields were generated for conditions of quiescent surroundings and also Mach 5 external flow, both with an ambient pressure of 30 torr. Although neither of these two boundary conditions properly describe the complex condition that exists, the results do provide an approximation to the range of pressure and velocity conditions that exist along the boundary. The intent of this analysis was to determine if the Lockheed method of characteristics plume program (Ref. 49) could be used to establish the pressure and velocity distributions. These distributions could then be used to determine the characteristics of the mixing and combustion region.

Some of the results of the analysis are shown in Figure 69, where plume boundaries and internal shock structure are plotted for the two external flow conditions. In both cases the pressure and Mach numbers along the boundary are nearly constant. For the quiescent conditions, the boundary Mach number is 5.02 at a pressure of 0.0394 atm and for the Mach 5 freestream condition, the boundary Mach number is 2.62 at a pressure of 0.9987 atm.

Because of the large variation in pressure between these two cases and the strong influence of external flow, it was decided that the analysis must be refined further to obtain a realistic description of the boundary conditions between the two streams. This refinement would involve making minor modifications to the method of characteristics program to provide a capability of treating combined boundary conditions, i.e., quiescent conditions that simulate the circulation region followed by a supersonic external flow of varying Mach number. Unfortunately, this modification exceeds the scope of the present program.

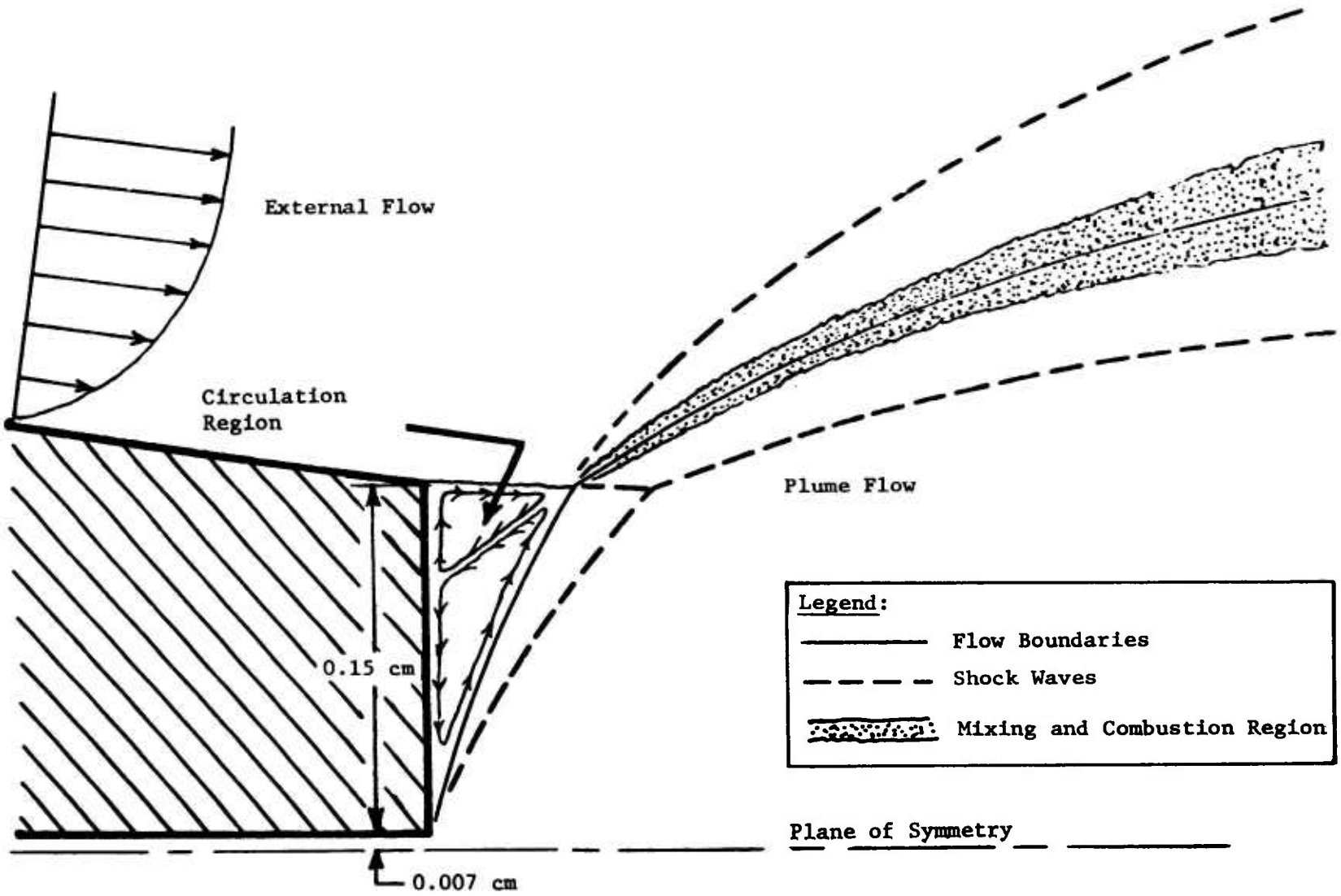

Figure 68. Injection Mixing Flow Field

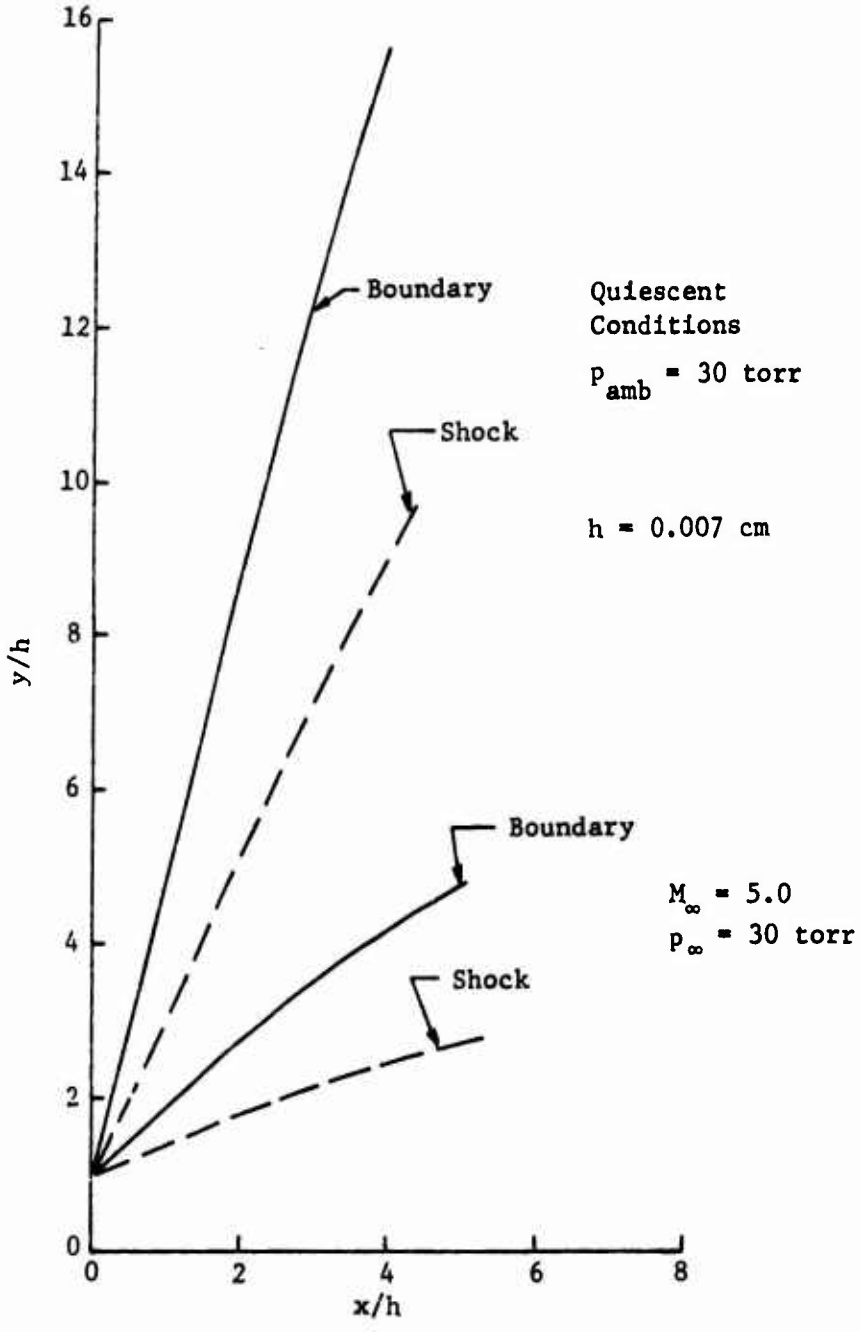

Figure 69. Plume Analysis Results

Once the plume flow field has been adequately established, the initial approach to the mixing analysis will involve superposition of a mixing layer on the plume boundary. The required profiles of velocity and temperature will be obtained from the plume and free-stream at the point of impingement. Flow direction at this point should approximately satisfy the mixing program assumption of parallel flow. Of course, this analysis is appropriate only while the mixing layer remains small relative to the plume, so that its influence on the overall flow is also small. How well this condition will be satisfied can only be determined by the actual computations and remains to be resolved.

Further refinement of the injection mixing analysis will probably involve reformulation of the basic equations to include provision for lateral pressure gradients. The effort required to accomplish this change is necessarily much greater than that involved in implementing the relatively straightforward superposition approach. Justification for such an effort must depend largely on the success or failure of the latter procedure in correlating the injection mixing data.

SECTION V

DISCUSSION OF RESULTS

As earlier discussions have indicated, the experimental objectives of this investigation were pursued in two different facilities using variations of a basic technique developed at Martin Marietta for observing the mixing and chemical reaction of hydrogen/oxygen streams. The primary diagnostic equipment employed with each of these facilities consisted of a Mach-Zehnder interferometer for mapping averaged density profiles across the mixing layer, a rapid scanning infrared spectrometer for mapping radiative emission within the mixing layer, pitot probes for surveying pressure across both the mixing layer and the nozzle exit region, and static side-wall pressure taps for determining nozzle exit static pressure. In addition, attempts were made to measure the nozzle exit temperature with an unshielded thermocouple probe.

The major emphasis in the experimental phase of this study was directed towards the injection mixing experiments. The injection facility also was used to perfect the diagnostic techniques and test procedures that were used later with the parallel mixing facility. The primary emphasis in the analytical phase of the study was devoted to refining and modifying an existing analytical model of the reacting turbulent shear layer. The remainder of this section will be devoted to a discussion of (1) the experimental results obtained in both the injection and the parallel mixing facilities, and (2) a comparison of the theoretical results with the experimental results obtained in the parallel mixing experiments.

1. EXPERIMENTAL RESULTS

a. Injection Mixing

Experimental observations within the test section region of the hydrogen injection facility have provided quantitative information about the overall characteristics of the mixing layer. In particular, the growth rate, radiative emission intensity, and averaged density profiles have been obtained under a variety of test section conditions for two different injection splitter plate geometries.

The snapshot interferograms presented in Figures 30 and 31 of Section III show the overall flow characteristics for two different injection geometries with five different injection conditions, including a no-reaction helium injection case and a no-injection nozzle flow case.

A comparison of the fringe-shift profiles between the 150-psi helium injection interferogram and the 150-psi hydrogen injection interferogram definitely indicates that the chemical reaction is responsible for the considerably greater fringe distortion that occurred within the mixing layer of the latter case. The other general conclusion that can be drawn from a simple observation of these interferometric records is that the downstream extent of the mixing layer is greater for the 150-psi injection cases than it is for the lower injection pressures. As explained in detail in Section III, a measure of the mixing layer width can be obtained from the interferograms. The results presented in Figure 36 indicate that, for the orifice injector geometry, the mixing layer width increases with increasing injection pressure. A decrease in mixing layer width is recorded for the slotted injector geometry, especially for the 10-torr nominal test section static pressure. In both cases, the mixing layer widths for the 50-psi injection pressure are almost identical for both the 10-torr and the 15-torr nominal background pressures.

Perhaps the most interesting aspect of the comparison between the slotted and the orifice injection cases is shown in the averaged density profiles presented in Figure 38. Several assumptions were required in arriving at these averaged density profiles, the most significant being that the minimum fringe shift was identified as due primarily to HF species. This assumption, although seemingly arbitrary, is based upon the theoretical results obtained in the parallel shear flow mixing analysis. As indicated in Figure 62 of Section IV, the peak HF species number density always corresponds to the minimum fringe-shift position. The averaged number density profiles presented in Figure 38 show the gradual decrease in number density moving downstream along the plane of injection. A comparison between results for the slotted hydrogen injection and the orifice hydrogen injection shows higher concentration (by a factor of 2) of hydrogen along the centerline plane for the slotted injection scheme. This is a direct result of the higher mass flow through the larger exit area of the slotted injector. It is also very significant to note that the indicated HF number densities (corresponding to minimum fringe-shift position) for the 150-psi and the 50-psi slotted hydrogen injection are almost identical. This observation is in agreement with the measured infrared emission intensities shown in Figure 47. That is, the specific radiative intensity at any downstream position does not change with increasing injection pressure, at least between 50 and 150 psi. This indicates that even at 50 psi the mass flow of hydrogen is sufficiently large that the reaction is mixing controlled. Hence, changing injection pressure above 50 psi will not change the degree of mixing on the molecular scale, although it does change the geometry of the mixing region.

The results of the pitot probe survey served to indicate that the flow fields were indeed uniform within the nozzle exit region and across the width of the test section. A limited effort was devoted to use of the temperature probe because of late delivery of the necessary parts. However, results were obtained that very clearly indicated that a shielded, vented one-mil thermocouple probe using a tungsten/tungsten-rhenium junction will adequately measure the temperature within reacting mixing layers for shock tunnel flows.

b. Parallel Mixing

Unlike the injection mixing case, the parallel mixing snapshot interferograms do not provide a significant level of information about the mixing zone until the data are completely reduced and compared with theoretical predictions. Typical interferograms of the parallel mixing layers are shown in Figure 39 and the reduced fringe-shift results at various downstream stations are shown in Figures 40 and 41 of Section III. Conditions for two of the experimental cases presented in Figure 40 have been used as input for the theoretical model discussed in Section IV and a detailed comparison for these two cases will now be presented and discussed.

2. ANALYTICAL RESULTS

A detailed description of the theoretical model, developed in this study, for predicting flow-field properties within a turbulent shear flow mixing layer was presented in Section IV. As discussed therein, the criterion for ascertaining the existence of turbulence in a shear layer is based on the momentum thickness Reynolds number, Re_θ.

A problem in defining the state of the mixing layer exists if the initial boundary layers on the separating surface are laminar. It is well known that free shear layers are much more unstable than boundary layers. The critical momentum thickness Reynolds number for boundary layers is about 500, while for free shear layers it is about 1/3 of this value. Customarily the free shear layer Reynolds number is defined in terms of the velocity difference across the layer, $|u_1 - u_2|$. However, examination of the formation of a free shear layer from initially separated streams reveals a region of low energy gas that originated in the wall region of the boundary layer and continues to exist for a considerable distance downstream in the free shear layer. Therefore, the shear that is characteristic of the initial stages of the free shear layer is probably more closely proportional to $(u_1 + u_2)/2$ than to $|u_1 - u_2|$. This reasoning, coupled

with the fact that free shear layers are notoriously unstable and critically subject to such influences as free stream turbulence, acoustic environment, and separation surface roughness, leads to the assumption that if the sum of the boundary layer momentum thickness Reynolds numbers is near the critical value for free shear layers ($Re_\theta \sim 150$), the shear layer will be turbulent. Such an assumption has led to good correlations between theory and experiment.

Clearly, a transition region must exist between the end of the separating surface with laminar boundary layers and a fully formed turbulent free shear layer. At present, however, the sensitivity of free shear layer stability to anomalous disturbances is so little understood that it is impractical to account for such a transition region.

Values of Re_θ for each nozzle have been computed for the parallel mixing cases and the results are shown in Table VII. In all cases, the summation of the two values for adjacent nozzles does exceed the critical value of 150 and the mixing region must be considered turbulent.

A theoretical analysis of the mixing layer for two different parallel mixing experiments (Runs 72091301 and 72111602) has been completed. Experimental test conditions were used as input quantities for the computer program, along with computed nozzle wall boundary layers assuming 1/7 power profiles. A value for the mixing layer growth rate parameter, σ (an empirical parameter of the eddy viscosity model), was fixed at 20 for these first calculations. This is a very reasonable starting value for σ based on earlier Martin Marietta results that are also in agreement with results observed by Shackleford of TRW (Ref 40). Figures 70 and 71 show the comparisons between computed fringe-shift profiles and experimental data points for the two sets of conditions. Several noteworthy features are evident from the theoretical results: (1) computed fringe-shift profiles show the mixing proceeding preferentially into the fluorine side of the stream, as indicated by the minimum fringe-shift position (maximum HF number density) moving upward into the fluorine carrying stream with distance downstream; (2) width of the computed mixing region very nearly matches that of the experimental data; and (3) shapes of the experimental profiles are reasonably well predicted for each of the two appreciably different test cases.

The experimental data and the theoretical profiles of Figures 70 and 71 at first observation do not appear to be in good agree-

ment. The experimental points shown in these figures are in their true position relative to the abscissa when it is interpreted as a line parallel to an extension of the splitter plate. The theoretical computation, on the other hand, assumes coincidence in the directions of the abscissa and the flow velocity vector. However, due to the existence of a small mismatch in initial stream pressures, the velocity vector does not lie parallel to the splitter plate, but rather is rotated slightly toward the hydrogen stream. If a similar rotation is applied to the axis of theoretical results, the profiles are shifted in a manner that places the minimum fringe-shift locations much closer to those obtained experimentally. Figures 72 and 73 show the comparisons based upon this assumption and the improved agreement that results. It should be pointed out that the first experimental profile always shows the greatest influence of the splitter plate boundary layers. This effect has been noted in earlier work and can be accounted for in the analytical program by adjusting the initial boundary layer profiles.

A frozen flow (σ = 37) calculation was also performed using the conditions for Run 72091301 in order to compare the effects of a reacting and a nonreacting system. The results of this calculation are shown in the top half of Figure 70 and it is clear that the chemically reacting results are very much different than those for the assumed nonreacting case. The basic difference between the fringe-shift profiles computed in the frozen-flow case (arbitrarily assuming that no chemical reaction occurs) and the nonequilibrium case is the more limited extent of the mixing zone, as indicated by the widths of the depressions in the fringe-shift profiles at the downstream positions; that is, the growth rate for a chemically reacting mixing layer is greater than that for a similar nonreacting mixing layer. This phenomenon has been observed in previous experiments in this laboratory involving mixing layers with hydrogen/oxygen combustion.

Spectroscopic data from the parallel mixing experiments clearly indicate that no radiation beyond 3.2 microns was present. A conservative estimate of the number of excited HF molecules obtained from the infrared scans indicates that approximately 8.5×10^{14} excited HF molecules are present in a specified volume in Run 72111602. Using the computed HF mass fraction, the total number of HF molecules within the same volume was found to be 2.4×10^{15}. These results provide additional evidence that the analytical program correctly reflects the physical phenomena in the mixing region.

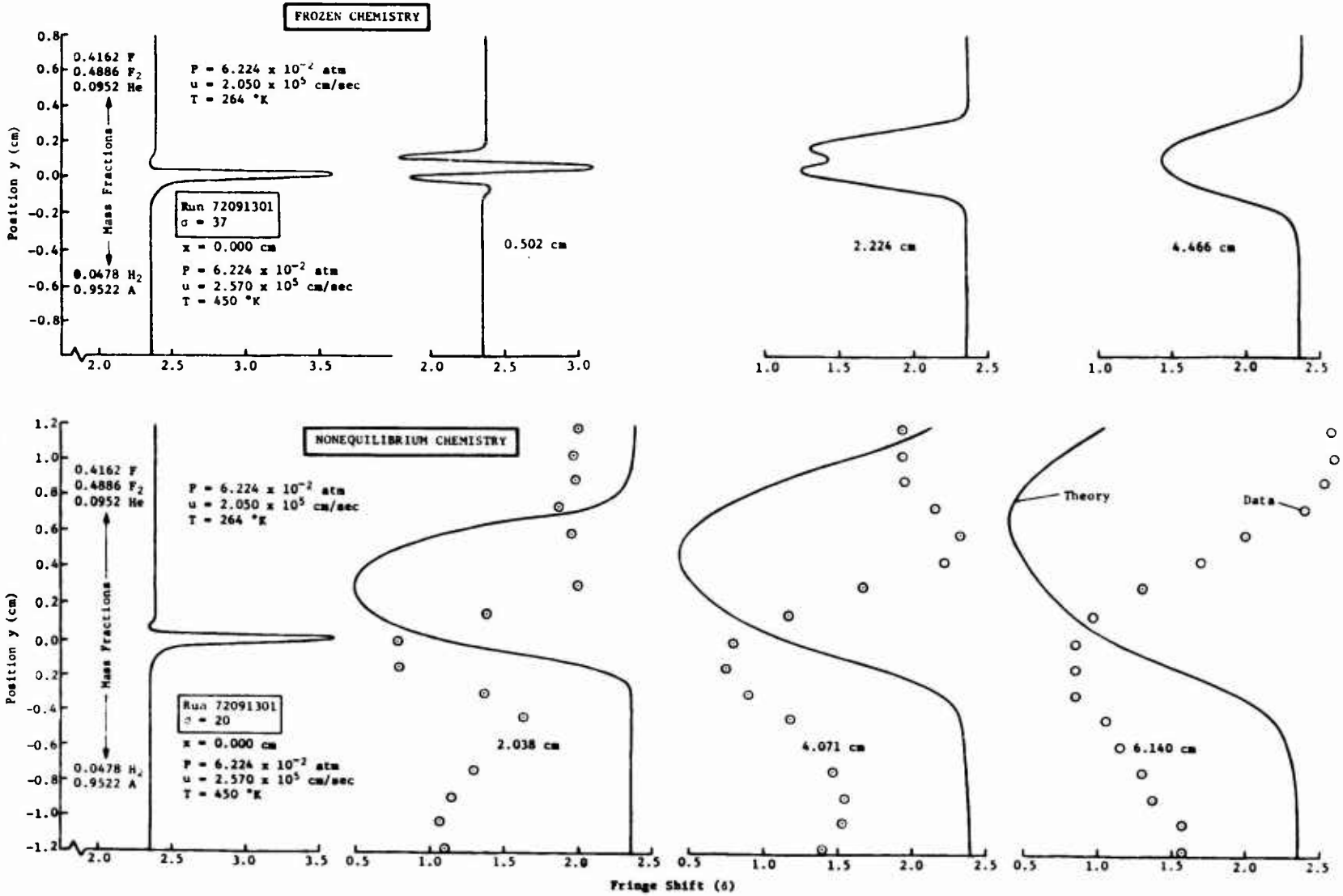

Figure 70. Run 72091301: Fringe-Shift Profiles

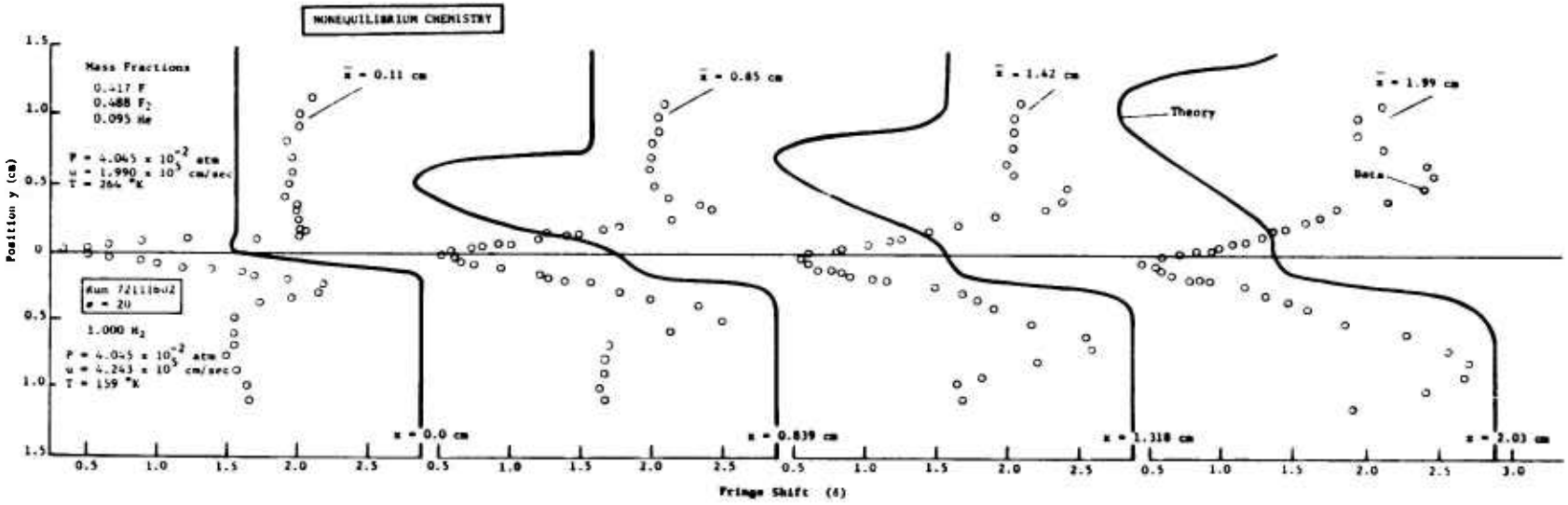

Figure 71. Run 72111602: Fringe-Shift Profiles

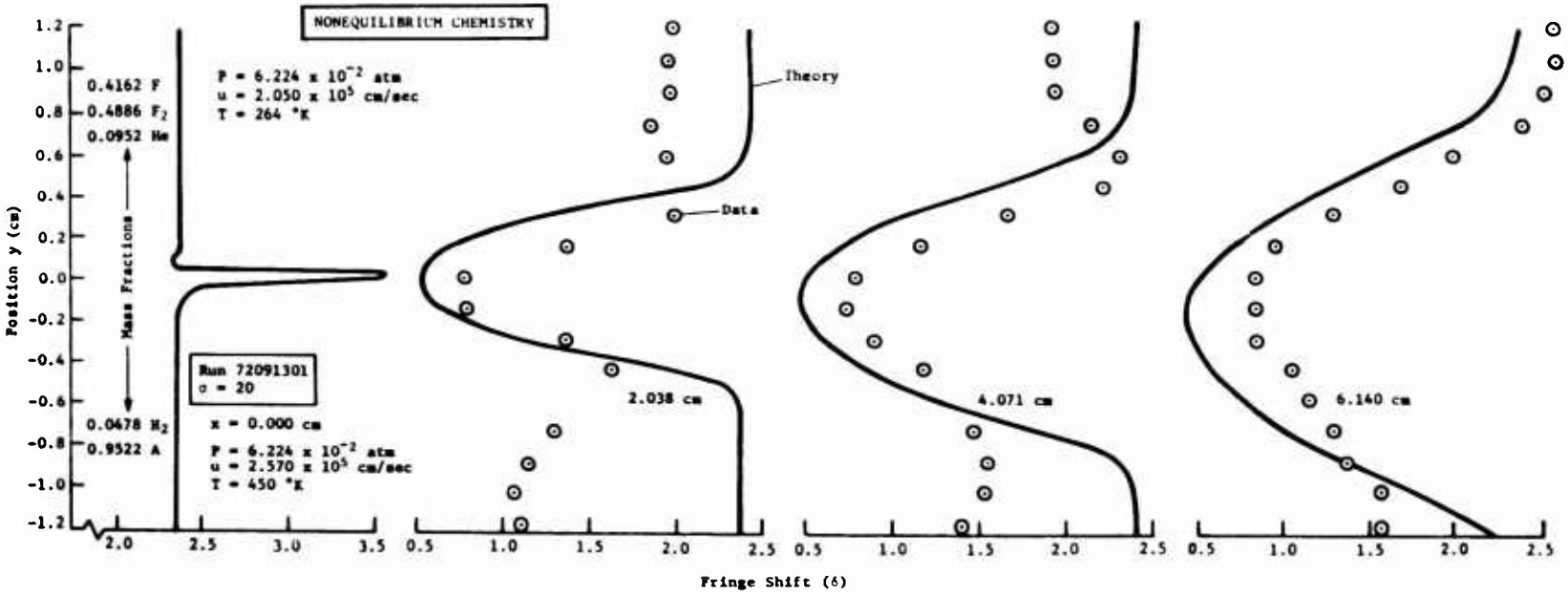

Figure 72. Run 72091301: Fringe-Shift Profiles

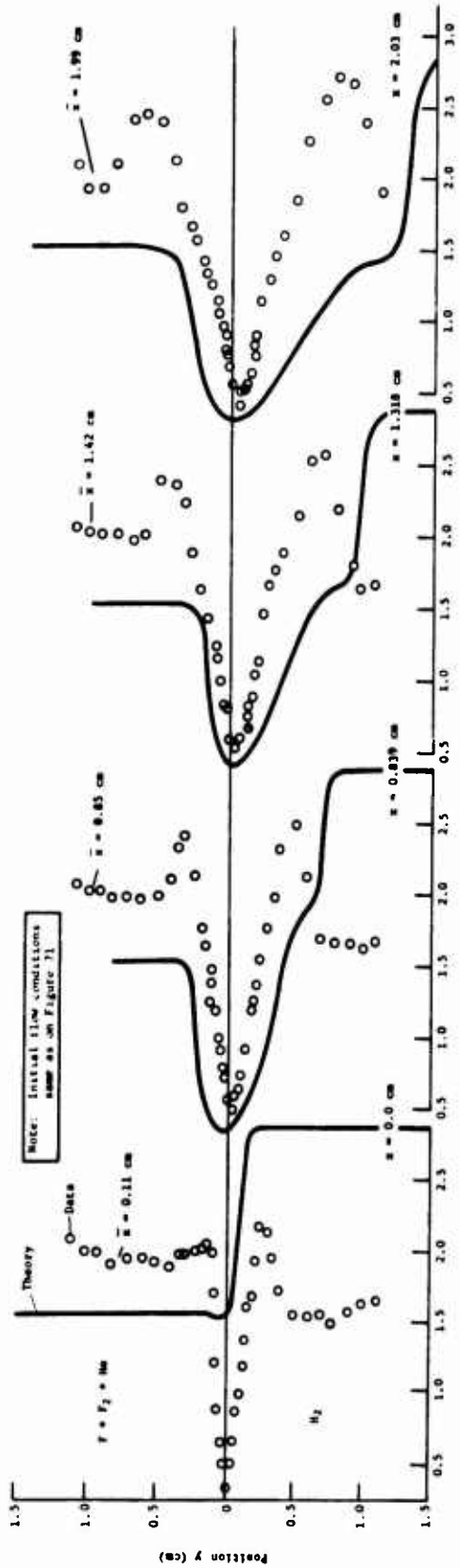

Figure 73. Run 72111602: Fringe-Shift Profiles

SECTION VI

CONCLUSIONS AND RECOMMENDATIONS

As indicated in the introductory remarks, initial studies with continuous flow chemical laser devices at several laboratories have demonstrated that a complex interrelationship does indeed exist between gas dynamic mixing phenomena and chemical kinetic reaction processes. An important objective of this study was to demonstrate the feasibility of using reasonably simple experimental techniques to simulate these complex mixing phenomena in such a manner that a variety of diagnostic techniques could be employed for detailed observation of the processes involved. This approach, in conjunction with supporting analytical efforts, should lead to an experimentally verified theoretical model of the mixing region that could subsequently be used to optimize the design of mixing regions for operational high-power chemical laser devices.

Two experimental facilities capable of closely simulating the operational conditions of existing continuous flow chemical laser devices have been described. Each of these facilities uses the reflected shock region of a conventional shock tube as a supply reservoir for supersonic two-dimensional nozzles. One facility is designed for investigating the mixing characteristics resulting from the sonic injection of cold hydrogen into a supersonic fluorine carrying stream. The second facility is designed for observing the shear layer mixing between two parallel supersonic streams when one stream contains fluorine and the other contains hydrogen. It has a unique split driven tube construction that produces two separate reflected shock region reservoirs to supply two adjacent two-dimensional nozzles. Both facilities include viewing windows with fields of view that encompass the mixing regions and the nozzle exit stations.

In our opinion, the results presented in this report clearly demonstrate that the experimental facilities are capable of simulating the mixing layer characteristics of either a hydrogen injection or a parallel mixing continuous flow laser device. Established experimental techniques have been adapted to each of these facilities to permit the mapping of critical flow-field variables within the mixing layer. An analytical procedure has been developed that predicts these flow-field properties in the particular case of parallel mixing and the predictions are in good agreement

with the experimental results for two widely different cases. These results demonstrate that the objective of an experimentally verified analytical procedure for detailed evaluation of the reactive mixing region within the optical cavity of a CW chemical laser device is realistically obtainable.

Recommendations for further work include --

1) extension of the analytical model to the injection mixing configuration;

2) extension of the experimental program to include wider selection of experimental configurations, including close duplication of operational device geometry;

3) addition of optical gain measurement to the diagnostics of the mixing region.

REFERENCES

1. Gaydon, A. G.; and Hurle, I. R.; The Shock Tube in High Temperature Chemical Physics, Reinhold Publishing Corporation, New York, 1963.

2. Liepmann, H. W.; and Roshko, A.; Elements of Gas Dynamics, John Wiley and Sons, Inc., New York, 1965.

3. Bray, K. N. C.; "Atomic Recombination in a Hypersonic Wind Tunnel Nozzle," J. Fluid Mech., Vol. 6, Part 1, pp. 1-32.

4. Shell, D. R.; and Prophet, H.; (Project Directors); JANAF Thermochemical Tables, Second Edition, NRSD-NBS 37, June 1971.

5. Vincent, W. G.; and Kruger, C. H.; Introduction to Physical Gas Dynamics, John Wiley and Sons, Inc., New York, 1965.

6. Schlichting, H.; Boundary Layer Theory, 4th Edition, McGraw-Hill Book Company, Inc., New York, 1960.

7. Ladenburg, R. W.; and Bershader, D.; Physical Measurements in Gas Dynamics, Princeton University Press, Princeton, 1954.

8. Gooderon, P. B.; Wood, G. P.; and Brevourt, M. J.; NACA TN 1857, 1949.

9. Winckler, J.; "The Mach Interferometer Applied to Studying an Axially Symmetric Supersonic Air Jet," Rev. of Scientific Insts., Vol 19, No. 5, May 1948.

10. Howes, W. L.; and Buchele, D. R.; "Optical Interferometry of Inhomogenous Gases," J. Opt. Soc. Am., 56, p. 1517, 1966.

11. Bunting, J. O.; and DeVoto, R. S.; Shock Tube Study of the Thermal Conductivity of Argon, SUDAR Report 313, Dept of Aeronautics and Astronautics, Stanford University, July 1967.

12. Rumpel, W. F.; Yanow, G.; and Penning, D. F.; "Measurement of the Indices of Refraction of Fluorine and Hydrogen Fluoride," J. Chem. Phys., 57, p. 3011, 1972.

13. Allen, C. W.; Astrophysical Quantities, University of London, Athlone Press, 1955.

14. Menard, W. A.; and Thomas, G. M.; Radiation Measurement Techniques, Technical Report No. 32-975, Jet Propulsion Laboratory, Pasadena, California, August 1966.

15. Stair, R.; Johnston, R. G.; and Halbach, E. W.; "Standard of Spectral Radiance for the Region of 0.25 to 2.6 Microns," J. Research NBS64A, p. 291, July-August 1960.

16. Shapiro, A. H.; The Dynamics and Thermodynamics of Compressible Fluid Flow, The Ronald Press, New York 1953.

17. Kovásznay, L. S. G.; "The Hot Wire Anemometer in Supersonic Flow," J. Aeronautical Sciences, Vol 17, No. 9, pp. 565-572, September 1950.

18. Morkovin, M. V.; Fluctuations and Hot Wire Anemometry in Compressible Flows, AGARDograph No. 24, NATO, Paris, 1956.

19. Morkovin, M. V.; "Effects of Compressibility on Turbulent Flows," The Mechanics of Turbulence, Gordon and Breach, New York, pp. 367-380, 1964.

20. Kovásznay, L. S. G.; "Turbulence in Supersonic Flow," J. Aeronautical Sciences, Vol 20, No. 10, pp. 657-674, October 1953.

21. Kistler, A. L.; "Fluctuation Measurements in a Supersonic Turbulent Boundary Layer," Phys. Fluids, Vol 2, No. 3, pp pp. 290-296, March 1959.

22. Demetriades, A.; "Turbulence Measurements in an Axisymmetric Compressible Wake," Phys. Fluids, Vol II, No. 9, pp. 1841-1852, November 1968.

23. Glass, D. R.; The Effects of Acoustic Feedback on the Spread and Decay of Supersonic Jets, AIAA Paper No. 68-80, 1968.

24. Sanderson, R. J.; and Steel, P. C.; Results of Experimental and Analytical Investigations in Compressible Turbulent Mixing, R-70-48638-003, Martin Marietta Corporation, Denver, Colorado, September 1970.

25. Wooldridge, C. E.; and Muzzy, R. J.; Boundary Layer Turbulence Measurements with Mass Addition and Combustion, AIAA Paper No. 65-820, 1965.

26. Kulgein, N. G.; "Transport Processes in a Combustible Turbulent Boundary Layer," J. Fluid Mech., Vol 12, Pt. 3, pp. 417-437, March 1962.

27. Harsha, P. T.; Free Turbulent Mixing; A Critical Evaluation of Theory and Experiment, AEDC-TR-71-36, February 1971.

28. Donaldson, C. duP.; A Progress Report on an Attempt to Construct and Invariant Model of Turbulent Shear Flows, ARAP Report No. 170, Aeronautical Research Associates of Princeton, Princeton, October 1971.

29. Heyman, R. J.; A Transformation Theory for Turbulent Axisymmetric Ejector Mixing, AFRPL-TR-65-229, January 1966, and AFRPL-TR-66-31, March 1966.

30. Sanderson, R. J.; A Shock Tube Facility for Turbulent Mixing Studies, R-66-5, Martin Marietta Corporation, Denver, Colorado, July 1966.

31. Heyman, R. J.; Sanderson, R. J.; and Steel, P. C.; "Turbulent Mixing Layers in Modern Flight Systems," Proc. AAS Symposium - Rocky Mountain Resources for Aerospace Science and Technology, June 1967.

32. Murphy, J. M. "Combustion in the Turbulent Mixing Zone Between Parallel Streams," Proc. J.S.M.E. Semi-International Symposium, Tokyo, pp. 233-285, September 1967.

33. Heyman, R. J.; Sanderson, R. J.; and Steel, P. C.; Combustion In Compressible Mixing Flows, Western States Section/Combustion Institute, Paper 68-28, October 1968.

34. Steel, P. C.; Turbulent Mixing Analysis Program, R-69-48638-003, Martin Marietta Corporation, Denver, Colorado, May 1969.

35. Heyman, R. J.; The Thermal Energy Equation for Turbulent Shear Flows, Western States Section/Combustion Institute, Paper 69-43, October 1969.

36. Sanderson, R. J.; and Steel, P. C.; Measurement of Physical Properties and Growth Rate in a Burning Supersonic Mixing Layer, Western States Section/Combustion Institute, Paper 70-16, 1970.

37. Sanderson, R. J.; and Steel, P. C.; "Results of a Shock Tube Experiment in Compressible Turbulent Mixing," Proc. 8th International Shock Tube Symposium, London, July 1971.

38. Hinze, J. O.; Turbulence, Chapter V, McGraw-Hill, New York 1969.

39. Drewry, J.; Supersonic Mixing and Combustion of Coaxial Hydrogen-Air Streams in a Duct, ARL 71-0286, Aerospace Research Laboratories, Wright-Patterson AFB, December 1971.

40. Shackleford, W. S.; Private Communication, August 1972.

41. Dryden, H. L.; "Transition from Laminar to Turbulent Flow," Turbulent Flows and Heat Transfer (C. C. Lin, ed.), High Speed Aerodynamics and Jet Propulsion, Vol 5, Chapter A, Princeton University Press, Princeton, 1959.

42. Landau, L. D.; and Lifshitz, E. M.; Fluid Mechanics, Pergamon Press, New York, pp. 114-116, 1959.

43. Edelman, R.; and Fortune, O.; Mixing and Combustion in the Exhaust Plumes of Rocket Engines Burning RP1 and Liquid Oxygen, Technical Report No. 631, General Applied Science Laboratories, Westbury, N.Y., November 1966.

44. Cohen, N.; A Review of Rate Coefficients for Reactions in the H_2-F_2 Laser System, The Aerospace Corporation, El Segundo, California (work supported by USAF, Contract F04701-71-C00172).

45. Moretti, G.; "A New Technique for the Numerical Analysis of Nonequilibrium Flows," AIAA J., Vol 3, No. 2, February 1965.

46. DeGroat, J.; and Abbett, M.; "A Computation of One-Dimensional Combustion of Methane," AIAA J., Vol 3, No. 2, February 1965.

47. Anon.; JANAF Thermochemical Tables, The Dow Chemical Company, Midland, Michigan, December 1960 (incl supplements through June 1972).

48. Abramovich, G. N.; The Theory of Turbulent Jets, Chapter 5, MIT Press, Cambridge, Mass., 1963.

49. Anon.; Users Manual - Variable O/F Ratio Method of Characteristics Program for Nozzle and Plume Analysis, LMSC-HREC D162220-IV.